UNIVERSITÉ DE LORRAINE
École doctorale: Chimie-Mécanique-Matériaux-Physique (C2MP)
Institut Jean Lamour, UMR 7198 CNRS, Campus ARTEM, 54011 Nancy, France

THÈSE

Présentée et soutenue publiquement le 16 Juillet 2020
pour l'obtention du titre de

DOCTEUR de L'UNIVERSITÉ DE LORRAINE

Spécialité : Sciences des matériaux
Par

Shantanu Misra

Towards highly-efficient telluride-based thermoelectric materials

Composition de jury :

Sylvie Hebert	Rapporteur	Directeur de recherche - CNRS, CRISMAT, ENSICAEN, Caen, France
Eric Alleno	Rapporteur	Chargé de Recherche - CNRS, Laboratoire ICMPE, Université Paris Est, Paris, France
Nicole Fréty	Examinateur	Professeur, Laboratoire ICG, l'Université de Montpellier, Montpellier, France
Marie-Pierre Planche	Examinateur	Maître de conférence, Laboratoire ICB, Université de Technologie de Belfort – Montbéliard, Belfort, France
Christophe Candolfi	Directeur de thèse	Maître de conférence, Institut Jean Lamour, Université de Lorraine, Nancy, France
Bertrand Lenoir	Co-directeur de thèse	Professeur, Institut Jean Lamour, Université de Lorraine, Nancy, France
Anne Dauscher	Invitée	Chargé de Recherche - CNRS, Institut Jean Lamour, Université de Lorraine, Nancy, France

The only source of knowledge is experience

- Albert Einstein

Dedicated to my family

Acknowledgements

Although this thesis work will always represent me but modern science is impossible without the support and trust of several people.

First, without a doubt, I would like to thank my supervisors, Dr. Christophe Candolfi and Prof. Bertrand Lenoir. It was an honor and pleasure to work with you that made this journey so easy and smooth. The amount of knowledge I have gathered from both of you is immense. Thank you for being so patient and assuring. Thank you for all the advices, ideas and moral support in guiding me through this PhD. Your wealth of knowledge in the field of both experimental and theoretical physics is inspiring. The environment you created in the lab was motivating and positive to work. Thank you for giving me an opportunity to learn and develop myself. With no hesitation, I can say that I could not have had any better supervisors.

I would like to thank my thesis jury members for taking the time to read my manuscript and considering it worthy of the title. Thank you to Prof. Nicole Fréty, Dr. Sylvie Hebert, Dr. Eric Alleno, and Dr. Marie Pierre-Planche for all your nice questions and strong words of appreciation. I would also want to add special acknowledgments to my follow-up committee members, Prof. Nicole Fréty and Dr. Gaëlle Dalaizir who constantly encouraged me to do good work.

Special thanks to Dr. Anne Dauscher who was always there to help me and support me in my professional as well as personal life. Right from clearing my administrative doubts to helping me analyze my microscopic images, you have done it all. Also a big thank you for hosting us at Ventron every year and allowing us to spend such wonderful time in the mountains of the Vosges.

I extend my sincere thanks to Philippe Masschelein for the incredible and non-stop support provided to make sure that all my experimental instruments were running smoothly. You were always there to fix any problem and hence I will always be grateful to you.

I would like to thank Director and all the members of Institut Jean Lamour, University of Lorraine who always assisted me in one or the other way over this journey. Special thanks to the Competence Centre at Institut Jean Lamour for making it possible to perform additional experiments without any complications. I own a special gratitude to all my collaborators who made this work more interesting and helped me discover things beyond my skill sets. Particular thanks to Dr. Bartlomiej Wiendlocha, AGH University of Science and Technology, Krakow, Poland for providing strong theorectical support that made this work complete in all fronts.

My whole hearted thanks to my fellow teammates Soufiane, Selma and Dorra. We were a small yet strong family. You not only helped me settle down in the lab but also made me laugh and always stay motivated. I am glad to have friends like you. I also own a big thanks to my friends from the lab with whom I have had countless funny moments. Thank you Vitalis, Agathe, Alexis, Kanika and Mostapha. I also want to thank all the amazing friends I made in Nancy who were always there to spend a chill evening with me and show me a life outside the PhD. Special mentions to Mainak, Divyesh and Mayank. I have to thank all my friends and colleagues from India and Japan who always pushed me to achieve more. I apologize that I cannot mention everyone here but you were and still be an important part of my life.

I would like to thank my previous supervisors Dr. D. K. Aswal, Director, National Physical Laboratory, New Delhi, India and Prof. Yasuhiro Hayakawa, Shizuoka University, Japan who actually introduced me to the topic of thermoelectricity and helped me develop it even before I began my PhD.

Finally, I would like thank my parents, Dr. Shiv Kumar Misra & Vandana Misra and my sister, Srishti Misra without whom everything was just next to impossible. You always believed in me when I did not myself. Even though you were thousands of kilometers away, your constant love and support was always there with me. I hope I made you all proud.

Abstract

The search to replace the toxic lead telluride (PbTe) alloys for thermoelectric applications in power generation has led to intensive studies of other telluride-based chalcogenide semiconductors. In this context, the binary SnTe has re-emerged over the last years as a promising candidate due to its rock-salt structure and electronic valence band structure similar to PbTe. Indium is a particularly intriguing dopant for SnTe as it leads to the appearance of a resonant level and superconductivity. Another noteworthy chalcogenide semiconductor, InTe has been recently shown to harbor promising thermoelectric properties due to its remarkably very low lattice thermal conductivity. The lack of detailed studies of its transport properties makes this compound a promising area of research in the field of thermoelectrics.

In this work, we report on a detailed experimental and theoretical investigations of the transport properties of these two Te-based chalcogenides (XTe; X = Sn, In) in a wide range of temperatures (2 – 800 K). In a first part, the influence of indium on the transport properties of $Sn_{1.03-x}In_xTe$ ($0 \leq x \leq 40$ %) is considered. The experimental results are supported by electronic band structure calculations performed using the Korringa-Kohn-Rostoker method with the coherent potential approximation (KKR-CPA). Both experimental and theoretical results demonstrate the resonant nature of In in $Sn_{1.03}Te$ with an optimum doping level of 2% giving the highest thermopower value for this system. Low-temperature transport properties measurements further highlight the complex evolution of the transport properties for low In contents.

Investigations performed on InTe were performed on both single-crystalline and polycrystalline samples. A large single crystal of InTe was grown by the vertical Bridgman method. The possibility to control the defect concentration in InTe was considered though the saturation annealing method, carried out on the In-rich and Te-rich side of the solidus. Comparable to the peak ZT of ~ 0.7 at 780 K achieved in single-crystalline InTe within the ab plane, a maximum ZT of ~ 0.9 at 710 K was obtained in polycrystalline InTe.

Contents

Notations and Nomenclature

dV	Voltage difference	υ	Speed of sound
α	Thermopower	l	Phonon mean free path
dT	Temperature difference	N	Number of atoms
q	Heat flux, elementary charge	k_B	Boltzmann constant
Π	Peltier coefficient	E	Energy
I	Current	E_F	Energy at the fermi level
dQ	Thomson heat	σ	Electrical conductivity
τ	Thomson coefficient, Relaxation time	DOS	Density of States
T	Absolute temperature	h	Planck's constant
COP	Coefficient of Performance	m^*	Effective mass
$\emptyset_F$	Overall heat extracted	n	Carrier concentration, number of atoms per formula unit
P	Power dissipated, Power factor, Number of phases in a system	μ	Carrier mobility
T_c	Temperature of the cold end	β	Material parameter
K	Thermal conductance	m_0	Free electron mass
R	Electrical resistance	p, p_h	Hole concentration
A	Area of cross-section	T_{FT}	Ferroelectric transition temperature
ρ	Electrical resistivity	SOC	Spin orbiting coupling
κ, κ_{total}	Total thermal conductivity	$\Delta\varepsilon_{VB_{L-\Sigma}}$	Energy separation between the maxima of the two last valence band in SnTe
ZT	Dimensionless thermoelectric figure-of-merit	VB	Valence band
T_c	Average temperature	CB	Conduction band
T_h	Temperature of the hot end	E_g	Energy band gap
ZT_{avg}	Average ZT	m^*_{DOS}	Density of states effective mass
η	Thermoelectric efficiency, Reduced fermi energy	N_V	Number of degenerate valleys
η_c	Carnot efficiency	m^*_b	Single valley effective mass
κ_e	Electronic thermal conductivity	RL	Resonant Level
κ_l, κ_{ph}	Lattice thermal conductivity	T_c	Superconductivity transition temperature
L	Lorenz number	δ	Inherent tin vacancies
C_p	Specific heat capacity	KKR	Korringa-Kohn-Rostoker
BSF	Boch Spectral Function	CPA	Coherent Potential Approximation

PXRD	Powder X-Ray Diffraction	*SEM*	Scanning Electron Microscope
E_D, E_0	Energy of the resonant level	*Γ,Δ*	Width of the resonant level
$\hbar$	Reduced planck's constant	*LDA*	Local Density Approximation
V	Unit cell volume	*SPS*	Spark Plasma Sintering
d	Experimental density	*m*	Mass of the pellet
Z	Multiplicity of the unit cell	*M*	Molar mass
N_A	Avogadro number	r_H	Hall factor
ρ_0	Residual resistivity	μ_H	Hall mobility
γ	Somerfield coefficient	θ_D	Debye temperature
R	Gas constant	m_{lh}^*	Light hole valence band effective mass
m_{hh}^*	Heavy hole valence band effective mass	*TVB*	Two Valence Band
TI	Temperature Independent	*TD*	Temperature Dependent
SPB	Single Parabolic Band	C_{ph}	Specific heat capactiy due to the phonons
T_H	Temperature at the highest point	T_L	Temperature of the lowest point
$\mu_0 H$	Magnetic field	*EDXS*	Energy Dispersive X-Ray Spectroscopy
CDW	Charge Density Wave	*PDOS*	Phonon Density of States
DFT	Density Functional Theory	*PAW*	Projector Augmented Wave
VASP	Vienna ab-initio Simulation Package	*GGA*	Generalized Gradient Approximation
V_0	Volume of the unit cell	*ADP*	Atomic Displacement parameter
N_D	Number of Debye oscillators per formula unit	θ_{Ei}	Einstein temperature
$p_i N_{Ei}$	Spectral weight	C_D	Lattice contribution in the specific heat capacity
C_{Ei}	Einstein contribution in the specific heat capacity	*F*	Number of degree of freedom
C	Number of components	$F_i(\eta)$	Fermi integral

General Introduction

Future energy usage mandates the need for alternative energy sources that have less environmental impact than the fossil fuels. Despite the limitation problems of energy resources, about 70% of the energy consumed in industries or private household is lost to the environment. Converting this waste heat into useful electrical energy would contribute to lower our environmental impact. One possible technology to tackle this problem includes the use of thermoelectric devices. Over recent years, thermoelectricity has become a forefront, green technology in capturing the waste heat dissipated to generate electrical power. Thermoelectric devices, that can directly convert waste heat into electrical energy or vice versa, are solid-state devices that can be used with any kind of thermal sources and have numerous advantages when compared to any other energy converting devices. These advantages include their compactness, noise- and vibration-free due to the absence of moving parts, their reliability for long-time operations and the absence of greenhouse gas emissions. These devices can thus be utilized for remote applications in extreme environments and in both small-scale as well as high-scale industries. Thermoelectric devices, should they be generators or refrigerators, can excel in the industries that are currently facing the problem of high cost and low performance. Thermoelectric (TE) generators are used in various domains for which the reliability of the devices outweighs their low conversion efficiency. One of the main application area is the powering of deep-space probes and rovers using Radioisotope Thermoelectric Generators (RTGs) by NASA, since 1961. The lifetime of these generators is comparable to human life time, as in the example of Voyager 1 and 2 missions that recently left the solar system and for which, the TE devices are still running after 42 years. The most recent mission to study Mars surface, Curiosity, is also powered by a RTG giving an output electrical power of around 110 Watts. Recently, it has been shown that using thermoelectric generators in automobiles may increase the fuel economy by 7–10%. Thermoelectricity has also been successfully introduced in solar TE generators and micro-generators where the power required is low. Thermoelectric cooling applications (that is, refrigeration) have been successfully used in air-conditioning, food refrigerators and cooling of charge coupled device's infrared detectors.

The binary semiconductor PbTe, along with $Si_{1-x}Ge_x$ alloys, has been one of the long-known and reliable material for RTGs due to its high thermoelectric performances and easily tunable transport properties. Over the last few decades, researchers have been constantly able to improve the dimensionless thermoelectric figure of merit, *ZT*, that governs the efficiency of

the thermoelectric devices, of PbTe-based materials for mid-temperature range applications. Despite being a promising material, PbTe presents the problem of lead toxicity, which makes it an impractical candidate for terrestrial commercial applications. The search for Pb-free compounds have lead researchers to reinvestigate chalcogenide semiconductors such as SnTe, GeTe and recently InTe.

The present thesis work focuses on two telluride-based chalcogenide materials (*X*Te; *X* = Sn, In) for mid-temperature range thermoelectric applications. SnTe has recently re-emerged as the first-choice replacement of PbTe due to its similar rock salt crystal structure and similar electronic valence band structure. The possibility to induce a Resonant Level (RL) in its valence band structure through substitution of In for Sn provides an interesting strategy to improve the thermoelectric properties. However, compared to the canonical RL-containing system PbTe:Tl, the role played by the In-induced RL on the transport properties of SnTe remains poorly understood. InTe is also a promising chalcogenide material due to its very low lattice thermal conductivity. However, due to very limited number of studies reported in the literature, InTe remains an intriguing material that warrants further theoretical and experimental investigations.

The main objective of this thesis work is to study and optimize the thermoelectric properties of telluride-based chalcogenide materials (*X*Te; *X* = Sn, In) over a wide range of temperatures (2 – 800 K). The manuscript is divided into four chapters.

Chapter 1 will be devoted to a brief presentation of the different principles, challenges and solutions existing in the field of thermoelectricity. In particular, the fundamental equations pertaining to thermoelectricity will be presented as well as the general guiding principles for identifying a good thermoelectric material. A brief overview of the most important and highly-efficient conventional as well as novel thermoelectric materials will conclude this chapter.

Chapter 2 provides a comprehensive literature survey of the general structural, chemical and physical properties of *p*-type SnTe. A general review of the thermoelectric properties of SnTe will be presented, highlighting the potential of SnTe as a TE material. Based on this overview, an additional in-depth review of the effect of In on the transport properties of SnTe will be given, covering the important phenomena such as resonant level, superconductivity and the proposed charge-Kondo effect.

Chapter 3 is dedicated to the in-depth study of the transport properties of In-doped SnTe over a wide range of temperatures (2 – 800 K). A first part will focus on a detailed introduction of the formation of resonant levels in bulk semiconductors. A thorough discussion of the structural, chemical and physical properties of the series $Sn_{1.03-x}In_xTe$ ($0 \leq x \leq 40$ %) will

follow. The transport properties will be supported by electronic band structure calculations performed using the Korringa-Kohn-Rostoker method with the coherent potential approximation (KKR-CPA), performed in collaboration with Dr. Bartlomiej Wiendlocha and Prof. Janusz Tobola from the AGH University of Science and Technology in Krakow (Poland). These calculations will allow us a better understanding of the influence of In on the low- and high-temperature properties, highlighting in particular specific signatures of the RL on the transport properties.

Chapter 4 will provide a complete literature review of the transport properties of InTe-based materials. Following this first part, we will present the basic physical properties of both single-crystalline InTe (grown using Bridgman technique) as well as polycrystalline InTe over a wide range of temperatures (5 – 800 K). Due to the inherent defect chemistry of this compound, the saturation annealing technique will be presented, followed by a presentation of the experimental implementation of this technique for polycrystalline InTe. This technique allows for probing the maximum deviations from the ideal stoichiometry on both the In-rich and Te-rich sides of the solidus. The measured transport properties will be discussed based on electronic band structure calculations realized in collaboration with Dr. Céline Barreteau and Dr. Jean-Claude Crivello from the Institut de Chimie et des Matériaux Paris-Est in Thiais (France). The transport properties of as-prepared and saturation-annealed polycrystalline samples will be presented, highlighting in particular the possible presence of a structural transition at low temperatures.

Chapter 1 Introduction to thermoelectricity

1.1 Overview

Thermoelectric effects are physical phenomena that directly convert heat into electrical energy or vice versa. This chapter aims to introduce the concepts and main applications of thermoelectricity. After briefly recalling the important historical events related to this field, the focus will shift on describing the fundamental equations that govern the thermoelectric effects. The equations related to thermoelectric efficiency and a detailed discussion of guiding principles for material selection will follow. The last part of the chapter describes the state-of-the-art and advanced thermoelectric materials discovered and optimized over the last few decades and the new research avenues aiming to design novel thermoelectric materials with enhanced thermoelectric performances.

1.2 Thermoelectricity

Thermoelectric effects originate from the coupling of electrical and thermal phenomena. There are three dominant effects in thermoelectricity: the Seebeck effect, the Peltier effect and the Thomson effect. Electrical and heat conduction are two irreversible diffusion phenomena that interact in a thermodynamic system when present simultaneously. The thermodynamic of irreversible processes describes in detail the physical phenomena occurring in such systems. This theory enables describing effects that occur in systems out-of-equilibrium, which are typically induced by an external supply of energy or matter. In this approach, the flows and generalized forces are fundamental quantities that can describe in a unified way the transport properties in continuous media and the relaxation phenomena as they approach equilibrium. Physically, when a system deviates from equilibrium, variations in the intensive thermodynamic variables occur, but on a macroscopic scale (that is, in temperature, chemical potential, etc.). This deviation results in gradients associated with generalized forces. As a result, these gradients can generate a flow of particles, such as electron or phonons, which describes the response of the system to these gradients. In a complex system, several forces can be simultaneously present and, in such a case, the flow depends on both the intensive local variables and their gradients. Therefore, each flow must be related to all of these forces. If the system is not too far from thermodynamic equilibrium, a linear relation between the generalized forces and the associated flows can be assumed. The coefficients linking both

quantities are the kinetic coefficients of the system and are themselves related to the transport coefficients which can be measured experimentally.

Onsager was one of the pioneer to establish the foundation of thermodynamics of irreversible processes.[1,2] Its application to thermoelectric phenomena was later on developed by Callen and Domenicali.[3,4] In the next paragraphs, this theory will not be discussed in detail and we will rather focus on the phenomenogical aspects of the thermoelectric effects. Readers interested in the theoretical aspects of these effects can refer to the excellent monograph of De Groot and Mazur.[5]

In 1823, Thomas Johann Seebeck showed that a temperature difference between two dissimilar metals or semiconductors (A and B) in a circuit produces an electric voltage under open circuit conditions, as shown in Figure 1.1.

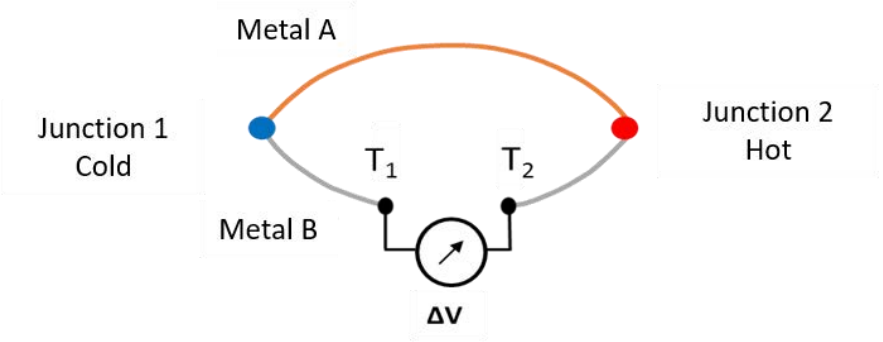

Figure 1.1: Illustration of the Seebeck effect.[6]

The voltage generated in the circuit is known as the Seebeck electromotive force, which directly depends on the temperature difference. This effect, dubbed as the Seebeck effect, can be mathematically defined as:[7]

Equation 1.1:

$$dV = \alpha_{AB}\, dT$$

where dV is the voltage difference, dT is the temperature difference (supposed to be small) and α_{AB} is the relative Seebeck coefficient ($\alpha_{AB} = \alpha_A - \alpha_B$) between the two materials. From Equation 1.1, the Seebeck coefficient or thermopower of a material, α, can be defined as:

Equation 1.2:

$$\alpha = \frac{dV}{dT}$$

This coefficient can be positive or negative depending on the charge carrier responsible of the electronic transport. It is worth mentioning that the first observation of what is now referred to as the Seebeck effect, was made by Alessandro Volta, 28 years prior to T. J. Seebeck using a frog.[8] Unfortunately, history did not keep in memory the discovery of Volta.

In 1832, a French watchmaker, Jean-Charles Athanase Peltier found that, when a current I flows through the same circuit (Figure 1.2) under isothermal conditions, a heat flux q at the junction is produced. This heat flux can be produced or absorbed depending on the direction of the applied current:

Equation 1.3:

$$q = \Pi_{AB}\, I$$

where Π is the relative Peltier coefficient, between the two materials A and B.[9]

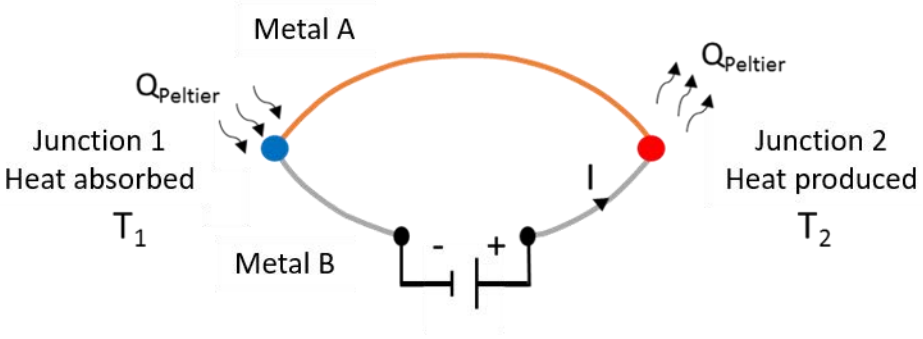

Figure 1.2: Illustration of the Peltier effect.[6]

If the demonstration of the Peltier effect involves two materials, it is important to underline that, as for the Seebeck effect, a Peltier coefficient, Π, can be defined for one material and should be considered as an intrinsic transport property of the material. This coefficient can be also positive or negative.

In 1855, William Thomson (later known as Lord Kelvin) provided a relation between the Seebeck and Peltier coefficients and theoretically predicted a third thermoelectric effect that was later demonstrated experimentally by Thomson himself. He showed that a material

exchanges heat with its environment when it is subjected to a temperature gradient and an electrical current, simultaneously. In other words, the heating or cooling rate in the material is proportional to the electrical current I and temperature difference dT through the Thomson coefficient τ given by:

Equation 1.4:

$$dQ = \tau I \, dT$$

where dQ is the Thomson heat and τ the Thomson coefficient that can be also positive or negative.The relations between α, Π and τ for a single material were given by Thomson as (also known as Kelvin's relations):[10–12]

Equation 1.5:

$$\Pi = \alpha T$$

Equation 1.6:

$$\tau = T \, d\alpha/dT$$

1.3 Thermoelectric device

The Seebeck and Peltier effects can be exploited advantageously for many modern devices that need to convert waste heat into electrical energy or vice versa. These devices include thermoelectric refrigerators (heat pumps) and thermoelectric power generators.

The basic structure of a conventional thermoelectric device is illustrated in Figure 1.3. An *n*-type (electrons are the main charge carriers) and a *p*-type (holes are the main charge carriers) semiconductors are connected through metallic contacts electrically in series and thermally in parallel. The same circuit could be tuned and used for both refrigerators and generators depending on the need. When an electric current passes through the thermocouple, heat is produced across the material. According to the direction of the current, heat is absorbed on one end and produced on the other end (Peltier effect). This device will act as a refrigerator or a heat pump. Conversely, if an external temperature difference is applied to the thermocouple (Seebeck effect), electrical power will be delivered to an external load and the device will act as a generator.

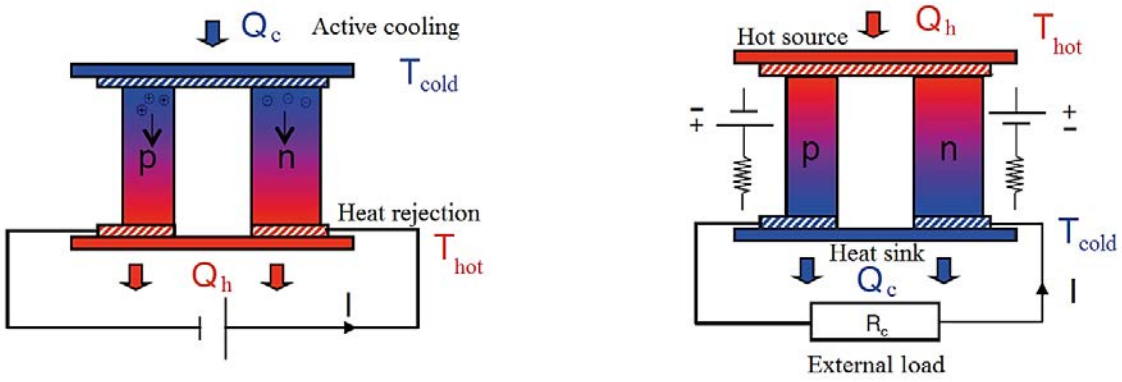

Figure 1.3: Schematic diagram of a single thermocouple for a) Refrigeration and b) Generation. The TE couple consists of *n*- and *p*-type semiconducting branches. Several TE couples are used to build a thermoelectric device.[13]

1.4 Performance of a thermoelectric device

1.4.1 Thermoelectric efficiency

Qualitatively, a good thermoelectric material should be characterized by a Seebeck or Peltier coefficient as high as possible to obtain a sizeable TE effect. The electrical resistivity ρ should be also minimized to reduce the heat losses via the Joule effect and the thermal conductivity κ should be as low as possible to maintain the temperature difference. All these coefficients play an important role in the performances of a thermoelectric device but the relation linking them is not straightforward. However, under the assumptions of fixed temperatures for the boundary conditions, temperature-independent transport coefficients, absence of heat losses and perfect electrical and thermal contacts, a simple relation between α, ρ and κ can be derived. The first derivation of this relation was made by Altenkirch in the case of a generator.[14,15]

Keeping in memory all these assumptions, let's see now what are the main equations governing the performances of a thermoelectric refrigerator and generator. For a detailed derivation and explanation, the reader can refer to the book by Macia-Barber.[16] The coefficient of performance (COP) of a thermoelectric refrigerator is defined as the ratio of the amount of heat extracted at the cold end, $\emptyset_F$, to the power P dissipated electrically:[17]

Equation 1.7:

$$COP = \frac{\emptyset_F}{P}$$

The overall heat extracted $\emptyset_F$ can be expressed as:

Equation 1.8:

$$\emptyset_F = I\,T_c\left(\alpha_p - \alpha_n\right) - K\Delta T - \frac{I^2R}{2}$$

where the first term represents the Peltier cooling contribution, the second term is the heat leakage from the hot junction due to Fourier diffusion and the last term describes the fraction of Joule heat generated in the legs flowing back to the cold junction. The coefficients K and R are the thermal conductance and the electrical resistance, respectively. Both depend on the geometry of the *n* and *p*-legs. The power P given by the external source is given by:

Equation 1.9:

$$P = \left(\alpha_p - \alpha_n\right)I\Delta T + RI^2$$

where the first term is the work done against the Seebeck voltage and the second term is the Joule heating due to the electrical resistance of the legs. From Equations 1.8 and 1.9, it is evident that the C.O.P. of the cooler depends on the current of the external source and on the geometry of the legs through K and R. Optimizing these parameters leads to a criterion on the geometry and to a maximal value of the coefficient of performance. The criteria on the geometry is given by:

Equation 1.10:

$$\frac{A_p}{A_n} = \sqrt{\frac{\rho_p\kappa_n}{\rho_n\kappa_p}}$$

where A, ρ and κ are the cross-section area, the electrical resistivity and the thermal conductivity of the legs, respectively. This relation shows that the transport properties of the thermoelectric materials should be similar in order to avoid a large mismatch in the cross-

section of the legs that could result in high stress levels, thereby affecting the mechanical robustness of the module. The maximum C.O.P. is defined by:

Equation 1.11:

$$C.O.P = \emptyset_C \frac{\sqrt{1+ZT_m} - \frac{T_h}{T_c}}{\sqrt{1+ZT_m}+1}$$

where $\emptyset_C$ is the Carnot efficiency (that is, the limit) for cooling which is equal to $T_c/\Delta T$, T_m is the average temperature of the coolers and Z_{np} is the so-called the thermoelectric figure of merit defined as:

Equation 1.12:

$$Z_{np} = \frac{(\alpha_p - \alpha_n)^2}{[(\rho_p \kappa_p)^{1/2} + (\rho_n \kappa_n)^{1/2}]^2}$$

The dimensionless thermoelectric figure of merit, $Z_{np}T_m$, impacts strongly the maximum COP of the cooler as can be seen in Figure 1.4 (a) where the maximum COP is plotted as a function of the temperature ratio T_h/T_c for various $Z_{np}T_m$ values. This figure evidences that achieving high COP requires high $Z_{np}T_m$ values. For comparison, a typical domestic cooler has a C.O.P. corresponding to a $Z_{np}T_m$ value of around 3.

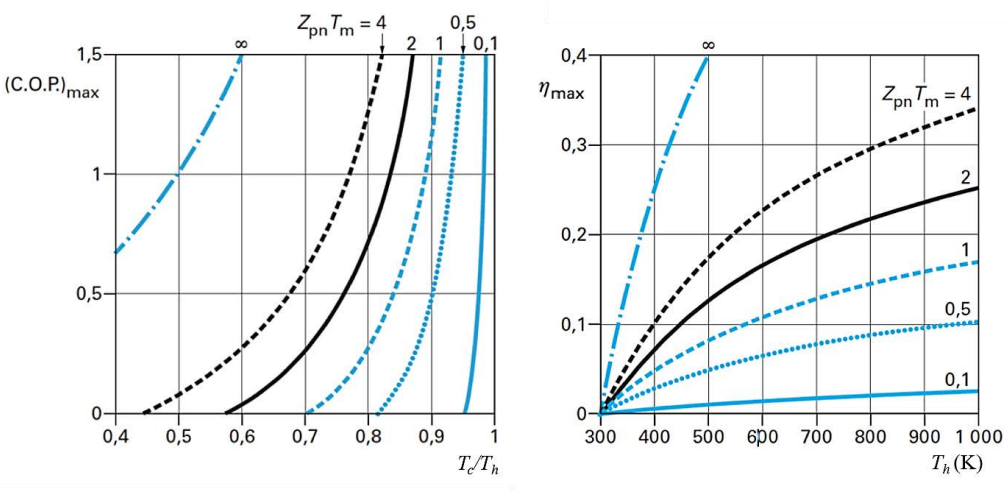

Figure 1.4: Maximum a) COP as a function of $\frac{T_h}{T_c}$ for different $Z_{np}T_m$ values. b) Efficiency as a function of the temperature of the hot end for different $Z_{np}T_m$ values (T_c = 300 K).[18]

Similarly, the thermoelectric efficiency η for a TE generator is defined as:

Equation 1.13:

$$\eta = \frac{P_O}{\phi_C}$$

where P_O is the output power delivered into the external load resistor and ϕ_C is the power extracted at the heat source. As for the cooler, the efficiency can be optimized by adjusting the geometry of the legs and by varying the load resistance. Taking into account these parameters, the maximum efficiency can be written as:[19]

Equation 1.14:

$$\eta_{max} = \frac{T_h - T_c}{T_h} \frac{\sqrt{1 + Z_{pn}T_m} - 1}{\sqrt{1 + Z_{pn}T_m} + \frac{T_h}{T_c}}$$

where $\frac{T_h - T_c}{T_h}$ is the Carnot efficiency η_C. The maximum output power generated is thermodynamically limited by the Carnot efficiency. Similarly, as shown in Figure 1.4 (b), achieving η_{max} also requires $Z_{np}T_m$ values as high as possible and large temperature differences to boost the Carnot efficiency.

1.4.2 Dimensionless Thermoelectric Figure of Merit

From Equations 1.11 and 1.14, it is clear that the $Z_{np}T_m$ value is the key parameter governing the performances of a thermoelectric device, should it be for cooling or for power generation. By analogy with the relation giving $Z_{np}T_m$, a dimensionless thermoelectric figure of merit *ZT* can be defined for a single thermoelectric material as:

Equation 1.15:

$$ZT = \frac{\alpha^2 T}{\rho \kappa_{total}}$$

where κ_{total} is the total thermal conductivity of the material and *T* the absolute temperature.

The three transport coefficients in Equation 1.15 determine the efficiency with which the material will convert heat into electrical energy and vice versa. What makes the optimization

of the *ZT* values a tremendous challenge is the interdependence of the three above-mentioned properties that will be discussed in the following sub-sections. To simplify, the optimization of the *ZT* value can be segmented into two parts: **i)** minimizing the heat transport while **ii)** optimizing the electronic properties.

1.4.2.1 Thermal conductivity

Thermal conductivity is a diffusion process involving quasi-particles that can transport heat. Some of the entities that are responsible for heat conduction in materials are phonons, that is, quantized lattice vibrations; free electrons and/or holes; electron-hole pairs; excitons; magnons; etc.[20] The heat conduction is limited by scattering events. Without any scattering processes, the thermal conductivity would be infinite. Scattering in materials arises due the various imperfections of the crystal lattice and to the conduction electrons or holes.[20] In non-magnetic materials, the total thermal conductivity is the sum of two terms:

Equation 1.16:

$$\kappa_{total} = \kappa_e + \kappa_{ph}$$

where κ_e is the electronic thermal conductivity and κ_{ph} (sometimes written as κ_l) is the thermal conductivity coming from the phonons (lattice) contribution.

The electronic part of the thermal conductivity (κ_e) is directly related to the electrical resistivity through the Wiedemann-Franz law as:[21]

Equation 1.17:

$$\kappa_e = \frac{LT}{\rho}$$

where *L* is the Lorenz number. This factor depends on the position of the chemical potential and the scattering mechanisms. For an ideal degenerate gas of electrons or holes, *L* is equal to 2.45×10^{-8} V^2 K^{-2}. The phonon contribution plays a very important role to improve the overall *ZT* of the material. This is the only term in the *ZT* formula (Equation 1.16) that is independent of other parameters and has no role on electronic properties. Kinetically, the lattice thermal conductivity can be expressed as:[22,23]

Equation 1.18:

$$\kappa_l = \frac{1}{3} C_p v l$$

where v is the speed of sound, l is the phonon mean free path and C_p is the isobaric specific heat of the material. In most cases, C_p is determined using the Dulong-Petit law, which states that, at high temperatures, the specific heat of a solid is $3Nk_B$ (N is the number of atoms and k_B is the Boltzmann constant) and hence, is temperature-independent.[24] At low temperatures, C_p is determined by the Debye theory.[25,26] When T is approaching 0 K, C_p rapidly decreases as $C_p \sim T^3$ which explains the marked decrease observed in the thermal conductivity of solids.[20]

Goldsmid *et al.* showed that materials made of atoms with high atomic weight would have lower speed of sounds, resulting in lower lattice thermal conductivity values.[27] It is also desirable to work with materials exhibiting low Debye temperatures due to resistive Umklapp processes, that is, phonon-phonon scattering, which reduces the lattice thermal conductivity. The phonon mean free path is directly dependent on the scattering mechanisms present in the material. More the scattering in the material, shorter will be the phonon mean free path, ultimately leading to lower lattice thermal conductivity. Experiments have also shown that complex compounds having crystal lattice made up of large atoms where the coordination number is high (forming complex polyhedra) limits the mean free path allowing the material to reach low lattice thermal conductivity. Apart from phonon-phonon scatterings in a material, introduction of external defects tends to reduce the lattice thermal conductivity significantly. Some mechanisms include alloy scattering, grain boundary scattering, isotope scattering, dislocation scattering, electron-phonon scattering, etc.[20] The discovery of new families of materials and techniques have validated these criteria and the most interesting ones will be discussed in the next sections of this chapter.

1.4.2.2 Electronic properties

Optimizing the electronic properties of a thermoelectric material is synonymous with increasing the power factor P ($= {}^{\alpha^2}/_{\rho}$). However, the thermopower and electrical resistivity are interdependent since they both vary with the carrier concentration. The thermopower can be related to the electronic band structure via the Mott formula:[28]

Equation 1.19:

$$\alpha = \frac{\pi^2 k_B^2 T}{3q} \times \frac{d\ ln\ \sigma\ (E)}{dE}\Big|_{E=E_F}$$

where q is the elementary charge, E is the energy and E_F is the energy at the Fermi level. This formula indicates that α is directly proportional to the logarithmic derivative of the electrical conductivity σ calculated at $E = E_F$. On further simplification, α is proportional to the first derivative of the density of states (DOS) near the Fermi level. The DOS, usually referred to as $g(E)$ and expressed in number of states per eV and per cm^{-3}, is the number of electronic states available per unit volume of the solid at energies between E and $E + dE$. It thus corresponds to the number of available states for electrons in a material at a particular energy. Mathematically the above-mentioned proportionality can be expressed as:

Equation 1.20:

$$\alpha \propto \frac{1}{DOS\ (E)} \times \frac{dDOS(E)}{dE}\Big|_{E=E_F}$$

Hence, increasing the DOS will favor high thermopower values. A high density of states can be achieved by the presence of several bands crossing the Fermi level for instance. If we consider a simple model for electron transport (parabolic band for a degenerate semiconductor), the relation between the carrier concentration and the thermopower can be expressed as:[29]

Equation 1.21:

$$\alpha = \frac{8\pi^2 k_B^2}{3qh^2} m^* T \left(\frac{\pi}{3n}\right)^{2/3}$$

where n is the carrier concentration, k_B is the Boltzmann constant, h is the Planck constant, q is the elementary charge and m^* is the density-of-states effective mass. Keeping only the material-dependent parameters, this relation simplifies to:

Equation 1.22:

$$\alpha \propto \frac{m^*}{n^{2/3}}$$

The electrical conductivity σ *(= 1/ρ)* is directly proportional to the charge carrier density by the following equation:

Equation 1.23:

$$\sigma = n\, q\, \mu$$

where μ is the carrier mobility. The mobility is defined as the ratio of the absolute value of the drift velocity by the electrical field. In terms of effective mass and relaxation time τ, μ is expressed as:[20]

Equation 1.24:

$$\mu = \frac{q\tau}{m^*}$$

Hence, high electron mobility will give rise to high electrical conductivity. However, high m^* will tend to decrease the mobility while, at the same time, will favor high thermopower values according to Equations 1.22 and 1.24. Similarly, increasing the effective mass (or decreasing the carrier concentration) will increase the thermopower but will concomitantly reduce the electrical conductivity. These two points show that both requirements are mutually incompatible, making the optimization of the power factor $\frac{\alpha^2}{\rho}$ a difficult task.

1.4.3 Selection of materials

To provide a general picture, a schematic view of the dependence of the thermoelectric properties on the carrier concentration at 300 K is shown in Figure 1.5.[30] Metals fail to be interesting thermoelectric materials due to their too high carrier concentration synonymous with low thermopower values (Equation 1.21). Moreover, insulators cannot be good candidates for the opposite reason, that is, their carrier concentration is in general very low yielding very high electrical resistivity values. It is clear that the maximum *ZT* value will be obtained between metals and insulators. At 300 K, it can be observed that the optimized carrier density is between 10^{18} to 10^{21} cm^{-3}. This region corresponds to highly-doped semiconductors and semimetals. Increasing the temperature will push this maximum to higher carrier density.

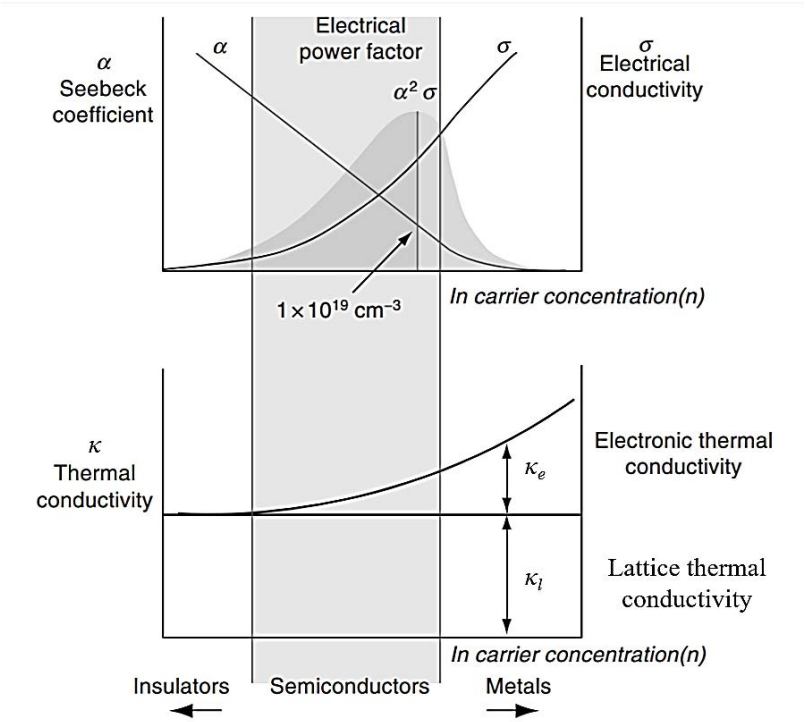

Figure 1.5: Schematic showing the relation of carrier concentration with the thermoelectric properties calculated at 300 K.[19]

Ioffe showed that qualitative information could be derived from the Boltzmann transport equation within the relaxation time approximation and considering only one band with a parabolic shape.[30] He stated that the Fermi level should be close to the edge of the valence bands (p-type material) or conduction bands (n-type material) to obtain a good compromise between high thermopower and low electrical resistivity. He also stated that the material parameter β is a key parameter to optimize in order to achieve high ZT values:

Equation 1.25:

$$\beta \propto \left(\frac{m^*}{m_0}\right)^{3/2} \frac{\mu}{\kappa_l}$$

where m_0 is the free electron mass. A large value of β is then highly recommended. Following this line, the ideal thermoelectric material should have large effective mass, high mobility of the charge carriers and low lattice thermal conductivity. These three properties are, however, mutually incompatible as high effective mass gives rise to low mobility. Hence, a compromise between these properties should be obtained. Keeping in mind the points discussed above, several guidelines have been developed as a guidance for the search and optimization of

compounds for thermoelectric applications. Summarizing some of these guidelines established for semiconductors in the last few decades are given in the following list: [17,19,30–33]

- Optimized materials should exhibit a carrier concentration in the range of 10^{18} – 10^{21} cm^{-3} depending on the working temperature,
- Materials composed of multi-element of high atomic weight forming large unit cell, with a low Debye temperature should be favored in order to limit the lattice thermal conductivity,
- A multi-valley band structure will be beneficial to maximize $\left(\frac{m^*}{m_0}\right)^{3/2}\mu$ without affecting too strongly the carrier mobility,
- High carrier mobility can be achieved in compounds with elements showing a low electronegativity difference,
- The energy band gap should fall in the range of 5 to 10 k_BT in order to minimize the presence of minority carriers (detrimental to achieve a high *ZT*),
- The Fermi level should be close to the edge of the valence bands (*p*-type material) or conduction bands (*n*-type material) to obtain a good compromise between high thermopower and low electrical resistivity,
- Increasing the atomic disorder in the system by forming solid solutions in order to increase phonon scattering and hence, to optimize the $\frac{\mu}{\kappa_l}$ ratio,
- Promote high effective mass and high DOS to increase the thermopower.

These various criteria and guidelines are set for providing a "recipe" with which a material may be optimized. Because the interdependence of these different properties makes it a very challenging task, various strategies have been developed in order to achieve *ZT* values rivalling or even surpassing those obtained in state-of-the-art thermoelectric materials, briefly presented in the next paragraph.

1.5 State-of-the-Art thermoelectric materials

Since the 1950s, numerous families of thermoelectric materials with high *ZT* values have been discovered and studied. These "conventional" thermoelectric materials have been implemented successfully in thermoelectric devices for both generation and refrigeration

applications. Indeed, most of the materials that are being used nowadays in the industries were already discovered before 1975 with *ZT* values on the order of 1, should it be at room or at high temperatures. Very few compounds presenting $ZT > 1$ were discovered around the end of the 20th century when new theoretical concepts were introduced and novel family of materials started to be studied. Some of these families have been termed as "advanced" or "novel" thermoelectric materials. A short survey of these materials is provided in the next sub-section. For a more detailed overview, several review papers can be consulted.[34–39]

1.5.1 Conventional materials

The most classical and conventional thermoelectric materials are Bi-Sb alloys, $(Bi,Sb)_2(Te,Se)_3$ solid solutions, Pb-Te based materials and Si-Ge alloys. They can be classified according to their operating temperature as shown in Figure 1.6.

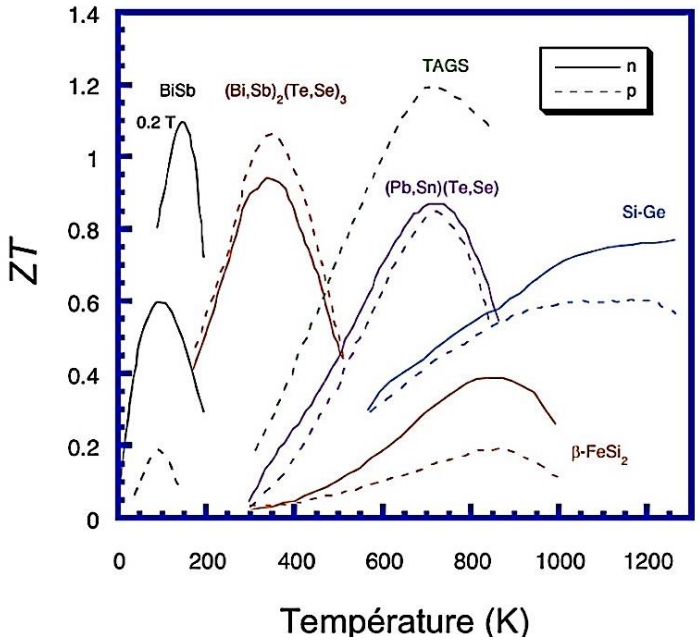

Figure 1.6: Typical *ZT* values of established p and n-type materials over a wide range of temperature.[18]

$Bi_{1-x}Sb_x$ alloys have been the only *n*-type materials that can be used for cryogenic applications due to their good thermoelectric properties near liquid-nitrogen temperatures. Smith and Wolfe reported a high $ZT > 1$ for undoped single-crystals Bi-rich alloys in the low temperature range of 20 and 220 K under a small magnetic field of 0.2 T.[40] However, the

absence of a good *p*-type material has hampered its use in TE devices.[41] For applications near room temperature, *n* and *p*-$(Bi,Sb)_2(Te,Se)_3$ solid solutions are the best candidates. For decades now, these materials have been commercially used for both cooling and power generation applications. These materials are the only known materials to date to exhibit a $ZT \sim 1$ at room temperature, making it a unique family of thermoelectric materials. However, above 450 K, these materials are chemically unstable and can no longer be used.[42]

At higher temperatures, materials that are chemically stable must be considered. PbTe-based alloys have been such materials which have been extensively used in this temperature range (500 – 800 K) due to their high thermoelectric performances. Both *n* and *p*-type electrical conduction can be achieved in PbTe either by doping or by manipulating the type of defects. For this reason PbTe alloys were used by NASA in radioisotope thermoelectric generators (RTGs) for space applications.[43] For instance, excess Te with respect to the stoichiometric ratio makes it a *p*-type material while excess Pb yields an *n*-type material.[44,45] Moreover, good thermoelectric properties can be achieved by the introduction of various dopants in the structure.[46,47] Due to oxidation and sublimation of Te, applications using these compounds are nevertheless limited to 800 K.

In the same temperature range, TAGS ($AgSbTe_2$ with GeTe) have proven to be better candidates than PbTe because they overcome the problem of chemical stability and are more efficient above 800 K.[19,48,49] β-$FeSi_2$ is also interesting in this respect despite its lower peak *ZT* values.[50] Strong efforts have been devoted to use this material in terrestrial power generators because of its advantages such as high chemical stability, non-toxic elements and low cost.[51]

At even higher temperatures, Si-Ge alloys are the materials of choice used for power generation applications.[52] Since there is minimal degradation of the material and performance, Si-Ge alloys are the best candidates for applications at temperatures higher than 1000 K. Si-Ge can also be tuned into both *p* and *n*-type material using different dopants.[53] NASA has been using these compounds in RTGs since 1976.[54] The maximum *ZT* value obtained for *n* and *p*-type $Si_{80}Ge_{20}$ was found to be 1.0 and 0.6, respectively, as reported by Vining *et al.*[55]

1.5.2 Novel thermoelectric materials

Despite significant efforts devoted to further enhance the thermoelectric performances of these conventional thermoelectric materials, their *ZT* values were mainly limited to around unity. In order to find novel materials harboring superior thermoelectric properties, new

families of materials have been studied since the 90s. These new research directions were guided by novel concepts, in addition to the above-mentioned general guiding principles. These concepts can be divided into two main areas: **i)** the study of low-dimensional systems (including bulk nanostructured materials) and **ii)** the identification and optimization of novel materials/structures.

The first line of research concerns the development of advanced materials by decreasing their dimensionality. Hicks and Dresselhaus proposed that using 2D, 1D and even 0D structures made of conventional materials could increase the *ZT* values substantially due to the sharp variations in the energy dependence of the density of states (DOS) leading to higher thermopower values than those of the 3D materials for the same carrier density.[56–58] Moreover, these nano-materials present the advantage of bringing additional degrees of freedom to modulate the electronic properties by manipulating their size. More detailed explanations about these aspects can be found in reviews focusing on nanostructured materials.[59–62] Spectacularly high *ZT* values were announced in superlattices composed of conventional materials due to a strong reduction of the lattice thermal conductivity.[63] However, these results were unfortunately never reproduced. The presence of nano-objects (nano-grains, nano-secondary phases, etc.) in bulk materials also contributed to decrease the lattice thermal conductivity and thus to increase the *ZT* values. For example, some substantial improvements have been obtained, as shown in Figure 1.7, in conventional materials, making the nanostructuration a worthwhile research area to pursue.

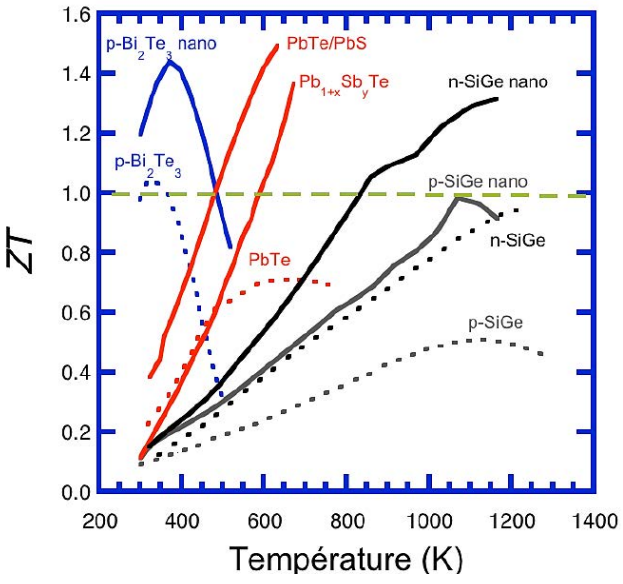

Figure 1.7: Temperature dependence of the *ZT* value for nanostructured conventional materials (continuous line) compared with their conventional form (dotted line).[18]

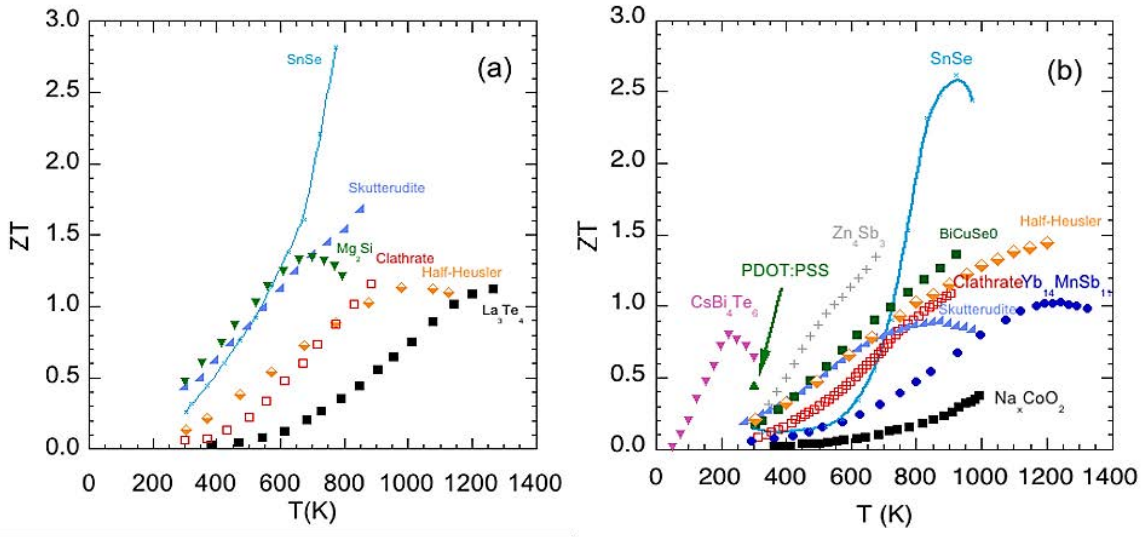

Figure 1.8: Temperature dependence of the *ZT* value for a) p-type and b) n-type advanced thermoelectric materials.[6]

Over the past three decades, huge efforts have been devoted to the identification and optimization of novel family of compounds (Figure 1.8). Slack proposed the concept of phonon glass-electron crystal (PGEC), that is, a material that would be able to conduct heat like a glassy compound while remaining crystalline with respect to electron's flow.[64] He suggested that when phonons have mean free paths on the order of their wavelength, the minimum lattice thermal conductivity could be achieved. Several review articles about these aspects can be consulted.[34,38,65,66]

In this context, the beneficial role of loosely-bound atoms in open, "cage-like" frameworks was proposed, leading to the study and emergence of cage-like compounds, with the skutterudites and clathrates being the most prominent examples. Both structures can show anomalous, glass-like thermal transport, depending on the composition and the nature of the element residing in the cages. Skutterudites have a general chemical formula of MX_3 where M is one of the group 9 transition metals such as Co, Rh or Ir and X is a pnictogen element, that is, P, As or Sb. The most important characteristic of skutterudites is the presence of two voids in the crystal structure where foreign elements can be inserted. The occupation of this site by loosely-bound atoms referred to as "rattlers", leads to extremely low lattice thermal conductivity at high temperatures. In order to take into account these "rattlers", the chemical formula can be written as $R_xM_4X_{12}$ where R is the rattling atoms with x its filling fraction ($x < 1$) (Figure 1.9). These filling atoms can be either alkali, alkaline-earth, or rare-earth elements.

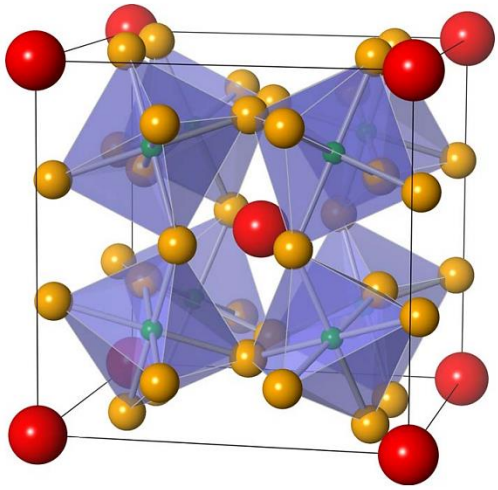

Figure 1.9: Crystal structure of filled skutterudites. Small green spheres represent transition metals, medium orange spheres are the pnictogens and large red spheres are the fillers.[67]

Thanks to their high chemical flexibility, skutterudites can be made both *n*- (based on $CoSb_3$) and *p*-type ($R_xFe_4Sb_{12}$) and show high thermoelectric performances near 800 K, making them ideal candidates for power generation applications. Due to their good mechanical properties, they are considered as prime candidates to become the active parts of the next-generation power-generation devices operating in the temperature range 500 – 800 K.[68,69] Recently, a very high *ZT* value of ~ 1.8 was obtained for *n*-type In doped $CoSb_3$ compound at 823 K due to a very low thermal conductivity.[70] The best *ZT* values obtained in *p*-type skutterudites are around ~ 1.2 at 750 K, which are lower than the *n*-type analogues but are high enough to develop thermoelectric legs based on these materials.[71]

Clathrates are open structures formed by polyhedral cages into which alkali metal and alkaline-earth elements can reside (Figure 1.10). Among the various crystal structures adopted by these compounds, the so-called type-I clathrates have been so far the most studied family. The entrapped atoms lead to a strong coupling between their low-energy phonon modes with those of the host framework, resulting in extremely low thermal conductivity values. In some clathrates such as $Sr_8Ga_{16}Ge_{30}$ or $Eu_8Ga_{16}Ge_{30}$, the off-centered position of Sr or Eu in the cages is the key property that leads to the glass-like thermal transport observed in these compounds. Combined with semiconducting-like properties that can be easily tuned due to the high chemical flexibility of these compounds, good thermoelectric performances at high temperatures can be achieved. While the highest *ZT* obtained in *n*-type clathrates so far is 1.2 at 1000 K for $Ba_8Ni_{0.31}Zn_{0.52}Ga_{13.06}Ge_{32.2}$, the *ZT* values are more limited in *p*-type compounds with a maximum *ZT* of 0.61 achieved at 760 K in $Ba_8Ga_{16}Al_3Ge_{27}$. However, their lower

mechanical robustness compared to skutterudites have strongly hampered their integration into thermoelectric devices.[72,73] Of note, recent experiments by Lory *et al.* based on detailed inelastic neutron scattering measurements challenges the widely-held classification of clathrates as PGEC materials.[74]

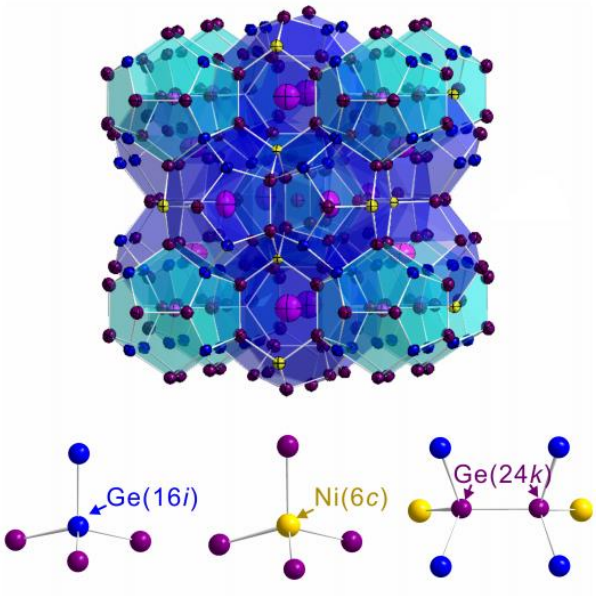

Figure 1.10: Crystal structure of type-I clathrates with surrounding atomic environment in different sites.[75]

Searching for materials crystallizing with complex crystal structures is another fruitful line of research for finding novel materials with very low lattice thermal conductivity values. Some of them have been shown to exhibit very high *ZT* values at high temperatures (typically between 800 and 1200 K). Amongst them, Zn_4Sb_3 has shown to be promising *p*-type thermoelectric compounds.[76,77] Zn_4Sb_3 has extremely low lattice thermal conductivity (almost half of that of Bi_2Te_3) with an unusual temperature dependence that was attributed to the presence of vacancies in the lattice with a relative complex structure.[76] However, further optimization of the overall thermoelectric properties is limited because of the difficulties to further dope them and the restricted compositional variations.

Recently, there has been sudden spike of interest in Zintl compounds due to their promising p-type thermoelectric properties at high temperatures.[78,79] The family of Zintl phases of general chemical formula $A_{14}MPn_{11}$, where *A* is an alkaline earth or rare-earth metal, *M* is a transition or main group metal and *Pn* is a pnictogen, have been shown to exhibit high thermoelectric performances. In particular, a very high *ZT* value of 1.0 at 1223 K has been

obtained in $Yb_{14}MnSb_{11}$, surpassing the values obtained in Si-Ge alloys. This high value originates from its complex crystal structure consisting of various distinct structural units (Figure 1.11) leading to very low lattice thermal conductivity of ~ 0.8 W m^{-1} K^{-1} and semiconducting-like electronic properties. This compound is currently considered as a prime candidate for replacing Si-Ge alloys in TEGs by NASA.[78]

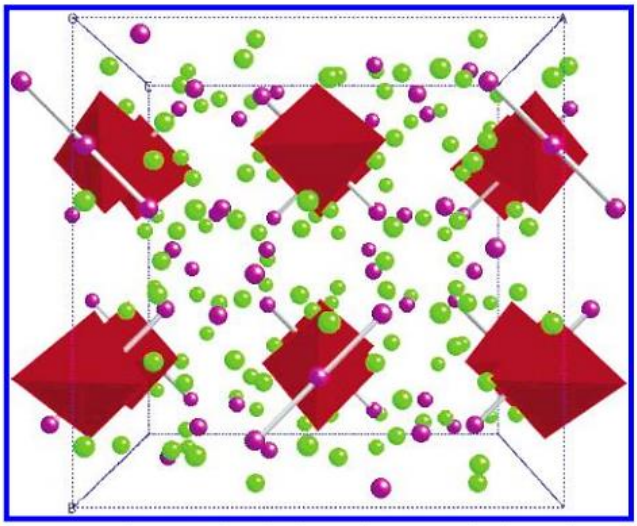

Figure 1.11: Crystal structure of $Yb_{14}MnSb_{11}$. Yb and Sb are represented by green and purple spheres respectively. $MnSb_4$ tetrahedron are represented as filled red polyhedron.[78]

Half-Heusler compounds are another family of materials that show high thermoelectric performances (ZT ~ 1.0 for both p and n-type materials), suggesting a possible development for mid-temperature range applications.[80,81] Basically, Half-Heusler compounds are similar to full Heuslers from which one Ni atom is replaced by an ordered lattice of vacancies leading to compounds based on MNiSn or MCoSb (M = Zr, Hf, Ti) as shown in Figure 1.12. Half-Heuslers are known to have a high thermopower above 300 K due to large electronic effective mass. Although these compounds have good mechanical robustness, good thermal stability and excellent electrical properties, they intrinsically exhibit high thermal conductivity. Recent improvement in the synthesis process has helped to overcome this problem, making them good candidates for the development of the next generation of thermoelectric modules.[80,82]

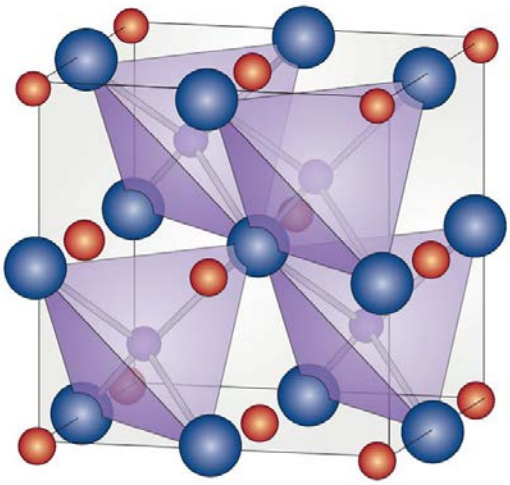

Figure 1.12: Crystal structure of a typical Half-Heusler compound.[82] (Representation: Purple balls - Ni, Blue balls - Zn and orange balls - Sr.)

Sulfur-based compounds are currently attracting significant attention due to the low-toxicity and low-cost of the elements forming these compounds. The two families that have shown high thermoelectric performances are colusites and tetrahedrites (Figure 1.13).

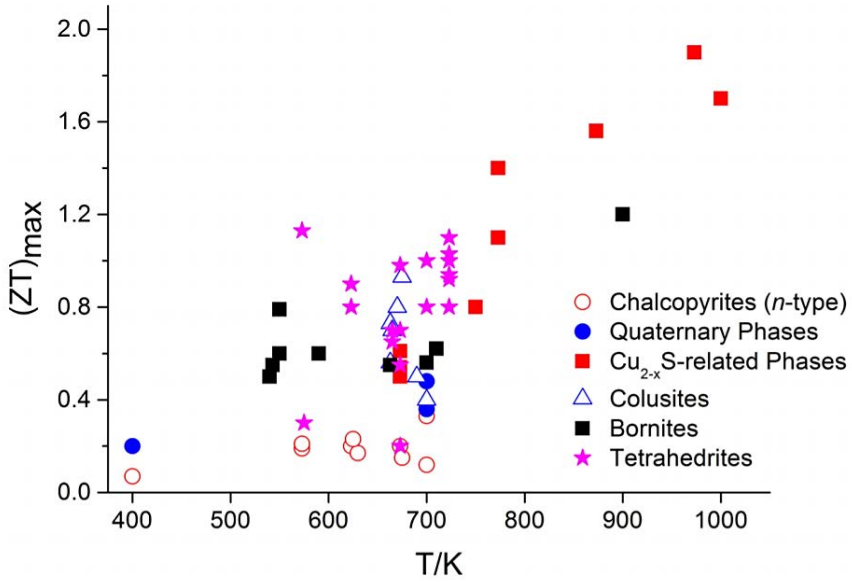

Figure 1.13: Maximum *ZT* values for compounds based on a Cu-S framework.[83]

Suekuni *et al.* first recognized colusite as a potential TE material ($Cu_{26}V_2Ge_6S_{32}$, see Figure 1.14) which showed high PF and low thermal conductivity of 0.6 W m^{-1} K^{-1} leading to a *ZT* of 0.73 at 663 K.[84] Bouyrie *et al.* studied the effect of different elements such as Co and Ni in $Cu_{26}Nb_2Ge_6S_{32}$.[85] It was observed that these dopants increased the PF without disturbing

the lattice thermal conductivity giving a high *ZT* of ~ 0.7 at 665 K for both Co and Ni-doped colusite.

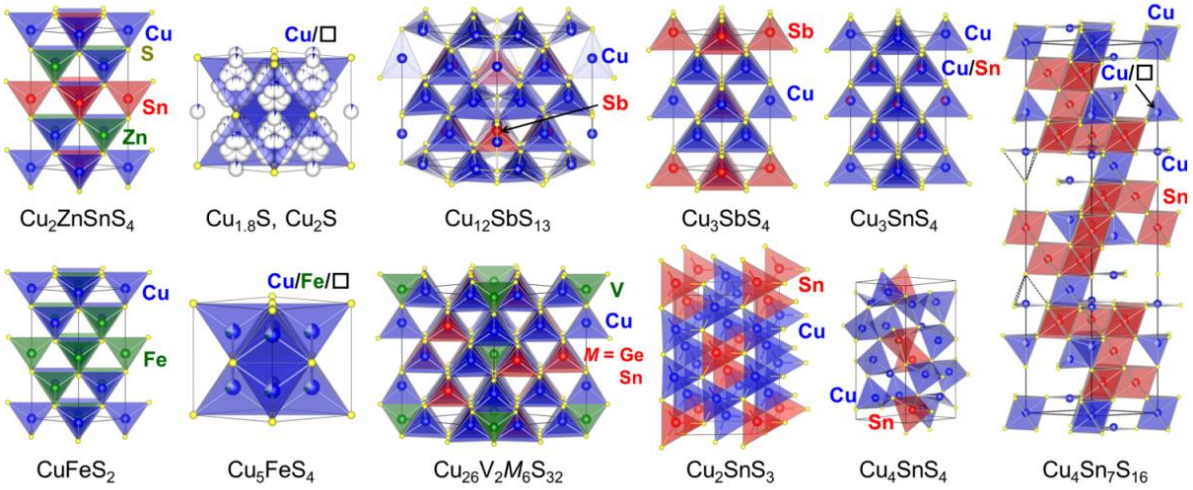

Figure 1.14: Crystal structure of various Cu-S based materials.[86]

The best result were obtained by Bourges *et al.* who recently reported a *ZT* close to unity at 700 K by reducing the lattice thermal conductivity through cationic disordering, induced by carefully controlling the high-temperature consolidation process.[87] Tetrahedrites, of chemical formula $Cu_{12}Sb_4S_{13}$, are another interesting minerals that have been widely studied for thermoelectric applications. The first study on the thermoelectric properties of tetrahedrites was carried out by Suekuni *et al.* in 2012 at low temperatures and then in 2013 at high temperatures.[88,89] The key characteristic of their complex crystal structure (Figure 1.14) is the peculiar chemical environment of some of the Cu atoms giving rise to a strongly anharmonic, low-energy optical mode. This mode significantly affects the heat-carrying acoustic phonons by reducing their phase space. This remarkable property explains why tetrahedrites possess very low lattice thermal conductivity. Combined with the possibility to optimize the hole concentration through various substitution, high *ZT* values on the order of 1.0 can be obtained near 700 K.[90]

In addition to the state-of-the-art thermoelectric material PbTe, several other chalcogenide semiconductors have been of great interest in the field of thermoelectricity due to their easily tunable electronic properties. Most of these chalcogenides were studied in the early 19th century but were only re-investigated in the later halves of the century due to improvement in the synthesis techniques. In this regard, the two families Sn*X* (*X*= Te, Se, S) and Pb*X* (*X*= Te, Se, S) have been thoroughly revisited over the last years. In addition to

nanostructuring the Pb*X* compounds resulting in several claims of very high *ZT* values above 2 near 900 K,[91] another strategy used to further enhance the thermoelectric performances of PbTe has been the formation of resonant levels via Tl doping.[92] This element creates a resonant level in the valence bands of PbTe causing a distortion in the DOS that boosts the thermopower values as seen in Figure 1.15.

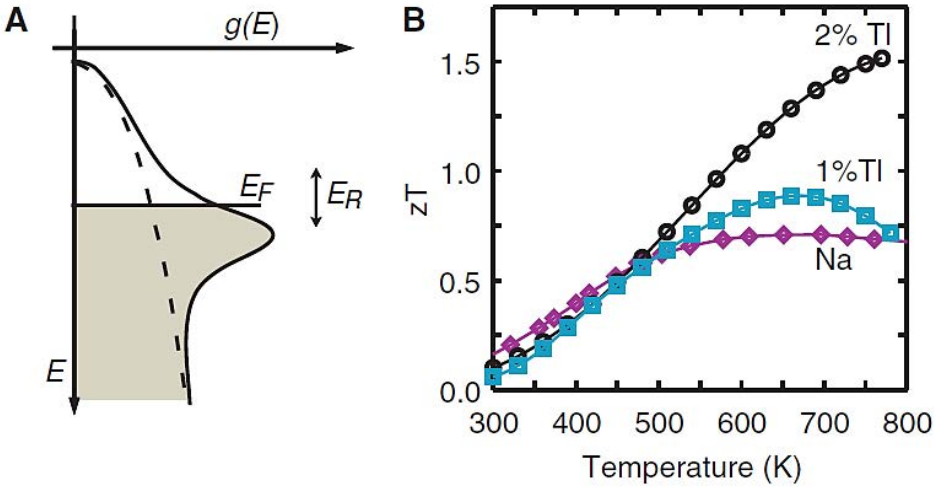

Figure 1.15: a) Schematic representation of DOS in Tl doped PbTe and b) Temperature dependence of *ZT* of Tl doped PbTe compounds showing a high *ZT* of ~ 1.5.[92]

The higher *ZT* value achieved in $Pb_{1-x}Tl_xTe$ (~ 1.5 at 773 K) makes this strategy intriguing for enhancing the thermoelectric properties of chalcogenide semiconductors.[92] This band engineering technique will be explained in detail in Chapter 3. A time line of the *ZT* values reported in PbTe-based materials over the last few decades is sketched in Figure 1.16.[46]

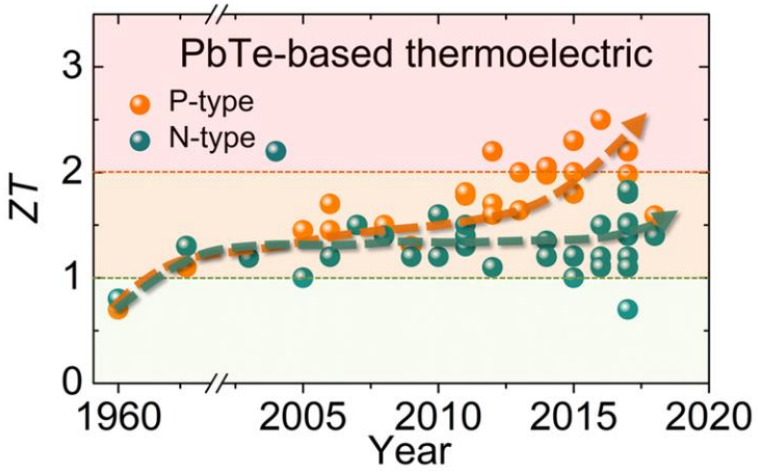

Figure 1.16: *ZT* time line representation of PbTe based materials.[46]

Both *n* and *p*-type PbSe materials have also been studied, with a high *ZT* of ~ 1.6 obtained at 900 K.[93] Amongst the lead chalcogenides, PbS-based materials have the poorest thermoelectric properties with a maximum *ZT* of 0.7 at 850 K in Cl-doped PbS due to rather high lattice thermal conductivity compared to PbTe and PbSe.[94] Nevertheless, PbS still remains an interesting alternative due to the low cost and abundance of sulfur, and its ability to operate at high temperatures. In any case, although Pb*X* compounds exhibit high *ZT* values, the toxicity of Pb is a significant issue preventing its use in thermoelectric devices for terrestrial applications in power generation.

As Pb-free alternatives to Pb*X* compounds, the Sn*X* materials have been reinvestigated over the last years. These studies followed the announcement of a record-breaking *ZT* value in SnSe that has brought a lot of interest and controversy in the field. In 2014, SnSe came back to limelight with *ZT* values as high as 2.6 at 900 K in undoped, *p*-type single crystals,[95] due to the extremely low lattice thermal conductivity values of 0.23 W m^{-1} K^{-1} at 900 K. Similar high performances were also claimed in *n*-type SnSe single crystals doped with Br or Bi yielding *ZT* as high as ~ 2.2 and 2.8 near 800 K, respectively.[96] However, the lower lattice thermal conductivity values measured in singe crystals with respect to polycrystalline samples as well as the strong difference with the values reported in the 1960s raised significant issues.[97–99] Several studies subsequently followed to determine the intrinsic value of the lattice thermal conductivity of SnSe, showing that the initial values measured by Zhao *et al.* were underestimated.[100,101] SnSe remains nevertheless an interesting area of research due to its low ability to transport heat and the possibility to obtain both *n* and *p*-type samples.[102–106] A review of the main chemical and physical properties of SnSe has been reported recently by Candolfi *et al.*[107] These results raised interest for its sulfur-analogue SnS because of its crystal and electronic band structures similar to SnSe. As mentioned above, sulfur is earth abundant and cheap comparatively to Te or Se, making SnS an interesting candidate for thermoelectric applications. So far, a peak *ZT* value of 0.64 has been obtained in $SnS_{0.2}Se_{0.8}$ at 823 K upon proper optimization.[108]

Recently, the thermoelectric properties of SnTe have been revisited.[109,110] While for long being overlooked due to its poor thermoelectric properties originating from its strong deviations from stoichiometry, this compound has reemerged as a credible candidate for mid temperature range applications. Finally, it is worth mentioning the recent results reported on the chalcogenide binary compound InTe. Jana *et al.* showed that polycrystalline InTe exhibits an ultralow lattice thermal conductivity value of 0.4 W m^{-1} K^{-1}.[111] This remarkable property is at the origin of the high *ZT* value achieved at 600 K with a peak value of 0.9. Due to absence

of a significant amount of literature data on the transport properties of either single-crystalline or polycrystalline InTe, this simple compound is a very interesting material for further experimental and theoretical investigations.

Because the study of the thermoelectric properties of SnTe and InTe will be at the heart of this thesis, their crystallographic and physical properties will be described in detail in the next two Chapters.

1.6 Conclusion

The search for new nonpolluting energy sources have become of great interest since the signing of Kyoto protocol in 1997 that commits to the reduction of greenhouse gases. In this context, generation of electricity from waste heat by thermoelectric devices provides a possible clean energy option. In this first Chapter, we have presented the basic thermoelectric phenomena and some general criteria and guidelines for the design and optimization of thermoelectric materials. Intensive studies over the last two decades have led to the discovery of new thermoelectric materials with high *ZT* values, higher than those of state-of-the-art thermoelectric materials in some case. The main challenge in the optimization of the thermoelectric properties of materials is the interdependence of the three transport properties defining the *ZT* values. This inherent strong difficulty can be partially overcome by opting for semiconducting chalcogenide compounds, which often exhibit a rich chemical flexibility that enables tuning the electronic properties combined with a poor ability to transport heat.

In Chapters 2 and 3, we will study specifically Te-based chalcogenides *X*Te (*X* = Sn, In). Although the thermoelectric properties of SnTe were studied in the 60s and revisited over the last years, there is still room for further improvement of its thermoelectric properties. SnTe is one of the known compounds where a resonant level can be created by indium doping. In the next Chapter, we will discuss in detail this specific mechanism that significantly enhances the thermopower and hence, the power factor. Not only will the transport properties of In-doped SnTe be studied at high temperatures but they will be also probed at low temperatures, a temperature range where the strong effect of the resonant level on the transport properties can be better visualized.

References

1. Onsager, L. Reciprocal Relations in Irreversible Processes. I. *Phys. Rev.* **37,** 405 (1931).
2. Onsager, L. Reciprocal Relations in Irreversible Processes. II. *Phys. Rev.* **38,** 2265 (1931).
3. Callen, H. B. On the theory of irreversible processes. (1947).
4. Domenicali, C. A. Irreversible Thermodynamics of Thermoelectricity. *Rev. Mod. Phys.* **26,** 237 (1954).
5. De Groot, S. R. & Mazur, P. *Non-equilibrium thermodynamics*. (Dover Publications, 1984).
6. El Oualid, S. Contribution à la modélisation et à la caractérisation de générateurs thermoélectriques. (2019).
7. Seebeck, T. J. *Ueber den Magnetismus der galvanischen Kette: Technical report for the Royal Prussian Academy of Science*. (K. Akad. Wiss. Berlin, 1821).
8. Volta, A. Nuova memoria Sull' elettricita a animale. Divisa in tre lettere diretta al signor Abate Anton Maria Vassali, proffessore di fisica nella R. Université Torino. 1794-1795. (1937).
9. Peltier, J.-C. Nouvelles expériences sur la caloricité des courants électrique. *Ann. Chim. Phys* **56,** 371 (1834).
10. Thomson, W. On a mechanical theory of thermo-electric currents. *Proceedings of the Royal society of Edinburgh* **3,** 91 (1857).
11. Rockwood, A. L. Relationship of thermoelectricity to electronic entropy. *Physical Review A* **30,** 2843 (1984).
12. Thomson, Sir William. *Mathematical and Physical papers*. **II,** (Cambridge Press, 1884).
13. Ohorodniichuk, V. Influence of nanostructuring on thermoelectric properties of p-type bulk materials based on (Bi, Sb, Te). (2014).
14. Altenkirch, E. Über den nutzeffekt der thermosäul. *Physikalische Zeitschrift* **10,** 12 (1909).
15. Altenkirch, E. Elektrothermische Kälteerzeugung und reversible elektrische Heizung. *Physikalische Zeitschrift* **12,** 920 (1911).
16. Maciá, E. *Thermoelectric materials: advances and applications*. (Jenny Stanford Publishing, 2015).
17. Goldsmid, H. J. Applications of Thermoelectricity. *Journal of Electronics and Control* **8,** 463 (1960).

18. Ibrahim, D. Synthèse et caractérisation de matériaux à base de SnTe pour la conversion d'énergie par effets thermoélectriques. (2018).
19. Rowe, D. M. *Thermoelectrics handbook: macro to nano*. (CRC press, 2018).
20. Heikes, R. R. & Ure, R. W. *Thermoelectricity: science and engineering*. (Interscience Publishers, 1961).
21. Franz, R. & Wiedemann, G. Ueber die Wärme-Leitungsfähigkeit der Metalle. *Annalen der Physik und Chemie* **165,** 497 (1853).
22. Debye, P. J. W., Nernst, W., Smoluchowski, M., Sommerfeld, A. & Lorentz, H. A. *Vorträge über die kinetische Theorie der Materie und der Elektrizität*. **6,** (BG Teubner, 1914).
23. Pohl, R. O. The applicability of the Debye model to thermal conductivity. *Zeitschrift für Physik* **176,** 358 (1963).
24. Dulong, P. L. & Petit, A. T. *Recherches sur la mesure des températures et sur les lois de la communication de la chaleur*. (De l'Imprimerie royale, 1818).
25. Debye, P. Zur Theorie der spezifischen Wärmen. *Annalen der Physik* **344,** 789 (1912).
26. Blackman, M. On the relation of Debye theory and the lattice theory of specific heats. *Proceedings of the Royal Society of London. Series A. Mathematical and Physical Sciences* **181,** 58 (1942).
27. Goldsmid, H. J. & Douglas, R. W. The use of semiconductors in thermoelectric refrigeration. *British Journal of Applied Physics* **5,** 386 (1954).
28. Mott, N. F. & Davis, E. A. *Electronic processes in non-crystalline materials*. (Oxford university press, 2012).
29. Wilson, A. H. *Semi-conductors & Metals: An Introduction to the Electron Theory of MetalsThe theory of metals*. (Cambridge University Press, 1939).
30. Ioffe, A. F., Stil'Bans, L. S., Iordanishvili, E. K., Stavitskaya, T. S., Gelbtuch, A. & Vineyard, G. Semiconductor thermoelements and thermoelectric cooling. *Physics Today* **12,** 42 (1959).
31. Mahan, G. & Sales, B. Thermoelectric materials: New approaches to an old problem. *Physics Today* **50,** 42 (1997).
32. Goodman, C. H. L. The prediction of semiconducting properties in inorganic compounds. *Journal of Physics and Chemistry of Solids* **6,** 305 (1958).
33. Slack, G. A. in *Solid State Physics* (eds. Ehrenreich, H., Seitz, F. & Turnbull, D.) **34,** 1 (Academic Press, 1979).

34. Tritt, T. M. Thermoelectric phenomena, materials, and applications. *Annual review of materials research* **41,** 433 (2011).
35. He, J. & Tritt, T. M. Advances in thermoelectric materials research: Looking back and moving forward. *Science* **357,** eaak9997 (2017).
36. Sootsman, J. R., Chung, D. Y. & Kanatzidis, M. G. New and Old Concepts in Thermoelectric Materials. *Angewandte Chemie International Edition* **48,** 8616 (2009).
37. Chen, G., Dresselhaus, M. S., Dresselhaus, G., Fleurial, J. P. & Caillat, T. Recent developments in thermoelectric materials. *Int. Mater. Rev.* **48,** 45 (2003).
38. Dresselhaus, M. S., Chen, G., Tang, M. Y., Yang, R., Lee, H., Wang, D., Ren, Z., Fleurial, J.-P. & Gogna, P. New directions for low-dimensional thermoelectric materials. *Adv. Mater.* **19,** 1043 (2007).
39. Selvan, K. V., Hasan, M. N. & Ali, M. S. M. State-of-the-Art Reviews and Analyses of Emerging Research Findings and Achievements of Thermoelectric Materials over the Past Years. *Journal of Electronic Materials* **48,** 745 (2019).
40. Wolfe, R. & Smith, G. E. Effects of a magnetic field on the thermoelectric properties of a bismuth-antimony alloy. *Applied Physics Letters* **1,** 5 (1962).
41. Lenoir, B., Scherrer, H. & Caillat, T. in *Semiconductors and Semimetals* (ed. Tritt, T. M.) **69,** 101 (Elsevier, 2001).
42. Chen, Y., Hou, X., Ma, C., Dou, Y. & Wu, W. Review of Development Status of Bi_2Te_3-Based Semiconductor Thermoelectric Power Generation. *Advances in Materials Science and Engineering* **2018,** (2018).
43. Holgate, T. C., Bennett, R., Hammel, T., Caillat, T., Keyser, S. & Sievers, B. Increasing the Efficiency of the Multi-mission Radioisotope Thermoelectric Generator. *Journal of Electronic Materials* **44,** 1814 (2015).
44. Brebrick, R. F. & Allgaier, R. S. Composition Limits of Stability of PbTe. *The Journal of Chemical Physics* **32,** 1826 (1960).
45. Brebrick, R. F. & Gubner, E. Composition Stability Limits of PbTe. II. *The Journal of Chemical Physics* **36,** 1283 (1962).
46. Xiao, Y. & Zhao, L.-D. Charge and phonon transport in PbTe-based thermoelectric materials. *npj Quantum Materials* **3,** 55 (2018).
47. LaLonde, A. D., Pei, Y., Wang, H. & Jeffrey Snyder, G. Lead telluride alloy thermoelectrics. *Materials Today* **14,** 526 (2011).

48. Yang, S. H., Zhu, T. J., Sun, T., He, J., Zhang, S. N. & Zhao, X. B. Nanostructures in high-performance $(GeTe)_x(AgSbTe_2)_{100-x}$ thermoelectric materials. *Nanotechnology* **19,** 245707 (2008).
49. Skrabek, E. & Trimmer, D. in *CRC handbook of thermoelectrics* 267 (CRC Press, 1995).
50. R. M. Ware & D. J. McNeill. Iron disilicide as a thermoelectric generator material. *Proceedings of the Institution of Electrical Engineers* **111,** 178 (1964).
51. Birkholz, U. & Schelm, J. Mechanism of Electrical Conduction in β-$FeSi_2$. *Physica Status Solidi (b)* **27,** 413 (1968).
52. Bhandari, C. M. & Rowe, D. M. Silicon–germanium alloys as high-temperature thermoelectric materials. *Contemporary physics* **21,** 219 (1980).
53. Nozariasbmarz, A., Agarwal, A., Coutant, Z. A., Hall, M. J., Liu, J., Liu, R., Malhotra, A., Norouzzadeh, P., Ö*ZT*ürk, M. C., Ramesh, V. P., Sargolzaeiaval, Y., Suarez, F. & Vashaee, D. Thermoelectric silicides: A review. *Japanese Journal of Applied Physics* **56,** 05DA04 (2017).
54. Vining, C. B. & Fleurial, J.-P. Silicon-Germanium: An overview of recent developments. in *Tenth Symposium on Space Nuclear Power and Propulsion* (1993).
55. Vining, C. B., Laskow, W., Hanson, J. O., Van der Beck, R. R. & Gorsuch, P. D. Thermoelectric properties of pressure-sintered $Si_{0.8}Ge_{0.2}$ thermoelectric alloys. *Journal of Applied Physics* **69,** 4333 (1991).
56. Hicks, L. D. & Dresselhaus, M. S. Thermoelectric figure of merit of a one-dimensional conductor. *Physical review B* **47,** 16631 (1993).
57. Hicks, L. D. & Dresselhaus, M. S. Effect of quantum-well structures on the thermoelectric figure of merit. *Physical Review B* **47,** 12727 (1993).
58. Hicks, L. D., Harman, T. C., Sun, X. & Dresselhaus, M. S. Experimental study of the effect of quantum-well structures on the thermoelectric figure of merit. *Physical Review B* **53,** R10493 (1996).
59. Minnich, A. J., Dresselhaus, M. S., Ren, Z. F. & Chen, G. Bulk nanostructured thermoelectric materials: current research and future prospects. *Energy Environ. Sci.* **2,** 466 (2009).
60. Lan, Y., Minnich, A. J., Chen, G. & Ren, Z. Enhancement of Thermoelectric Figure-of-Merit by a Bulk Nanostructuring Approach. *Adv. Funct. Mater.* **20,** 357 (2010).
61. Li, J.-F., Liu, W.-S., Zhao, L.-D. & Zhou, M. High-performance nanostructured thermoelectric materials. *NPG Asia Materials* **2,** 152 (2010).

62. Chen, Z.-G., Han, G., Yang, L., Cheng, L. & Zou, J. Nanostructured thermoelectric materials: Current research and future challenge. *Progress in Natural Science: Materials International* **22,** 535 (2012).
63. Harman, T. C., Taylor, P. J., Walsh, M. P. & LaForge, B. E. Quantum dot superlattice thermoelectric materials and devices. *science* **297,** 2229 (2002).
64. Slack, G. A. Design concepts for improved thermoelectric materials. *MRS Online Proceedings Library Archive* **478,** (1997).
65. Zlatic, V. & Hewson, A. *New materials for thermoelectric applications: theory and experiment*. (Springer, 2012).
66. Goldsmid, H. J. & Nolas, G. S. A review of the new thermoelectric materials. in *Proceedings ICT2001* 1 (IEEE, 2001).
67. Wee, D., Kozinsky, B., Marzari, N. & Fornari, M. Effects of filling in CoSb 3 : Local structure, band gap, and phonons from first principles. *Physical Review B* **81,** (2010).
68. Guo, J. Q., Geng, H. Y., Ochi, T., Suzuki, S., Kikuchi, M., Yamaguchi, Y. & Ito, S. Development of skutterudite thermoelectric materials and modules. *Journal of electronic materials* **41,** 1036 (2012).
69. Rull-Bravo, M., Moure, A., Fernandez, J. F. & Martín-González, M. Skutterudites as thermoelectric materials: revisited. *Rsc Advances* **5,** 41653 (2015).
70. Rogl, G., Grytsiv, A., Yubuta, K., Puchegger, S., Bauer, E., Raju, C., Mallik, R. C. & Rogl, P. In-doped multifilled n-type skutterudites with *ZT*=1.8. *Acta Materialia* **95,** 201 (2015).
71. Rogl, G., Grytsiv, A., Rogl, P., Bauer, E., Kerber, M. B., Zehetbauer, M. & Puchegger, S. Multifilled nanocrystalline p-type didymium – Skutterudites with *ZT*>1.2. *Intermetallics* **18,** 2435 (2010).
72. Iversen, B. B., Palmqvist, A. E. C., Cox, D. E., Nolas, G. S., Stucky, G. D., Blake, N. P. & Metiu, H. Why are Clathrates Good Candidates for Thermoelectric Materials? *Journal of Solid State Chemistry* **149,** 455 (2000).
73. Nolas, G. S. & Slack, G. A. Thermoelectric clathrates: cagelike crystals may soon help to pump heat with electricity and to create electricity with heat. *American Scientist* **89,** 136 (2001).
74. Lory, P.-F., Pailhès, S., Giordano, V. M., Euchner, H., Nguyen, H. D., Ramlau, R., Borrmann, H., Schmidt, M., Baitinger, M., Ikeda, M., Tomeš, P., Mihalkovič, M., Allio, C., Johnson, M. R., Schober, H., Sidis, Y., Bourdarot, F., Regnault, L. P., Ollivier, J., Paschen, S., Grin, Y. & de Boissieu, M. Direct measurement of individual phonon

lifetimes in the clathrate compound $Ba_{7.81}Ge_{40.67}Au_{5.33}$. *Nature Communications* **8,** (2017).

75. Dong, Y., Ding, X., Yan, X., Zhang, L., Tang, Z., Chen, W., Rogl, P. & Paschen, S. Crystal Chemistry and Thermoelectric Properties of Type-I Clathrate $Ba_8Ni_{\sim 3.8}Si_xGe_{42.2-x}$ (x = 0, 10, 20, 42.2). *Materials* **11,** 946 (2018).
76. Caillat, T., Fleurial, J.-P. & Borshchevsky, A. Preparation and thermoelectric properties of semiconducting Zn4Sb3. *Journal of Physics and Chemistry of Solids* **58,** 1119 (1997).
77. Mozharivskyj, Y., Pecharsky, A. O., Bud'ko, S. & Miller, G. J. A promising thermoelectric material: Zn_4Sb_3 or $Zn_{6-\delta}Sb_5$. Its composition, structure, stability, and polymorphs. Structure and stability of $Zn_{1-\delta}Sb$. *Chemistry of Materials* **16,** 1580 (2004).
78. Brown, S. R., Kauzlarich, S. M., Gascoin, F. & Snyder, G. J. $Yb_{14}MnSb_{11}$: New High Efficiency Thermoelectric Material for Power Generation. *Chemistry of Materials* **18,** 1873 (2006).
79. Rauscher, J. F., Cox, C. A., Yi, T., Beavers, C. M., Klavins, P., Toberer, E. S., Snyder, G. J. & Kauzlarich, S. M. Synthesis, structure, magnetism, and high temperature thermoelectric properties of Ge doped $Yb_{14}MnSb_{11}$. *Dalton transactions* **39,** 1055 (2010).
80. Fu, C., Bai, S., Liu, Y., Tang, Y., Chen, L., Zhao, X. & Zhu, T. Realizing high figure of merit in heavy-band p-type half-Heusler thermoelectric materials. *Nature communications* **6,** 8144 (2015).
81. Zhu, T., Fu, C., Xie, H., Liu, Y. & Zhao, X. High Efficiency Half-Heusler Thermoelectric Materials for Energy Harvesting. *Advanced Energy Materials* **5,** 1500588 (2015).
82. Zeier, W. G., Schmitt, J., Hautier, G., Aydemir, U., Gibbs, Z. M., Felser, C. & Snyder, G. J. Engineering half-Heusler thermoelectric materials using Zintl chemistry. *Nature Reviews Materials* **1,** 16032 (2016).
83. Powell, A. V. Recent developments in Earth-abundant copper-sulfide thermoelectric materials. *Journal of Applied Physics* **126,** 100901 (2019).
84. Suekuni, K., Kim, F. S., Nishiate, H., Ohta, M., Tanaka, H. I. & Takabatake, T. High-performance thermoelectric minerals: colusites $Cu_{26}V_2M_6S_{32}$ (M= Ge, Sn). *Applied Physics Letters* **105,** 132107 (2014).
85. Bouyrie, Y., Ohta, M., Suekuni, K., Jood, P. & Takabatake, T. Addition of Co, Ni, Fe and their role in the thermoelectric properties of colusite $Cu_{26}Nb_2Ge_6S_{32}$. *Journal of Alloys and Compounds* **735,** 1838 (2018).

86. Suekuni, K. & Takabatake, T. Research Update: Cu–S based synthetic minerals as efficient thermoelectric materials at medium temperatures. *APL Materials* **4,** 104503 (2016).
87. Bourgès, C., Bouyrie, Y., Supka, A. R., Al Rahal Al Orabi, R., Lemoine, P., Lebedev, O. I., Ohta, M., Suekuni, K., Nassif, V. & Hardy, V. High-performance thermoelectric bulk colusite by process controlled structural disordering. *Journal of the American Chemical Society* **140,** 2186 (2018).
88. Suekuni, K., Tsuruta, K., Ariga, T. & Koyano, M. Thermoelectric properties of mineral tetrahedrites $Cu_{10}Tr_2Sb_4S_{13}$ with low thermal conductivity. *Applied Physics Express* **5,** 051201 (2012).
89. Suekuni, K., Tsuruta, K., Kunii, M., Nishiate, H., Nishibori, E., Maki, S., Ohta, M., Yamamoto, A. & Koyano, M. High-performance thermoelectric mineral $Cu_{12-x}Ni_xSb_4S_{13}$ tetrahedrite. *Journal of Applied Physics* **113,** 043712 (2013).
90. Lu, X., Morelli, D. T., Xia, Y. & Ozolins, V. Increasing the Thermoelectric Figure of Merit of Tetrahedrites by Co-Doping with Nickel and Zinc. *Chemistry of Materials* **27,** 408 (2015).
91. Fu, T., Yue, X., Wu, H., Fu, C., Zhu, T., Liu, X., Hu, L., Ying, P., He, J. & Zhao, X. Enhanced thermoelectric performance of PbTe bulk materials with figure of merit ZT >2 by multi-functional alloying. *Journal of Materiomics* **2,** 141 (2016).
92. Heremans, J. P., Jovovic, V., Toberer, E. S., Saramat, A., Kurosaki, K., Charoenphakdee, A., Yamanaka, S. & Snyder, G. J. Enhancement of Thermoelectric Efficiency in PbTe by Distortion of the Electronic Density of States. *Science* **321,** 554 (2008).
93. Gayner, C., Kar, K. K. & Kim, W. Recent progress and futuristic development of PbSe thermoelectric materials and devices. *Materials Today Energy* **9,** 359 (2018).
94. Wang, H., Schechtel, E., Pei, Y. & Snyder, G. J. High Thermoelectric Efficiency of n-type PbS. *Advanced Energy Materials* **3,** 488 (2013).
95. Zhao, L.-D., Lo, S.-H., Zhang, Y., Sun, H., Tan, G., Uher, C., Wolverton, C., Dravid, V. P. & Kanatzidis, M. G. Ultralow thermal conductivity and high thermoelectric figure of merit in SnSe crystals. *Nature* **508,** 373 (2014).
96. Duong, A. T., Nguyen, V. Q., Duvjir, G., Duong, V. T., Kwon, S., Song, J. Y., Lee, J. K., Lee, J. E., Park, S., Min, T., Lee, J., Kim, J. & Cho, S. Achieving ZT=2.2 with Bi-doped n-type SnSe single crystals. *Nature Communications* **7,** (2016).

97. Wasscher, J. D., Albers, W. & Haas, C. Simple evaluation of the maximum thermoelectric figure of merit, with application to mixed crystals $SnS_{1-x}Se_x$. *Solid-State Electronics* **6,** 261 (1963).
98. Maier, H. & Daniel, D. R. SnSe single crystals: Sublimation growth, deviation from stoichiometry and electrical properties. *Journal of Electronic Materials* **6,** 693 (1977).
99. Albers, W., Haas, C., Ober, H., Schodder, G. R. & Wasscher, J. D. Preparation and properties of mixed crystals $SnS_{(1-x)}Se_x$. *Journal of Physics and Chemistry of Solids* **23,** 215 (1962).
100. Ibrahim, D., Vaney, J.-B., Sassi, S., Candolfi, C., Ohorodniichuk, V., Levinsky, P., Semprimoschnig, C., Dauscher, A. & Lenoir, B. Reinvestigation of the thermal properties of single-crystalline SnSe. *Applied Physics Letters* **110,** 032103 (2017).
101. Wei, P.-C., Bhattacharya, S., He, J., Neeleshwar, S., Podila, R., Chen, Y. Y. & Rao, A. M. The intrinsic thermal conductivity of SnSe. *Nature* **539,** E1 (2016).
102. Carrete, J., Mingo, N. & Curtarolo, S. Low thermal conductivity and triaxial phononic anisotropy of SnSe. *Applied Physics Letters* **105,** 101907 (2014).
103. Chen, C.-L., Wang, H., Chen, Y.-Y., Day, T. & Snyder, G. J. Thermoelectric properties of p-type polycrystalline SnSe doped with Ag. *J. Mater. Chem. A* **2,** 11171 (2014).
104. Chen, Y.-X., Ge, Z.-H., Yin, M., Feng, D., Huang, X.-Q., Zhao, W. & He, J. Understanding of the Extremely Low Thermal Conductivity in High-Performance Polycrystalline SnSe through Potassium Doping. *Advanced Functional Materials* **26,** 6836 (2016).
105. Guan, X., Lu, P., Wu, L., Han, L., Liu, G., Song, Y. & Wang, S. Thermoelectric properties of SnSe compound. *Journal of Alloys and Compounds* **643,** 116 (2015).
106. Kutorasinski, K., Wiendlocha, B., Kaprzyk, S. & Tobola, J. Electronic structure and thermoelectric properties of n- and p-type SnSe from first principles calculations. *Phys. Rev. B* **91,** 205201 (2015).
107. Skipidarov, S. & Nikitin, M. *Novel Thermoelectric Materials and Device Design Concepts*. (Springer International Publishing, 2019).
108. Asfandiyar, Wei, T.-R., Li, Z., Sun, F.-H., Pan, Y., Wu, C.-F., Farooq, M. U., Tang, H., Li, F., Li, B. & Li, J.-F. Thermoelectric SnS and SnS-SnSe solid solutions prepared by mechanical alloying and spark plasma sintering: Anisotropic thermoelectric properties. *Scientific Reports* **7,** (2017).
109. Li, W., Wu, Y., Lin, S., Chen, Z., Li, J., Zhang, X., Zheng, L. & Pei, Y. Advances in Environment-Friendly SnTe Thermoelectrics. *ACS Energy Letters* **2,** 2349 (2017).

110. Moshwan, R., Yang, L., Zou, J. & Chen, Z.-G. Eco-Friendly SnTe Thermoelectric Materials: Progress and Future Challenges. *Advanced Functional Materials* **27,** 1703278 (2017).
111. Jana, M. K., Pal, K., Waghmare, U. V. & Biswas, K. The Origin of Ultralow Thermal Conductivity in InTe: Lone-Pair-Induced Anharmonic Rattling. *Angewandte Chemie* **128,** 7923 (2016).

Chapter 2

Properties of Tin Telluride

2.1 Introduction

As discussed in Chapter 1, PbTe has been for long known as an excellent material for thermoelectric applications in power generation. PbTe, and its ternary and quaternary derivatives are used for mid-range-temperature applications (500 – 800 K) where the state-of-the-art thermoelectric material Bi_2Te_3 cannot be used anymore. Recent studies have claimed that very high *ZT* values (> 2) may be obtained in PbTe-based compounds.[1,2] While this compound has a simple cubic structure making its transport properties isotropic,[1,3] the presence of Pb makes this compound toxic and difficult to be used for large-scale industrial purposes. Thus, the search for alternative materials without Pb has been the focus of strong experimental efforts. In this context, numerous studies have been oriented towards lead-free telluride semiconductors such as GeTe or SnTe.[4–6] GeTe exhibits a *p*-type metallic behavior due to very high hole concentration making it a very complex system to modify and control its transport parameters.[7–9] Moreover, Ge is very expensive making GeTe less attractive for commercial applications. On the other hand, SnTe can be considered as the sister compound of PbTe due to its similar rock-salt cubic crystal structure and valence band structure.

SnTe was first intensively investigated in the middle of the 20th century before being abandoned in the 1960s owing to its inherent poorer thermoelectric performances compared to PbTe. In the past decade, SnTe has come back to the forefront of research in both chemistry and solid-state physics due to several interesting physical features. In addition to its non-trivial topological nature and the emergence of superconductivity in In-doped samples with critical temperatures as high as 4.5 K,[10–19] notable improvement in the synthesis process and control of the hole concentration led to a spectacular increase in the *ZT* values up to 1.5 near 900 K.[5] These promising results have left a huge scope for further investigation, offering many opportunities in optimizing and improving the thermoelectric properties of SnTe-based materials.

In this chapter, the crystallographic, physical and chemical properties of the binary SnTe will be discussed. First, we will describe the Sn-Te phase diagram and the main crystallographic properties of SnTe with a particular emphasis on its inherent defect chemistry. Second, we will compare the electronic band structures of SnTe with its sister compound PbTe. Finally, we will then discuss the topic at the heart of this thesis, that is, the effect of substituting In for Sn on the low- and high-temperature transport properties across the full range of In

concentrations accessible under ambient pressure. Physical phenomena including resonant levels (RL), superconductivity and charge Kondo effect will be briefly presented.

2.2 General properties of SnTe

2.2.1 Phase diagram

Fay carried out the first study of the Sn-Te binary phase diagram in 1907.[20] Following this pioneering work, a large sum of studies have been devoted to clarify this phase diagram. Figure 2.1 shows the Sn-Te diagram derived by Kattner *et al.* in 1985,[21] where only one defined compound, SnTe, is observed.

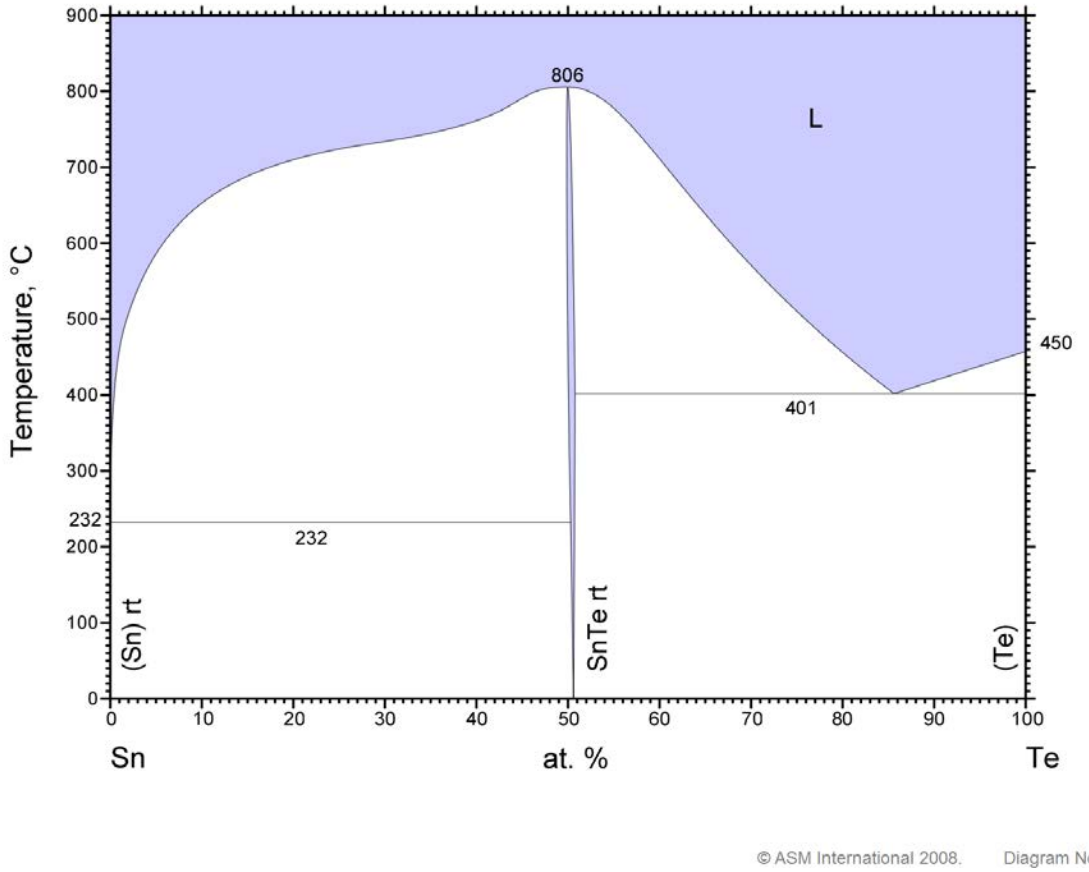

Figure 2.1: Binary phase diagram of Sn-Te derived by Kattner *et al.*[21] SnTe forms congruently at 806°C from a melt of Sn and Te close to 50 at %.

Closer inspection of the homogeneity range of this compound, shown in Figure 2.2, evidences that SnTe cannot be prepared with an exact stoichiometry as most of the

thermoelectric compounds. The maximum deviations from the ideal 50-50 stoichiometry ranges between 50.1 and 50.9 at % and is strongly temperature dependent. At the melting point of 806°C (1079 K), the Te content is 50.4 at %. These deviations from the ideal stoichiometry are due to the presence of defects in the crystal structure, regardless of the synthesis conditions employed.

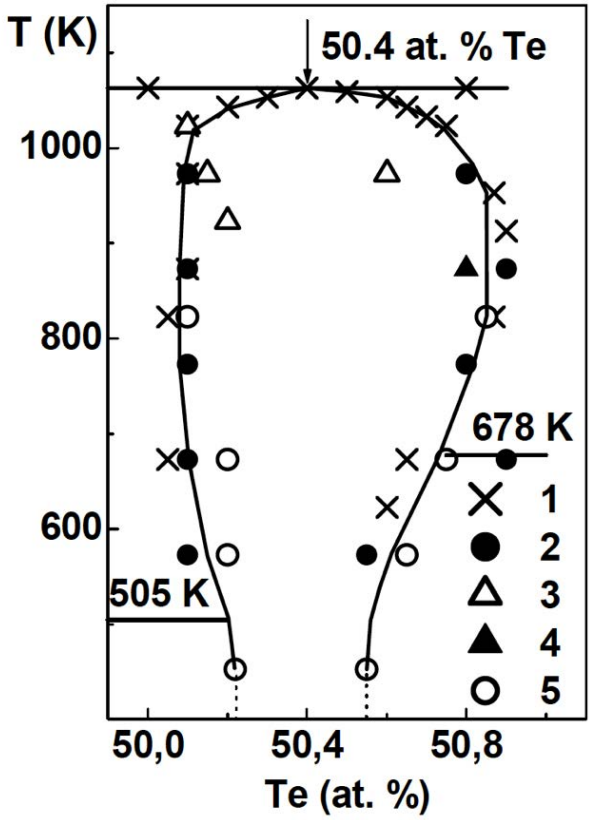

Figure 2.2: Homogeneity region of SnTe.[22]

[1 – (Brebrick[23,24]; Brebrick & Strauss[25]) 2 – (Shelimova & Abrikosov[26]), 3 – (Tairov *et al.*[27]) 4 – (Maselsky & Lubell[28]) 5 – (Rogacheva *et al.*[29])]

Although these results clearly indicate that the chemical formula of this compound should be written as $Sn_{1-\delta}Te$, the simple formula SnTe is nevertheless often used in the literature. Various studies have investigated in detail the influence of the vacancy concentration on the transport properties and on possible strategies to control them. In this regard, Brebrick was the first to systematically measure the hole concentration by Hall effect measurements on samples carefully prepared by saturation annealing under thermodynamic equilibrium.[23,30,31] More information about this specific and important technique will be presented in Chapter 4 dedicated to the binary InTe.[32]

2.2.2 Defect chemistry

The IV-VI binary compounds "*MN*" where *M* is a metalloid (Sn, Pb) and *N* is a chalcogen (Te, Se or S) atom are semiconductors, which are prone to defect chemistry (vacancies and/or antisite defects) resulting in deviations from their ideal stoichiometry. These native defects can act as donors or acceptors depending on the specific compound. Experimentally, it has been shown that compounds with excess of metal *M* are *n*-type materials, while compounds with excess of chalcogen *N* exhibit a *p*-type electrical conductivity. It is generally accepted that all these defects are ionized.

Due to this fact, it is impossible to grow a perfectly stoichiometric crystal of Sn_1Te_1 due to excess Te, or equivalently, Sn vacancies.[33] The fact that the hole concentration *p* increases with the Te content confirms that Sn vacancies behave as acceptors.[24] Brebrick and Mazelsky *et al.* showed that Sn vacancies (V_{Sn}) account for the dependence of the lattice parameter and density of the Te concentration.[23,34] The degree of ionization was studied by Brebrick *et al.* who concluded that these defects are doubly ionized.[25] Hall effect measurements have led to the same conclusion.[23,25,30,35–37] Assuming that the composition of $Sn_{1-x}Te_x$ ($x \sim 0.5$) can be changed by Sn vacancies that are the only point defects in the system (while maintaining the rock-salt crystal structure), V_{Sn} can be calculated as[24]:

Equation 2.1:

$$[V_{Sn}] = 2S\frac{x-\frac{1}{2}}{x} \sim 4S(x-1/2)$$

where *S* is the number of Sn sites per cm^3. Since $S = 1.58\times10^{22}$ cm^3, this relation can be rewritten as:

Equation 2.2:

$$[V_{Sn}] = 6.32\times10^{22}(x-1/2)$$

If we further consider that the degree of ionization of Sn is two, the hole concentration *p* is then simply given by:

Equation 2.3:

$$p = 2[V_{Sn}]$$

2.2.3 Crystal structure of SnTe

SnTe crystallizes with a *fcc* (face centered cubic) rock salt (NaCl-type) structure, sometimes also denoted as β-SnTe at 300 K (Figure 2.3). The crystal structure is described in the space group *Fm3m* with inherent Sn vacancies as already discussed in the previous section of this chapter. The lattice constant determined for SnTe is a = 6.32 Å at 300 K. Te atoms form a *fcc* lattice with Sn atoms filling the octahedral voids (Figure 2.4). Each Sn atom is octahedrally coordinated to six neighboring Te atoms and hence can be considered to be a "close-packed" arrangement of $SnTe_6$ structural unit.[10,38]

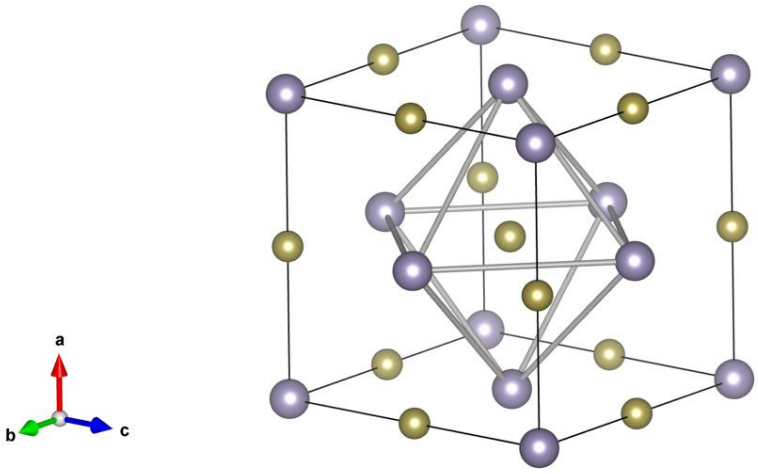

Figure 2.3: Crystal structure of SnTe, Sn atoms are shown in purple and Te atoms are shown in gold.[32]

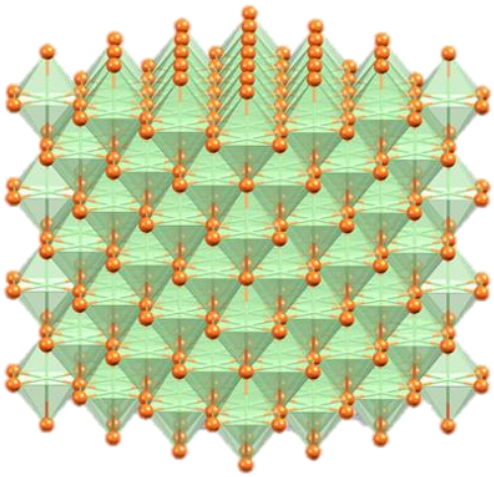

Figure 2.4: Closed-packed arrangement of octahedra formed by Te atoms at the center of which Sn atoms reside.

SnTe also exists in two other allotropes, namely α-SnTe that occurs at low temperatures with a change of the lattice symmetry from cubic to rhombohedral. This transition, revealed by Iizumi *et al.*[39], corresponds to a ferroelectric structural transition, which will be discussed in the next section. At high pressures, the crystal structure, denoted as γ-SnTe, becomes orthorhombic, similar to the binaries semiconductors SnS and SnSe.[41]

2.2.4 Structural ferroelectric phase transition

Upon cooling, SnTe undergoes a structural phase transition to a rhombohedral structure, unlike its sister compound PbTe.[39,42,43] This distortion consists of an elongation of the bonds along the [111] direction, following a shift of Sn atoms along the [100] direction.[42] This transition was later on demonstrated to be a ferroelectric transition, that is, a spontaneous polarization develops below the transition temperature T_{FT}. T_{FT} was shown to strongly depend on the hole concentration governed by the concentration of Sn vacancies. Increasing the hole concentration lowers the transition temperature, which reaches 0 K in samples with hole concentrations ~ 10^{21} cm^{-3} as seen in Figure 2.5. T_{FT} is typically around 100 K for hole concentrations of about 10^{20} cm^{-3}. This ferroelectric transition seems to disappear for hole concentrations greater than ~10^{21} cm^{-3}.

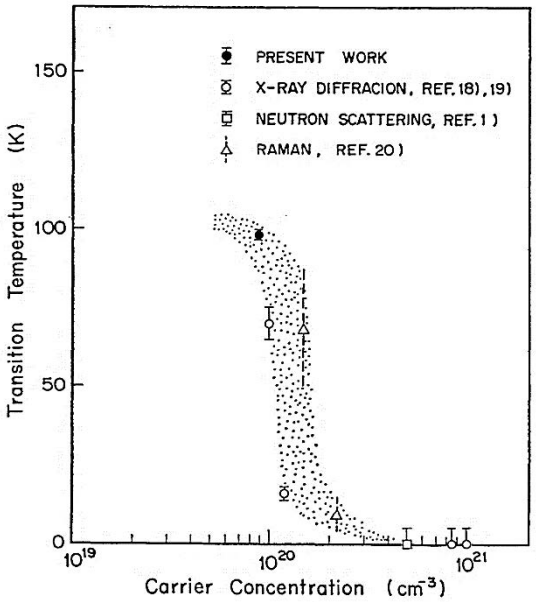

Figure 2.5: General relation of the ferroelectric transition temperature T_{FT} with the carrier concentration[39] (Also included are data from XRD[44,45], Neutron scattering[46] and Raman spectroscopy[43]).

2.2.5 Electronic band structure

The electronic band structure of SnTe has been widely discussed in the literature.[40,47] Dimmock *et al.* demonstrated that SnTe is a narrow-band-gap semiconductor with a gap of 0.18 eV by photoluminescence experiments.[48] Two years later, Rogers claimed that the valence bands of SnTe are actually dominated by two main valence bands.[49] Strictly speaking, these so-called two valence bands are not two different bands but two maxima of the last valence band. One of the valence band is a non-parabolic band, referred to as the light valence band, located at the L point of the Brillouin zone while the second parabolic band is referred to as the heavy valence band and is located at the Σ point, that is, half way between Γ and K in the k_Z = 0 plane. (Figure 2.6). The energy offset between these two maxima has been experimentally determined to be around 0.3 – 0.4 eV at 300 K.[40,50]

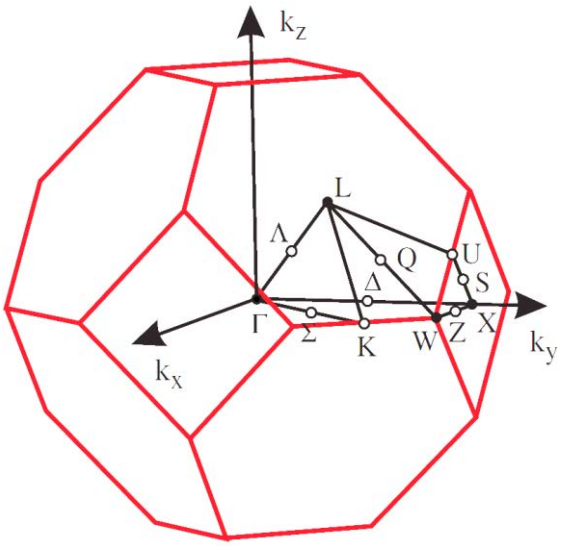

Figure 2.6: Brillouin zone of SnTe.[40]

Figure 2.7 shows the electronic band structure of SnTe calculated with and without spin-orbiting coupling (SOC).[51] These calculations reveal that the direct band gap calculated with SOC is 100 meV at the L point. While this value is consistent with earlier reports,[52,53] it is however, lower than the experimental value of 180 meV.[23,48,49,54]

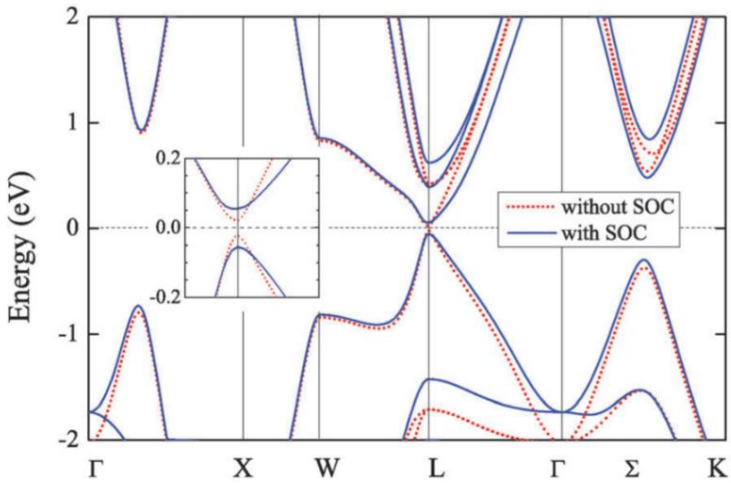

Figure 2.7: Electronic band structure calculated with and without spin-orbiting coupling in SnTe (the Fermi level is arbitrarily set to 0 eV).[51]

Similarly, there is a small difference between the calculated (240 meV) and experimental value (300 meV) of the energy separation between the two maxima of the last valence band ($\Delta\varepsilon_{VB_{L-\Sigma}}$).[23,49,51,54] Nevertheless, the better agreement between theory and experiments when taking into account SOC indicates that this coupling is essential in SnTe.[51]

As shown in Figure 2.8, the electronic band structure of SnTe is similar to that of PbTe with only differences in the energy separations of the various bands. The energy offset ($\Delta\varepsilon_{VB_{L-\Sigma}}$) separating the two maxima of the valence bands is higher in SnTe (0.3 eV) compared to PbTe (0.05 ~ 0.1 eV) at 300 K. Another difference is in the energy band gap of ~ 0.18 eV in SnTe compared to ~ 0.3 eV in PbTe at 300 K.[55]

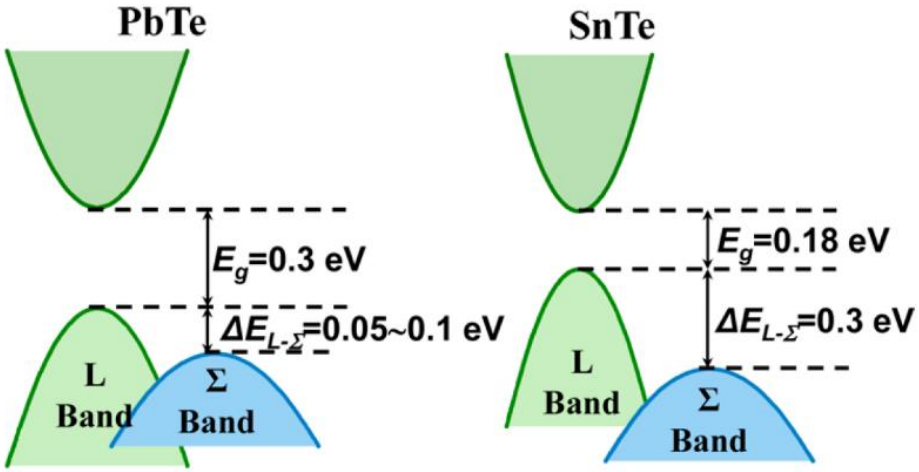

Figure 2.8: Electronic band structure comparison between PbTe and SnTe at 300 K.[55]

As already mentioned, many studies have shown that the good thermoelectric performances obtained at high temperatures in PbTe is mainly due to the contribution of the heavy valence band at the Σ point of the Brillouin zone. The convergence of the light and heavy valence bands leads to an increased number of degenerate valleys, which consequently increases the density-of-states effective mass and, ultimately, the thermopower values and hence, the *ZT* values. Because of these similarities between the electronic band structure of both compounds, numerous studies have been carried out to investigate the role of the heavy valence band on the thermoelectric properties of SnTe and on the influence of various substituting atoms on either the Sn or Te site.[5,55]

2.3 SnTe as a *p*-type thermoelectric material

Over the last years, intensive efforts have been devoted to enhance the thermoelectric performances of SnTe-based compounds, leading to a better understanding of the physics and chemistry of this interesting chalcogenide semiconductor. Many of these studies have been directed towards improving the power factors or lowering the lattice thermal conductivity by band structure engineering, reducing the hole concentration via substitutions of Sn or Te by various elements, modifying the synthesis process or manipulating the microstructure to significantly improve its *ZT* values. These spectacular results make this compound an interesting choice for mid-temperature range thermoelectric applications. In this part, we will briefly discuss the main results relevant to the understanding of the next chapter on the thermoelectric properties of In-substituted SnTe. For an intensive literature survey about the thermoelectric properties of SnTe and its multi-component derivatives, the interested reader can refer to the following reviews and thesis.[5,32,55]

2.3.1 Transport properties in binary SnTe compound

As discussed at the beginning of this chapter, the inherent high concentration of Sn vacancies makes SnTe a poor thermoelectric material compared to PbTe with a maximum *ZT* of ~ 0.4 at ~ 800 K.[5,55] Brebrick showed that single crystals of SnTe prepared by saturation annealing can have a hole concentration varying between 1×10^{20} and 2×10^{21} cm^{-3}.[31,54]

Following these pioneering studies and in an effort to counterbalance them, Tan *et al.* recently proposed to introduce excess Sn in the nominal composition, that is, Sn self-

compensation.[56] The authors showed that an excess of 3 at % of Sn ($Sn_{1.03}Te$) reduces the carrier concentration to ~ 2×10^{20} cm^{-3} at 300 K. As a result, the peak *ZT* value achieved was increased to ~ 0.6 at 800 K. Many subsequent studies used this simple strategy as a mean to lower the hole concentration (Figure 2.9) instead of using saturation annealing that are long and fastidious.[57,58] Consistent with the results obtained by Brebrick *et al.*, the temperature and hole-concentration dependences of the thermopower are subtle and non-trivial due to the contribution of the two main valence bands to the electronic transport.[23,54]

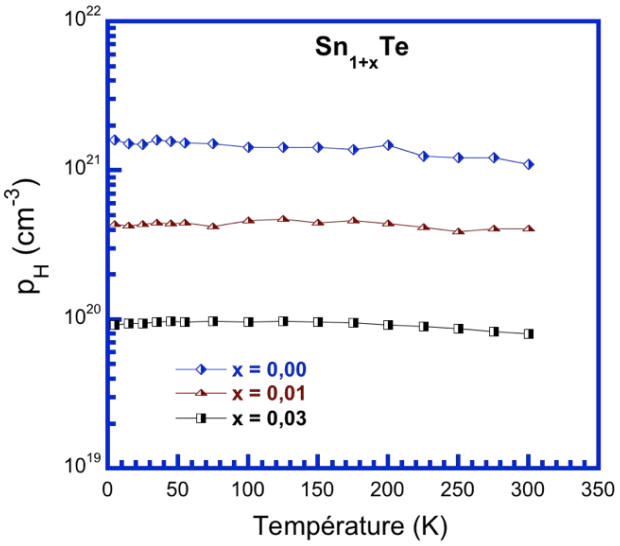

Figure 2.9: Temperature dependence of the hole concentration in $Sn_{1+x}Te$ for different values of x.[32]

Several anomalies, with respect to transport properties usually observed in simple semiconductors, are observed in SnTe. Firstly, at room temperature, the thermopower decreases with decreasing the hole concentration. This behavior is opposite to the generally observed behavior in semiconductors for which decreasing the hole carrier concentration implies an increase in the thermopower values. This unusual trend can be better visualized in Figure 2.10 that reports the hole concentration dependence of the thermopower, a relationship also known as the Ioffe-Pisarenko plot. At 300 K, these results show that the thermopower increases when the hole concentration varies from 2×10^{20} to 10^{21} cm^{-3}, a concentration at which α shows a maximum.

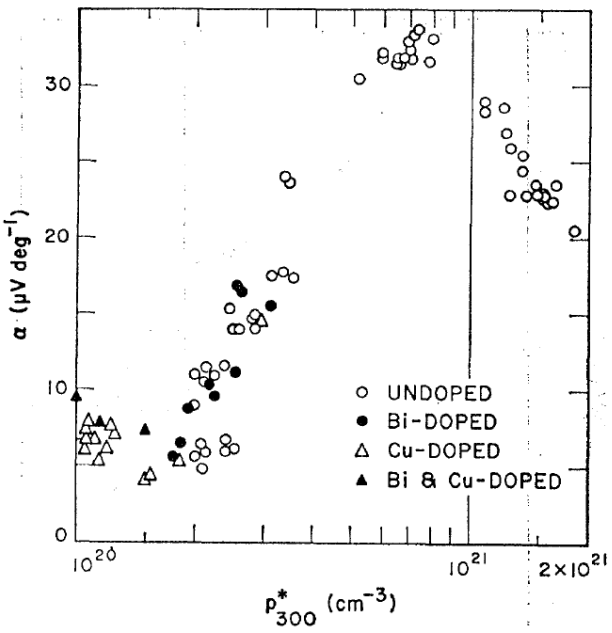

Figure 2.10: Ioffe-Pisarenko plot for Single crystal SnTe prepared by Brebrick *et al.*[54]

Above 10^{21} cm^{-3}, α decreases again. These results have been interpreted as highlighting the role of the second, heavy-hole valence band in SnTe.[49,54] In the case of two valence bands, the total thermopower is given as:

Equation 2.4:

$$\alpha = \frac{\alpha_{lh}\sigma_{lh} + \alpha_{hh}\sigma_{hh}}{\sigma_{lh}\sigma_{hh}}$$

where, α_{lh} and α_{hh} are the Seebeck coefficients of the light and heavy valence band, respectively, and σ_{lh} and σ_{hh} are the electrical conductivity of the light and heavy valence bands, respectively.

At high temperatures, the influence of the second, heavy-hole valence band is of increasing importance as the temperature increases, as shown in Figure 2.11. This is notably visualized by the inflection point at 580 K through which all the curves are passing. Above this temperature, the variation of α as a function of the hole concentration is reversed compared to that observed at 300 K. This reversed trend can be qualitatively understood by considering the valence band structure of SnTe. When the hole concentration of pristine SnTe is high, the chemical potential is located deep inside the valence bands and hence, is host by the heavy-hole band. The contribution of this band is thus significant, resulting in high thermopower

values. The self-compensation intentionally introduced in SnTe reduces the hole concentration that is accompanied by a shift of the chemical potential towards the top of the valence bands. In this region, the main contribution comes from the light-valence band, with the heavy-hole valence band being farther away in energy. As a result, lower α values emerge. This scenario also explains the behavior of α upon warming. As the temperature increases, the energy offset between the light-hole and the heavy-hole band decreases. The influence of the heavy-hole band on the transport is thus of increasing importance which enables reaching high thermopower values near 800 K.[49,54,56] The contribution of the second band is also confirmed by Hall effect measurements at high temperatures.[56]

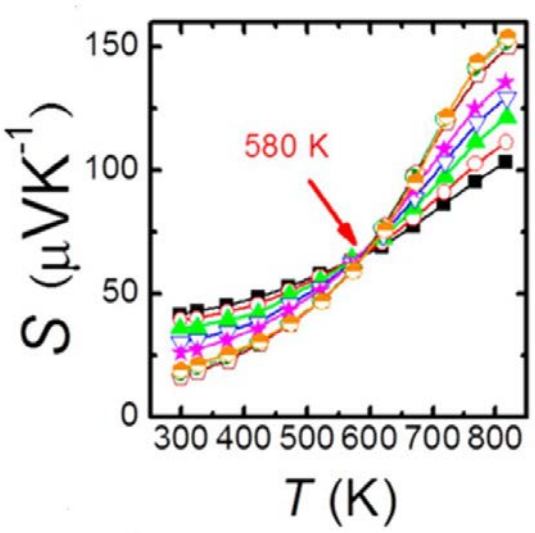

Figure 2.11: Temperature dependence of α for $Sn_{1+x}Te$ compounds showing an inflection point at 580 K.[56]

2.3.2 Improvement of power factor

Many elements have been successfully introduced in SnTe revealing a large chemical flexibility, paving the way towards further improvements of its thermoelectric properties. One possibility of improving the *ZT* values is by optimizing the power factor of SnTe-based compounds through different strategies such as optimizing the hole concentration, increasing the hole effective mass, achieving valence-band convergence, creating resonant levels, increasing the band gap, etc.

Apart from self-compensation with excess Sn in SnTe, several elements have been used to reduce and optimize the hole concentration. For instance, elements such as Bi, Te and Gd

were used to compensate the vacancy concentration.[50,59] Substituting I for Te also proved to be an efficient strategy to decrease the hole concentration down to 4×10^{19} cm^{-3},[50,60] yielding a peak *ZT* of 0.6 for $SnTe_{0.985}I_{0.015}$. However, due to the presence of electron-hole pairs (the so-called ambipolar effect) above 600 K, I is not a suitable dopant for improving the thermoelectric properties at higher temperatures.[50] Elements such as Ca or Mg lead to a decrease in the energy offset $\Delta\Sigma_{VB_{L-\Sigma}}$ that separates the two valance bands when substituted for Sn.[60,61] This band convergence will tend to increase the density of states effective mass m^*_{DOS} given by:

Equation 2.5:

$$m^*_{DOS} = (N_v)^{2/3} m^*_b$$

where N_v is the number of degenerate valleys. Because the thermopower values are directly proportional to m^*_{DOS}, higher values will be obtained at high temperatures. For instance, a higher value of ~ 180 $\mu V.K^{-1}$ has been obtained for $Sn_{0.94}Ca_{0.09}Te$ at 873 K compared to the values measured in pristine SnTe.[61] A similar increase in α up to ~ 200 $\mu V.K^{-1}$ was obtained for $Sn_{0.95}Mg_{0.08}Te$ at 856 K.[60] Mn has also proven to be an interesting dopant in SnTe for achieving valence-band convergence leading to a peak *ZT* of 1.25 for $SnMn_{0.07}Te$ at 920 K.[62] Theoretically, Tan *et al.* calculated the reduction of the energy offset for various dopants in SnTe (Figure 2.12).[51]

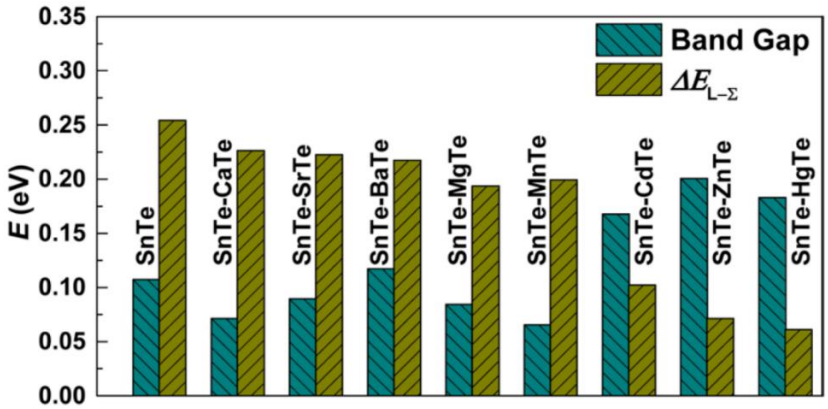

Figure 2.12. Band gap and energy offset calculated by Tan *et al.* for SnTe and $Sn_{26}ATe_{27}$ compounds (A = Ca, Sr, Ba, Mg, Mn, Cd, Zn, Hg).[51,55,60,61,63]

High temperatures promote the excitation of minority carriers across the band gap giving rise to a ambipolar effect. This effect is all the more pronounced as the band gap of the

compound is small.[64] Of note, this effect always has a negative impact on the thermoelectric properties via a rapid decrease in the thermopower values. The detrimental influence of the minority carriers can be shifted to higher temperatures by either increasing the band gap of the compound or by increasing the level of doping. Mn and Hg have been shown to be the elements of choice to increase the band gap and shift the bipolar peak at higher temperatures, ultimately leading to better thermoelectric performances.[53,65]

While In has been for long the only known element giving rise to a resonant level (see the next section) in SnTe,[66] a recent study has proposed that Zn also form a RL in the valence band of SnTe. The beneficial influence of the RL results in significantly higher thermoelectric performances, both at room and high temperatures (Figure 2.13).[67] However, the truly resonant nature of Zn in SnTe remains to be firmly established.

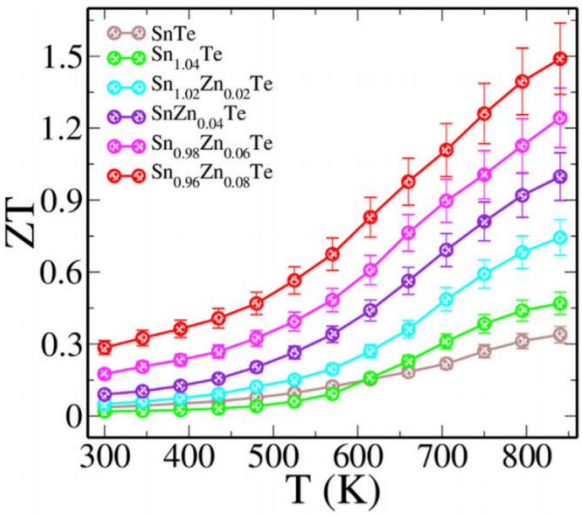

Figure 2.13: Temperature dependence of *ZT* in $Sn_{1.04-x}Zn_xTe$ based compounds.[67]

2.3.3 Reduction of the lattice thermal conductivity

A second important strategy followed to improve the thermoelectric properties of SnTe is by decreasing its lattice thermal conductivity. As already discussed in Chapter 1, the formation of solid solutions, mass and size mismatch between the Sn, Te and the substituting elements, multiple substitutions or nanostructuration are all possible strategies to reduce the phonon heat transport due to the increase in phonon scattering.[53,56,60,61,66,68–77] Another way is the formation of nanostructures (nanoprecipitates) which is formed when a solvent exceeds its equilibrium solubility limit under suitable synthesis conditions. The introduction of all-scale

hierarchical architecture provides another way of reducing the lattice thermal conductivity through the combination of point defects, nanostructuring and mesoscale structuring.[78] Figure 2.14 shows the comparison of the lowest values of lattice thermal conductivity achieved by these various methods for SnTe-based materials.

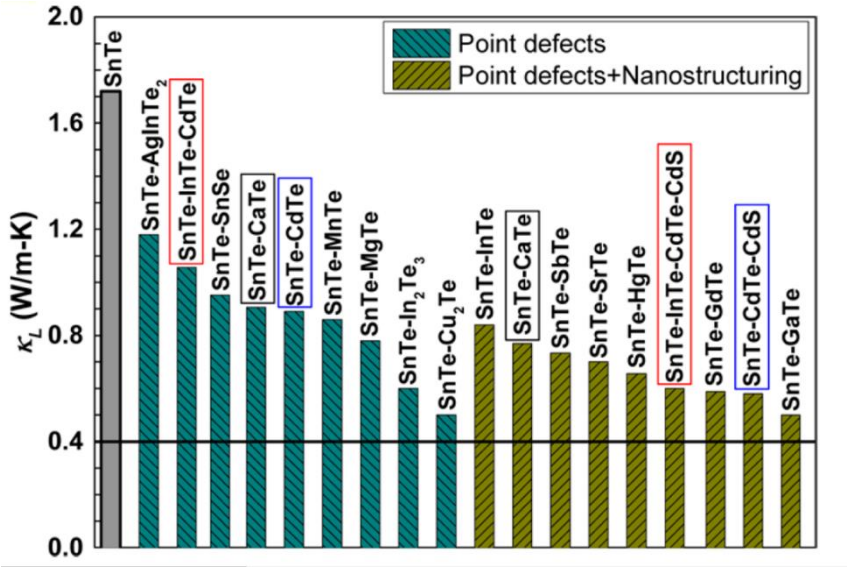

Figure 2.14: Comparison of lattice thermal conductivity obtained by different techniques for different elements.[53,56,60,61,66,68–71,73–77,79] Black line depicts the minimum value estimated by the Debye- Cahill model.[55,80]

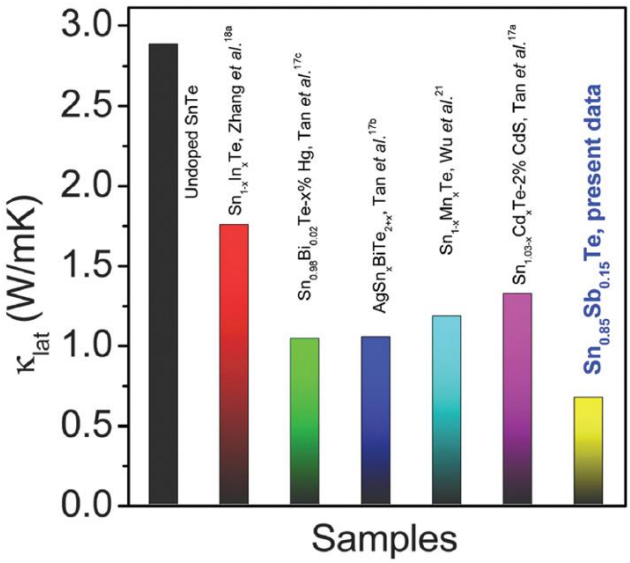

Figure 2.15: Comparison of lattice thermal conductivity at 300 K for different high performing SnTe based compounds.[53,53,56,65,66,75]

Several dopants and alloys have been proposed to realize this. For instance, Banik *et al.* showed that SnTe-SbTe system leads to the formation of Sb-rich precipitates leading to ultra-low lattice thermal conductivity (see Figure 2.15) yielding a high *ZT* of ~ 1 at 800 K.[75]

2.3.4 Combined effects

The above-mentioned various strategies mainly focus on either improving the electronic part or decreasing the lattice thermal conductivity in SnTe. Several studies have attempted to combine these effects in order to further enhance the thermoelectric performances of SnTe. In this context, some of the most interesting compounds include Cd and In co-doping in SnTe with nanoprecipitates of CdS that led to a high *ZT* of ~ 1.4 at ~ 923 K.[69] Combined effect of resonant level, valence band convergence and nanoprecipitates were observed for the $Sn_{0.97}Cd_{0.015}In_{0.015}$- 3% CdS compound.

The highest *ZT* obtained so far for SnTe-based compound was achieved in Mn-doped SnTe with inclusion of Cu_2Te precipitates resulting in a peak *ZT* of 1.6 at 900 K (See Figure 2.16).[6] A combination of band convergence and interstitial defects was proposed to be the key effects leading to this strong increase in the *ZT* values. Although it is important to note that the thermal stability of these nanostructured samples should be taken in account and carefully evaluated.

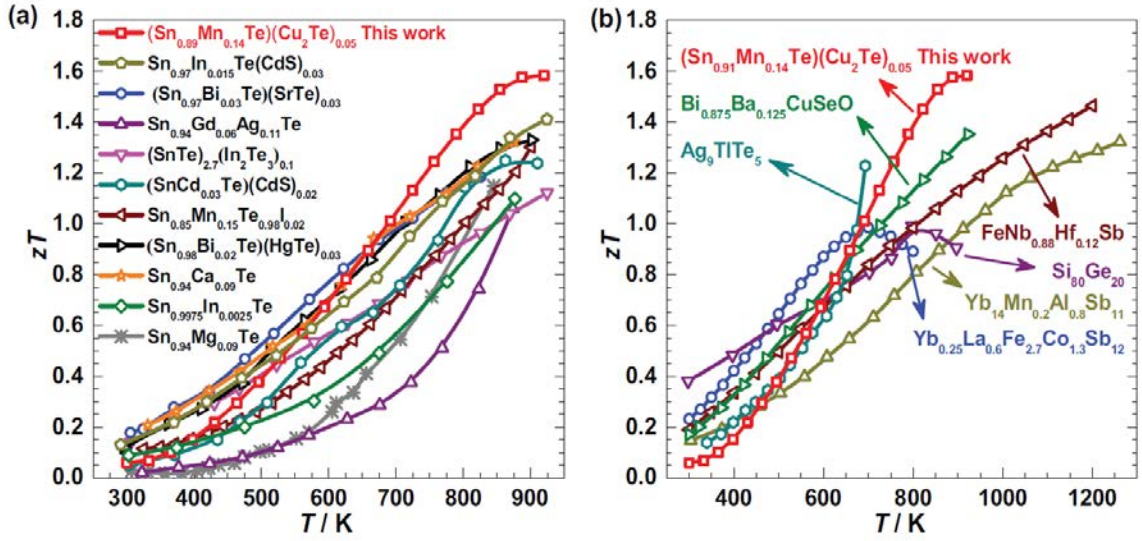

Figure 2.16: a) Comparison of peak *ZT* for different SnTe-based compounds as a function of temperature b) Comparison of *ZT* with other thermoelectric materials.[6]

2.4 Effect of substituting In for Sn in SnTe

2.4.1 Resonant Levels

One possible way of optimizing the power factor of semiconductors is through the introduction of an impurity that gives rise to a resonant level (RL) at the edge of either the valence or conduction bands.[81–83] The impurity atoms distort locally the electronic band structure beyond the rigid-band model. A significant increase in the thermopower and, hence, in the power factor is observed when the chemical potential resides in this distortion due to the increased DOS (more detailed explanations about the effect of RL will be presented in Chapter 3).

RL are often found in chalcogenide semiconductors doped with group III elements (for instance, Tl in PbTe or In in SnTe). Zhang *et al.* evidenced that substituting In for Sn gives rise to a RL in the valence band structure of SnTe.[66] Their initial investigation on the high-temperature thermoelectric properties of the series $Sn_{1-x}In_xTe$ for x = 0.0025, 0.005 and 0.01 identified the lowest In content studied as the optimum concentration, as shown in Figure 2.17. Combined with reduced lattice thermal conductivity achieved by ball milling, the resonant-driven enhancement of the power factor led to an improved *ZT* value of 1.1 at 873 K.

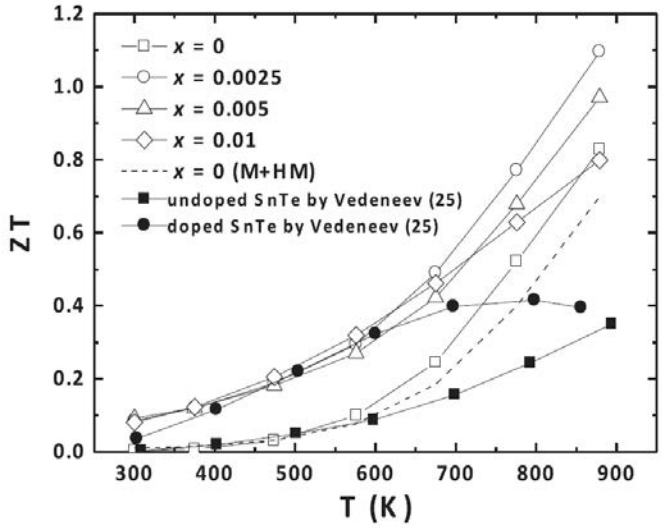

Figure 2.17: Temperature dependence of *ZT* for In-doped SnTe indicating x = 0.0025 as the optimum In concentration [66] (Data obtained by Vedeneev *et al.*[59] are also included).

2.4.2 Superconductivity

The increased density-of-states at the Fermi level induced by the RL often results in the emergence of superconductivity. In PbTe, the formation of a Tl-induced RL results in a superconducting transition beyond a critical Tl concentration of around 0.3%.[84,85] What made this observation particularly intriguing is the high critical temperatures T_c of up to 1.5 K achieved at relatively low hole densities of around 10^{20} cm^{-3} for which, the BCS theory predicts that T_c should be several orders of magnitude lower than the experimental values. The fact that a conventional phonon-mediated pairing interaction is unable to account for this anomalously high T_c triggered the development of alternative scenarios. While the presence of additional carrier pockets in the Brillouin zone resulting in increased density of states, interband scattering or the creation of Te vacancies counterbalancing the additional holes provided by Tl have been proposed,[85,86] a number of circumstantial evidence points to a possible role played by charge fluctuations of the Tl atoms between Tl^+ and Tl^{3+} valence states.[87–90] For instance, Costi *et al.* showed, by means of Hall effect measurements (Figure 2.18), that Tl acts as an acceptor, that is, Tl is in the +1 oxidation state (Pb is +2), at low Tl concentrations (x < 0.5 %),. Above this concentration, Tl fluctuates between +1 and +3 and the hole concentration begins to saturate with evidence of self-compensation of Tl valence (average valence of +2).[87]

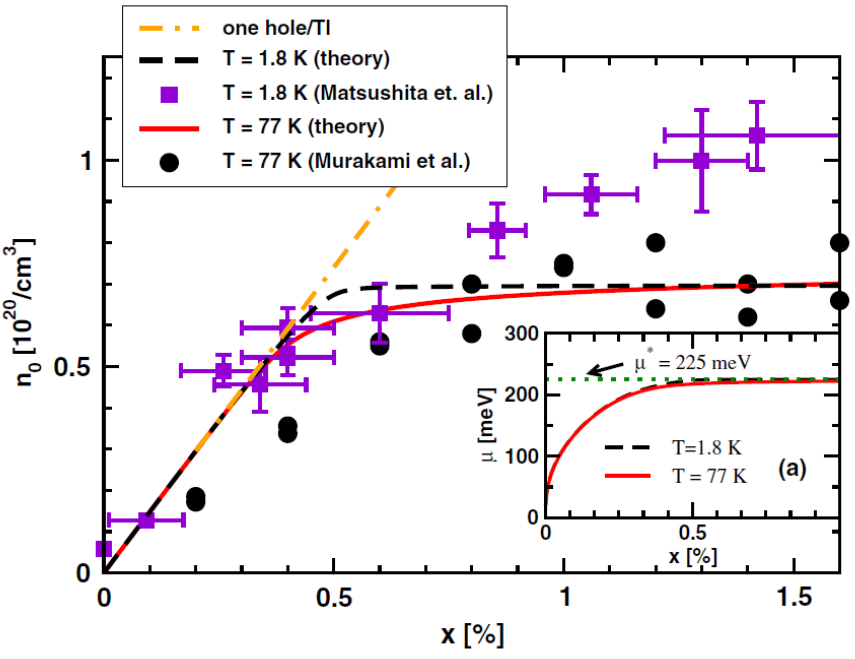

Figure 2.18: Hole concentration plotted as a function of the Tl content in $Pb_{1-x}Tl_xTe$.[87]

A negative U model of superconductivity was proposed in which the valence fluctuations between +1 and +3 act as a mechanism of Cooper pairing and hence, leads to superconductivity.[88,91] Electron scattering from these valence fluctuations could be the reason for such behavior. Recent photoemission spectroscopy measurements have lent experimental credit to this scenario by evidencing the presence of the two valences Tl^{1+} and Tl^{3+} and the absence of a second band at the Fermi energy, ruling out the presence of additional pockets in the Brillouin zone.[92,93] When the Sn vacancy concentration is higher than 10^{20} cm^{-3}, SnTe shows a transition to superconductivity with critical temperature less than 0.3 K, in agreement with the BCS theory.[94] This behavior persists for hole concentrations of up to 2×10^{21} cm^{-3}. This scenario drastically changes upon introducing In on the Sn site: superconductivity develops even for low In contents. T_c can be as high as 2 K for an In content of around 10 %, as shown in Figure 2.19.[11,13–17,19,95–98]

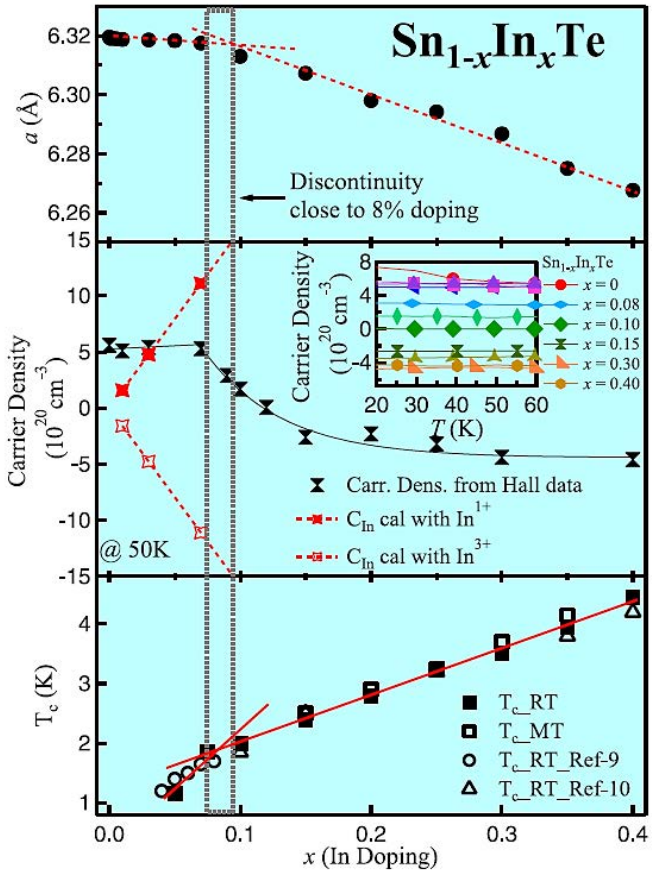

Figure 2.19: Temperature dependence of a) the lattice parameter, b) hole concentration and c) T_c in the $Sn_{1-x}In_xTe$ system.[14]

Erickson *et al.* showed that the soft-phonon mode associated with the ferroelectric phase transition, preserved in the $Sn_{1-x}In_xTe$ compounds, is not the reason for this enhanced critical temperature.[11] Similar to $Pb_{1-x}Tl_xTe$, anomalous superconducting properties are also observed in $Sn_{1-x}In_xTe$ for x up to 40%. At this concentration that corresponds to the solubility limit of In in SnTe, T_c ultimately reaches 4.5 K (see Figure 2.20).[14,15,95] By analogy with the $Pb_{1-x}Tl_xTe$ compounds, alternative scenarios to the BCS theory has been advanced to explain the anomalous superconducting properties of $Sn_{1-x}In_xTe$, notably including the charge-Kondo effect (see below).[11,87,91,92] The deep connection between the resonant behavior and superconductivity is, however, yet to be fully understood, making the series $Sn_{1-x}In_xTe$ worthy of further theoretical and experimental studies.[99]

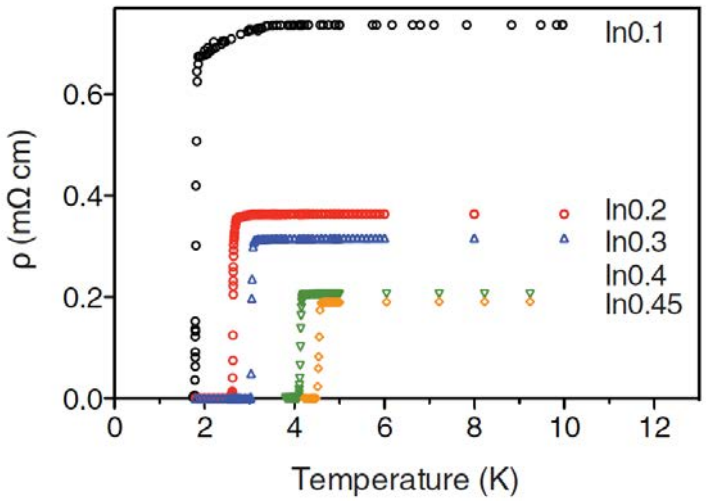

Figure 2.20: Temperature dependence of the electrical resistivity showing T_c as high as 4.5 K for $Sn_{0.55}In_{0.45}Te$.[95]

2.4.3 Charge-Kondo effect

The Kondo effect can be explained as an anomaly in the temperature dependence of the electrical resistivity upon cooling to helium temperatures that occurs in metals containing a small concentration of magnetic impurities.[100] Similarly, the interaction between the charge carriers and an impurity that is not magnetic can give rise to a phenomenon referred to as the charge-Kondo effect. For this effect to occur, the impurity should exhibit a valence-skipping mechanism, that is, fluctuations between two valence states. This effect has been shown theoretically to provide a superconducting pairing interaction, possibly explaining most of the normal-state and superconducting properties of the $Pb_{1-x}Tl_xTe$ compounds.[87,91,101]

Low-temperature thermopower measurements have shown non-linear behavior of thermopower reaching negative values in the $Pb_{1-x}Tl_xTe$ compounds (Figure 2.21). This anomalous dependence of the thermopower with x has been proposed as an experimental evidence for a charge-Kondo effect.[90]

Due to the valence-skipping nature of In observed in various compounds,[102,103] these striking similarities with $Pb_{1-x}Tl_xTe$ suggest that a valence-fluctuation scenario might equally apply to $Sn_{1-x}In_xTe$. Erickson *et al.* first claimed the existence of a charge-Kondo effect in $Sn_{1-\delta-x}In_xTe$, where δ stands for the inherent Sn vacancies.[11] However, the valence state of In has not been directly probed in this particular system, still making the presence of a charge-Kondo effect an open question.

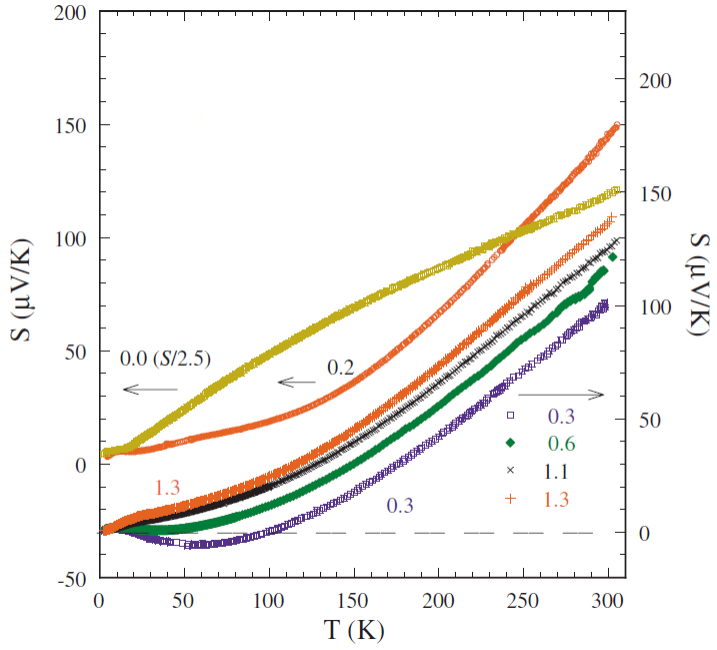

Figure 2.21: Temperature dependence of the thermopower for $Pb_{1-x}Tl_xTe$ (x = 0.0 and 0.2 % with left hand scale & x = 0.3, 0.6, 1.1 and 1.3 % with right hand scale).[90]

2.5 Conclusion

The above-mentioned considerations show that In is a very interesting dopant in SnTe, should it be for improving its thermoelectric properties or for fundamental reasons due to its connection to exotic properties emerging at low temperatures. Although there have been several works on this system, some keys issues, which will be presented and discussed in detail

in the next Chapter, still warrant further experimental and theoretical investigations and have motivated a part of the present thesis work:

- *Low-temperature transport property measurements in $Sn_{1-x}In_xTe$ for low values of x.*
  Although prior studies have mainly focused on the evolution of superconductivity with *x* at high In contents,[11,13–15,96,98] no detailed investigation of the low-temperature transport properties of the series $Sn_{1-x}In_xTe$ has been reported so far.

- *Justification of different transport anomalies in $Sn_{1-x}In_xTe$ and comparison with $Pb_{1-x}Tl_xTe$ at low temperatures.*
  Because the non-monotonic evolution of the low-temperature thermopower in $Pb_{1-x}Tl_xTe$ has been interpreted in terms of the charge-Kondo effect,[90] it is of interest to extend these measurements to the series $Sn_{1-x}In_xTe$ to determine the extent to which both systems behave similarly. Apart from the charge-Kondo effect, investigating other possibilities such as the presence of electron pockets in the Brillouin zone leading to interband scattering or phonon-drag effect is of particular interest.

- *In-depth study of transport properties at high temperatures to clarify the presence and effect of the In-induced RL in SnTe.*
  Compared to other RL systems for which the optimum doping level is typically around 2%, the In concentration reported by Zhang *et al.* is significantly lower, possibly due to the large amount of Sn vacancies inherently present in pristine SnTe.[66] Because the heavy hole doping induced by these vacancies may shift the chemical potential away from the RL, it is of interest to determine in more detail their influence on the thermoelectric properties of In-substituted SnTe. In this regard, extending these investigations to the series with Sn excess ($Sn_{1.03-x}In_xTe$) may help to better highlight the influence of the RL on the transport properties due to the lower hole concentration of the binary compound $Sn_{1.03}Te$.

References

1. Fu, T., Yue, X., Wu, H., Fu, C., Zhu, T., Liu, X., Hu, L., Ying, P., He, J. & Zhao, X. Enhanced thermoelectric performance of PbTe bulk materials with figure of merit *ZT* >2 by multi-functional alloying. *Journal of Materiomics* **2,** 141 (2016).
2. Jood, P., Ohta, M., Yamamoto, A. & Kanatzidis, M. G. Excessively Doped PbTe with Ge-Induced Nanostructures Enables High-Efficiency Thermoelectric Modules. *Joule* **2,** 1339–1355 (2018).
3. Wu, H. J., Zhao, L.-D., Zheng, F. S., Wu, D., Pei, Y. L., Tong, X., Kanatzidis, M. G. & He, J. Q. Broad temperature plateau for thermoelectric figure of merit *ZT*>2 in phase-separated $PbTe_{0.7}S_{0.3}$. *Nature Communications* **5,** 4515 (2014).
4. Wu, L., Li, X., Wang, S., Zhang, T., Yang, J., Zhang, W., Chen, L. & Yang, J. Resonant level-induced high thermoelectric response in indium-doped GeTe. *NPG Asia Materials* **9,** e343 (2017).
5. Moshwan, R., Yang, L., Zou, J. & Chen, Z.-G. Eco-Friendly SnTe Thermoelectric Materials: Progress and Future Challenges. *Advanced Functional Materials* **27,** 1703278 (2017).
6. Li, W., Zheng, L., Ge, B., Lin, S., Zhang, X., Chen, Z., Chang, Y. & Pei, Y. Promoting SnTe as an Eco-Friendly Solution for p-PbTe Thermoelectric via Band Convergence and Interstitial Defects. *Advanced Materials* **29,** 1605887 (2017).
7. Kolomoets, N. V., Lev, E. Y. & Sysoeva, L. M. Electrical propoerties and valence band structure of Germanium Telluride. *Soviet Physics-Solid State* **6,** 551 (1964).
8. Kolomoets, N. V., Lev, E. Y. & Sysoeva, L. M. Nature of charge carriers in GeTe. *Soviet Physics-Solid State* **5,** 2101 (1964).
9. Levin, E. M., Besser, M. F. & Hanus, R. Electronic and thermal transport in GeTe: A versatile base for thermoelectric materials. *Journal of Applied Physics* **114,** 083713 (2013).
10. Hsieh, T. H., Lin, H., Liu, J., Duan, W., Bansil, A. & Fu, L. Topological crystalline insulators in the SnTe material class. *Nature Communications* **3,** 982 (2012).
11. Erickson, A. S., Chu, J.-H., Toney, M. F., Geballe, T. H. & Fisher, I. R. Enhanced superconducting pairing interaction in indium-doped tin telluride. *Physical Review B* **79,** 024520 (2009).

12. Erickson, A. S., Geballe, T. H., Fisher, I. R., Wu, Y. Q. & Kramer, M. J. Anomalous scattering in superconducting indium-doped tin telluride. *arXiv:1009.0090 [cond-mat]* (2010).
13. Novak, M., Sasaki, S., Kriener, M., Segawa, K. & Ando, Y. Unusual nature of fully gapped superconductivity in In-doped SnTe. *Physical Review B* **88,** 140502(R) (2013).
14. Haldolaarachchige, N., Gibson, Q., Xie, W., Nielsen, M. B., Kushwaha, S. & Cava, R. J. Anomalous composition dependence of the superconductivity in In-doped SnTe. *Physical Review B* **93,** 024520 (2016).
15. Balakrishnan, G., Bawden, L., Cavendish, S. & Lees, M. R. Superconducting properties of the In-substituted topological crystalline insulator SnTe. *Physical Review B* **87,** 140507 (2013).
16. Smylie, M. P., Claus, H., Kwok, W.-K., Louden, E. R., Eskildsen, M. R., Sefat, A. S., Zhong, R. D., Schneeloch, J., Gu, G. D., Bokari, E., Niraula, P. M., Kayani, A., Dewhurst, C. D., Snezhko, A. & Welp, U. Superconductivity, pairing symmetry, and disorder in the doped topological insulator $Sn_{1-x}In_xTe$ for $x \geq 0.10$. *Physical Review B* **97,** 024511 (2018).
17. Kobayashi, K., Ai, Y., Jeschke, H. O. & Akimitsu, J. Enhanced superconducting transition temperatures in the rocksalt-type superconductors $In_{1-x}Sn_xTe$ ($x \leq 0.5$). *Physical Review B* **97,** 104511 (2018).
18. Maeda, S., Hirose, R., Matano, K., Novak, M., Ando, Y. & Zheng, G. Spin-singlet superconductivity in the doped topological crystalline insulator $Sn_{0.96}In_{0.04}Te$. *Physical Review B* **96,** 104502 (2017).
19. Xu, Z., Schneeloch, J. A., Zhong, R. D., Rodriguez-Rivera, J. A., Harriger, L. W., Birgeneau, R. J., Gu, G. D., Tranquada, J. M. & Xu, G. Low-energy phonons and superconductivity in $Sn_{0.8}In_{0.2}Te$. *Physical Review B* **91,** 054522 (2015).
20. Fay, H. Tellurium-Tin alloys. *J. Am. Chem. Soc.* **29,** 1265 (1907).
21. Kattner, U., Lukas, H. L. & Petzow, G. Optimization and calculation of the Sn-Te system. *Journal of the Less Common Metals* **114,** 129 (1985).
22. Rogacheva, E. in *Stoichiometry and Materials Science - When Numbers Matter* (ed. Innocenti, A.) (InTech, 2012).
23. Brebrick, R. F. Deviations from stoichiometry and electrical properties in SnTe. *Journal of Physics and Chemistry of Solids* **24,** 27 (1963).
24. Brebrick, R. F. Composition stability limits for the rocksalt-structure phase $(Pb_{1-y}Sn_y)_{1-x}Te_x$ from lattice parameter measurements. *Journal of Physics and Chemistry of Solids* **32,** 551 (1971).

25. Brebrick, R. F. & Strauss, A. J. Partial Pressures in Equilibrium with Group IV Tellurides. II. Tin Telluride. *The Journal of Chemical Physics* **41,** 197 (1964).
26. Shelimova, L. E. & Abrikosov, N. K. Sn-Te system in the region of SnTe compound. *Zhurnal neorgan. khimii* **9,** 1879 (1964).
27. Miloslavov, S. A., Tairov, S. M. & Ormont, B. F. Definition of Charged Point Defect Concentration in Alloys of the PbTe-SnTe System. *Izv. Akad. Nauk SSSR, Neorg. Mater.* **6,** 2063 (1970).
28. Maselsky, R. & Lubell, M. S. Nonstoichiometry in some group IV tellurides. *Advanc. Chem. Ser* **39,** 210–217 (1963).
29. Rogacheva, E. I., Gorne, G. V., Zhigareva, N. K. & Ivanova, A. B. Homogeneity region of tin monotelluride. *Izvestiya Akademii Nauk SSSR, Neorganicheskie Materialy* **27,** 267 (1991).
30. Brebrick, R. F. Composition stability limits of binary semiconductor compounds. *Journal of Physics and Chemistry of Solids* **18,** 116 (1961).
31. Brebrick, R. F. Analysis of the solidus lines for PbTe and SnTe. *Journal of Electronic Materials* **6,** 659 (1977).
32. Ibrahim, D. Synthèse et caractérisation de matériaux à base de SnTe pour la conversion d'énergie par effets thermoélectriques. (2018).
33. O'Neill, C. D., Sokolov, D. A., Hermann, A., Bossak, A., Stock, C. & Huxley, A. D. Inelastic x-ray investigation of the ferroelectric transition in SnTe. *Physical Review B* **95,** 144101 (2017).
34. Mazelsky, R. & Lubell, M. S. in *Nonstoichiometric Compounds* (ed. Ward, R.) **39,** 210 (American Chemical Society, 1963).
35. Houston, B. B., Allgaier, R. S., Babiskun, I. & Siebenmann, P. G. Relationship between Real and Nominal Carrier Concentrations in p-Type SnTe. *Bull. Am. Phys, Soc.* **9,** 60 (1964).
36. Bis, R. F. & Dixon, J. R. Applicability of Vegard's Law to the $Pb_xSn_{1-x}Te$ Alloy System. *Journal of Applied Physics* **40,** 1918 (1969).
37. Sagar, L. A. & Miller, R. C. *Report of the International Conference on the Physics of Semiconductors, Exeter, 1962*. (The Institute of Physics and the Physical Society, London, 1962).
38. Lefebvre, I., Szymanski, M. A., Olivier-Fourcade, J. & Jumas, J. C. Electronic structure of tin monochalcogenides from SnO to SnTe. *Physical Review B* **58,** 1896 (1998).

39. Iizumi, M., Hamaguchi, Y., F. Komatsubara, K. & Kato, Y. Phase Transition in SnTe with Low Carrier Concentration. *Journal of the Physical Society of Japan* **38,** 443 (1975).
40. Littlewood, P. B., Mihaila, B., Schulze, R. K., Safarik, D. J., Gubernatis, J. E., Bostwick, A., Rotenberg, E., Opeil, C. P., Durakiewicz, T., Smith, J. L. & Lashley, J. C. Band Structure of SnTe Studied by Photoemission Spectroscopy. *Physical Review Letters* **105,** 086404 (2010).
41. Kafalas, J. A. & Mariano, A. N. High-Pressure Phase Transition in Tin Telluride. *Science* **143,** 952 (1964).
42. Fano, V., Fedeli, G. & Ortalli, I. Phase transition in SnTe by Mössbauer spectroscopy. *Solid State Communications* **22,** 467 (1977).
43. Brillson, L. J., Burstein, E. & Muldawer, L. Raman observation of the ferroelectric phase transition in SnTe. *Physical Review B* **9,** 1547 (1974).
44. Muldawer, L. Low temperature transformation in SnTe. *Bull. Am. Phys, Soc.* **16,** 84 (1971).
45. Muldawer, L. New studies of the low temperature transformation in SnTe. *J. Nonmetals* **1,** 177 (1973).
46. Pawley, G. S., Cochran, W., Cowley, R. A. & Dolling, G. Diatomic Ferroelectrics. *Physical Review Letters* **17,** 753 (1966).
47. Rabii, S. Energy-Band Structure and Electronic Properties of SnTe. *Physical Review* **182,** 821 (1969).
48. Dimmock, J. O., Melngailis, I. & Strauss, A. J. Band structure and laser action in Pb x Sn 1− x Te. *Physical Review Letters* **16,** 1193 (1966).
49. Rogers, L. M. Valence band structure of SnTe. *Journal of Physics D: Applied Physics* **1,** 845 (1968).
50. Zhou, M., Gibbs, Z. M., Wang, H., Han, Y., Xin, C., Li, L. & Snyder, G. J. Optimization of thermoelectric efficiency in SnTe: the case for the light band. *Phys. Chem. Chem. Phys.* **16,** 20741 (2014).
51. Tan, X. J., Shao, H. Z., He, J., Liu, G. Q., Xu, J. T., Jiang, J. & Jiang, H. C. Band engineering and improved thermoelectric performance in M-doped SnTe (M = Mg, Mn, Cd, and Hg). *Physical Chemistry Chemical Physics* **18,** 7141 (2016).
52. Wang, N., West, D., Liu, J., Li, J., Yan, Q., Gu, B.-L., Zhang, S. B. & Duan, W. Microscopic origin of the p -type conductivity of the topological crystalline insulator SnTe and the effect of Pb alloying. *Physical Review B* **89,** 045142 (2014).

53. Tan, G., Shi, F., Doak, J. W., Sun, H., Zhao, L.-D., Wang, P., Uher, C., Wolverton, C., Dravid, V. P. & Kanatzidis, M. G. Extraordinary role of Hg in enhancing the thermoelectric performance of p-type SnTe. *Energy & Environmental Science* **8,** 267 (2015).
54. Brebrick, R. F. & Strauss, A. J. Anomalous Thermoelectric Power as Evidence for Two-Valence Bands in SnTe. *Physical Review* **131,** 104 (1963).
55. Li, W., Wu, Y., Lin, S., Chen, Z., Li, J., Zhang, X., Zheng, L. & Pei, Y. Advances in Environment-Friendly SnTe Thermoelectrics. *ACS Energy Letters* **2,** 2349 (2017).
56. Tan, G., Zhao, L.-D., Shi, F., Doak, J. W., Lo, S.-H., Sun, H., Wolverton, C., Dravid, V. P., Uher, C. & Kanatzidis, M. G. High Thermoelectric Performance of p-Type SnTe via a Synergistic Band Engineering and Nanostructuring Approach. *Journal of the American Chemical Society* **136,** 7006 (2014).
57. Ibrahim, D., Ohorodniichuk, V., Candolfi, C., Semprimoschnig, C., Dauscher, A. & Lenoir, B. Improved Thermoelectric Properties in Melt-Spun SnTe. *ACS Omega* **2,** 7106 (2017).
58. Acharya, S., Pandey, J. & Soni, A. Soft phonon modes driven reduced thermal conductivity in self-compensated $Sn_{1.03}Te$ with Mn doping. *Applied Physics Letters* **109,** 133904 (2016).
59. Vedeneev, V. P., Krivoruchko, S. P. & Sabo, E. P. Tin telluride based thermoelectrical alloys. *Semiconductors* **32,** 241 (1998).
60. Banik, A., Shenoy, U. S., Anand, S., Waghmare, U. V. & Biswas, K. Mg Alloying in SnTe Facilitates Valence Band Convergence and Optimizes Thermoelectric Properties. *Chemistry of Materials* **27,** 581 (2015).
61. Al Rahal Al Orabi, R., Mecholsky, N. A., Hwang, J., Kim, W., Rhyee, J.-S., Wee, D. & Fornari, M. Band Degeneracy, Low Thermal Conductivity, and High Thermoelectric Figure of Merit in SnTe–CaTe Alloys. *Chemistry of Materials* **28,** 376 (2016).
62. He, J., Tan, X., Xu, J., Liu, G.-Q., Shao, H., Fu, Y., Wang, X., Liu, Z., Xu, J., Jiang, H. & Jiang, J. Valence band engineering and thermoelectric performance optimization in SnTe by Mn-alloying via a zone-melting method. *J. Mater. Chem. A* **3,** 19974 (2015).
63. Dong, X., Yu, H., Li, W., Pei, Y. & Chen, Y. First-principles study on band structures and electrical transports of doped-SnTe. *Journal of Materiomics* **2,** 158 (2016).
64. Gong, J. J., Hong, A. J., Shuai, J., Li, L., Yan, Z. B., Ren, Z. F. & Liu, J.-M. Investigation of the bipolar effect in the thermoelectric material $CaMg_2Bi_2$ using a first-principles study. *Physical Chemistry Chemical Physics* **18,** 16566 (2016).

65. Wu, H., Chang, C., Feng, D., Xiao, Y., Zhang, X., Pei, Y., Zheng, L., Wu, D., Gong, S., Chen, Y., He, J., Kanatzidis, M. G. & Zhao, L.-D. Synergistically optimized electrical and thermal transport properties of SnTe via alloying high-solubility MnTe. *Energy & Environmental Science* **8,** 3298 (2015).
66. Zhang, Q., Liao, B., Lan, Y., Lukas, K., Liu, W., Esfarjani, K., Opeil, C., Broido, D., Chen, G. & Ren, Z. High thermoelectric performance by resonant dopant indium in nanostructured SnTe. *Proceedings of the National Academy of Sciences* **110,** 13261 (2013).
67. Bhat, D. K. & Shenoy, U. S. Zn: a versatile resonant dopant for SnTe thermoelectrics. *Materials Today Physics* **11,** 100158 (2019).
68. Banik, A., Shenoy, U. S., Saha, S., Waghmare, U. V. & Biswas, K. High Power Factor and Enhanced Thermoelectric Performance of SnTe-$AgInTe_2$: Synergistic Effect of Resonance Level and Valence Band Convergence. *Journal of the American Chemical Society* **138,** 13068 (2016).
69. Tan, G., Shi, F., Hao, S., Chi, H., Zhao, L.-D., Uher, C., Wolverton, C., Dravid, V. P. & Kanatzidis, M. G. Codoping in SnTe: Enhancement of Thermoelectric Performance through Synergy of Resonance Levels and Band Convergence. *Journal of the American Chemical Society* **137,** 5100 (2015).
70. Li, W., Chen, Z., Lin, S., Chang, Y., Ge, B., Chen, Y. & Pei, Y. Band and scattering tuning for high performance thermoelectric $Sn_{1-x}Mn_xTe$ alloys. *Journal of Materiomics* **1,** 307 (2015).
71. Pei, Y., Zheng, L., Li, W., Lin, S., Chen, Z., Wang, Y., Xu, X., Yu, H., Chen, Y. & Ge, B. Interstitial Point Defect Scattering Contributing to High Thermoelectric Performance in SnTe. *Advanced Electronic Materials* **2,** 1600019 (2016).
72. Tan, G., Zhao, L.-D. & Kanatzidis, M. G. Rationally Designing High-Performance Bulk Thermoelectric Materials. *Chemical Reviews* **116,** 12123 (2016).
73. Zhao, L.-D., Zhang, X., Wu, H., Tan, G., Pei, Y., Xiao, Y., Chang, C., Wu, D., Chi, H., Zheng, L., Gong, S., Uher, C., He, J. & Kanatzidis, M. G. Enhanced Thermoelectric Properties in the Counter-Doped SnTe System with Strained Endotaxial SrTe. *Journal of the American Chemical Society* **138,** 2366 (2016).
74. Tan, G., Zeier, W. G., Shi, F., Wang, P., Snyder, G. J., Dravid, V. P. & Kanatzidis, M. G. High Thermoelectric Performance $SnTe–In_2Te_3$ Solid Solutions Enabled by Resonant Levels and Strong Vacancy Phonon Scattering. *Chemistry of Materials* **27,** 7801 (2015).

75. Banik, A., Vishal, B., Perumal, S., Datta, R. & Biswas, K. The origin of low thermal conductivity in $Sn_{1-x}Sb_xTe$: phonon scattering via layered intergrowth nanostructures. *Energy & Environmental Science* **9,** 2011 (2016).
76. Banik, A. & Biswas, K. Lead-free thermoelectrics: promising thermoelectric performance in p-type $SnTe_{1-x}Se_x$ system. *Journal of Materials Chemistry A* **2,** 9620 (2014).
77. Zhang, L., Wang, J., Cheng, Z., Sun, Q., Li, Z. & Dou, S. Lead-free SnTe-based thermoelectrics: enhancement of thermoelectric performance by doping with Gd/Ag. *Journal of Materials Chemistry A* **4,** 7936 (2016).
78. Biswas, K., He, J., Blum, I. D., Wu, C.-I., Hogan, T. P., Seidman, D. N., Dravid, V. P. & Kanatzidis, M. G. High-performance bulk thermoelectrics with all-scale hierarchical architectures. *Nature* **489,** 414 (2012).
79. Al Rahal Al Orabi, R., Hwang, J., Lin, C.-C., Gautier, R., Fontaine, B., Kim, W., Rhyee, J.-S., Wee, D. & Fornari, M. Ultralow Lattice Thermal Conductivity and Enhanced Thermoelectric Performance in SnTe:Ga Materials. *Chemistry of Materials* **29,** 612 (2017).
80. Cahill, D. G., Watson, S. K. & Pohl, R. O. Lower limit to the thermal conductivity of disordered crystals. *Physical Review B* **46,** 6131 (1992).
81. Heremans, J. P., Jovovic, V., Toberer, E. S., Saramat, A., Kurosaki, K., Charoenphakdee, A., Yamanaka, S. & Snyder, G. J. Enhancement of Thermoelectric Efficiency in PbTe by Distortion of the Electronic Density of States. *Science* **321,** 554 (2008).
82. Mahan, G. D. & Sofo, J. O. The best thermoelectric. *Proceedings of the National Academy of Sciences* **93,** 7436 (1996).
83. Heremans, J. P., Wiendlocha, B. & Chamoire, A. M. Resonant levels in bulk thermoelectric semiconductors. *Energy Environ. Sci.* **5,** 5510 (2012).
84. Nemov, S. A. & Ravich, Y. I. Thallium dopant in lead chalcogenides: investigation methods and peculiarities. *Physics-Uspekhi* **41,** 735 (1998).
85. Kaıdanov, V. I. & Ravich, Y. I. Deep and resonance states in AIVBVIsemiconductors. *Soviet Physics Uspekhi* **28,** 31 (1985).
86. Wiendlocha, B. Thermopower of thermoelectric materials with resonant levels: PbTe:Tl versus PbTe:Na and $Cu_{1-x}Ni_x$. *Physical Review B* **97,** 205203 (2018).
87. Costi, T. A. & Zlatić, V. Charge Kondo Anomalies in PbTe Doped with Tl Impurities. *Physical Review Letters* **108,** 036402 (2012).
88. Dzero, M. & Schmalian, J. Superconductivity in Charge Kondo Systems. *Physical Review Letters* **94,** 157003 (2005).

89. Matsuura, H. & Miyake, K. Theory of Charge Kondo Effect on Pair Hopping Mechanism. *Journal of the Physical Society of Japan* **81,** 113705 (2012).
90. Matusiak, M., Tunnicliffe, E. M., Cooper, J. R., Matsushita, Y. & Fisher, I. R. Evidence for a charge Kondo effect in $Pb_{1-x}Tl_xTe$ from measurements of thermoelectric power. *Physical Review B* **80,** 220403 (2009).
91. Matsushita, Y., Bluhm, H., Geballe, T. H. & Fisher, I. R. Evidence for Charge Kondo Effect in Superconducting Tl-Doped PbTe. *Physical Review Letters* **94,** 157002 (2005).
92. Giraldo-Gallo, P., Walmsley, P., Sangiorgio, B., Riggs, S. C., McDonald, R. D., Buchauer, L., Fauqué, B., Liu, C., Spaldin, N. A., Kaminski, A., Behnia, K. & Fisher, I. R. Evidence of Incoherent Carriers Associated with Resonant Impurity Levels and Their Influence on Superconductivity in the Anomalous Superconductor $Pb_{1-x}Tl_xTe$. *Physical Review Letters* **121,** 207001 (2018).
93. Walmsley, P., Liu, C., Palczewski, A. D., Giraldo-Gallo, P., Olson, C. G., Fisher, I. R. & Kaminski, A. Direct spectroscopic evidence for mixed-valence Tl in the low carrier-density superconductor $Pb_{1-x}Tl_xTe$. *Physical Review B* **98,** 184506 (2018).
94. Allen, P. B. & Cohen, M. L. Carrier-Concentration-Dependent Superconductivity in SnTe and GeTe. *Phys. Rev.* **177,** 704 (1969).
95. Zhong, R. D., Schneeloch, J. A., Shi, X. Y., Xu, Z. J., Zhang, C., Tranquada, J. M., Li, Q. & Gu, G. D. Optimizing the superconducting transition temperature and upper critical field of $Sn_{1-x}In_xTe$. *Physical Review B* **88,** 020505 (2013).
96. Sato, T., Tanaka, Y., Nakayama, K., Souma, S., Takahashi, T., Sasaki, S., Ren, Z., Taskin, A. A., Segawa, K. & Ando, Y. Fermiology of the Strongly Spin-Orbit Coupled Superconductor $Sn_{1-x}In_xTe$: Implications for Topological Superconductivity. *Physical Review Letters* **110,** 206804 (2013).
97. Sasaki, S., Ren, Z., Taskin, A. A., Segawa, K., Fu, L. & Ando, Y. Odd-Parity Pairing and Topological Superconductivity in a Strongly Spin-Orbit Coupled Semiconductor. *Physical Review Letters* **109,** 217004 (2012).
98. Bushmarina, G. S., Drabkin, I. A., Kompaniets, V. V., Parfen'ev, R. V., Shamshur, D. V. & Shakhov, M. A. Superconducting transition in SnTe doped with In. *Fizika Tverdogo Tela* **28,** 1094 (1986).
99. Nemov, S. A., Proshin, V. I., Tarantasov, G. L., Parfen'ev, R. V., Shamshur, D. V. & Chernyaev, A. V. Transverse Nernst-Ettingshausen effect, resonant scattering, and superconductivity in SnTe: In. *Physics of the Solid State* **51,** 491 (2009).

100. Kondo, J. Resistance Minimum in Dilute Magnetic Alloys. *Progress of Theoretical Physics* **32,** 37 (1964).
101. Matsushita, Y., Wianecki, P. A., Sommer, A. T., Geballe, T. H. & Fisher, I. R. Type II superconducting parameters of Tl-doped PbTe determined from heat capacity and electronic transport measurements. *Physical Review B* **74,** 134512 (2006).
102. Kang, C.-J. & Kotliar, G. Material design of indium-based compounds: Possible candidates for charge, valence, and bond disproportionation and superconductivity. *Phys. Rev. Materials* **3,** 015001 (2019).
103. Pardoe, J. A. J. & Downs, A. J. Development of the Chemistry of Indium in Formal Oxidation States Lower than +3. *Chem. Rev.* **107,** 2 (2007).

Chapter 3 Effect of Indium on the transport properties of self-compensated SnTe

3.1 Introduction

The formation of a resonant level (RL) has proven to be an interesting mechanism, whereby increasing the thermopower in semiconductors via a distortion of the electronic band structure beyond a rigid-band model. As already mentioned in Chapter 2, Zhang *et al.* reported that a small amount of In leads to the formation of a RL in SnTe.[1] This study, carried out at high temperatures, has been realized for only three different compositions ($Sn_{1-x}In_xTe$; x = 0.0025, 0.005 and 0.01), leaving the possibility that the thermoelectric properties of SnTe may be further enhanced by carefully optimizing the In concentration.

This chapter will be dedicated to an in-depth experimental and theoretical study of the effect of the RL on the transport properties of SnTe. Because self-compensation of the Sn vacancies by intentionally introducing excess Sn has been shown to be an efficient mean to decrease the hole concentration, we will focus our attention to the series $Sn_{1.03-x}In_xTe$. Studying the effect of In on the transport properties of samples with low hole concentration may help to better determine the influence of In. The measurements of the transport properties, performed in a wide range of temperatures (2 – 800 K), will be enriched by electronic band structure calculations of the electronic density of states and Bloch spectral functions (BSF). Before exploring in detail these various aspects, the first part of this Chapter will be dedicated to a general presentation of the formation of a RL in bulk semiconductors and its role on the transport properties, especially on the thermopower.

The second part of this Chapter will present the theoretical results obtained on this series of compounds by means of electronic band structure calculations performed using the Korringa-Kohn-Rostoker method with the coherent potential approximation (KKR-CPA). The CPA formalism enables treating explicitly the chemical disorder introduced by the substitution of In for Sn and the Sn vacancies, without using time-consuming supercell models. In addition, the distinct role of In on the electronic properties of SnTe will be further highlighted by the issues raised by the RL on the carrier lifetime inferred from the width of the BSF. This part of the thesis, as well as BSF formalism, have been realized in collaboration with Dr. Bartlomiej Wiendlocha and Prof. Janusz Tobola from the AGH University of Science and Technology in Krakow (Poland).

The last part of this Chapter will be devoted to the experimental findings on the effect of In on the transport properties of $Sn_{1.03}Te$. First, the solid-state synthesis process of the series $Sn_{1.03-x}In_xTe$ will be described to validate the technique borrowed from the literature. To

confirm the purity and homogeneity of the synthesized compounds, all the samples were structurally and chemically characterized using powder X-ray diffraction (PXRD) and scanning electron microscopy (SEM) with energy dispersive X-ray spectroscopy (EDXS). The physical properties (electrical resistivity, thermopower, thermal conductivity and Hall effect) have been systematically studied at low temperatures (2 – 300 K), and then above room temperature (300 – 800 K). The comparison between these experimental results and the theoretical predictions will be further underlined, providing strong evidence for the resonant nature of In in SnTe.

3.2 Introduction to Resonant Level

Over the last few decades, most of the literature concerning the improvement of the thermoelectric properties has been directed towards either optimizing the carrier concentration through doping or lowering the lattice thermal conductivity by forming solid solutions. Because the thermopower can be linked to the density of states (DOS) at the Fermi level E_F, increasing the DOS can give rise to enhanced thermopower values when the chemical potential resides in this enhanced DOS. Such an increase necessarily requires going beyond a rigid band approximation, which usually provides an adequate description of the effect of most impurities. Hence, how can we increase the DOS of a bulk semiconductor?

An increase in the DOS can occur in four physical situations: **i)** in multi-band electronic structure (referred to as band convergence) **ii)** Kondo gaps/hybridization gaps, **iii)** in dilute Kondo alloys and **iv)** via the formation of resonant levels (RL).[2] The first mechanism is related to the convergence of one or several electronic bands near the Fermi level, usually achieved by substitutions or formation of solid solutions. The two mechanisms **ii)** and **iii)** are somehow related to each other. Kondo gaps and dilute Kondo alloys are associated with the presence of magnetic impurities (containing *d* or *f* electrons) in a metal/semiconductor.[2]

In contrast to these Kondo mechanisms, RL occurs without the presence of magnetic impurities and arises through a coupling between the host and dilute impurities states. RL arises when the electronic states of the impurity atom hybridize with those of the host framework, giving rise to a local distortion of the electronic density of states in the conduction or valence bands. This can be viewed as the formation of a "virtual bound state", which has an energy that falls inside the valence or conduction bands. This "virtual state" was first observed in metals by Friedel and was explained later for semiconductors.[3–6] As shown in Figure 3.1, the situation

is different from a conventional impurity that forms an additional isolated energy level close to the conduction or valence band edge.[3,4]

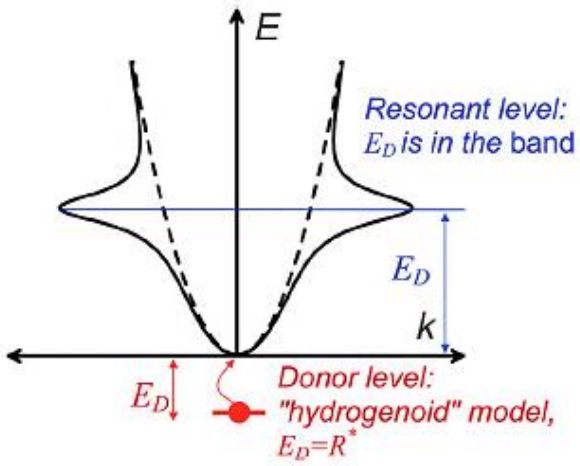

Figure 3.1: Representation of a parabolic-like conduction band (dotted line) with a resonant impurity forming a resonant level inside the conduction band (at E_D from the minimum).[2] In comparison, a conventional doping element forms an additional, isolated energy level close to the conduction band edge, but inside the band gap. A similar representation holds for the valence bands.

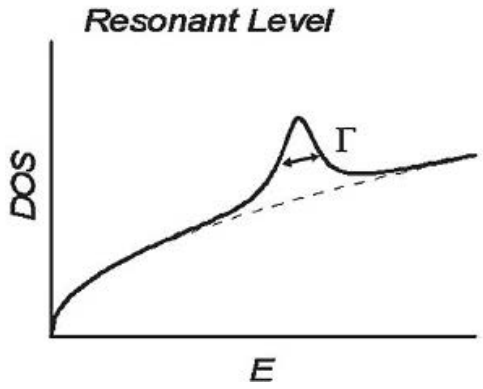

Figure 3.2: Simplified representation of the effect of a RL on the DOS as a function of the energy.[2] Γ is the width of the resonant level (also denoted as Δ).

In the case of RL, the virtual state has the same energy (E_D) as an energy of the extended states of the host framework, so that both will resonate to build up two extended states of slightly different energies, which in turn will have the same energies as other extended states with which they will resonate, and so on. Consequently, the total DOS increases, forming a localized hump, with a certain width Δ near E_D as sketched in Figure 3.2.

In the 60s and 70s, a period during which RLs in PbTe were studied in detail, the excess DOS due to the RL was modeled by a Lorentzian function of energy E with a full width at half maximum Δ:

Equation 3.1:

$$L(E) = \frac{1}{\pi} \frac{\frac{1}{2}\Delta}{(E - E_D)^2 + \left(\frac{1}{2}\Delta\right)^2}$$

where E_D is the resonant impurity band center. The increase in the DOS contributes to boost the thermopower if the doping is such that the Fermi level, E_F, is close to E_D. A second effect due to RL that can also influence positively the thermopower is "resonant scattering" or "selective scattering". This effect is related to the fact that the resonant state diffuses charge carriers in a way that is extremely sensitive to their energy. The diffusion is particularly large when the carriers are degenerate since, in this case, the contributions to the thermopower of the hot carriers with $E > E_F$, and of the cold ones with $E < E_F$, are of opposite signs. If the relaxation time depends smoothly on energy, then these contributions will largely cancel out. However, if it is highly sensitive to energy, they do not cancel out. This provides an effective energy-filtering mechanism that affects the thermopower; hence the denomination "resonant scattering".

The relaxation time associated with this mechanism, $\tau(E)$, was first proposed by Ravich.[5,7] Its inverse (that is, frequency resonant scattering) is modeled by the same function (a Lorentzian function) as the DOS RL:

Equation 3.2:

$$\tau(E) = \tau_0 \left(1 + \left(\frac{E - E_D}{\frac{\Delta}{2}} \right)^2 \right)$$

where τ_0 is the minimum value of $\tau(E)$ reached for $E = E_D$. τ_0 is inversely proportional to the number of impurities or defects responsible for the resonant states.[7]

To understand qualitatively how these two effects (DOS and resonant scattering) affect the thermopower, one can refer to the Mott's relation relating the thermopower to the energy-dependent electrical conductivity $\sigma(E)$ for a degenerate, single-band system:

Equation 3.3:

$$\alpha = \frac{\pi^2 k_B^2 T}{3q} \times \frac{d\, ln\, \sigma\,(E)}{dE}\Big|_{E=E_F}$$

where k_B is the Boltzmann constant and q is the elementary charge. Since $\sigma(E) = n(E)q\mu(E)$ (where $n(E)$ is the concentration of carriers having the energy E and $\mu(E)$ is their mobility), Equation 3.3 leads to the following expanded equation:

Equation 3.4:

$$\alpha = \frac{\pi^2}{3}\frac{k_B}{q}(k_B T)\left[\frac{1}{n(E)}\frac{dn(E)}{dE} + \frac{1}{\mu(E)}\frac{d\mu(E)}{dE}\right]_{E=E_F}$$

$$= \frac{\pi^2}{3}\frac{k_B}{q}(k_B T)\left[\frac{g(E)}{n(E)} + \frac{1}{\mu(E)}\frac{d\mu(E)}{dE}\right]_{E=E_F}$$

Equation 3.4 shows that two major terms contribute to the thermopower as previously discussed: **i)** $g(E)/n(E)$ that corresponds to the DOS term, and **ii)** $(1/\mu(E))/(d\mu(E)/dE)$ that corresponds to the scattering term. It is clear from Equation 3.4 that an excess of DOS is favorable since it will increase the first term. The second term of Equation 3.4 can be also enhanced if the relaxation time $\tau(E)$, which is proportional to the mobility, is strongly energy dependent. Experimentally, an increase in α related to the presence of a RL can be evidenced by an increase in the DOS effective mass (see Equation 1.21, Chapter 1) over its value in the host solid. In contrast, if the resonant scattering is the dominant contribution, a strong increase in the scattering exponent, that characterizes the main scattering mechanism, is expected. From these considerations, and depending on the value of E_D, Δ and E_F, the presence of a RL can be beneficial to enhance the thermopower. Of course, the RL will also impact the two other electronic properties, namely the electrical resistivity and the electronic thermal conductivity. The presence of an additional scattering mechanism (resonant scattering) and an increase in the DOS effective mass will affect the mobility of the charge carriers and consequently will increase (decrease) the electrical conductivity (electronic thermal conductivity). A significant improvement of *ZT* due to the RL is expected in semiconductors when the Fermi level E_F is close to a band edge and to the central energy E_D and when Δ is narrow.[8] However, Δ should not be too narrow to avoid localization effects that would strongly limit the mobility of the

charge carriers. Experimentally, even if all these conditions are not strictly realized, moderate or spectacular improvements were observed in several chalcogenide semiconductors such as Sn-doped Bi_2Te_3, Tl-doped PbTe, Ti-doped PbTe, Sn-doped α-As_2Te_3, In-doped SnTe, In-doped GeTe and Ag-doped Mg_2Sn.[1,2,9–16]

3.3 Electronic band structure calculations

3.3.1 Overview

As described in the preceding paragraph, resonant impurities tend to increase the thermopower due to the increase in the DOS and the presence of resonant scattering. To confirm theoretically the first mechanism, calculations of the DOS can be performed to determine the changes of the electronic band structure implied by the RL. In the present case, these calculations were performed using the KKR-CPA method which has two major advantages over other calculation methods. First, it allows taking into account the disorder induced by the substitution of In for Sn without resorting to supercell model. This enables calculating the DOS of SnTe with the In concentrations considered experimentally. Second, in the specific case of SnTe, this method further allows to take into account simultaneously the presence of a small concentration of Sn vacancies, which tend to shift the chemical potential deeper inside the valence bands. Considering these two aspects is thus important to compare the theoretical predictions to the experimental data.

The electronic dispersion curves provide interesting information of the shape and the number of bands that contribute to the transport in semiconductors. However, the calculation of these curves relies on the translational symmetry of the Bloch wave functions. Because the presence of disorder breaks this symmetry, the dispersion curves are no longer well defined. The disorder introduced tends to broaden these curves, which reflects the shorter lifetime of the charge carriers that are more strongly scattered. To analyze the influence of the RL on the electronic bands and overcome this difficulty, the dispersion curves are replaced by the so-called Bloch spectral density functions (BSFs). BSFs $A(k, E)$ allows us to investigate the electronic dispersion relations in disordered materials, where electrons are scattered due to the lack of translational symmetry and presence of impurities (wave vector is not a conserved quantum number anymore). In such a case, the traditional description of the electronic structure, using the electronic dispersion relations $E(k)$, have to be generalized, and the KKR-

CPA technique allows to do it by calculating BSF.[17,18] The meaning of BSF is sketched in Figure 3.3.

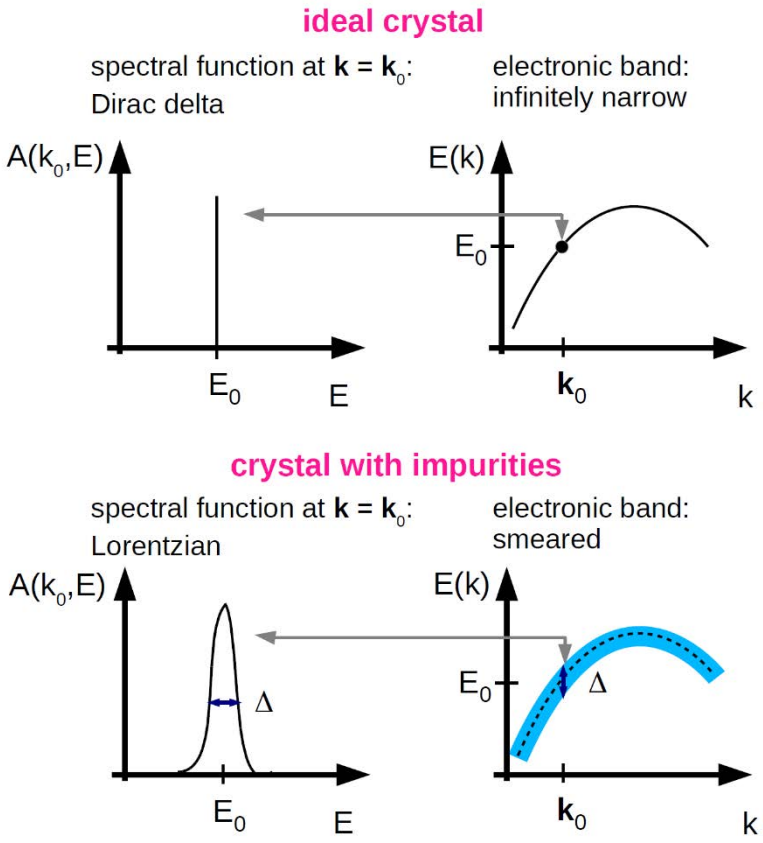

Figure 3.3

Figure 3.3: Schematic explanation of the relation between the Bloch spectral density functions $A(k, E)$ and electronic bands *E(k)* in the case of idea crystal and crystal with impurities.

In the case of a perfect crystalline material (upper panel of Figure 3.3), BSF for a single wave vector k_0 (and one spin direction) is a Dirac delta function of energy: $A(k_0, E) = \delta(E - E_{k_0})$, thus it is zero for all energies except the point E_0, where electron has its energy eigenvalue (E_0 can be also written as E_D). The "peak" in the $\delta(E - E_{k_0})$ function shows the position of an infinitely narrow electronic band, with infinite lifetime of the Bloch electrons (no scattering takes place at $T = 0$ K in a perfect crystal). The name "spectral density function" also describes another characteristic of the BSF as *k*-resolved density of states: the integral of $A(k_0, E)$ over all energies is equal to 1, i.e. the number of electronic states available at k_0 for each spin direction (in the case of a hypothetical single-band material, while in the multi-band case, each band/BSF contributes 1 state per spin), and the integral over all k gives the usual density of

states function.[17] In non-magnetic materials, BSFs are added for both spin directions, and the corresponding integrals are equal to 2.

In the case where impurities are present in the material (bottom panel of Figure 3.3), spectral function broadens and in most cases it adopts the shape of the Lorentz function (See Equation 3.1). In such a case, the electronic lifetime τ becomes finite and is related to the FWHM of the spectral function as $\tau = \frac{\hbar}{\Delta}$.[19] Of note, the electronic lifetime corresponds here to the Boltzmann relaxation time, the equivalence of which can be demonstrated within the KKR-CPA framework.[19] The stronger is the impurity-induced scattering, the broader becomes the spectral function and more smeared the band structure picture. The situation is more complicated for resonant impurities, as BSF becomes very broad and non-Lorentzian in shape. As a consequence, relaxation time is not well defined, and thus, only rough estimations of τ may be obtained. In addition to this, due to the rough estimation of the relaxation time, the calculation of transport properties by Boltzmann equations become impossible as the velocity of the charge carriers cannot be defined anymore. Nevertheless, this approach has been already successfully applied to the study of the influence of resonant impurities on the electronic band structure of several thermoelectric materials, such as Tl-doped PbTe (denoted hereafter as PbTe:Tl),[13,14] Ti-doped PbTe,[15] or Ag-doped Mg_2Sn.[16] This method further allows to distinguish between localized (e.g. PbTe:Ti) and delocalized (e.g. PbTe:Tl) RL,[20] as well as between resonant and non-resonant impurity behavior.[16] More details about BSFs can be found in Refs. 17 and 21.

3.3.2 Results and Discussions

Electronic structure calculations were performed using the KKR-CPA method, implemented in the Munich SPR-KKR package.[18] The experimental rock-salt crystal structure and lattice parameter (6.32 Å) of SnTe were used. Regular k-point mesh was used in calculations, using 1500 – 5000 *k*-points for the self-consistent cycle and 4 – 20×10^5 for the density of states (DOS) and Bloch spectral density functions (BSF) calculations (number of points given in the irreducible part of the Brillouin zone). The crystal potential was constructed within the framework of the local density approximation (LDA), using Vosko, Wilk and Nussair formula for the exchange-correlation part.[22] For all atoms, angular momentum cut-off $l_{max} = 3$ was set and full-potential full-relativistic calculations were performed. High

convergence limits were put on the self-consistent cycle (10^{-5} Ry for the Fermi level E_F and for the total energy). The position of E_F was obtained using the Lloyd formula.[21]

As the presence of Sn vacancies is an inherent property of SnTe, making it naturally heavily hole doped, Sn vacancies were added in our calculations to simulate the system close to the experimental one. Figure 3.4 (a) shows the density of states of SnTe containing 0.32% of Sn vacancies. Sn vacancies act, as expected, as two-hole acceptors, shifting the Fermi level deeper into the valence bands. This vacancy concentration corresponds to a hole concentration of 10^{20} cm^{-3}, as typically observed in synthesized SnTe samples, and is very close to the experimental value estimated in $Sn_{1.03}Te$ (0.25% of vacancies corresponding to a hole concentration of 8.0×10^{19} cm^{-3}).[23] As a first approximation, vacancies do not visibly modify the electronic structure of SnTe, the effect of which is thus mostly a rigid-band-like shift in E_F.

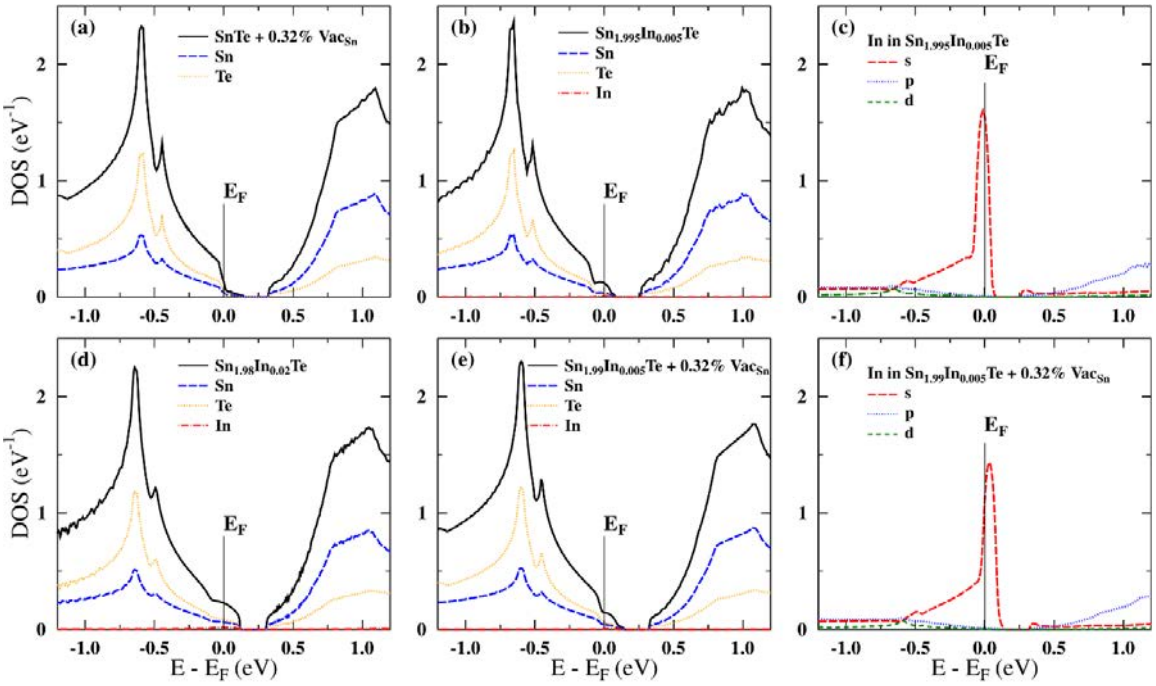

Figure 3.4: Densities of states as a function of the energy for SnTe: a) with 0.32% Sn vacancies; b) doped with 0.5% In, with partial In DOS in panel c); d) doped with 2% In; e) doped with 0.5% In and with 0.32% Sn vacancy, with partial In DOS in panel f). In panels a), b), d) and e), atomic contributions are weighted by their concentration. In panels c) and f), the DOS is given per In atom.

The situation is radically different when considering the DOS of SnTe doped with 0.5% of In and without Sn vacancies (Figure 3.4 (b)) where the In-induced formation of the RL can be clearly seen (Figure 3.4 (c)). The carrier concentration of this system is 7.9×10^{19} cm^{-3}, as In

is a monovalent acceptor (that is, in a In^{1+} valence state). The mechanism of In (usually a trivalent element with the $5s^2 5p^1$ valence shell configuration) becoming an acceptor against Sn (divalent in SnTe as shown by Mössbauer spectroscopy)[23–25] is similar to that of In in Bi or Tl in PbTe.[13,14,26,27] It is explained as follow. One 5s electron of In forms a hyper-deep (HD) state in the low-energy region, below the *p*-like main valence band (VB), which bounds one 5p electron from Te taken from the main VB. One *5p* electron of In contributes to the main valence band block, and the second *5s* electron of In forms the resonant state. As a result, upon substituting In for Sn, the main VB is left with one electron less, making In an acceptor. The main difference with the Bi:In system is that In does not create a RL near E_F in Bi. The formation of the DOS "hump", in agreement with previous reports,[8,20,27] is related to the presence of In atoms. As shown in Figure 3.4 (c) where the partial DOS of In atoms is shown, the DOS peak formed by In *5s* states defines the resonant behavior of In in SnTe. When the In concentration increases to 2% (Figure 3.4 (d)), the DOS "hump" broadens and the hole concentration increases. We further considered the DOS of 0.5% In-doped SnTe containing 0.32% of Sn vacancies (Figures 3.4 (e) and 3.4 (f)) in order to analyze the influence of Sn vacancies on the formation of the RL. Three effects are observed: **i)** the In-induced RL is also formed in the presence of vacancies; **ii)** E_F is deeper in the valence bands due to the additional holes given by the vacancies; **iii)** the RL is slightly smeared resulting in a slightly lower partial In DOS (see Figure 3.4 (f)). As in these calculations, three "atoms" (Sn, In and vacancy) occupy the same crystallographic site, one might expect some additional RL smearing effect due to enhanced disorder, compared to the vacancy-free compound.

To analyze the influence of vacancy and RL on the electronic bands, Bloch spectral density functions were computed for the same compositions. Figure 3.5 shows the two-dimensional projections of BSF plotted in a way similar to the usual dispersion relations in several BZ directions, with the color marking the value of the BSF. Figure 3.5 (a) presents the BSF of *p*-type SnTe containing 0.32% of Sn vacancy. The general features of the electronic structure of SnTe are in agreement with previous density-functional calculations and experimental studies.[28–30] What is worth noting is that the minimum of the conduction band appears to be slightly off the L point, which is better seen when bands in the off-high-symmetry $L - \Sigma$ direction are plotted. While signatures of this effect may have been seen in other studies, (e.g. in Ref. 28 in the W-L direction),[28] no direct comparison is possible, since bands in *the* $L - \Sigma$ direction were not previously computed in literature. Moreover, this effect may be related to the inaccuracy of the local density approximation used in these calculations as well.

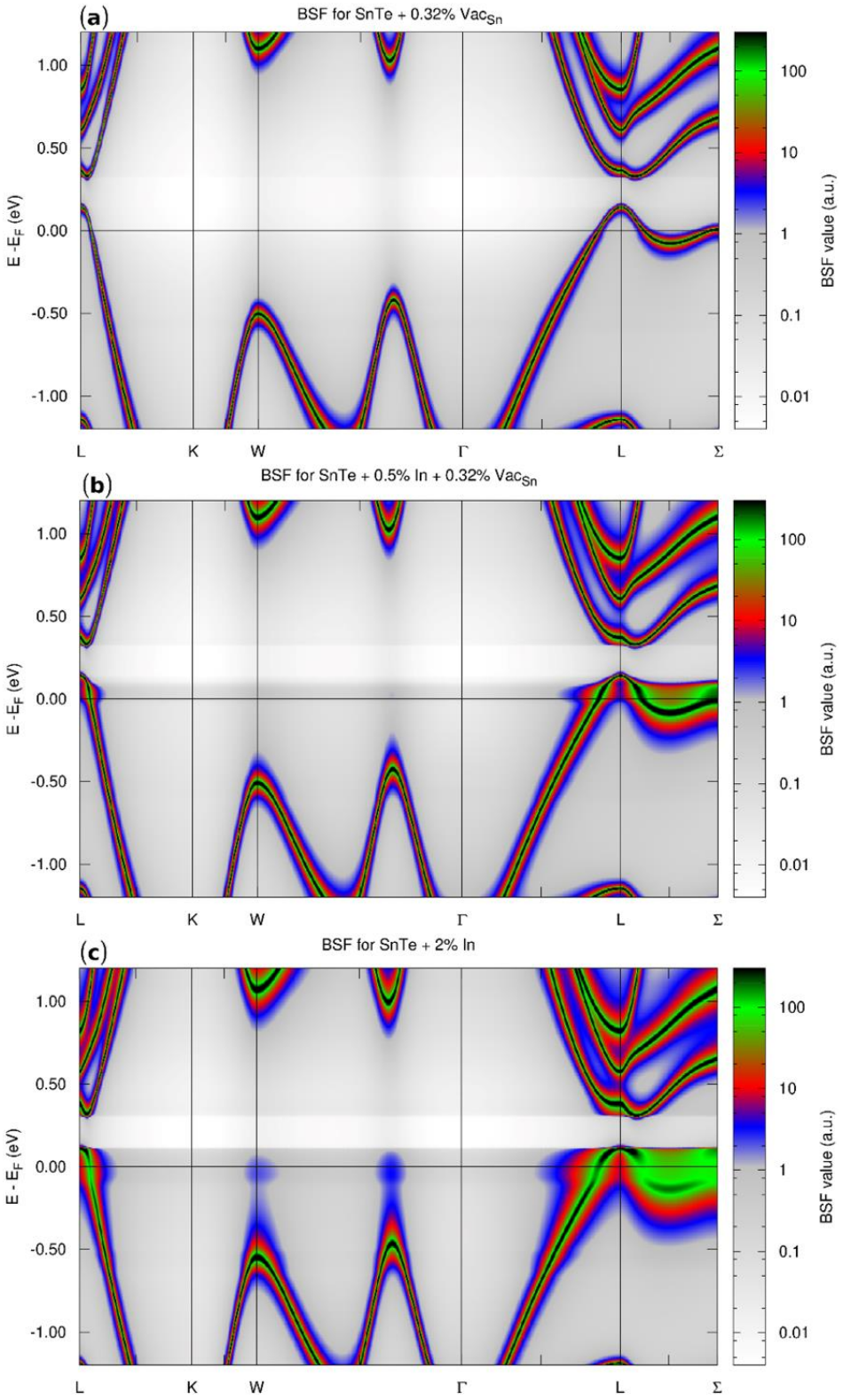

Figure 3.5: Two-dimensional projection of the Bloch spectral functions in high symmetry directions for SnTe: a) containing 0.32% Sn vacancies; b) doped with 0.5% In and with 0.32% Sn vacancy; c) doped with 2% In. Colors mark BSF values, plotted in logarithmic scale. Black color corresponds to BSF values higher than 300 a.u. In resonant impurity leads to the smearing of the $L - \Sigma$ valence band near the band edge.

In contrast to PbTe, we are not aware of any calculation going beyond the local density approximation (LDA) or the generalized gradient approximation (GGA) for SnTe, that is, using the GW method. The L- and Σ-band separation is here about 0.15 eV, which is lower than the energy offset obtained in prior studies (around 0.30 eV). This underestimation is a direct consequence of the inaccuracy of the local density approximation. Of note, this error will manifest itself in calculations of the density-of-states effective mass m^*_{DOS} as a function of the hole concentration, discussed below, as a too early increase. We note that a similar situation was reported for PbTe.[14] As far as the effect of vacancies on the electronic band structure is concerned, we observe a minor band smearing, leaving sharp, well-defined bands (Figure 3.5 (a), also see Figure 3.6 (a) for zoomed in plots).

In contrast, as shown in Figure 3.5 (b), strong band smearing is observed for 0.5% In-doped SnTe containing 0.32% of Sn vacancies. This effect is obviously related to the presence of resonant In impurities and is very similar to what has been observed in PbTe:Tl.[13,14] In the presence of In-induced RL, electronic states are shifted towards the valence band edge and form a "cloud" around the $L - \Sigma$ band. However, these electronic states do not form an isolated impurity band due to the hybridization between the resonant In and host SnTe states. These conclusions hold true when the In concentration reaches 2% (Figure 3.5 (c)): the number of electronic states around the $L - \Sigma$ band increases (which is responsible for the larger DOS "hump" in Figure 3.4 (d)) and band smearing is enhanced without forming an impurity band.

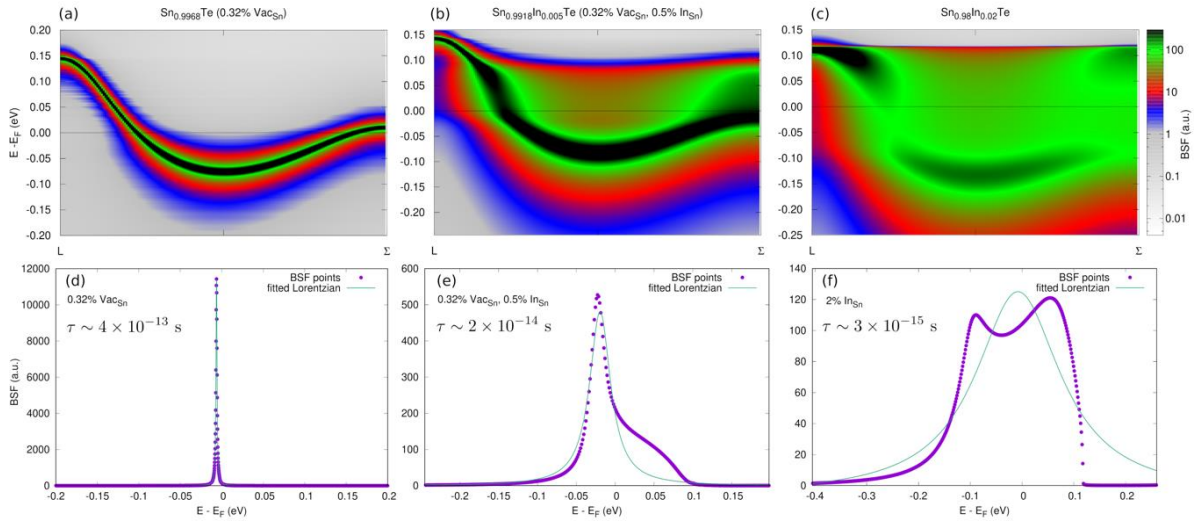

Figure 3.6: Zoomed in BSF plot between $L - \Sigma$ points with the calculated relaxation time for SnTe: a) containing 0.32% Sn vacancies; b) doped with 0.5% In and with 0.32% Sn vacancy; c) doped with 2% In.

To quantify the level of hybridization between the resonant and host states, the In atomic contribution to the DOS at E_F has been calculated. The results indicate that, even for 2% In, it does not exceed 10%. Thanks to this hybridization, the localization of the RL or the formation of a narrow impurity band is avoided. The strong band smearing, induced by RL, causes enhanced carrier scattering, which will dominate the transport properties of the system at low temperatures. As mentioned before, by analyzing the width of the spectral function Δ (that is, the width of the smeared band), the electronic life time $\tau = \hbar/\Delta$ may be estimated. For k-points in the middle of L – Σ path, this approach yields $\tau \sim 2\times10^{-14}$ s for 0.5% In-doped SnTe and $\tau \sim 4\times10^{-13}$ s for SnTe containing 0.32% of Sn vacancies (See Figure 3.6).

Increasing the In content to 2%, however, further reinforces the band smearing, the shape of which significantly deviates from a Lorentzian shape used in models developed by Ravich for the PbTe:Tl resonant system.[5,7] In such a case, the carrier life time becomes ill-defined indicating that models based on a single relaxation time to describe the resonant scattering are not correct. Similar magnitude of the carrier life time was obtained for PbTe:Tl.[14] These results highlight the importance of resonant scattering. Since these calculations correspond to $T = 0$ K, this predicted reduction of the lifetime due to the RL, compared to self-doped SnTe, will lead to enhanced residual resistivities at low temperatures. Such an increase in the residual resistivity was observed for the PbTe:Tl system when compared to PbTe:Na,[14] and may be used as an independent, experimental verification of the existence of the RL. As we shall see below, this point will be backed up by our experimental data. Note that the link between the evolution of the residual resistivity and the carrier lifetime should remain qualitative due to the fact that a direct relation between the carrier lifetime and relaxation time that appears in transport quantities is not straightforward. In addition, as we shall also see, the scattering of holes due to the RL is strongly inelastic and hence, a single scattering lifetime cannot be defined, in contrast to the model proposed for the Tl-induced RL in PbTe.[7]

Enhanced carrier scattering due to the presence of RL is also responsible for the larger, concentration-dependent resistivity of SnTe:In samples at $T > 300$ K, as discussed below in the experimental section. It should be stressed here that scattering on RL, which is strong in SnTe:In samples, is much less temperature-dependent than scattering of carriers on phonons. Because of this difference, the transport properties of "resonant" samples are expected to exhibit weaker dependence on temperature than rigid-band-impurities-doped samples. At higher temperatures where the carrier relaxation time due to scattering on phonons is on the same order of magnitude as the scattering on RL ($\tau \sim 10^{-14}$ s), differences in ρ for samples with

and without resonant impurities is not as large as the difference in carrier life times at $T = 0$ K might have suggested. The ratio of the electrical resistivities for the most (2% In) and least (0% In) resistive samples in our studies (presented later in this chapter) changes from 5.4 at 300 K to 1.3 at 800 K. This weaker temperature sensitivity is expected to give rise to enhanced peak power factor and *ZT* values, but also to higher *ZT* over a broader temperature range, yielding higher average *ZT*, which is an important parameter for practical applications.

A qualitative link between the RL-induced increase in DOS and its effect on thermopower can be inferred from the calculation of the DOS effective mass m^*_{DOS} of the studied materials, using the method discussed in Refs. 14 and 31.

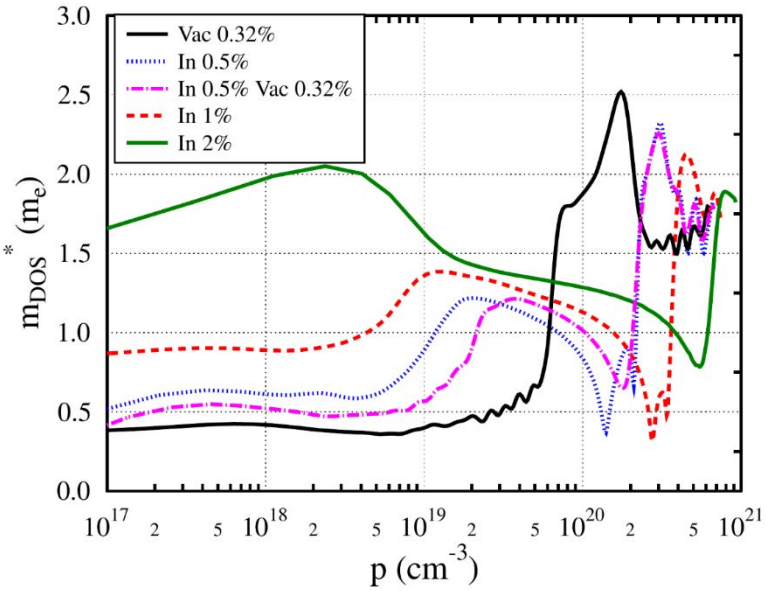

Figure 3.7: Hole dependence of the density of states effective mass m^*_{DOS} for SnTe containing vacancies and doped with In. Resonant doping visibly increases the effective mass of the light band. The rapid increase in m^*_{DOS}, observed in the case of SnTe + 0.32% Sn vacancies near. 7×10^{19} cm^{-3}, is caused by the too high position of the top of the "Σ band", which should appear at significantly higher hole concentrations.

The following equation was used to calculate the DOS effective mass:

Equation 3.5:

$$m^*_{DOS}(E) = \frac{\hbar^2}{m_e}\sqrt[3]{\frac{\pi^4 g(E) g'(E)}{V^2}}$$

where $g(E)$ is the DOS per energy per unit formula, m_e is the bare mass of the electron and V is the unit cell volume. The results of these computations as a function of the carrier concentration (obtained by rigidly shifting E_F in the DOS computed for the actual material's composition) are shown in Figure 3.7. Absolute mass values are affected by the LDA inaccuracy in two ways, as can be analyzed for the "self-doped" SnTe case. First, the light-band mass, which has been determined to be about $0.168m_0$ (m_0 is the bare electron mass) in prior studies,[1,32,33] is about $0.4m_0$ in our case. Secondly, the rapid increase in m^*_{DOS} near 7×10^{19} cm^{-3} in the case of SnTe with 0.32% Sn vacancies is caused by the too high position of the top of the heavy-hole Σ band, the effect of which should appear at higher hole concentrations. Nevertheless, the region of interest is the region before the heavy-hole band is reached. In spite of these inaccuracies, a relative increase of the m^*_{DOS} due to In doping is clearly observed. Hence, higher In concentrations will result in higher m^*_{DOS}, and ultimately, in higher thermopower values.

Summarizing this theoretical part, KKR-CPA calculations confirm the formation of a resonant level when In is substituted on the Sn site in SnTe. Most importantly, this effect is not affected by the presence of Sn vacancies, which have nevertheless a small, but visible effect on the details of the RL. Electronic bands are smeared but no separated impurity band is formed, which would have been detrimental to electrical conduction. Finally, the In-induced RL increases the DOS effective mass, proportionally to the In concentration. As we will see below, the experimental results lend strong support to these predictions.

3.4 Experimental study of the series $Sn_{1.03-x}In_xTe$

3.4.1 Synthesis

In order to study the influence of In on the structural, chemical and physical properties of SnTe, two different sets of In-doped polycrystalline samples were synthesized using a conventional metallurgy approach under well-controlled and reproducible conditions. Because SnTe contains inherent Sn vacancies, the first set of samples synthesized were self-compensated in order to better highlight the “real” effect of In on the transport properties of SnTe. Hence, in this case, the following samples were considered: $Sn_{1.03-x}In_xTe$ (x = 0, 0.0005, 0.0015, 0.0025, 0.0035, 0.0045, 0.0075, 0.01 and 0.02). Above x = 0.02, Hall Effect

measurements (described in detail below) have suggested that Sn vacancies are likely no longer present or that their concentration, if any, plays a minor role compared to In. Hence, above 2% In content, the following series was considered: $Sn_{1-x}In_xTe$ (x = 0.05, 0.07, 0.08, 0.10, 0.125, 0.2, 0.3 and 0.4). The maximum In content (x = 0.4) used in this second series corresponds to the solubility limit of In in SnTe.[34–36] The purity and form of the elements used for these syntheses are summarized in Table 3.1.

Table 3.1: Summary of the elements used.

Element	Purity (%)	Form	Re-purification
Sn	99.999	Shots	Yes
Te	99.999	Granules/ powder	Yes
In	99.999	Shots	Used as received

Prior to use, Sn and Te were purified to eliminate any traces of oxides from their surfaces. Sn shots were cleaned by successive passage in a bath of HCl (37 %) mixed in a 2:1 volume ratio with distilled water. These shots were then rinsed 5 times each with distilled water and ethanol before being quickly dried and stored in an Ar-filled glove box (O_2 % ≤ 0.1 ppm and H_2O % ≤ 0.1 ppm; Figure 3.8) to avoid any contact with ambient air.

Figure 3.8: MBraun made Argon Glove box.

For purifying Te, a quartz tube (whose one end is closed) of outer diameter of 18 mm and thickness of 1.5 mm was prepared (as all of the tubes used in this thesis work) manually with a fire torch and then cleaned in successive baths of diluted hydrofluoric acid (HF), nitric acid (HNO_3) and water before storing it in ethanol. The tube was then degassed under secondary vacuum (Figure 3.9) at 900 °C for at least 4 hours.

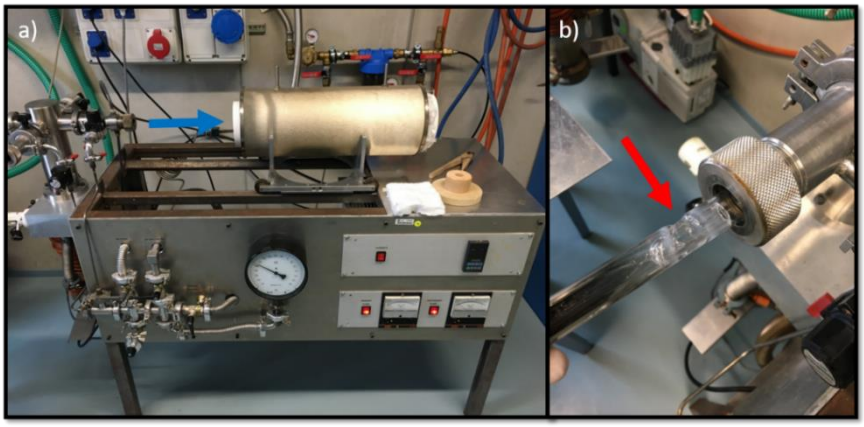

Figure 3.9: a) Homemade secondary vacuum pumping station (blue arrow represents the movable furnace used to degas the quartz tube) b) Quartz tube just after being sealed under secondary vacuum (red arrow shows the small quartz tube used for the sealing).

Figure 3.10: Sealed quartz tube with Tellurium to be placed in the vertical rocking furnace.

Te granules were then placed inside a carbon-coated quartz tube with another small tube of quartz to be sealed under a mixture of helium-hydrogen gas (~ 400 mbar) as seen in Figure 3.10. Once sealed, the quartz tube was placed in a rocking vertical furnace (Figure 3.11) for few hours at 500 °C and then rapidly quenched into room-temperature water. After polishing the surface of the resulting Te ingot to remove any traces of oxides, the ingot was rinsed with ethanol and stored inside the glove box. All the elements were then weighed inside the glove box in stoichiometric amounts according to the targeted chemical composition with the final amount of each sample being approximately 5 g. Similar to the previously mentioned technique, the quartz tubes with the elements (plus the small tube) were placed inside the pumping system for sealing.

Figure 3.11: High-temperature vertical rocking furnace.

It is important to note that, for all samples, the distance between the elements and the small quartz tube was kept constant (~ 8 cm) to ensure a nearly equivalent sample-to-volume ratio. This point is important to ensure that the vapor pressure of gaseous (mainly Te_2 and SnTe) is equivalent from sample to sample, allowing for a better control of the final stoichiometry and hence, to more clearly underline the role played by In on the transport properties. After degassing the tubes under primary vacuum for about 5 minutes, the mixture was finally maintained under secondary vacuum for around 4 h and then sealed. Once sealed, all the tubes were placed in a high-temperature vertical rocking furnace, subjecting the tubes

to the heating program showed in Figure 3.12. All the samples were then quenched into room-temperature water.

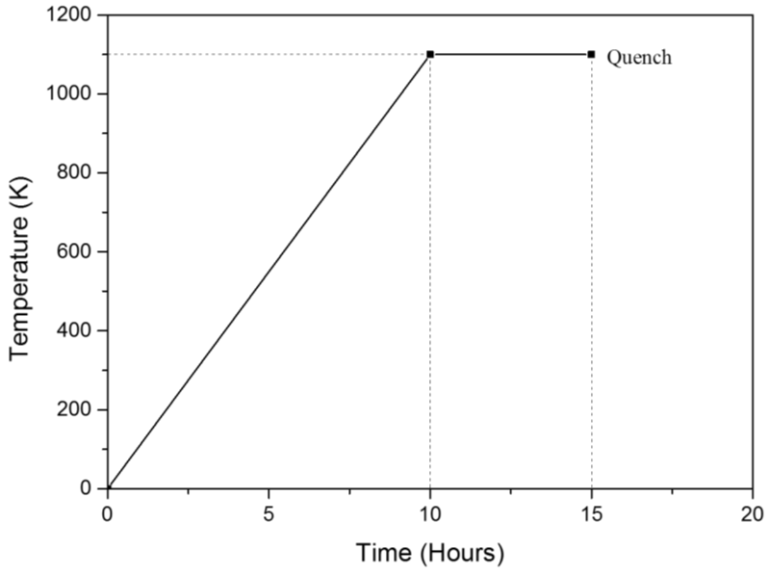

Figure 3.12: Synthesis profile used for $Sn_{1.03-x}In_xTe$ samples.

The ingots (Figure 3.13) were hand crushed into fine powders inside the glove box using an agate mortar. The consolidation of the samples was carried out using the spark plasma sintering (SPS) technique. A short description of the instrument and principle of this technique can be found in Appendix A.

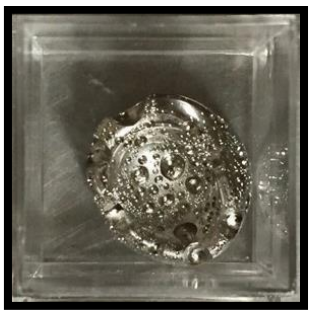

Figure 3.13: Resultant ingot obtained after quenching the tubes.

A graphite die was used according to a well-established experimental protocol,[37,38] with hole diameter ~ 10.4 mm, yielding a final ingot of ~ 10 mm in diameter, for all samples. A thin layer of graphite sheet was placed to entirely cover the area where the powder is placed to facilitate the extraction of the sample. Two graphite punches were placed on either side of the die, where the pistons were placed, as can be seen in Figure 3.14.

Figure 3.14: Graphite die and the pistons used for SPS process.

A thermocouple monitoring the temperature during the process was placed in the side hole of the matrix. The entire SPS process was performed under continuous vacuum to avoid any unwanted oxidation. All the samples were consolidated following the same temperature and pressure profiles (Figure 3.15) established by Ibrahim *et al.*[38] It is also important to note that at the end of each SPS program, the applied pressure was released to zero and the system was allowed to cool down in "free fall". After the densification process, the samples were carefully polished to remove any traces of graphite.

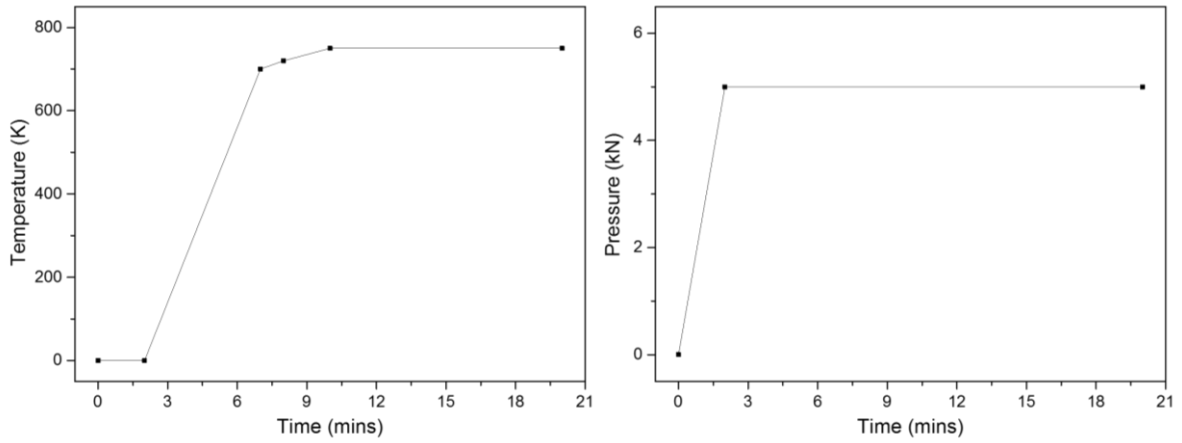

Figure 3.15: Pressure and temperature profiles used during SPS for the $Sn_{1.03-x}In_xTe$ samples.

A detailed summary of the entire synthesis process is shown in Figure 3.16.

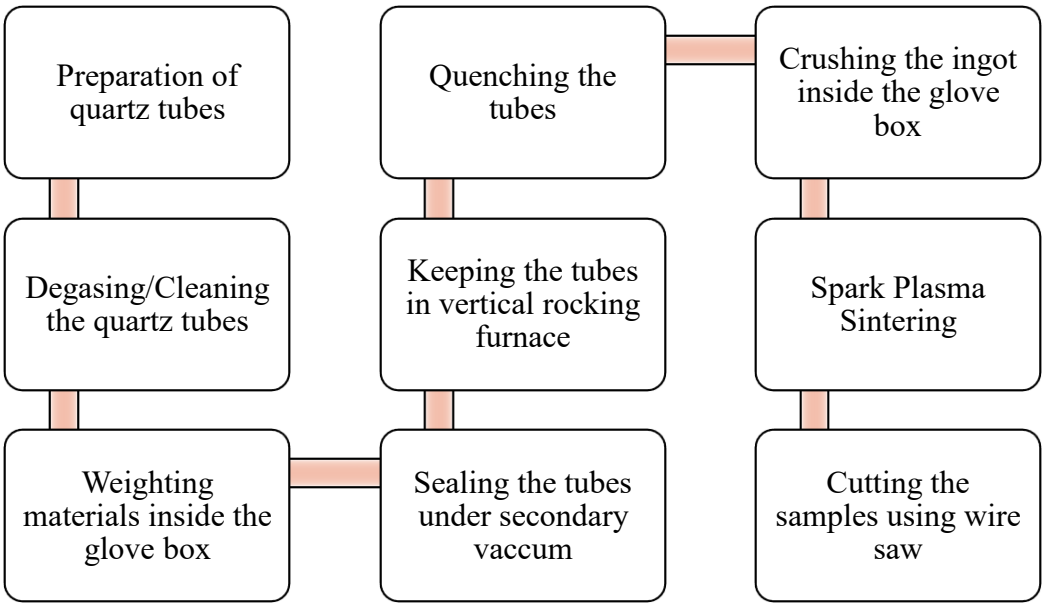

Figure 3.16: Summary of the synthesis process followed for the series $Sn_{1.03-x}In_xTe$.

In order to determine whether dense bulk samples were obtained, the relative densities of each sample (see Table 3.2) was calculated using the simple formula:

Equation 3.6:

$$Relative\ Density = \frac{density_{experimental}}{density_{theoretical}}$$

The experimental density was calculated using the formula:

Equation 3.7:

$$d = \frac{m}{V}$$

where d is the experimental density, m is the mass of the consolidated cylinder and V is its volume. The experimental densities were then compared to the theoretical values calculated using the formula:

Equation 3.8:

$$d_{theoretical} = \frac{ZM}{VN_A}$$

where Z (= 4) is the multiplicity of the unit cell, M is the molar mass of SnTe-based sample, N_A is the Avogadro number and V is the volume of the crystal lattice calculated using the lattice constant determined by Rietveld refinements against the powder X-ray diffraction data. It is important to mention here that although all the samples were near-perfectly densified, samples above $x > 0.08$ were brittle in nature and the fragility increased with Indium content. Due to this fact, there have been occasions for some samples when the measurement of some physical properties was not possible.

Table 3.2: Relative density of the In doped SnTe series.

Sample	Relative Density (%)
$Sn_{1.03}Te$	99
$Sn_{1.0295}In_{0.0005}Te$	99
$Sn_{1.0285}In_{0.0015}Te$	99
$Sn_{1.0275}In_{0.0025}Te$	98
$Sn_{1.0265}In_{0.0035}Te$	97
$Sn_{1.0255}In_{0.0045}Te$	98
$Sn_{1.0225}In_{0.0075}Te$	98
$Sn_{1.02}In_{0.01}Te$	97
$Sn_{1.01}In_{0.02}Te$	96
$Sn_{0.95}In_{0.05}Te$	96
$Sn_{0.93}In_{0.07}Te$	98
$Sn_{0.92}In_{0.08}Te$	97
$Sn_{0.9}In_{0.1}Te$	98
$Sn_{0.875}In_{0.125}Te$	97
$Sn_{0.8}In_{0.2}Te$	98
$Sn_{0.7}In_{0.3}Te$	96
$Sn_{0.6}In_{0.4}Te$	97

3.4.2 Structural and chemical characterizations

The crystal structure and phase purity were analyzed by powder X-ray diffraction (PXRD) using a Bruker D8 Advance diffractometer at 300 K. The chemical composition and spatial distribution of the elements was assessed by electron dispersive X-ray spectroscopy using a Quanta FEG scanning electron microscope. The details and principle of these instruments are described in the Appendix B.

The PXRD patterns collected for the series $Sn_{1.03-x}In_xTe$, $0 \leq x \leq 0.02$ (Figure 3.17) show that all the synthesized samples are single phased within the detection limits of this technique. All the peaks can be indexed to the NaCl-type cubic structure of SnTe described in the $Fm\bar{3}m$ space group. However, two additional peaks at 30.7° and 32.1° that correspond to elemental Sn can be observed. The presence of these peaks is consistent with the Sn excess systematically introduced in the initial compositions and located at the grain boundaries, as shown by transmission electron microscopy.[24]

The PXRD patterns of the $Sn_{1-x}In_xTe$ samples for $0.05 \leq x \leq 0.4$ (Figure 3.18) also showed that the samples are single phase with peaks indexed to the NaCl-type cubic structure. The absence of In-rich secondary phases up to the In content of 30% is in agreement with prior studies that reported a solubility limit of In of around 40%.[34–36] For $x = 0.4$ sample, additional traces (peaks marked by # in Figure 3.18) of secondary phases were observed that indicate the formation of tetragonal InTe. This pattern was in good agreement with prior studies.[34,35] Moreover, when compared to low In content series (Figure 3.17), the "extra" peaks of elemental Sn are not observed in the series $Sn_{1-x}In_xTe$; $0.05 \leq x \leq 0.4$ due to the absence of self-compensation used during the synthesis process.

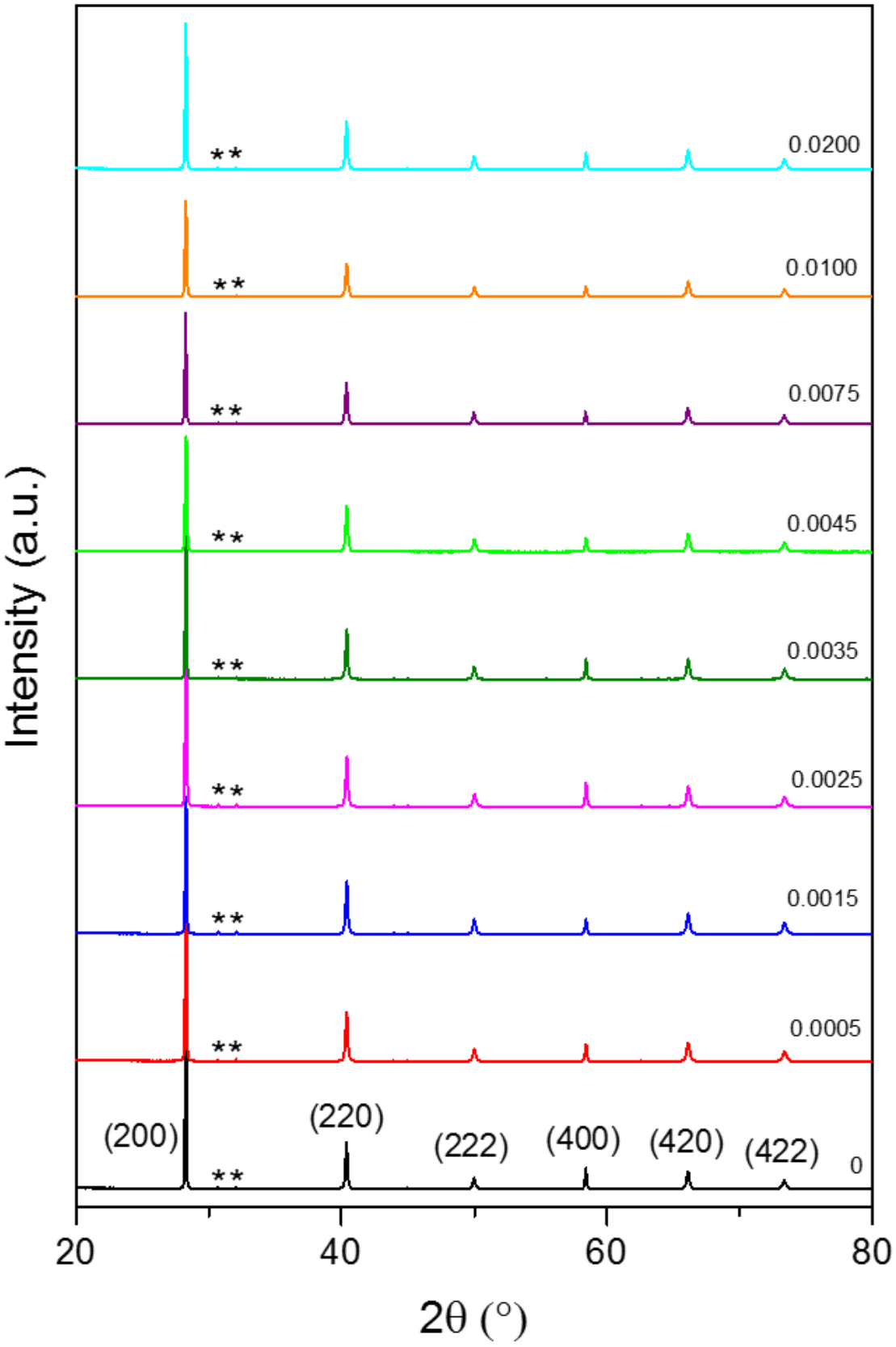

Figure 3.17: PXRD patterns for $Sn_{1.03-x}In_xTe$ ($0 \leq x \leq 0.02$). For clarity, all the patterns of the In-containing samples have been vertically offset. The asterisks mark the positions of the reflections of elemental Sn.

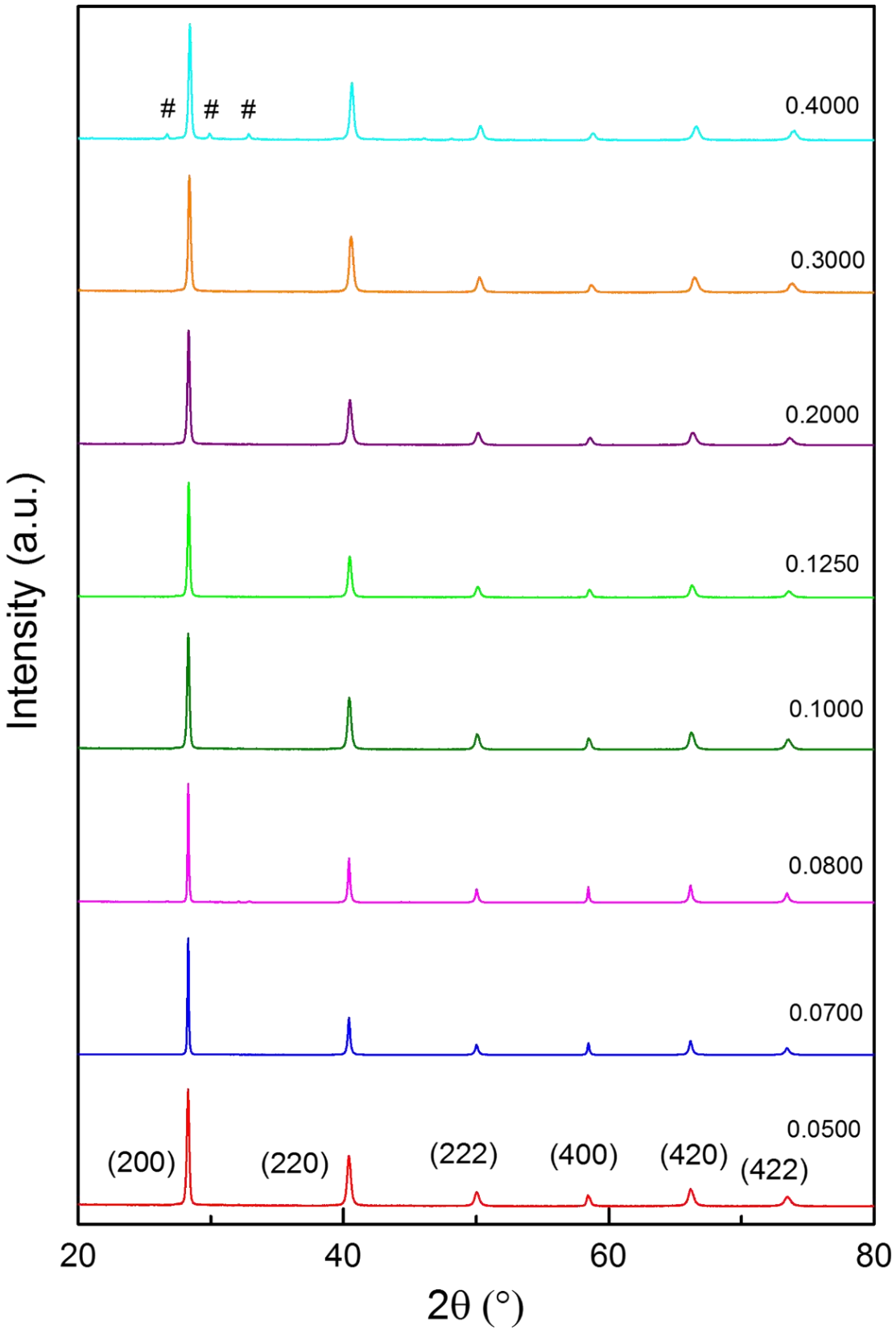

Figure 3.18: PXRD patterns of the series $Sn_{1-x}In_xTe$ ($0.05 \leq x \leq 0.4$). For clarity, all the patterns of the In-containing samples have been vertically offset. The hashtag symbol marks the peak position of binary InTe phase.

The lattice parameter of the x = 0.02 sample (a = 6.3197(2) Å) is slightly lower than that determined for the x = 0.0 sample (a = 6.3242(2) Å) indicating that In exerts a chemical pressure on the unit cell. For In concentrations below 1%, no evident shift in the lattice parameter was observed due to the very low In contents investigated. The lattice parameter hardly varies up to about x = 0.08 (a = 6.316(2) Å). In this extended concentration range, no clear evolution in the lattice parameter can be observed. This situation is further complicated by the fact that a is strongly sensitive to the exact concentration of Sn vacancies, at least for samples below 2% In. Above 10% of In, a decreases almost linearly up to 40% (a = 6.274(2) Å). These results are consistent with prior studies evidencing that In substitution leads to a decrease in the unit cell parameter a, which weakly shrinks for In concentrations up to about 9% before decreasing more rapidly up to the 40% substitution level.[34,35] Hence, it can be concluded that there is a shrinkage in the unit cell of the crystal as we increase the In content which is consistent with the systematic decrease in a as seen in Figure 3.19.

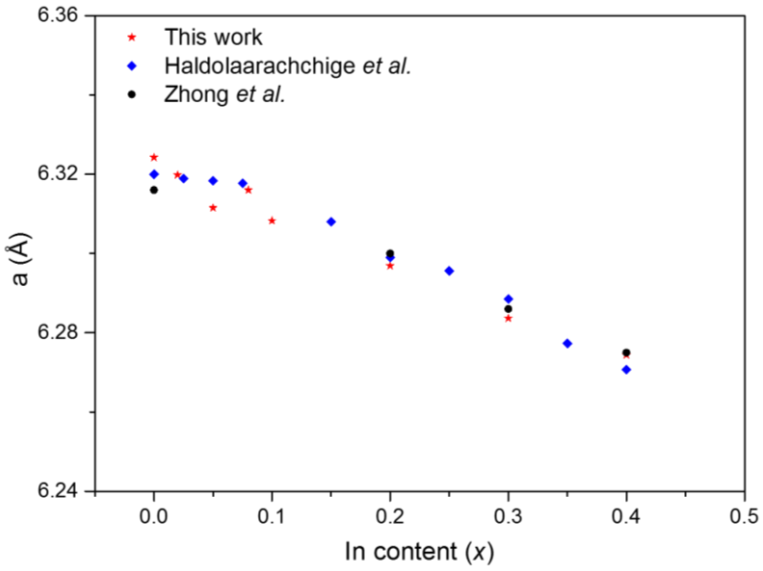

Figure 3.19: Lattice parameters derived using Rietveld analysis for polycrystalline In doped SnTe samples. Lattice parameters from Zhong *et al.* and Haldolaarachchige *et al.* are also added for comparison.[34,35]

EDXS analysis for binary $Sn_{1.03}Te$ revealed a homogeneous distribution of Sn and Te. Elemental Sn is not visible by this technique but, as mentioned previously, can be observed by transmission electron microscopy.[38] In the present case, the detection of small concentrations of In (below 2%) was not possible due to the limitation of this technique. For the x = 0.02 sample (Figure 3.20), this analysis evidenced a homogenous distribution of In and the presence

of elemental Sn as indicated by the visible small Sn-rich areas.[38] The fact that elemental Sn is observable in this sample and not in the binary $Sn_{1.03}Te$ might be related to the suppression of a fraction of Sn vacancies due to the In substitution. In this case, the composition $Sn_{0.98}In_{0.02}Te$ would be stoichiometric and the excess Sn introduced in the initial composition would then become detectable. To confirm or contradict this hypothesis, additional syntheses of samples without excess Sn in the initial composition are necessary. The excess Sn used would then become more visible suggesting that excess Sn in the initial composition would not be necessary for In concentrations higher than 2%.

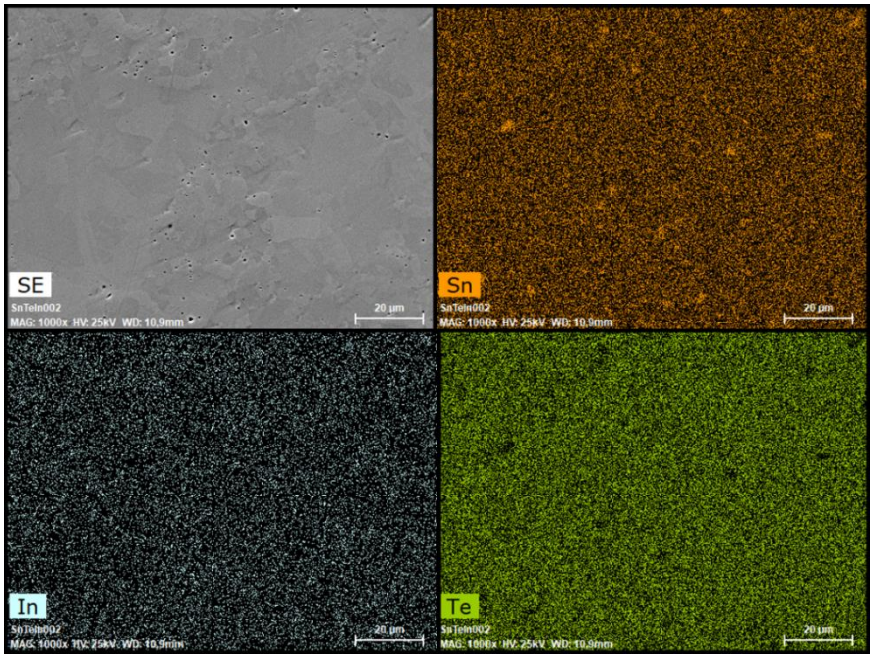

Figure 3.20: Elemental mapping for $Sn_{1.01}In_{0.02}Te$ performed by SEM – EDXS analysis.

Figure 3.21 and 3.22 show the elemental mapping for x = 0.08 and 0.1 respectively. Indium is homogenously distributed in both samples. As there is no self-compensation in these samples, elemental Sn rich areas were not observed, with both Sn and Te also homogenously distributed. These images are in good agreement with PXRD patterns (Figure 3.18) as no additional peaks were present.

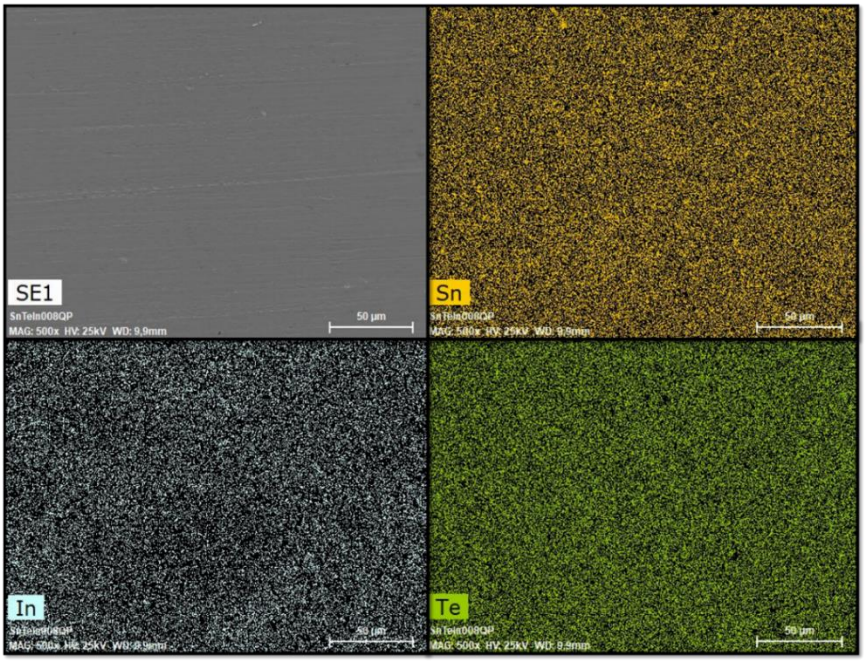

Figure 3.21: Elemental mapping for $Sn_{0.92}In_{0.08}Te$ performed by SEM – EDXS analysis.

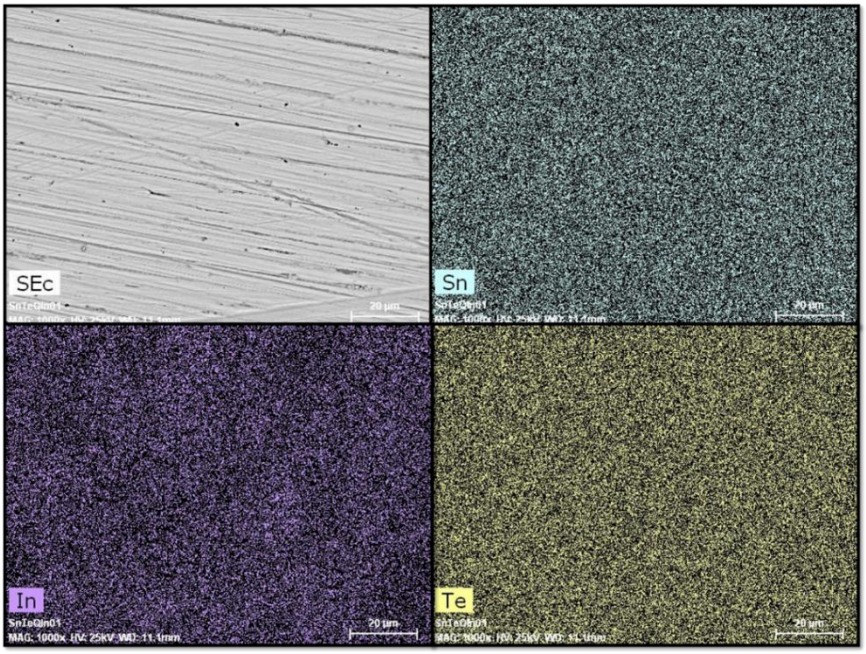

Figure 3.22: Elemental mapping for $Sn_{0.9}In_{0.1}Te$ performed by SEM – EDXS analysis.

Figure 3.23 shows the elemental mapping for x = 40% sample. As suggested by the PXRD pattern, In shows a non-homogenous distribution with In-rich areas easily observable. These analyses confirm the presence of secondary In rich phases (identified as seen above as quadratic InTe) and further suggest that the solubility limit of In is slightly lower than 40%.

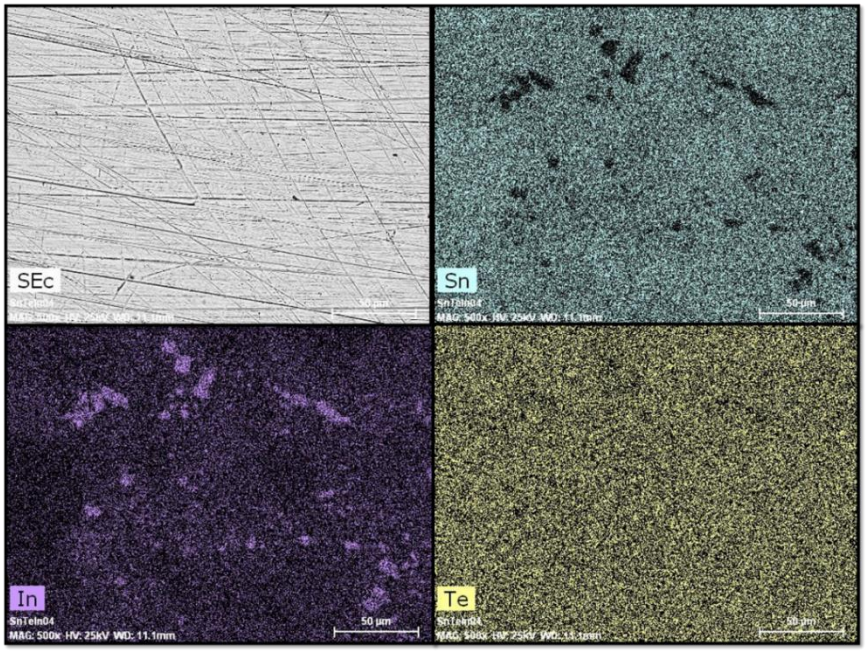

Figure 3.23: Elemental mapping for $Sn_{0.6}In_{0.4}Te$ performed by SEM – EDXS analysis.

3.4.3 Transport properties

The electronic band structure calculations discussed previously have suggested that the optimum effect of RL should occur around an In content of 2%. Above this concentration, the hybridization of the RL and the host states increases, which gives rise to degraded transport properties from a RL point of view, with signs of superconductivity emerging at low temperatures.[1,34,35,39] Hence, to validate these hypotheses experimentally, this section is further divided into three sub-sections.

The first sub-section focuses on the low-temperature transport properties of $Sn_{1.03-x}In_xTe$ ($0 \leq x \leq 0.02$). As already mentioned, no detailed investigation has been performed so far for this In concentration range. Low-temperature measurements can thus provide relevant insights into the effect of RL on the transport properties (5 – 300 K). The second part of this section is dedicated to the in-depth study of the transport properties above room temperature (300 – 800 K). The final sub-section will discuss the transport properties of the samples with In concentrations spanning the range 2 – 40%. Additional low-temperature measurements have also been performed for these samples in order to probe the emergence of superconductivity at high In contents.

3.4.3.1 Low-temperature transport properties for $Sn_{1.03-x}In_xTe$ ($0 \leq x \leq 0.02$)

The temperature dependences of the electrical resistivity ρ for the series $Sn_{1.03-x}In_xTe$ are presented in Figure 3.24 (a). For all samples, ρ exhibits metallic character, consistent with the degenerate nature of transport in SnTe.[24,40–42] Despite the very low In doping levels studied, ρ significantly increases with increasing x from 1.36 μΩ.m for x = 0.0 up to 7.25 μΩ.m for x = 0.02 at 300 K. This large difference in ρ ($\rho(x = 0.02)\,/\rho(x = 0.0) \approx 5.5$ at 300 K) is enhanced upon cooling resulting in a strong increase in the residual electrical resistivity ρ_0 on going from x = 0.0 to x = 0.02 ($\rho(x = 0.02)\,/\rho(x = 0.0) \approx 13.3$ at 5 K). For all samples, the slight but noticeable change in the slope observed below about 100 K can be better visualized in Figure 3.24 (b) where ρ has been normalized to the room-temperature value.

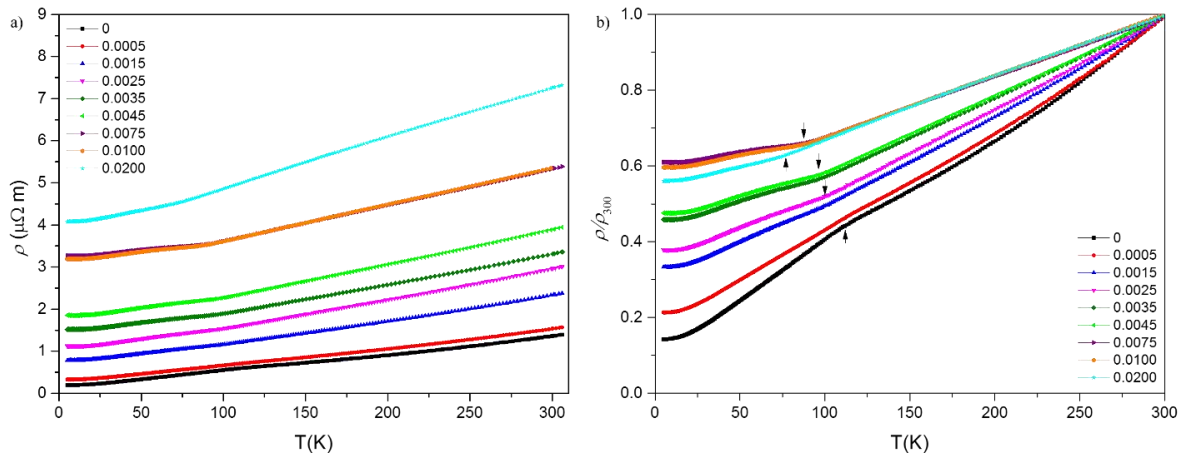

Figure 3.24: Temperature dependence of a) the electrical resistivity ρ for the series $Sn_{1.03-x}In_xTe$ and b) ρ normalized to the room-temperature value ρ_{300K}. Black arrows mark the ferroelectric transition temperature T_{FT}.

This anomaly corresponds to the well-documented ferroelectric structural phase transition.[43–46] Prior studies showed that the transition temperature T_{FT} tends to decrease with increasing p from 100 K at ~ 10^{20} cm^{-3} to 0 K at ~ 10^{21} cm^{-3}.[47–51] In the present series, T_{FT} was estimated from the midpoint of the change in the first derivative $\partial\rho/\partial T$ (Table 3.3). In agreement with prior studies,[24,32,52–72] the lower hole concentration achieved in the x = 0.0 sample, thanks to the initial Sn excess introduced, results in the emergence of the ferroelectric transition at a higher T_{FT} of 112 K.[43–46] The weak structural distortion that accompanies this

transition has little influence on the electrical resistivity and hence, does not affect significantly the resonant nature of In.

Table 3.3: Ferroelectric transition temperature T_{FT} for $Sn_{1.03-x}In_xTe$ samples.

Sample	Transition Temperature (K)
$Sn_{1.03}Te$	112
$Sn_{1.0295}In_{0.0005}Te$	112
$Sn_{1.0285}In_{0.0015}Te$	100
$Sn_{1.0275}In_{0.0025}Te$	97
$Sn_{1.0265}In_{0.0035}Te$	95
$Sn_{1.0255}In_{0.0045}Te$	95
$Sn_{1.0225}In_{0.0075}Te$	87
$Sn_{1.02}In_{0.01}Te$	86
$Sn_{1.01}In_{0.02}Te$	76

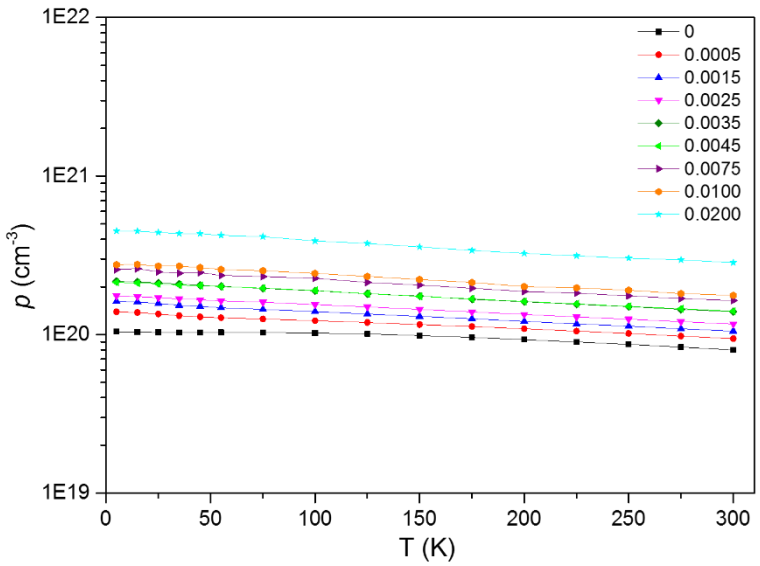

Figure 3.25: Temperature dependence of the hole concentration p for the series $Sn_{1.03-x}In_xTe$.

Consistent with the expected trend in $T_{FT}(p)$, T_{FT} smoothly decreases with increasing the In content to 76 K in the x = 0.02 sample (Figure 3.24 (b)). The fact that $T_{FT}(p)$ follows the trend observed in self-compensated SnTe samples suggests that In behaves as an acceptor. The temperature dependence of p, shown in Figure 3.25, confirms this hypothesis. p hardly evolves upon cooling, in agreement with the degenerate nature of the transport, and increases

continuously with increasing the In content from 8.0×10^{19} cm^{-3} for x = 0.0 to 2.85×10^{20} cm^{-3} for x = 0.02.

This slight increase in p is accompanied by a significant decrease in the Hall mobility μ_H values at 5 K, which drops by two orders of magnitude from 3200 cm^2 V^{-1} s^{-1} for x = 0.0 to 30 cm^2 V^{-1} s^{-1} for x = 0.02 (Figure 3.26).

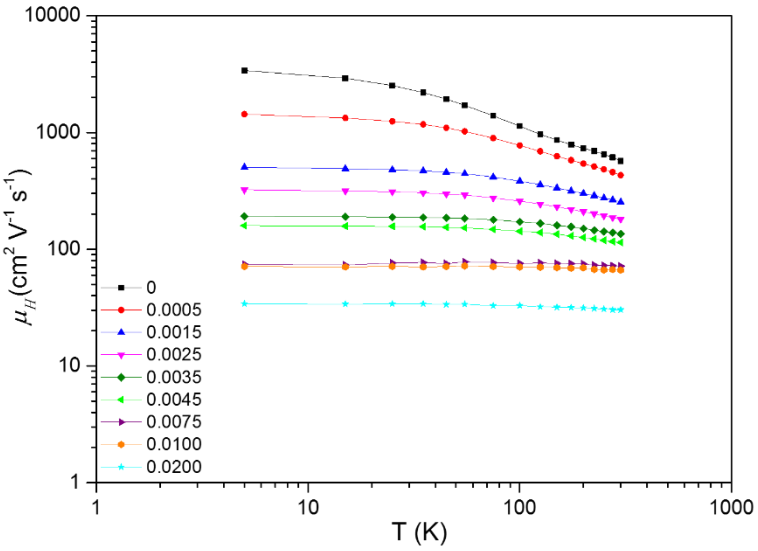

Figure 3.26: Hall mobility μ_H as a function of temperature.

Furthermore, a progressive change in the scattering mechanisms occurs concomitantly with increasing x. While $\mu_H(T)$ follows a $T^{-0.5}$ law in the x = 0.0 sample above 30 K characteristic of alloy scattering,[24] $\mu_H(T)$ remains nearly constant over the entire temperature range in the x = 0.02 sample. This behavior is indicative of hole scattering by ionized impurities in a degenerate system ($\propto T^0$), which is independent of the degree of non-parabolicity of the electronic bands.

Measurements of the temperature dependence of the thermopower α, shown in Figure 3.27, reveal a complex evolution with both temperature and x. While at 300 K, α increases with increasing x, no simple trend between α and x emerges at lower temperatures. The strongly non-linear $\alpha(T)$ of $Sn_{1.03}Te$ has been attributed to the presence of a phonon-drag contribution superimposed to the diffusion thermopower expected to vary linearly with temperature for a degenerate hole gas.[24] An In concentration as low as 0.05% is sufficient to significantly lower this phonon drag contribution.

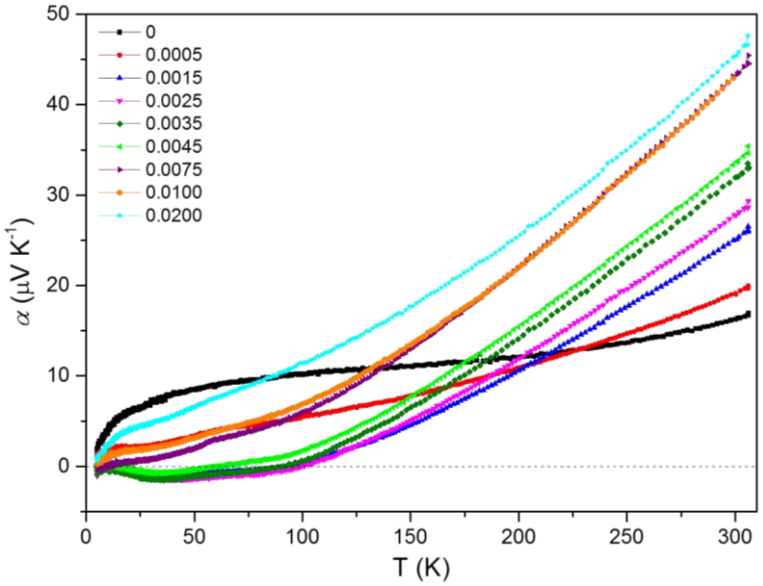

Figure 3.27: Temperature dependence of the thermopower α for the series $Sn_{1.03-x}In_xTe$.

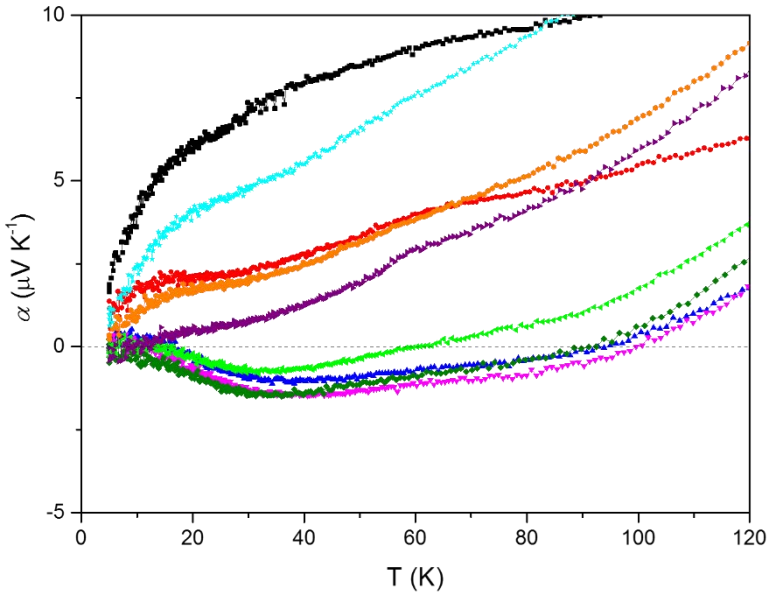

Figure 3.28: Magnification of the low-temperature region where the transition from *p* to *n*-type α values occurs for $0.0015 \leq x \leq 0.0045$.

A magnification of the low-temperature region (Figure 3.28) shows that this contribution nevertheless survives as indicated by the local maximum observed near 15 K for $x = 0.0005$. A further increase in x to 0.0015 then leads to a crossover from positive to negative values near 100 K. The negative sign remains unaffected down to 5 K and with increasing x to 0.0035. Such a change from a dominant hole-like to electron-like response suggests either the development of electron pockets with increasing x or a possible negative phonon-drag

contribution. For x = 0.0045, the temperature range over which α is negative is reduced to below 60 K. Finally, positive values are recovered over the whole temperature range for $x \geq$ 0.0075. None of the samples show a linear temperature dependence characteristic of a diffusive regime. Moreover, the superlinear dependence observed below 200 K in the x = 0.01 sample is lessened in the x = 0.02 sample.

Figure 3.29 (a) shows the temperature dependence of the total thermal conductivity κ. The x = 0.0 sample is characterized by a large room-temperature value of 7.8 W m^{-1} K^{-1} and a low-temperature Umklapp peak that reaches nearly 14 W m^{-1} K^{-1} at 35 K. The overall shape of $\kappa(T)$ is not affected by the substitution of In for Sn. However, increasing the In content results in a significant decrease in the κ values and in the magnitude of the Umklapp peak. This evolution with x is mainly due to the marked increase in the ρ values which strongly reduces the electronic contribution κ_e according to the Wiedemann-Franz law $\kappa_e = LT/\rho$ where L is the Lorenz number. Using a single-parabolic-band approximation and neglecting the variations in temperature of L below 300 K leads to an estimate of the lattice thermal conductivity $\kappa_{ph} = \kappa - \kappa_e$, shown in Figure 3.29 (b) as a function of temperature. As expected from the low doping levels studied, the κ_L values only weakly varies with the In concentration up to x = 0.0075. Above this concentration, larger differences appear at low temperatures due to point-defect scattering effects that start to play a more significant role on the heat transport.[44]

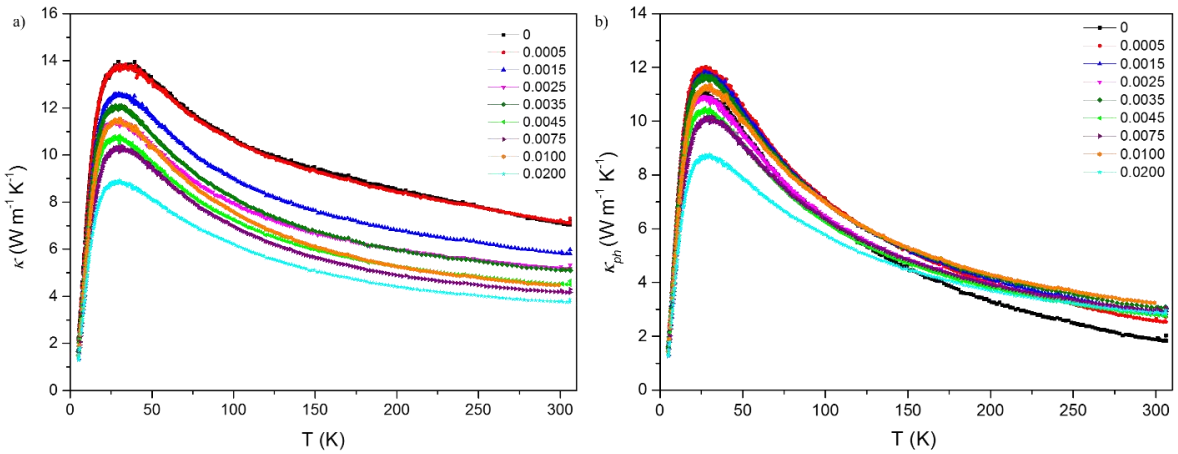

Figure 3.29: Temperature dependence of the a) total thermal conductivity κ for the series $Sn_{1.03-x}In_xTe$ and b) lattice thermal conductivity κ for the series $Sn_{1.03-x}In_xTe$ calculated using a single band model.

The presence of an In-induced RL provides a consistent picture that explains several traits observed in this series. The variation in the residual electrical resistivity ρ_0 with x, shown in

Figure 3.30, reflects the significant drop in μ_H by two orders of magnitude at 5 K. This strong sensitivity to the In content is clearly beyond what may be expected from strain field effects and mass fluctuations induced by the substitution of In for Sn due to the very low doping levels and the small difference in molar mass. Although the presence of grain boundary scattering contributes to decreasing μ_H, this strong effect is rather a natural consequence of enhanced scattering of holes by the RL which strongly decreases their electronic lifetime as indicated by the analysis of the Bloch spectral functions. The linearity observed in $\rho_0(x)$ further suggests that In atoms act as independent scattering centers in the whole concentration range. Of note, the presence of a small concentration of Sn vacancies, estimated to be around 0.25% in the parent $Sn_{1.03}Te$ compound,[24] cannot account for the strong increase in ρ_0. Recent low-temperature transport property measurements on the binary SnTe prepared by various synthesis routes have shown that ρ_0 remains below 0.5 μΩ.m at 5 K despite variations in the vacancy concentration from 0.25 to nearly 1.8%.[24] Thus, the marked increase in ρ_0 as x increases supports the major role played by the RL on the low-temperature transport properties.

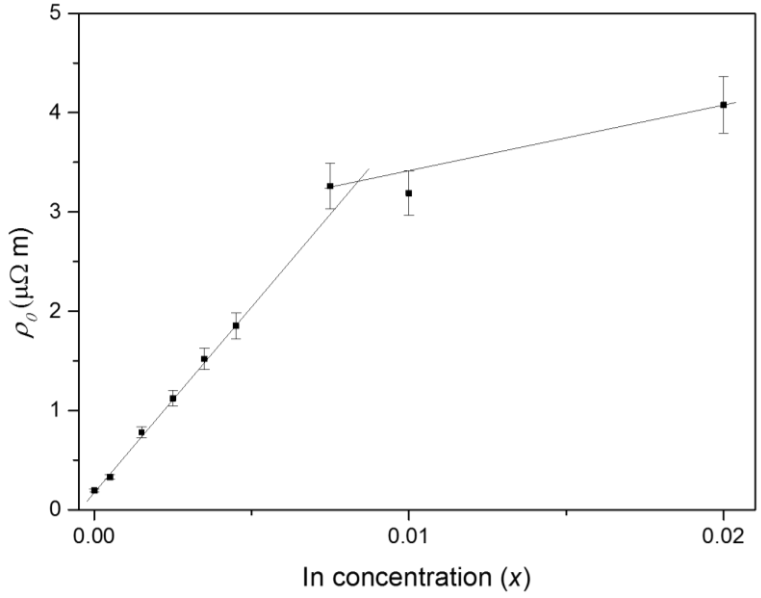

Figure 3.30: Residual electrical resistivity ρ_0 as a function of the In concentration x. The solid lines are guides to the eye.

From simple electron counting rules, In should behave as a hole dopant in $Sn_{1.03}Te$ due to its number of valence electrons with one fewer electron than Sn, that is, In^{1+} versus Sn^{2+}. Detailed investigations of the superconducting properties as a function of x between 0.05 and 0.40 revealed that a simple hole-doping picture only holds true up to about 0.09, a critical value

above which the impact of In on the electronic band structure is too severe for a rigid-band-like shift of the chemical potential to be a consistent description of the system.[34,35,39,73–75] The non-rigid-like behavior above x = 0.09 further manifests in the Hall data with a crossover from a dominant hole-like to electron-like response at 50 K.[34] For substitution levels lower than 0.09, the compounds remain p-type regardless of the In content with a good correlation between the In concentration and measured hole densities. Our experimental results support well this last conclusion with a hole-dopant behavior persisting across the entire doping range.

Of note, p_H is related to the chemical hole concentration p by the relation $p_H = r_H p$ where r_H is the Hall factor, usually assumed to be equal to unity. However, it was shown in $Pb_{1-x}Tl_xTe$ that the RL affects this factor in degenerate samples, the extent to which depends on the concentration of the resonant impurity and temperature.[76] The deviations from unity were predicted to be the largest at low temperatures and low Tl concentrations while the effect on r_H remains moderate near room temperature. In the present $Sn_{1.03-x}In_xTe$ series, assuming $r_H \approx 1$, and hence $p_H \approx p$, near 300 K should therefore provide a reasonable estimate of p.

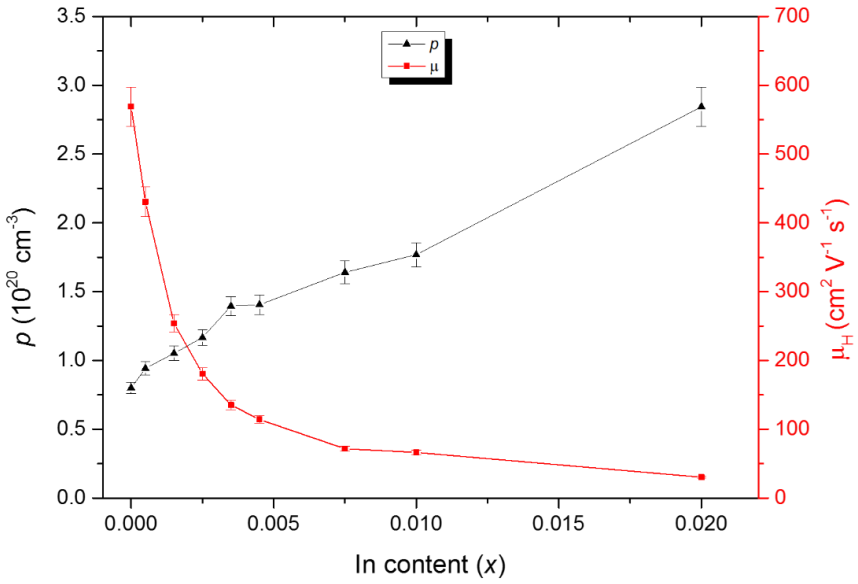

Figure 3.31: Variations in the hole concentration p and Hall mobility μ_H as a function of the In concentration x at 300 K. The solid lines are guides to the eye.

The dependence of p and μ_H on x, shown in Figure 3.31, confirms a rapid and strong reduction in μ_H with increasing x despite the very low doping levels considered herein. Meanwhile, p tends to slightly but continuously increase with x suggesting that In behaves as an acceptor impurity in $Sn_{1.03}Te$ in agreement with our electronic band structure calculations.

The evolution of these two parameters with x confirms that the reduction of μ_H is the main factor that drives the observed increase in ρ. Such a reduction in μ_H is expected in the presence of a RL, as mentioned above.

As shown in Figure 3.32, where the hole density p as a function of x is presented, $p(x)$ increases quasi-linearly with x. For $x \geq 0.01$, a very good agreement is achieved between the experimental p values and the expected hole concentration calculated by assuming that each In atom provides one hole (i.e. In^{1+} valence state). The slight but clear disagreement at lower doping levels likely reflects the concentration of Sn vacancies which tend to disappear as x increases. From these data, it seems reasonable to postulate that vacancies are no longer present beyond $x = 0.01$ or, at least, that their concentration is sufficiently low to have a negligible influence on the measured p. Thus, these results confirm that In behaves as a hole dopant with a formal In^{1+} valence state, thereby severely constraining the possible amount of In^{3+} present in this In concentration range. This is further confirmed by the slope of p versus the concentration of In atoms per cm^{-3} (Figure 3.32, inset) which corresponds to about 0.6 holes per In atom.

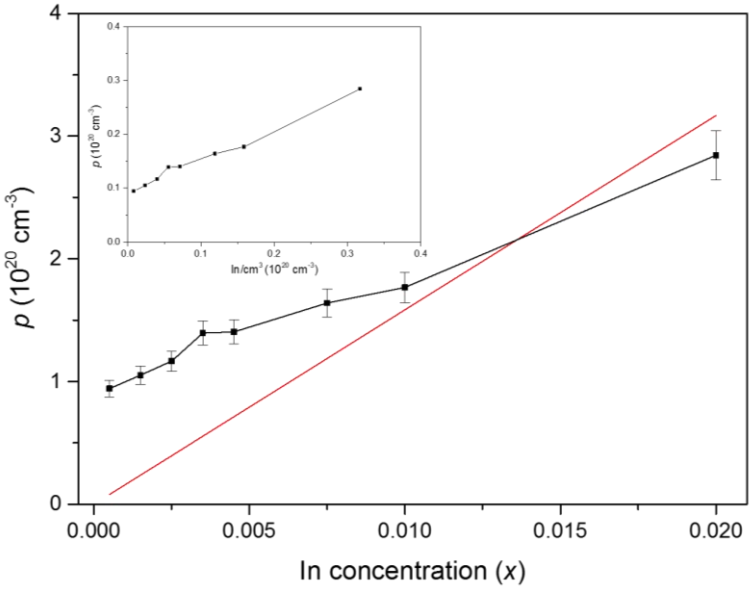

Figure 3.32: Hole concentration p as a function of the In concentration x at 300 K. The solid black line is a guide to the eye. The solid red line represents the expected variations in the hole concentration p_H assuming a In^{1+} valence state. (Inset graph represents In per cm^3 plotted vs carrier concentration where the slope determines the number of holes per In atoms)

One intriguing aspect revealed by our experimental results is the non-monotonic evolution of the thermopower with x and, notably, the crossover from positive to negative values for $0.0015 \leq x \leq 0.0045$. Several scenarios may be invoked to explain the overall trend in $\alpha(x,T)$ that include a charge-Kondo effect, a RL-induced effect or a phonon-drag contribution. The first scenario, a charge-Kondo effect, has been discussed in the series of p-type samples $Pb_{1-x}Tl_xTe$ for which the $\alpha(x,T)$ data are qualitatively similar to those obtained here for the series $Sn_{1.03-x}In_xTe$.[77] In particular, a crossover from positive to negative α values below 100 K has been evidenced for a Tl content of 0.3%. Above this value, positive α values are recovered which slightly increase with increasing x to 1.1% and eventually to 1.3%.[77] Because of these strong similarities between these sister compounds, it is tempting to posit that $Sn_{1.03-x}In_xTe$ also harbors a charge-Kondo effect. However, this mechanism requires In in both In^{1+} and In^{3+} charge states, the presence of which is not supported by our Hall effect data. The fact that both Tl and In act as resonant impurities suggests that the complex evolution of $\alpha(x,T)$ below 100 K may arise from band structure modifications induced by the RL. However, low-temperature measurements of α on the series $Pb_{0.99}Na_{0.01}Te_{1-x}S_x$ for x = 0.0, 0.04 and 0.120 have also evidenced a temperature region extending from 50 to 120 K over which α is negative.[78] In this series, neither Na nor S behave as resonant impurities demonstrating that the presence of a RL is not a prerequisite to the positive-to-negative crossover in α.

To determine whether a similar dependence $\alpha(\mu_0 H)$ is observed in the series $Sn_{1.03-x}In_xTe$, α of the x = 0.0035 sample has been measured at 4, 7, 10 and 14T. The high field measurements (10 and 14 T) have been made in collaboration with Dr. Jiri Hejtmanek and Dr. Petr Levinsky from the Academy of Science of the Czech Republic in Prague. As seen in Figure 3.33, these additional measurements under magnetic fields $\mu_0 H$ of up to 14T showed that positive values are progressively recovered with increasing $\mu_0 H$. The overall $\alpha(\mu_0 H)$ evolution has been interpreted as a positive phonon-drag peak superimposed to a negative diffusion contribution to α that evolves into a positive contribution when subjected to high magnetic fields. The phonon-drag contribution results from the interaction between electrons and phonons. The latter, that move against the thermal gradient, transfer their momentum to the electrons which are thus pushed to one end of the material, thereby contributing to the thermoelectric field already present.[4,79,80] In addition, the shape of α(T) is practically unaffected by the application of the magnetic field, as observed in $Pb_{0.99}Na_{0.01}Te_{1-x}S_x$ for x = 0.04.

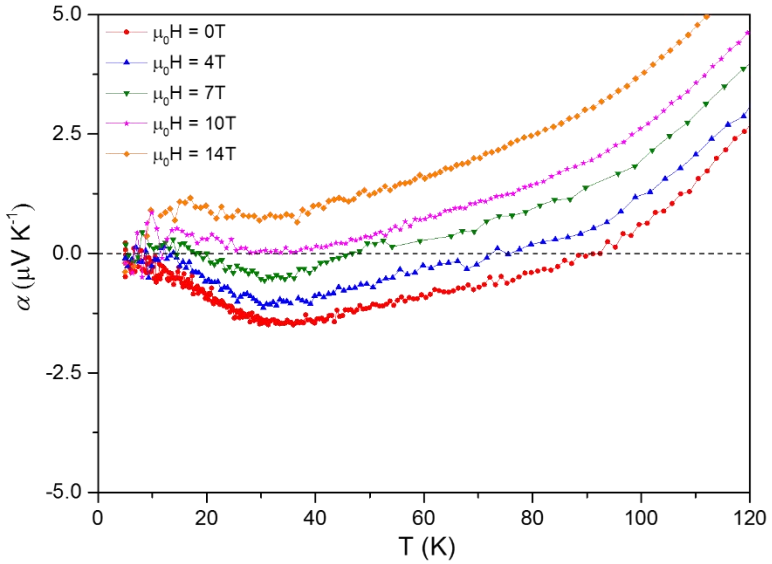

Figure 3.33: Temperature dependence of the thermopower α of the x = 0.0035 sample under magnetic fields $\mu_0 H$ of 0, 4, 7, 10 and 14T.

The similar behavior of $\alpha(\mu_0 H)$ in these two series thus suggests that a negative diffusion contribution also exists in $Sn_{1.03-x}In_xTe$ which evolves with both the In content and, for a fixed x value, with $\mu_0 H$. The fact that α tends to positive values at high magnetic fields further suggests that the dominant charge carriers are holes, in agreement with the Hall data. We note that, as an alternative scenario, possible electron pockets emerging upon In substitution may be split by the high magnetic field imposed, thereby progressively suppressing their contribution to α. However, the extremal cross-section of these electron pockets should be sufficiently small in order to reach the quantum limit at a magnetic field as low as 10T. Because this limit is lower than that observed in semi-metals such as bismuth, this possibility seems unlikely to be realized in the present case and reinforces the scenario of a negative diffusion thermopower. In $Pb_{0.99}Na_{0.01}Te_{1-x}S_x$, this negative contribution has been attributed to interband scattering between the L and Σ valleys of the valence bands.[78] Given the strong similarities between these two series of compounds, it is then plausible that interband scattering also influences the temperature dependence of α in SnTe.

Owing to the use of ^4He in our measurement system at low temperatures, we were not able to measure the electrical resistivity below 1.9 K (as seen in Figure 3.24 (a)) to confirm the presence of a possible superconducting transition, as observed in In-doped SnTe samples.[34,39,73,81–86] Hence, additional specific heat measurements were performed for the x = 0.0035 sample down to 0.40 K (Figure 3.34 (a)) using the ^{3}He option of the PPMS in collaboration with Dr. Jiri Hejtmanek and Dr. Petr Levinsky from the Academy of Science of

the Czech Republic in Prague. No abrupt lambda-type anomaly is observed in these data indicating that this sample is not superconducting down to 0.40 K. This result is consistent with those reported by Erickson *et al.* showing that SnTe becomes superconducting only for In concentrations higher than $x \geq 0.017$ in the $Sn_{1-x}In_xTe$ system.[39] Hence, it is possible that the sample with the highest In content in the present study (x = 2 %) might be superconducting. Additional measurements will be helpful in confirming or contradicting this hypothesis.

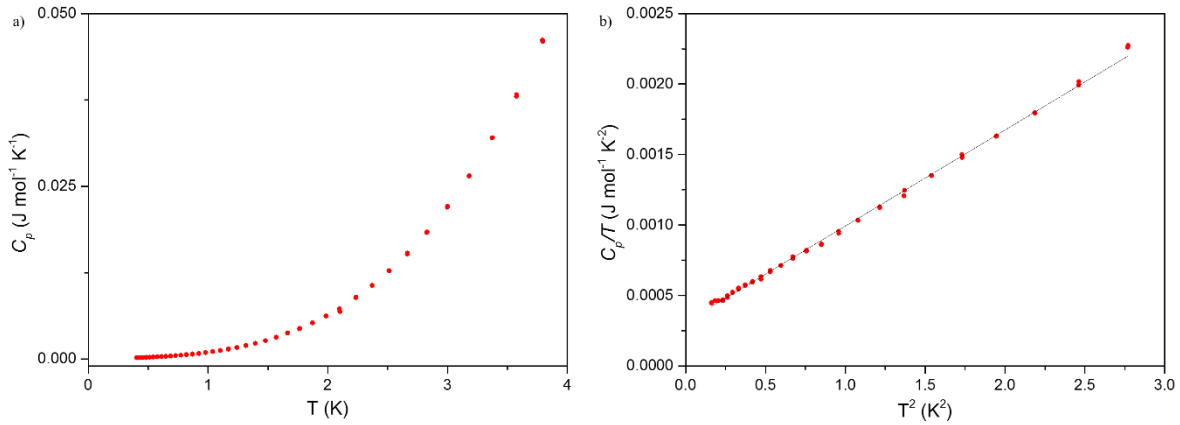

Figure 3.34: a) Temperature dependence of the specific heat C_p of the x = 0.0035 sample at low temperature and b) C_p/T as a function of T^2 for the x = 0.0035 sample. The black solid line represents the best linear fit to the plotted data.

Plotting the C_p/T data versus T^2 at very low temperatures, that is below 1.5 K, enables deriving the electronic and lattice contribution (see Figure 3.34 (b)). A linear fit of these data using the conventional Fermi-liquid relation:

Equation 3.9:

$$C_p/T = \gamma + \beta T^2$$

gives a Sommerfeld coefficient γ of 0.31 mJ mol^{-1} K^{-2} and a β parameter, describing the βT^2 lattice contribution, of 0.68 mJ mol^{-1} K^{-4}. Within the Debye model, β is related to the Debye temperature θ_D through the following relation:

Equation 3.10:

$$\theta_D = \left[\frac{12\pi^4 nR}{5\beta}\right]^{1/3}$$

where n is the number of atoms per formula unit (2 in the present case) and R is the gas constant. This relation yields a θ_D value of 179 K, in good agreement with prior reports.[34,39,83,87,88]

3.4.3.2 High-temperature transport properties for $Sn_{1.03-x}In_xTe$ ($0 \leq x \leq 0.02$)

Figures 3.35 and 3.36 show the temperature dependences of the electrical resistivity and thermopower, respectively, measured between 300 and 800 K. Both the $\rho(T)$ and $\alpha(T)$ data of the $x = 0$ sample are consistent with prior studies revealing a metallic behavior up to about 600 K above which a stronger rise with temperature is observed.[1,32,52–72] This peculiar effect has been attributed to the contribution of the heavy-hole valence band which coexists with a light-hole valence band that dominates transport at lower temperatures.[40,41,89] This general trend is hardly affected upon substituting In for Sn up to about $x = 0.0045$. Above this value, further increasing the In concentration tends to lessen the superlinear variation above 600 K.

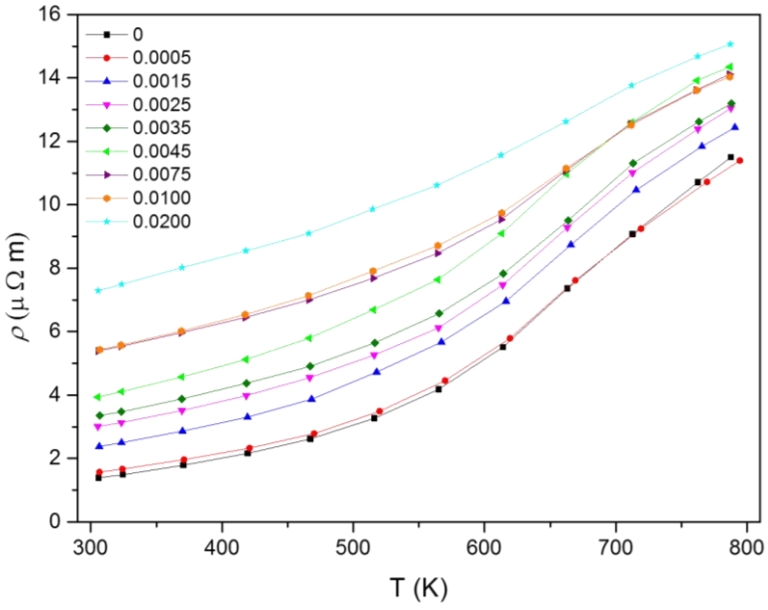

Figure 3.35: Temperature dependence of the electrical resistivity ρ of the $Sn_{1.03-x}In_xTe$ samples ($0 \leq x \leq 0.02$). The solid lines are guides to the eye.

While observable on the $\rho(T)$, this effect is more clearly evidenced in the $\alpha(T)$ data where the high-temperature increase is no longer visible in the $x = 0.02$ sample. The most remarkable effect induced by In substitution mainly occurs near room temperature where both α and ρ significantly increase with increasing the In content in a stepwise manner. Given the

very low In concentrations introduced, this finding provides strong experimental evidence that these concomitant enhancements arise from an In-induced RL. The fact that α and ρ continuously evolve upon increasing the In content can be explained by the local DOS enhancement predicted by our electronic band structure calculations and possibly by resonant scattering. While the DOS peak governs the increase in α, both the decrease in the carrier lifetime and the increase in the DOS effective mass induced by the RL lead to a strong reduction of the hole mobility (Figure 3.26) and hence, of the ρ values.

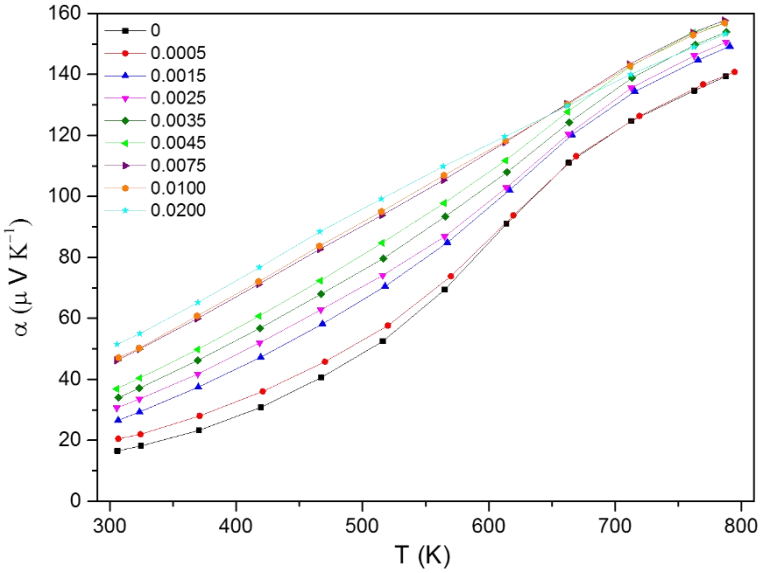

Figure 3.36: Temperature dependence of thermopower α of the $Sn_{1.03-x}In_xTe$ samples ($0 \leq x \leq 0.02$). The solid lines are guides to the eye.

Despite this detrimental impact on the ρ values, the best compromise near room temperature is achieved in the $x = 0.075$ and 0.01 samples which show the highest power factor, P (Figure 3.37). Upon warming, P no longer evolves linearly with the In content above 550 K due to the significant increase in α experienced notably by the $x = 0$ and 0.005 samples. Nevertheless, except for the $x = 0.02$ sample for which P is clearly lowered, all the samples exhibit slightly enhanced, similar P values which are shifted towards higher temperatures. The maximum value of 1.8×10^{-3} W m^{-1} K^{-2} is achieved at 800 K. These results are consistent with those obtained by Zhang *et al.* for the series $Sn_{1-x}In_xTe$.[1] The enhancement of the power factor at high temperatures, as we have already mentioned, is possible due to the fact that phonon scattering and resonant level scattering are on the same order of magnitude near room

temperature. Upon warming, the scattering on RL is less temperature-dependent, although still strong, which allows to take advantage from the increase in α.

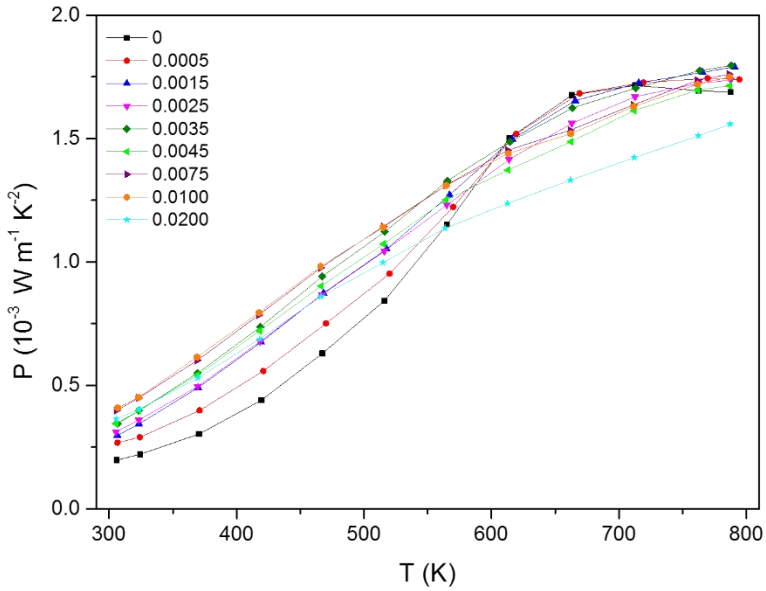

Figure 3.37: Power factor α^2/ρ as a function of temperature for the series $Sn_{1.03-x}In_xTe$ ($0 \leq x \leq 0.02$). The solid lines are guides to the eye.

One straightforward and convenient way of revealing the resonant nature of an impurity atom is tied to the carrier concentration dependence of the thermopower known as the Ioffe-Pisarenko plot. The resonant behavior manifests itself by significant deviations from the conventional dependence followed by a rigid-band-like impurity. In the present case, this analysis is complicated by the presence of two valence bands that govern the transport of SnTe and the number of band parameters that need to be taken into account. Pioneering studies on SnTe by Brebrick *et al.* have shown that a two-valence-band model using a combination of a parabolic heavy-hole band and non-parabolic light-hole band provides a good description of the experimental data over two orders of magnitude of the hole concentration.[40,41,89] As shown in Figure 3.38, the comparison of our experimental data at 300 K with the theoretical curve show that all the data of the In-substituted samples strongly deviate from the predicted variation. For the x = 0.0 sample, as discussed elsewhere,[24] the deviation from theory may come from the single set of band parameters used to calculate the Pisarenko curve, some of which may likely vary with varying the Sn vacancy concentration. For the In-containing samples, a steep rise in the α values with increasing the In content is observed around 10^{20} cm^{-3} while the model predicts only little variations around this hole concentration. Moreover, the

peak value of α seems to be enhanced and shifted towards lower hole concentration compared to the extremum predicted slightly below 10^{21} cm^{-3}. The marked difference between a rigid-band model and experiment provides another strong evidence of the resonant character of In in $Sn_{1.03}Te$.

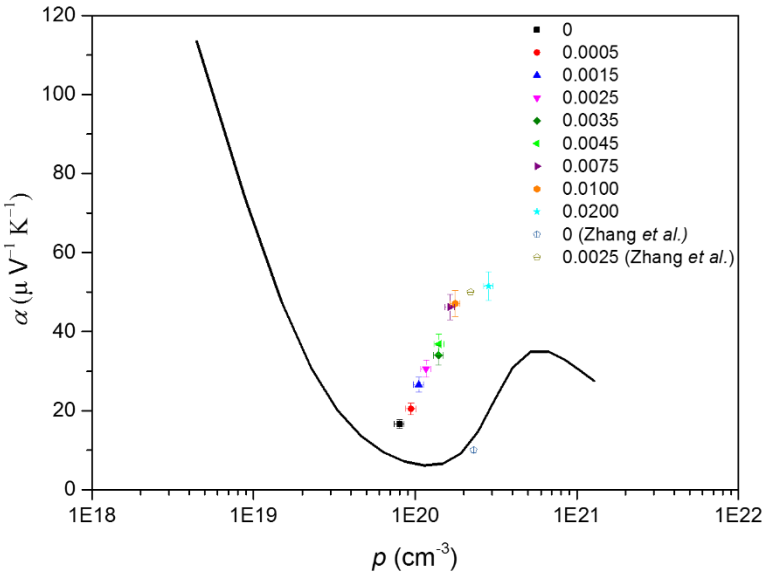

Figure 3.38: Ioffe-Pisarenko plot showing the thermopower α as a function of the hole concentration p at 300 K. The solid black curve corresponds to the theoretical dependence determined using a two-valence-band model. For comparison purposes, the values reported by Zhang *et al.* have been added.[1] (Error bars of 7 % are included for both α and p).

As a consistency check, we tried to determine whether changes in the band parameters used to calculate the theoretical curve could explain the observed trend. The results, presented in Figure 3.39, show that the density-of-states effective masses of the heavy-hole and light-hole bands are the two main parameters that control the peak in α and its position. However, an increase in the magnitude of the peak and its shift towards lower hole concentration are observed when both effective masses significantly decrease, in contradiction with the evolution of m^*_{DOS} predicted by our electronic band structure calculations. It seems therefore difficult to reconcile these theoretical results with the experimental data without considering the presence of an In-induced RL. Since the main role of the RL may be qualitatively understood as an increase in the density-of-states effective mass, its influence on the hole concentration dependence of the thermopower cannot be captured by the above-mentioned two-valence-band model using a single set of band parameters.

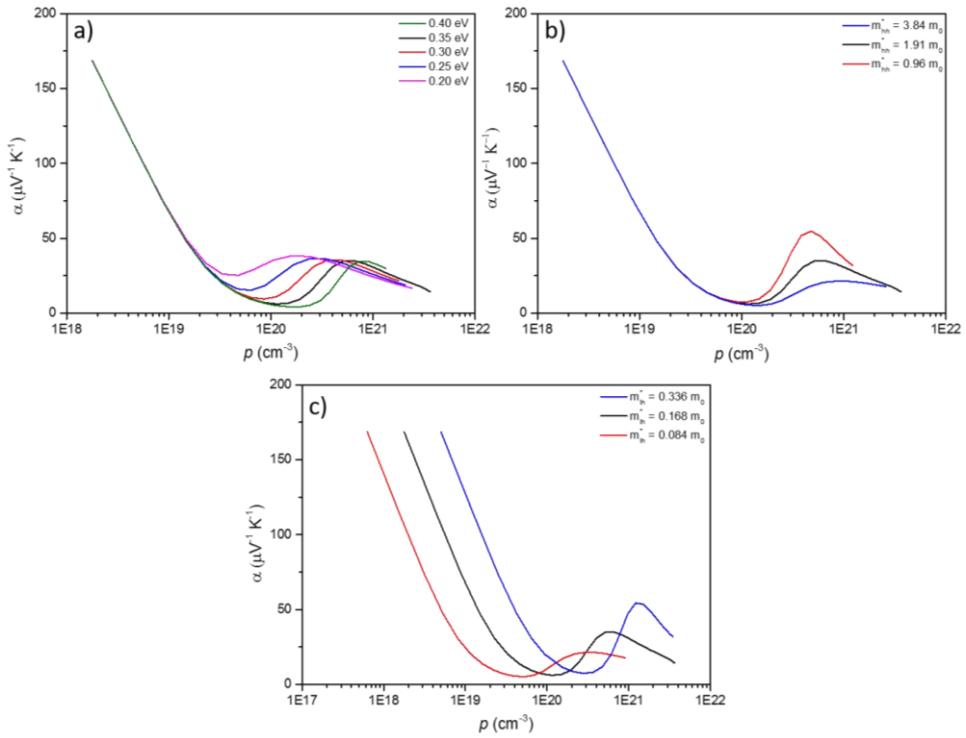

Figure 3.39: Evolution of the Ioffe-Pisarenko curve calculated by a two-valence-band model upon varying a) the density-of-states effective masses of the light-hole valence band m^*_{lh}, b) of the heavy-hole valence band m^*_{hh}, and c) the energy offset ΔE between the light and heavy-hole valence bands. The black arrows mark the evolution of the curve when the corresponding band parameter increases. The values usually admitted for SnTe at 300 K are $0.168m_0$, $1.92m_0$ and 0.30 eV for m^*_{lh}, m^*_{hh} and ΔE, respectively.

Figure 3.40 shows the temperature dependence of the total thermal conductivity κ. For all samples, κ decreases with increasing temperature and tends to saturate above 700 K to values ranging between 2.1 and 2.7 W m^{-1} K^{-1}. In contrast to the roughly similar values observed at the highest temperatures, κ strongly varies with the In concentration near room temperature from 7.9 W m^{-1} K^{-1} in the x = 0 sample down to 3.9 W m^{-1} K^{-1} in the x = 0.02 sample. While the temperature dependences of κ up to x = 0.0045 are very similar, clear differences emerge for higher In concentrations. In addition to a strongly-lessened decrease with temperature, a crossover near 500 K is clearly visible. Above this temperature, κ no longer decreases with increasing x for $x \geq 0.0045$ but surprisingly shows the opposite trend. This reversed variation with x likely reflects significant differences in the electronic thermal conductivity κ_e. This hypothesis is justified by the low In concentrations and the small difference in molar mass between Sn and In which are expected to result in weak mass, binding force and strain field differences induced by In alloying. Thus, according to the relation

proposed by Callaway and Klemens to determine the evolution of κ_{ph} in solid solutions,[90,91] the difference between κ_{ph} of pure $Sn_{1.03}Te$ and that of the In-containing samples should be very small.

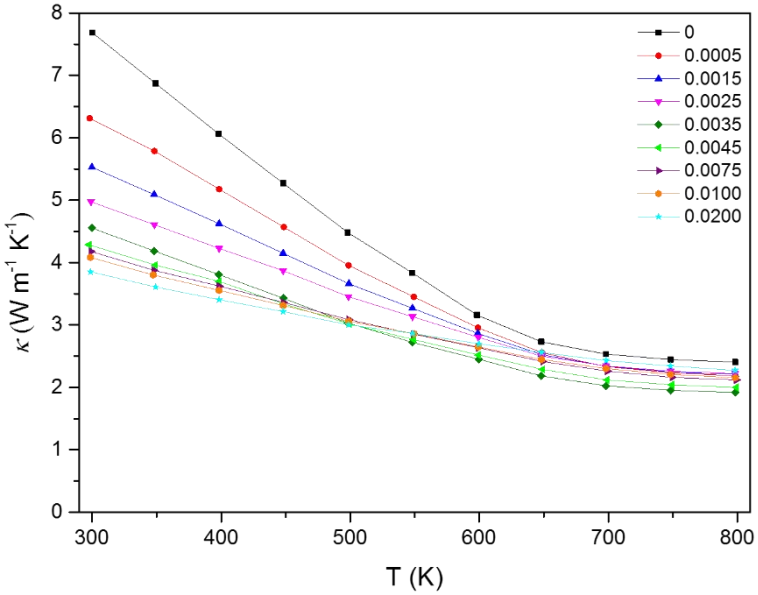

Figure 3.40: Total thermal conductivity κ as a function of the temperature for the series $Sn_{1.03-x}In_xTe$ ($0 \leq x \leq 0.02$). The solid lines are guides to the eye.

Although disentangling the electronic and lattice contributions to κ by estimating κ_e via the Wiedemann-Franz law $\kappa_e = LT/\rho$ would shed further light on this behavior, this subtraction requires to obtain a correct estimate of the Lorenz number L and of its temperature dependence. However, this parameter is difficult to determine in SnTe due to its strong dependence on the details of the electronic band structure and on temperature. In prior studies, a single-parabolic band model is usually used to determine the temperature dependence of L.[24,52,54,55,70,92–94] Alternatively, as SnTe has two main valence bands, the two-valance-band model that was shown to capture well the evolution of the thermopower with the hole concentration may be also considered. For this model, two possibilities exist: using temperature-independent band parameters or considering their temperature dependence determined by fitting experimental data obtained in this temperature range. To determine the most appropriate model in the present case, if any, we have calculated the temperature dependence of L for these three band structure models (Figure 3.41). The results show that the single parabolic band model and the two-valence-band model with temperature-independent band parameters yield similar values over the entire temperature range.

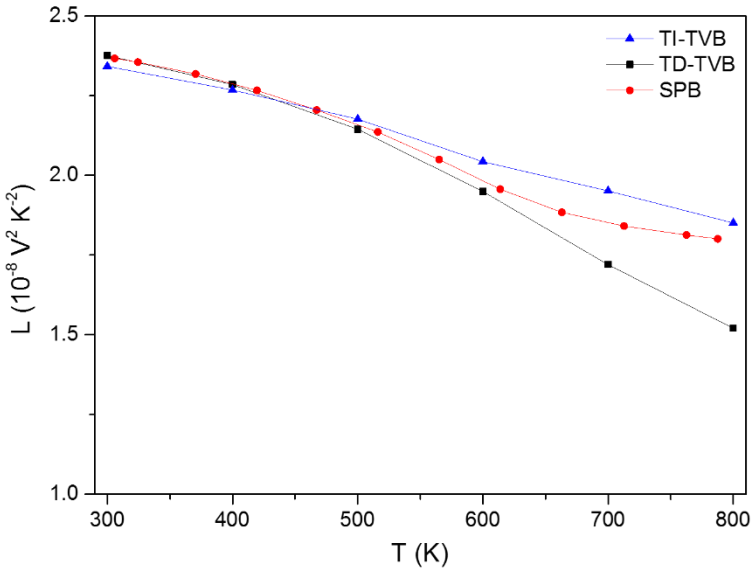

Figure 3.41: Lorenz numbers for binary $Sn_{1.03}Te$ calculated using a a) temperature-independent two-valence-band model (blue curve), a b) temperature-dependent two-valence-band model (black curve) and a c) single-parabolic band model (red curve).

The two-valence-band model with temperature-dependent band parameters results in lower values above 500 K compared to the two other models, approaching the value of 1.5×10^{-8} V^2 K^{-2}, that is, the lowest value for acoustic phonon scattering. Figure 3.42 depicts the temperature dependence of Lorenz number calculated using the single parabolic band model.

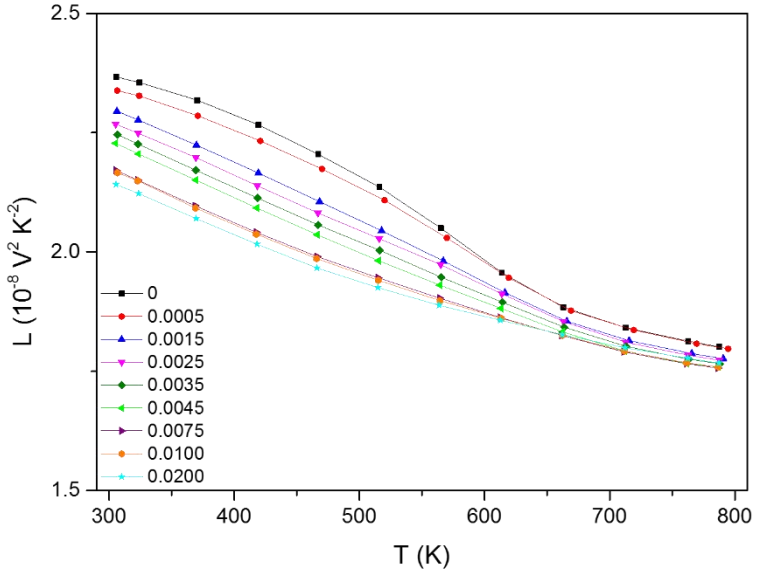

Figure 3.42: Temperature dependence of the Lorenz number *L* for the series $Sn_{1.03-x}In_xTe$ calculated by a single parabolic band (SPB) model.

Using these temperature dependences, we have calculated the electronic and lattice thermal conductivities for the different samples of this series (Figures 3.43). All these models yield κ_{ph} values that strongly vary with the In concentration. For all the three models, κ_{ph} drops to 0.5 W m^{-1} K^{-1} around 500 K in the x = 0.0005 sample. These results contradict the model of Callaway and Klemens which does not predict significant variations in κ_{ph} for such low In concentrations.

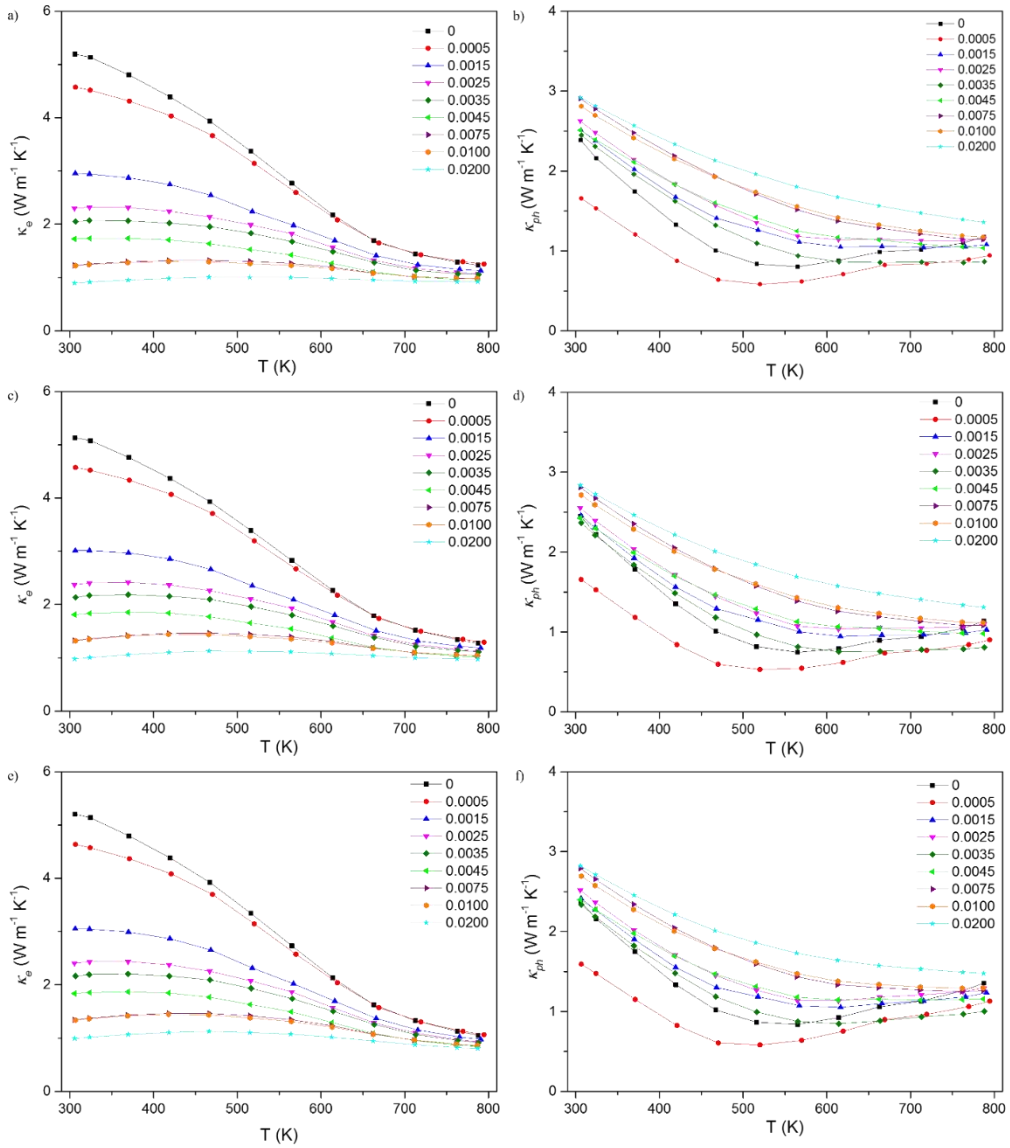

Figure 3.43: Temperature dependence of the a) electronic thermal conductivity κ_e (SPB model) b) lattice thermal conductivity κ_{ph} (SPB model) c) electronic thermal conductivity κ_e (TI-TVB model) d) lattice thermal conductivity κ_{ph} (TI-TVB model) e) electronic thermal conductivity κ_e (TD-TVB model) and f) lattice thermal conductivity κ_{ph} (TD-TVB model) of the series $Sn_{1.03-x}In_xTe$.

Hence, it seems that neither a single-parabolic-band model nor a two-valence-band model with temperature-dependent (or independent) band parameters provides a satisfying approach to determine L. These three models tend to overestimate L giving rise to large differences in κ_{ph} among the samples, which are not expected given the very low Sn vacancy concentration in $Sn_{1.03}Te$ (estimated to be around 0.25%)[24] and the narrow In concentration range investigated herein. In addition, none of these models capture well the change in the transport regime observed above 500 K, the temperature above which the second heavy-valence band plays a significant role on the electronic conduction and hence, on L.

Considering as valid the hypothesis that the effect of alloying with In up to x = 0.02 hardly affects κ_{ph}, the strong increase in ρ with x then provides an alternative approach to estimate experimentally the temperature dependence of L in the present case. The weak temperature dependence of κ and the absence of significant upturn in α above 500 K in the x = 0.02 sample further suggests a negligible role of the second heavy-hole valence band. Assuming that the L values calculated for the x = 0.02 sample yield a correct estimate of κ_{ph}, we used the same κ_{ph} values to calculate the temperature dependence of κ_e expected for the other samples (Figure 3.44).

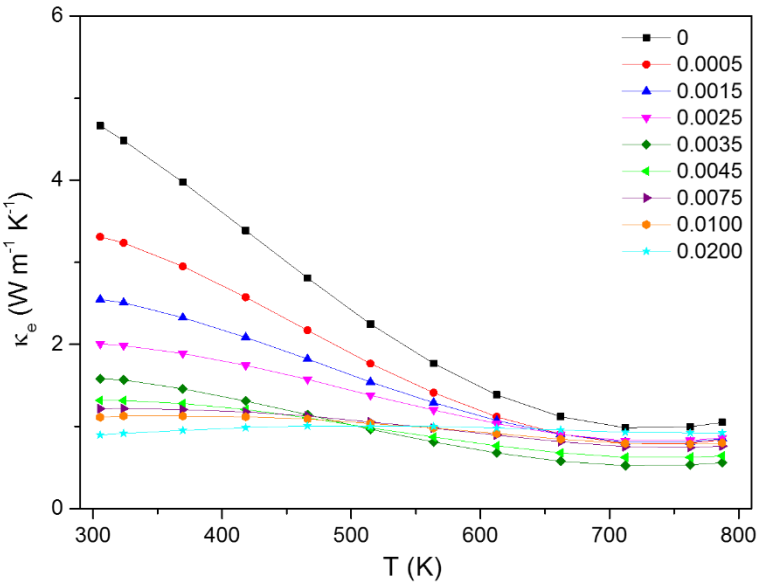

Figure 3.44: Electronic thermal conductivity κ_e evaluated by subtracting the lattice thermal conductivity κ_{ph} of the x = 0.02 sample from κ which is assumed to be constant across the series.

Following this approach, the expected temperature dependences of L were derived from $\kappa_e(T)$ for all samples (Figure 3.45). Except for the x = 0.02 sample, the L values are strongly temperature dependent and drop well below the non-degenerate limit of 1.5×10^{-8} V^2 K^{-2} expected for acoustic phonon scattering. For the x = 0.0035 sample, L even reaches 0.8×10^{-8} V^2 K^{-2} above 600 K. The upturn in L observed at high temperatures for low doping levels is likely an artifact, possibly due to minority carrier activation across the band gap of 0.18 eV. These results show that the Lorenz numbers should be significantly lower than those predicted by simple transport models to obtain consistent estimates of κ_{ph} across the entire series of samples. Such low values likely reflect the multiband character of the valence bands which has been shown to give rise to significant deviations from the L values expected in single-band systems.[95,96]

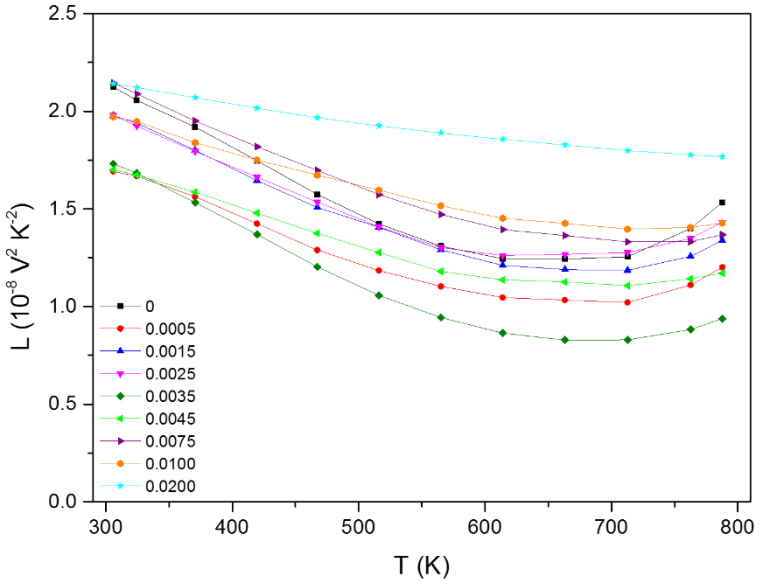

Figure 3.45: Temperature dependence of the Lorenz number L for the $Sn_{1.03-x}In_xTe$ samples ($0 \leq x \leq 0.02$) predicted using the Wiedemann–Franz law. The electronic thermal conductivity κ_e was evaluated by subtracting from κ the lattice thermal conductivity κ_{ph} of the x = 0.02 sample assumed to be constant across the series. The solid lines are guides to the eye.

In addition, because the relaxation time strongly depends on energy when the chemical potential nears the RL due to its significant width in energy (see Figure 3.5), scattering of the carriers becomes strongly inelastic, thereby leading to significant variations in the Lorenz number. In particular, this effect has been discussed in the PbTe:Tl compounds for which, large

deviations of L from its degenerate limit has been shown to occur depending on the position of the chemical potential with respect to the resonant-band center (that is, $\Delta/2$).[76] The fact that the largest deviations of L are observed in the x = 0.0035 sample, which features the most pronounced RL effect, is an intriguing indication that the RL has a strong impact on the Lorenz number. It is thus likely that these two combined effects are responsible for the anomalous Lorenz numbers inferred and provide a consistent explanation of the large differences in the L values observed from sample to sample despite the very narrow In composition range covered in this series.

The temperature dependence of the ZT values, shown in Figure 3.46, evidences a clear increase at 800 K upon substituting In for Sn. A maximum ZT value of 0.75 is achieved for x = 0.0035 which represents an increase of 35 % compared to the ZT value of the pristine sample $Sn_{1.03}Te$. This peak value is lower than that achieved by Zhang *et al.* due to the lower total thermal conductivity achieved by a reduction of the grain size via ball-milling.[1] In our case, the significant increase observed in the ρ values with increasing x is the main limiting factor that prevents higher peak ZT values from being achieved at higher In concentrations.

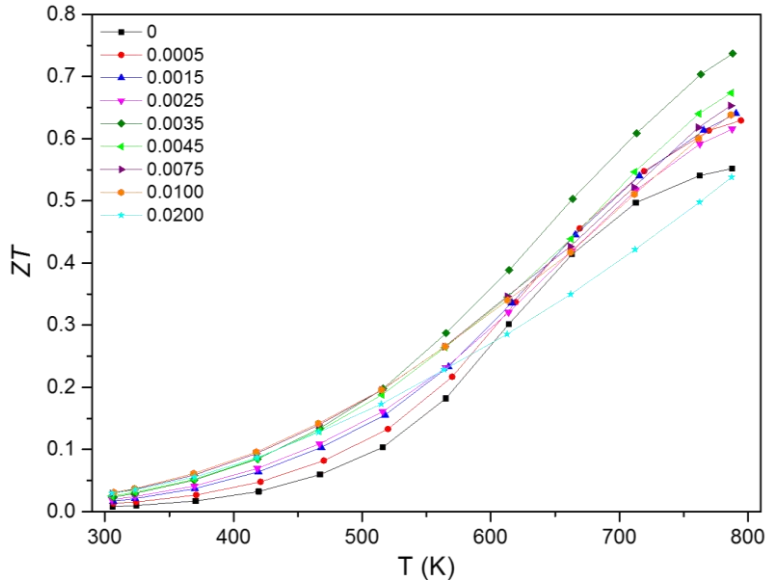

Figure 3.46: Dimensionless thermoelectric figure of merit ZT as a function of temperature for the $Sn_{1.03-x}In_xTe$ samples ($0 \leq x \leq 0.02$). The solid lines are guides to the eye.

However, interestingly, the average ZT value, ZT_{avg}, an important parameter for practical applications determined by integrating with respect to temperature over an extended

temperature range,[97] is maximized in the x = 0.0035 sample. The average ZT of these samples was calculated using the following equation:

Equation 3.11:

$$ZT_{avg} = \frac{\int_{T_L}^{T_H} ZT(T)dt}{T_H - T_L}$$

where T_H and T_L are the high and low temperature of the range over which ZT_{avg} was calculated.

Compared to the pristine sample where $ZT_{avg} = 0.45$ over the 600 – 800 K temperature range, a concentration as low as x = 0.0035 is sufficient to increase this value to 0.58 over the same temperature range (Table 3.4). This result shows that the weak temperature dependence of the RL helps to enhance ZT_{avg} even though the increase in the peak ZT value is moderate.

Table 3.4: Average ZT values calculated over the 300 – 600 K and 600 – 800 K temperature ranges for all samples.

Indium content (x)	**Average *ZT***	
	300 - 600 K	**600 – 800 K**
0.0	0.09	0.46
0.0005	0.11	0.51
0.0015	0.12	0.51
0.0025	0.13	0.49
0.0035	0.15	0.58
0.0045	0.15	0.52
0.0075	0.15	0.50
0.0100	0.15	0.49
0.0200	0.13	0.41

3.4.3.3 Transport properties for $Sn_{1-x}In_xTe$ ($0.05 \leq x \leq 0.4$)

The temperature dependence of the electrical resistivity for the series $Sn_{1-x}In_xTe$ below and above room temperature are presented in Figure 3.47. All the samples exhibit metallic behavior consistent with their degenerate nature. In agreement with the results obtained for

samples with $x \leq 0.02$, room-temperature values increase with increasing the In concentration. However, this holds true only up to $x = 0.05$. A maximum value of 9.55 μΩm at 300 K was obtained for $x = 0.05$ above which the samples become more metallic with ρ systematically decreasing down to 2.39 μΩm for $x = 0.40$ at 300 K (see Figure 3.47 (a)). Furthermore, as already mentioned in the case of the $x = 0.02$ sample at high temperatures, no clear evidence of the role of a second valence band is observed. In this In concentration range, ρ exhibits a nearly-linear dependence throughout the temperature range. At 800 K, the absence of a second valence band leads to lower ρ values when compared to $x = 0.02$ (Figure 3.47 (b)).

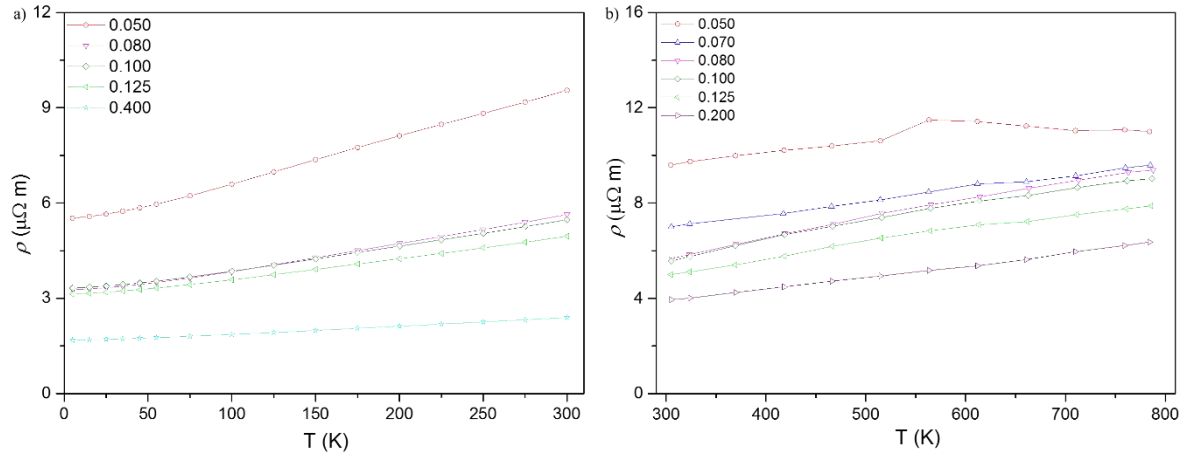

Figure 3.47: a) Below and b) Above ambient temperature dependence of electrical resistivity for samples in $Sn_{1-x}In_xTe$ series. The solid lines are guide to the eye.

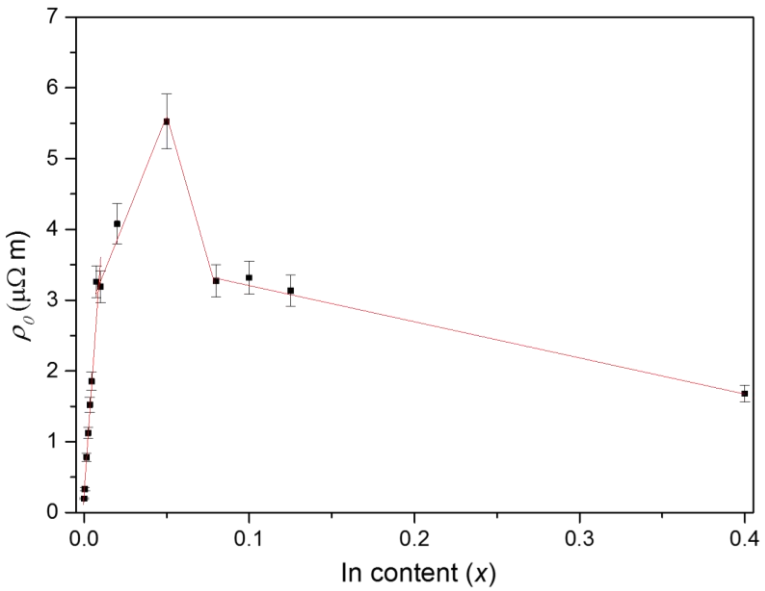

Figure 3.48: Compositional dependence of the residual electrical resistivity ρ_0 measured at 5 K for the two series of samples synthesized. The red solid lines are guides to the eye. An error bar of 7% has been included.

At lower temperatures, as the In content approaches 40%, ρ appears less temperature-dependent (Figure 3.47 (a)). The residual electrical resistivity values ρ_0, measured at 5 K, for the two series of samples are plotted with respect to the In content (Figure 3.48). We can divide the entire range of samples into two main regimes; below and above x = 0.05. Below x = 0.05, the ρ_0 values significantly increases with a maximum of 5.55 μΩm achieved for x = 0.05. Above this In content, the ρ_0 value drops when x increases to 0.075 and then smoothly decreases to 1.68 μΩm for the x = 0.40 sample.

As made previously, the temperature dependence of the electrical resistivity ρ at low temperatures were normalized to the room-temperature values (Figure 3.49). The sudden change in the slope or a kink that corresponds to the ferroelectric structural phase transition is hardly visible in this In concentration range. In an attempt to identify the transition temperature T_{FT}, we used to the same approach consisting in plotting the temperature dependence of the first derivative of the electrical resistivity. The midpoint of the change in the first derivative was then considered as the transition temperature. Weak anomalies could be only observed in the x = 0.05 and 0.08 samples (not shown) suggesting ferroelectric transition temperatures of ~ 40 K and ~ 19 K, respectively. This strong decrease in the transition temperature is in good agreement with the literature, showing that it smoothly reduces as the In content increases before vanishing for samples above $x \geq 0.1$.[43,47,81] Strong variations from sample to sample is observed confirming that the presence of enhanced disorders plays an important role in the charge transport as the In content increases.

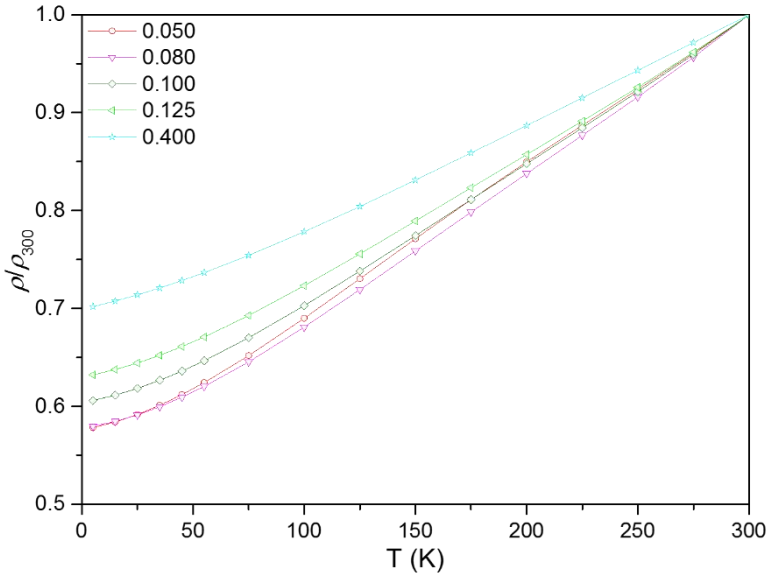

Figure 3.49: Temperature dependence of the electrical resistivity normalized to the 300 K values for samples in $Sn_{1-x}In_xTe$ series. The solid lines are guide to the eye.

As mentioned previously, In-doped SnTe has been shown to undergo a superconducting transition.[34,39,73,81–86] Hence, additional electrical resistivity measurements down to 1.9 K were performed for the x = 0.08, 0.125 and 0.4 samples.

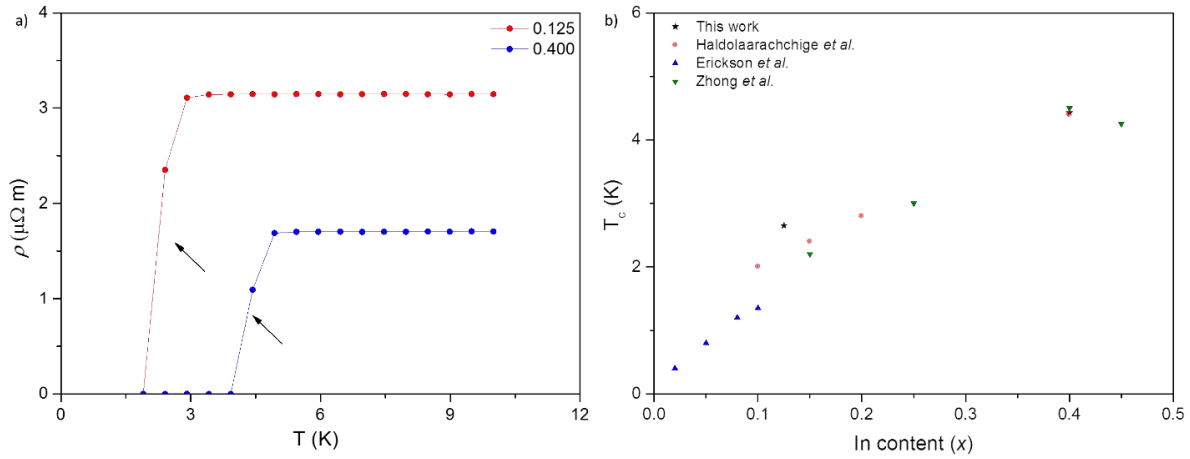

Figure 3.50: a) Temperature dependence of the electrical resistivity ρ for the x = 0.125 and 0.40 samples exhibiting a superconducting transition. The solid lines are guide to the eye. Black arrow depicts the transition temperature and b) Comparison of the superconducting transition temperature T_c for various polycrystalline $Sn_{1-x}In_xTe$ samples.[34,35,39]

We have defined the critical temperature as the mid-point between the onset of the decrease in ρ and the point where ρ reaches zero (black arrows in Figure 3.50 (a)). Superconductivity emerges in these last two samples while no evidence of superconductivity was observed in the x = 0.08 sample (not shown). In the earlier work, Erickson *et al.* confirmed that the critical temperature should be around 1.2 K for x = 0.08.[39] As mentioned before, due to the use of ^4He in our measurement system, we were not able to measure the electrical resistivity below 1.9 K to confirm this point. For x = 0.125, a critical temperature of ~ 2.65 K was obtained which increases to a value as high as ~ 4.4 K for x = 0.40 (Figure 3.50 (a)). These values are in good agreement with those reported in the literature as can be seen in Figure 3.50 (b).[34,35,39] A typical transition width of ~ 1 K is observed for both samples due to their polycrystalline nature, which usually tends to broaden this transition.[39,83] It is worth mentioning that there is no indication of any relation between the ferroelectric transition temperature and superconducting critical temperature. These two phenomena can be thus considered as two independent phenomena, as already suggested by Erickson *et al.*[39]

The temperature dependence of the thermopower for all samples is shown in Figure 3.51 at low and high temperatures. The α values strongly decreases with increasing the In content,

indicative of an increase in the metallic character of transport. A maximum α value of 41.5 μV K^{-1} is obtained at 300 K for the x = 0.05 sample, which is lower than that measured for the x = 0.02 sample (51.5 μV K^{-1}). Upon cooling, the thermopower decreases smoothly with temperature down to around 75 K. Below this temperature, a non-linear behavior is observed for all samples, similar to what is observed in the binary $Sn_{1.03}Te$ (see Figure 3.36). This non-linear trend strengthens with increasing the In content, as already observed for the binary sample and attributed to the possible presence of a phonon-drag contribution.[54] It is worth mentioning here that no crossover to negative values was observed for any of the samples with α values remaining positive in the entire temperature range. At 800 K, the α values follow a similar trend with a decrease occurring with increasing the In content. Of note, similar to the electrical resistivity measurements, no evidence of the presence of a second band is observed at high temperatures. In contrast, for all samples, α evolves linearly with temperature down to 2.8 μV K^{-1} for the x = 0.30 sample.

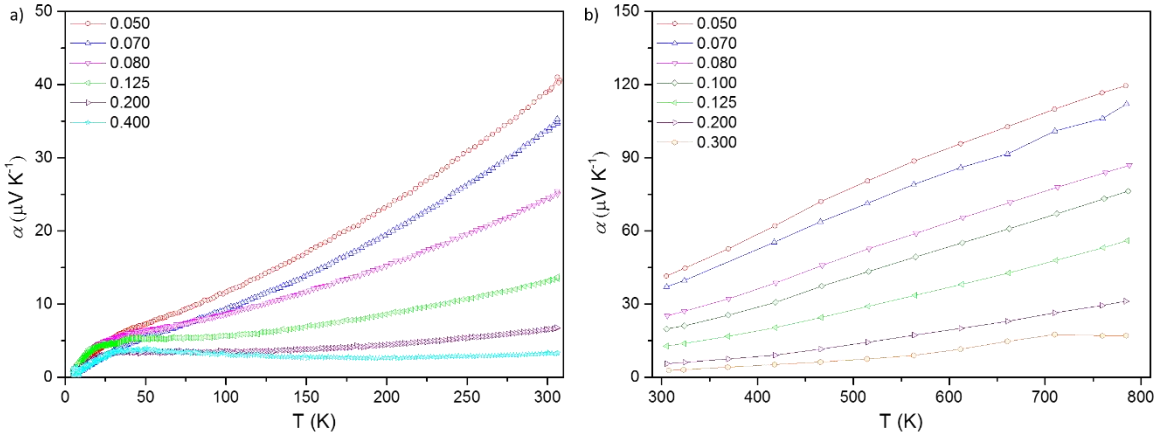

Figure 3.51: a) Low and b) high-temperature temperature dependence of the thermopower for the $Sn_{1-x}In_xTe$ series. The solid lines are guides to the eye.

At high temperatures, due to the lower α values and the decreasing electrical resistivity values, the power factor of all samples are lower than that achieved in the x = 0.02 sample (Figure 3.52).

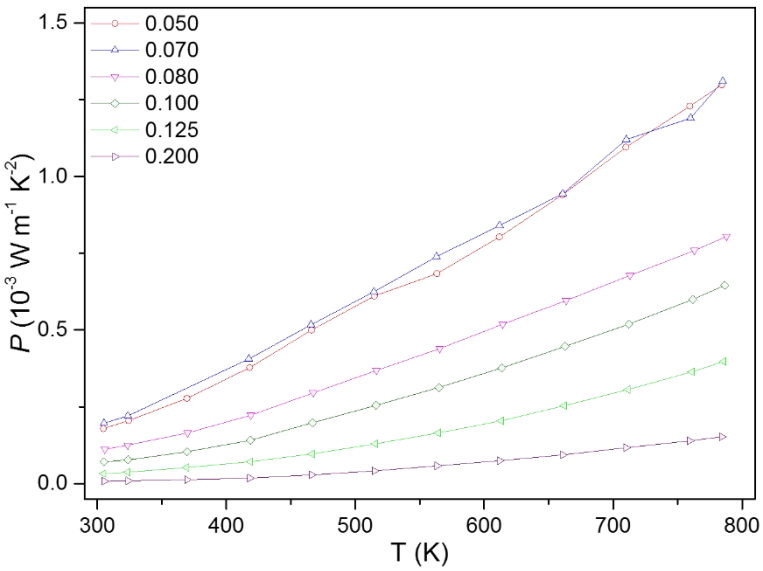

Figure 3.52: High temperature dependence of power factor for samples of $Sn_{1-x}In_xTe$ series. The solid lines are guide to the eye.

Figure 3.53 (a) shows the temperature dependence of the hole concentration. Similar to samples with In concentrations of up to 2%, the carrier concentration of all these samples hardly evolve with temperature, confirming their degenerate nature. The overall trend is similar, with the hole concentration increasing with increasing the In content to reach a maximum value of 3.4×10^{21} cm^{-3} for x = 0.125 at 300 K. Figure 3.53 (b) show the room temperature values of the hole concentration as a function of the In content up to x = 0.20. In acting as an acceptor impurity in SnTe holds true for the entire series as the hole concentration monotonically increases with increasing the In content. Up to 12.5%, the Hall data exhibit a positive sign suggesting that holes are the dominant charge carriers in these samples. Above x = 0.20, however, significant changes upon cooling occurs. In addition to an increase in the hole concentration to about 7.9×10^{21} cm^{-3} at 300 K, the sign of the Hall signal turns into negative between 75 and 55 K, indicative of a dominant electron-like contribution in this temperature range. Within a single carrier picture, the Hall data corresponds to an electron concentration of 1.6×10^{21} cm^{-3} at 35 K (Figure 3.53 (c)). For x = 0.40, the Hall signal remains electron-like throughout the temperature range giving a value of 2.97×10^{22} cm^{-3} at 300 K. This value does not significantly change with temperature giving a near-residual value of 2.02×10^{22} cm^{-3} at 15 K (see Figure 3.53 (c)). This crossover from positive to negative Hall data may be due to the appearance of electron pockets in the Brillouin zone as x increases. The fact that they dominate the Hall signal further suggests that these electrons are highly mobile. Because high In contents

likely modifies the electronic band structure beyond a rigid-band approximation, further calculations may help to determine the origin of this behavior.

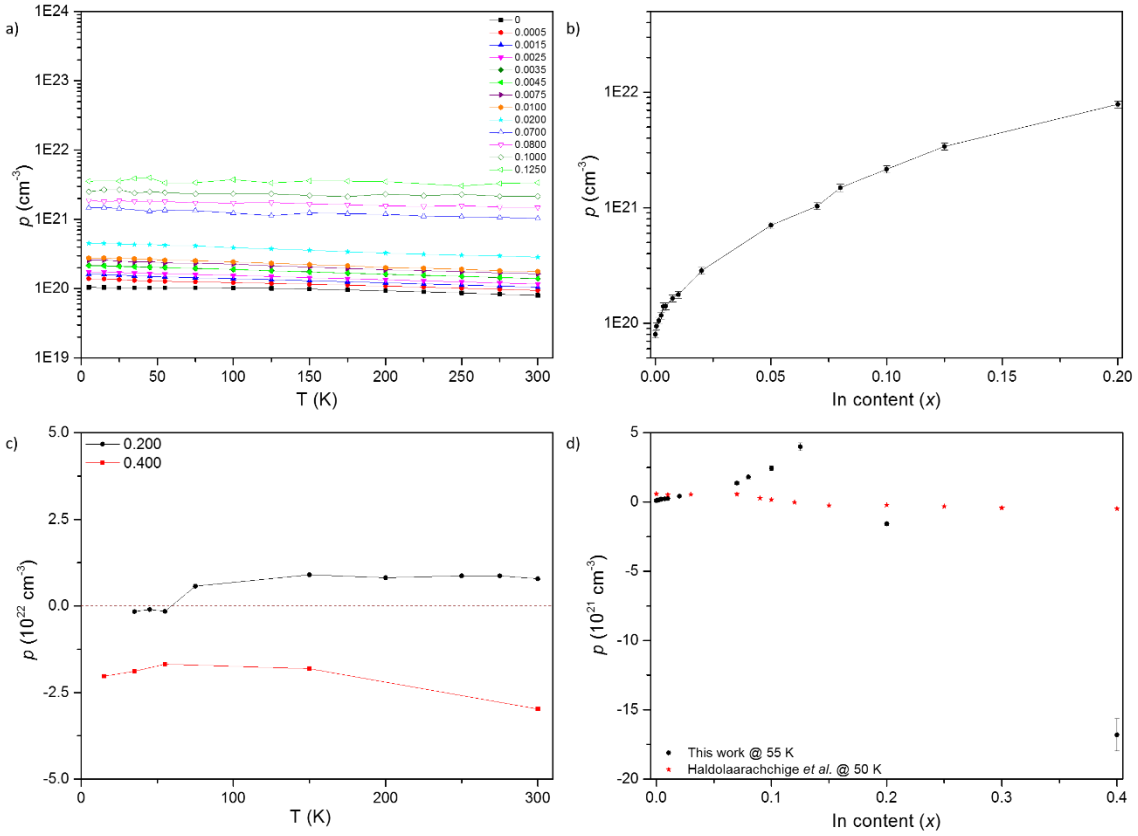

Figure 3.53: a) Temperature dependence of the hole concentration for the entire In doped SnTe series. b) Carrier concentration as a function of the In content at room temperature for the entire In doped SnTe series (An error bar of 7% is included). c) Carrier concentration for the x = 0.20 and 0.40 samples evidencing the transition from p to n-type. d) Carrier concentration as a function of the In content at 55 K compared with the values reported in the literature.[34] (An error bar of 7% is included). The solid lines are guide to the eye.

We note that similar results have been reported by Haldolaarachchige *et al.*, showing that this crossover is a robust phenomenon inherent to samples with high In contents.[34] To further investigate this surprising crossover, a comparison with the polycrystalline samples prepared by Haldolaarachchige *et al.* was considered. The carrier density measured at ~ 55 K was plotted as a function of the In content (Figure 3.53 (d)). A small difference in the carrier density is observed between our and their binary samples, due to differences in the starting chemical composition and synthesis techniques. The major difference between the two studies is the In content where the positive-to-negative crossover occurs. While Haldolaarachchige *et al.*

observed a *p*-to-*n*-type transition at around $x = 0.10 – 0.12$, we observe this transition around $x = 0.20$. This is a strong indication and confirmation that In acts as a single hole dopant, that is, is in a In^{1+} valence state up to about $x = 0.125$. This point is confirmed by the increase in the carrier concentration up to this concentration.[34] However, above this concentration, it cannot be excluded that an additional contribution coming from In^{3+} species is present since the carrier density tends to decrease suggesting the presence of an increasing electron contribution. It is thus probable that contributions of both In^{1+} and In^{3+} exist at these high In contents, a point that would nevertheless need further experimental and theoretical confirmation.

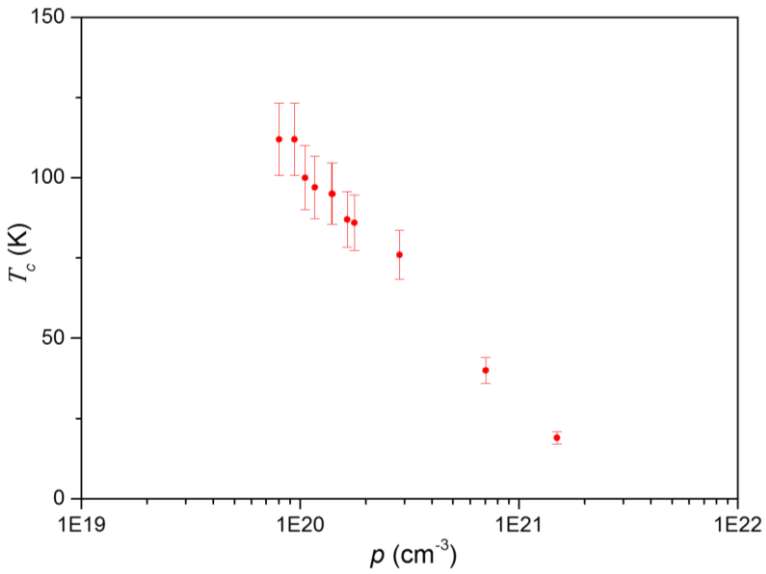

Figure 3.54: Evolution of the ferroelectric transition temperature with respect to the carrier concentration for the entire In doped SnTe series. (An error bar of 10% is included).

The dependence of the ferroelectric transition temperature as a function of the measured carrier density is shown in Figure 3.54. A nearly-linear trend is observed with the transition temperature T_c decreasing with increasing the carrier concentration before disappearing for $x = 0.10$. From this dependence, it can be estimated that the ferroelectric transition should disappear at a carrier density of around 2.5×10^{21} cm^{-3}. It is important to mention that this limit differs from that estimated in several previous studies reported in the literature. This is likely due to several factors such as the different techniques used to determine this limit (Raman spectroscopy, Inelastic neutron scattering, Neutron Bragg reflection, X-ray Diffraction, etc.), the nature of the samples measured (polycrystals or single crystals), the amount of vacancies present in the synthesized samples, etc.[39,43,47–49,81]

The temperature dependence of the Hall mobility μ_H is shown in Figure 3.55 (a). Similar to other samples, the μ_H values keeps on decreasing with increasing the In content up to x = 0.125. $\mu_H(T)$ follows a $\sim T^0$ law for In contents higher than 5% suggesting that the scattering mechanism is unchanged upon increasing x and that ionized impurities remain the main scattering mechanism. Figure 3.55 (b) shows the μ_H values measured at 300 K as a function of the In content. μ_H monotonically decreases with increasing x. However, the strong decrease observed at low In contents due to the RL is strongly lessened above x = 0.05. Above this In content, the hybridization of the In states and the SnTe states has likely led to the disappearance of the DOS hump. Thus, the effect of RL is no longer present.

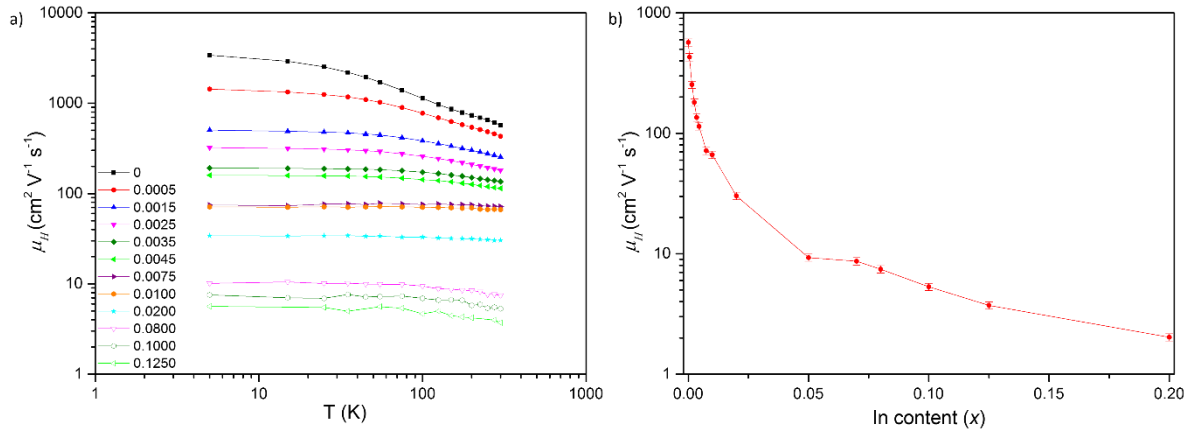

Figure 3.55: Hall mobility as a function of a) temperature for the entire In doped SnTe series and b) the In content x at 300 K for the entire In doped SnTe series (an error bar of 7% is included). The solid lines are guide to the eye.

The Ioffe-Pisarenko plot for all the samples is presented in Figure 3.56. For comparison purposes, we have added the samples of both series. However, at high In contents, whether or not a two-valence band is still pertinent remains an open question even if our data nicely fits the predictions of the two-bands model. Given the significant changes observed at low temperatures in the Hall data, it is likely that high In doping levels induce severe modifications of the electronic band structure. With due care due to this important point, these data confirm that the maximum RL effect is obtained for an In content of 2%. Above this value, the thermopower decreases with further increasing the In content, which may be understood as a broadening of the DOS peak induced by the RL due to a stronger hybridization of the In states with those of the host framework. Additionally, the chemical potential may have concomitantly moved away from the DOS peak.[40,41,89]

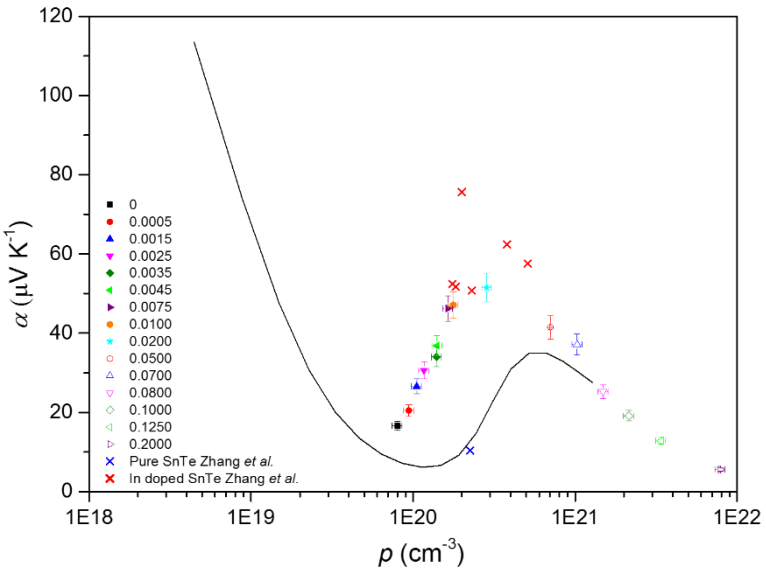

Figure 3.56: Ioffe-Pisarenko plot for samples up to x = 0.40. The x = 0.02 provides the best compromise between In-induced RL and thermopower values. (Error bars of 7% have been included for both axes). The values obtained in this work are compared with the values measured by Zhang *et al.*[1]

As mentioned above, the fact that the samples with high In contents seem to closely follow the Ioffe-Pisarenko plot for carrier concentrations above 10^{21} cm^{-3} may be fortuitous. These samples may in fact follow another curve corresponding to a different band structure model such as, for instance, a single parabolic or non-parabolic band model. Additional electronic band structure calculations would be interesting to determine which of these models would best describe these data.

Figure 3.57 shows the Hall mobility as a function of the hole concentration at three different temperatures 300, 75 and 5 K. Regardless of the temperature, these data evidence the strong decrease in μ_H with increasing the In content for hole concentrations below 10^{21} cm^{-3}. Above this concentration, which roughly corresponds to samples with high In contents, the decrease in μ_H is weaker. Interestingly, a kink can be observed at around 3×10^{20} cm^{-3} where the slope of the $\mu_H(p)$ curves changes at all temperatures. This anomaly, as suggested by Kobayashi *et al.*, may be due to subsidiary valleys in the valence bands in agreement with the literature.[81,98]

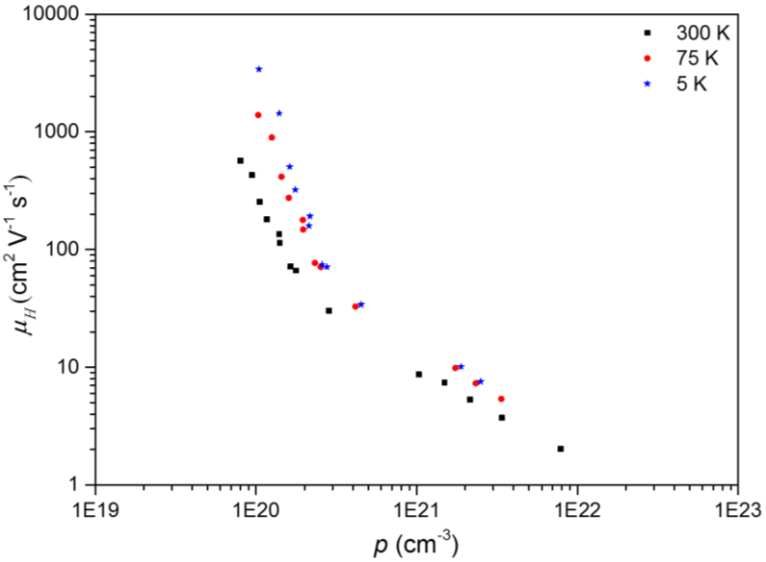

Figure 3.57: Hall mobility μ_H as a function of the hole concentration p at 300 K, 75 K and 5 K.

Figure 3.58 shows the temperature dependence of total thermal conductivity κ below 300 K. A clear trend at room temperature is observed with κ increasing to a value of 4.6 W m^{-1} K^{-1} for x = 0.40. This trend, however, no longer holds upon cooling. The Umklapp peak near 35 K, first increases on going from x = 0.05 to x = 0.08, before tending to decrease with further increasing x up to x = 0.40. At this highest In concentration, the Umklapp peak is no longer visible due to the strongly enhanced disorder induced by the high In content.

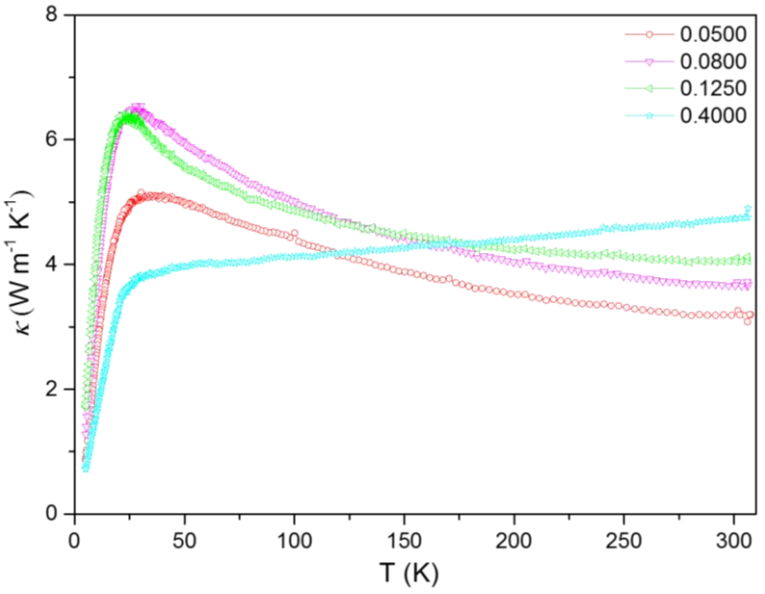

Figure 3.58: Low temperature dependence of the total thermal conductivity for $Sn_{1-x}In_xTe$ series.

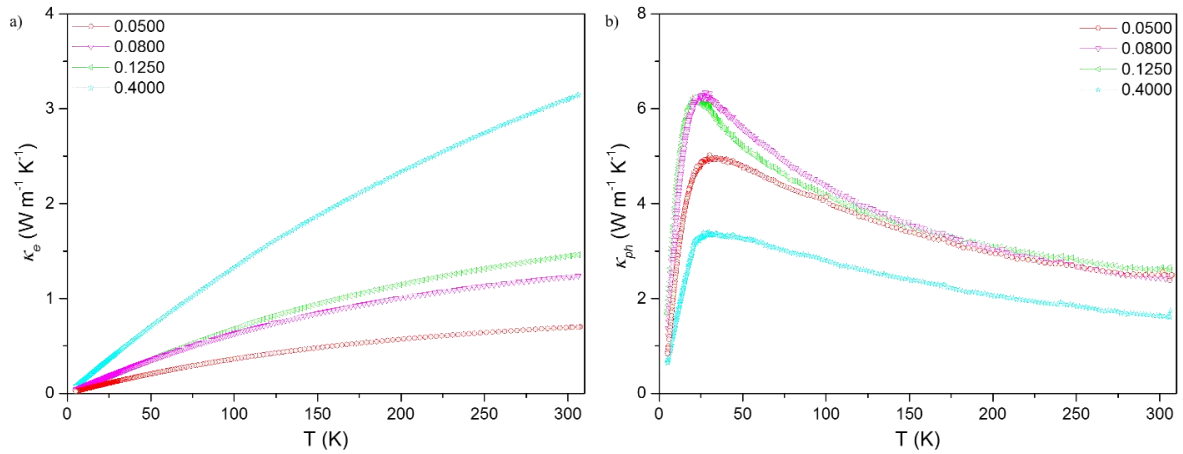

Figure 3.59: a) Electronic and b) lattice thermal conductivity computed by Wiedemann-Franz law using the Lorenz numbers calculated by a single parabolic band model.

Figures 3.59 depicts the electronic and lattice contributions of the thermal conductivity calculated using the Wiedemann-Franz law. The Lorenz numbers have been estimated using a single parabolic band model similar to the one used in the previous sections of this chapter. As expected from the high electrical resistivity values measured in these samples, the main contribution to the thermal conductivity comes from the lattice thermal conductivity κ_{ph}.

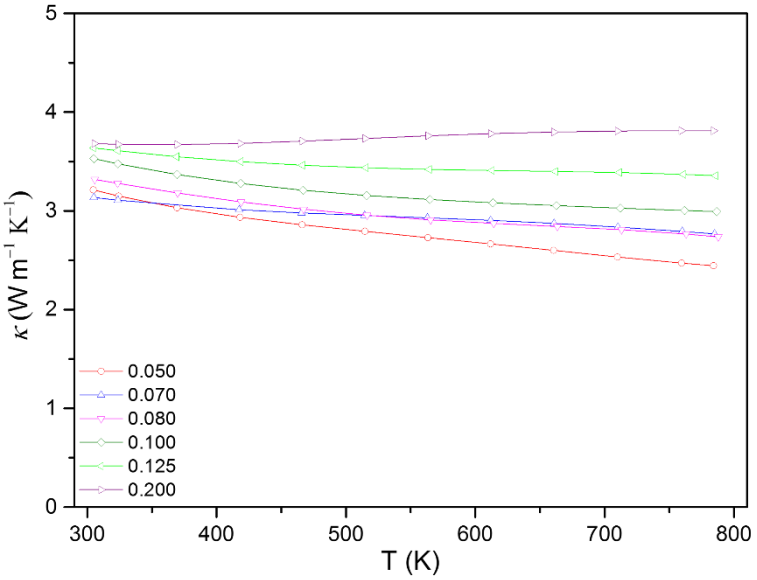

Figure 3.60: Temperature dependence of the total thermal conductivity κ at high temperatures for $Sn_{1-x}In_xTe$ series. The solid lines are guide to the eye.

The temperature dependences of κ, κ_e and κ_{ph} above 300 K are shown in Figure 3.60 and 3.61. The κ values are quite low and nearly temperature-independent for high In

concentrations. A small difference in the κ values can be observed at 300 K in Figures 3.58 and 3.60 due to the two different set-ups used to perform these measurements. κ_{ph} and κ_e have been determined by using a single-parabolic band model to calculate the Lorenz number. At 300 K, κ_e increases with increasing x. As at low temperatures, the main contribution to the thermal conductivity comes from κ_{ph} which tend to decrease and saturate for all the samples in this series. At 800 K, due to the metallic behavior of these samples, the contribution of κ_e increases as the In content increases.

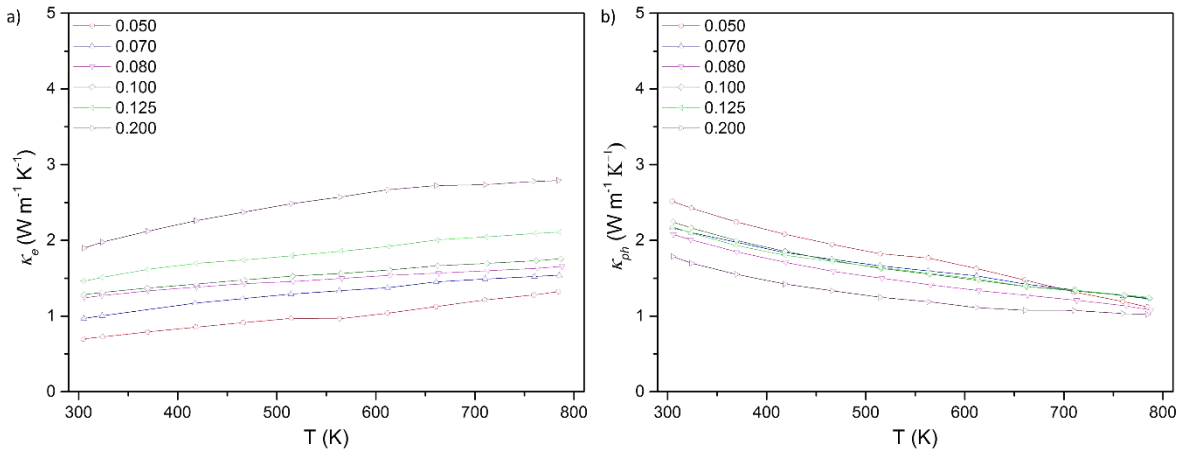

Figure 3.61: a) Electronic and b) lattice thermal conductivity κ_e as a function of temperature calculated using the Lorenz numbers calculated by a single parabolic band model.

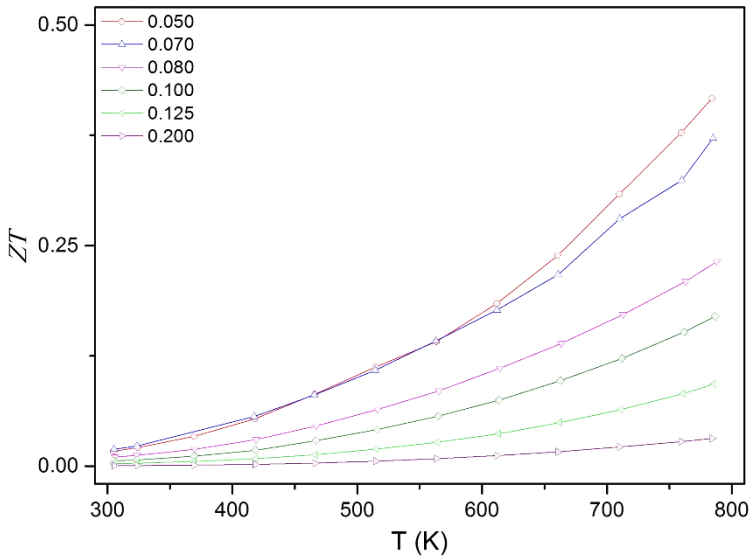

Figure 3.62: *ZT* values as a function of temperature for samples of the $Sn_{1-x}In_xTe$ series. The solid lines are guide to the eye.

Figure 3.62 shows the *ZT* values of the different samples at high temperatures. A maximum *ZT* of ~ 0.42 is achieved for $x = 0.05$ sample at 785 K. This value is lower than those obtained for samples containing lower In contents which show a peak *ZT* of 0.75 for $x = 0.0035$ sample. Above $x = 0.05$, the *ZT* values systematically decrease with increasing the In content to reach a modest value of ~ 0.03 for $x = 0.20$.

3.5 Conclusion

In this Chapter, we have reported an in-depth, combined theoretical and experimental investigation of the influence of the In-induced RL on the low- and high-temperature transport properties of the $Sn_{1.03}Te$ compound. The large number of samples synthesized, with In concentration varying from 0.05% up to 40%, enabled us to show that, despite the very low substitution levels probed herein, the transport properties are strongly sensitive to the In concentration. For $x \leq 0.05$, the main characteristics of the variations with x can be well explained within an In-induced resonant-level scenario, conforming to the main predictions of our electronic band structure calculations performed using the KKR-CPA method.

At low temperatures, our results further evidenced a complex evolution of the low-temperature thermopower α with x. A surprising crossover from positive to negative values that sets in near 100 K exists over a narrow In concentration range $0.0015 \leq x \leq 0.0045$. The magnetic field dependence of $\alpha(\mu_0 H)$, measured for the $x = 0.0035$ sample, nevertheless suggests a dominant hole-like response, as indicated by the progressive shift of α towards positive values with increasing $\mu_0 H$ up to 14T. The presence of negative α values over restricted temperature and compositional ranges are strikingly similar to those observed in Tl-doped PbTe. However, unlike $Pb_{1-x}Tl_xTe$ where the disproportionation of Tl into Tl^{1+} and Tl^{3+} has been confirmed experimentally, the x dependence of the hole concentration suggests that In behaves as a hole dopant (that is, In is in a In^{1+} valence state). Because such a valence fluctuation mechanism has been shown to provide a superconducting pairing interaction and a charge Kondo effect, these results require further investigations to determine whether a valence-skipping scenario is equally applicable to In-doped SnTe. Therefore, the series $Sn_{1.03-x}In_xTe$ with very low doping levels provides another valuable system where these theoretical scenarios may be further tested. Photoemission spectroscopy and sub-kelvin specific heat & electrical resistivity measurements will be some key experiments to clarify the valence state of In atoms and determine whether superconductivity already emerges at these low doping levels.

At high temperatures, significant differences were observed with a stepwise increase with x in the thermopower and electrical resistivity. Compared to prior studies on In-substituted SnTe, the maximum power factor is shifted towards higher In concentrations due to the Sn self-compensation used herein. This difference highlights the needs to adjust the carrier concentration in RL-containing systems so that the position of the chemical potential is optimized against that of the RL. The progressive increase in the In content has also a profound influence on the thermal transport with a clear evolution in the temperature dependence of the total thermal conductivity as x increases. In particular, the strong increase in ρ with x enabled us to shed light on the difficult task to correctly evaluate the Lorenz number in SnTe due to the multiband nature of the top of its valence bands. Based on a set of reasonable assumptions, our analysis unraveled very low Lorenz numbers that even drop below the non-degenerate limit. This result highlights that, despite the high degeneracy of the charge carrier gas, the multiband character of the electronic bands and the presence of the RL combine to significantly lower the Lorenz numbers above 300 K, making it difficult to adequately estimate the lattice thermal conductivity. Although the beneficial influence of the RL observed at 300 K is somewhat lessened at 800 K, an increase in the ZT values is nevertheless obtained with a peak value of 0.75 at 800 K for x = 0.0035, which represents an increase of 35% compared to $Sn_{1.03}Te$. Another important consequence of the RL for practical applications is its weak temperature dependence that yields a higher average ZT value compared to $Sn_{1.03}Te$.

For In concentrations higher than x = 0.05, our experimental data show that the RL has very likely disappeared. Although the transport properties evolve smoothly towards a more metallic character with increasing x, high In contents probably strongly modify the electronic band structure. These modifications are notably highlighted by the crossover in the Hall data from positive to negative Hall coefficients. While the exact origin of this behavior remains unsettled, it may be due to the development of electron pockets in the Brillouin zone with increasing x. In this regard, further measurements of the transport properties of these samples under high magnetic field may provide further evidence in favor of this scenario. In agreement with prior studies on samples containing high In concentrations, superconductivity emerges at low temperatures with critical temperatures increasing with x to reach a maximum of 4.4 K in the x = 0.40 sample, in agreement with the literature data.

Finally, the sensitivity of the transport properties to the concentration of the RL impurity further evidences that the combination of an RL impurity with a co-doping element should be carefully chosen to avoid the shift of the chemical potential away from the RL or the disappearance of the RL due to band structure modifications induced by the second element.

References

1. Zhang, Q., Liao, B., Lan, Y., Lukas, K., Liu, W., Esfarjani, K., Opeil, C., Broido, D., Chen, G. & Ren, Z. High thermoelectric performance by resonant dopant indium in nanostructured SnTe. *Proceedings of the National Academy of Sciences* **110,** 13261 (2013).
2. Heremans, J. P., Wiendlocha, B. & Chamoire, A. M. Resonant levels in bulk thermoelectric semiconductors. *Energy Environ. Sci.* **5,** 5510 (2012).
3. Friedel, J. On some electrical and magnetic propoerties of metallic solid solutions. *Canadian Journal of Physics* **34,** 1190 (1956).
4. Blatt, F. J., Schroeder, P. A., Foiles, C. L. & Greig, D. *Thermoelectric Power of Metals*. (Plenum Press, New York, 1976).
5. Nemov, S. A. & Ravich, Y. I. Thallium dopant in lead chalcogenides: investigation methods and peculiarities. *Physics-Uspekhi* **41,** 735 (1998).
6. Volkov, B. A., Ryabova, L. I. & Khokhlov, D. R. Mixed-valence impurities in lead telluride-based solid solutions. *Physics-Uspekhi* **45,** 819–846 (2002).
7. Ravich, Y. I. in *CRC Handbook of thermoelectrics* (ed. Rowe, D. M.) (CRC Press, 1995).
8. Mahan, G. D. & Sofo, J. O. The best thermoelectric. *Proceedings of the National Academy of Sciences* **93,** 7436 (1996).
9. Heremans, J. P., Jovovic, V., Toberer, E. S., Saramat, A., Kurosaki, K., Charoenphakdee, A., Yamanaka, S. & Snyder, G. J. Enhancement of Thermoelectric Efficiency in PbTe by Distortion of the Electronic Density of States. *Science* **321,** 554 (2008).
10. Wu, L., Li, X., Wang, S., Zhang, T., Yang, J., Zhang, W., Chen, L. & Yang, J. Resonant level-induced high thermoelectric response in indium-doped GeTe. *NPG Asia Materials* **9,** e343 (2017).
11. Wiendlocha, B., Vaney, J.-B., Candolfi, C., Dauscher, A., Lenoir, B. & Tobola, J. An Sn-induced resonant level in β-As_2Te_3. *Physical Chemistry Chemical Physics* **20,** 12948 (2018).
12. König, J. D., Nielsen, M. D., Gao, Y.-B., Winkler, M., Jacquot, A., Böttner, H. & Heremans, J. P. Titanium forms a resonant level in the conduction band of PbTe. *Physical Review B* **84,** 205126 (2011).
13. Wiendlocha, B. Fermi surface and electron dispersion of PbTe doped with resonant Tl impurity from KKR-CPA calculations. *Physical Review B* **88,** 205205 (2013).

14. Wiendlocha, B. Thermopower of thermoelectric materials with resonant levels: PbTe:Tl versus PbTe:Na and $Cu_{1-x}Ni_x$. *Physical Review B* **97,** 205203 (2018).
15. Wiendlocha, B. Localization and magnetism of the resonant impurity states in Ti doped PbTe. *Applied Physics Letters* **105,** 133901 (2014).
16. Kim, S., Wiendlocha, B., Jin, H., Tobola, J. & Heremans, J. P. Electronic structure and thermoelectric properties of p-type Ag-doped Mg_2Sn and $Mg_2Sn_{1-x}Si_x$ (x = 0.05, 0.1). *Journal of Applied Physics* **116,** 153706 (2014).
17. Faulkner, J. S. & Stocks, G. M. Calculating properties with the coherent-potential approximation. *Physical Review B* **21,** 3222 (1980).
18. Ebert, H. The Munich SPR-KKR package, version 7.7.3. (2018). at <http://ebert.cup.uni-muenchen.de/SPRKKR>
19. Butler, W. H. Theory of electronic transport in random alloys: Korringa-Kohn-Rostoker coherent-potential approximation. *Physical Review B* **31,** 3260–3277 (1985).
20. Wiendlocha, B., Kutorasinski, K., Kaprzyk, S. & Tobola, J. Recent progress in calculations of electronic and transport properties of disordered thermoelectric materials. *Scripta Materialia* **111,** 33 (2016).
21. Ebert, H., Ködderitzsch, D. & Minár, J. Calculating condensed matter properties using the KKR-Green's function method—recent developments and applications. *Reports on Progress in Physics* **74,** 096501 (2011).
22. Vosko, S. H., Wilk, L. & Nusair, M. Accurate spin-dependent electron liquid correlation energies for local spin density calculations: a critical analysis. *Canadian Journal of Physics* **58,** 1200 (1980).
23. Keune, W. Lattice-dynamical study of SnTe by Mössbauer spectroscopy. *Physical Review B* **10,** 5057 (1974).
24. Ibrahim, D., Candolfi, C., Migot, S., Ghanbaja, J., Dauscher, A., Le Caër, G., Malaman, B., Semprimoschnig, C. & Lenoir, B. Comprehensive study of the low-temperature transport properties of polycrystalline $Sn_{1+x}Te$ (x = 0 and 0.03). *Physical Review Materials* **3,** 085404 (2019).
25. Fano, V., Fedeli, G. & Ortalli, I. Phase transition in SnTe by Mössbauer spectroscopy. *Solid State Communications* **22,** 467 (1977).
26. Ahmad, S., Hoang, K. & Mahanti, S. D. Ab Initio Study of Deep Defect States in Narrow Band-Gap Semiconductors: Group III Impurities in PbTe. *Physical Review Letters* **96,** 056403 (2006).

27. Tan, X. J., Liu, G. Q., Xu, J. T., Shao, H. Z., Jiang, J. & Jiang, H. C. Element-selective resonant state in M-doped SnTe (M = Ga, In, and Tl). *Physical Chemistry Chemical Physics* **18,** 20635 (2016).
28. Littlewood, P. B., Mihaila, B., Schulze, R. K., Safarik, D. J., Gubernatis, J. E., Bostwick, A., Rotenberg, E., Opeil, C. P., Durakiewicz, T., Smith, J. L. & Lashley, J. C. Band Structure of SnTe Studied by Photoemission Spectroscopy. *Physical Review Letters* **105,** 086404 (2010).
29. Rabii, S. Energy-Band Structure and Electronic Properties of SnTe. *Physical Review* **182,** 821 (1969).
30. Okoye, C. M. I. Electronic and optical properties of SnTe and GeTe. *Journal of Physics: Condensed Matter* **14,** 8625 (2002).
31. Kutorasinski, K., Wiendlocha, B., Tobola, J. & Kaprzyk, S. Importance of relativistic effects in electronic structure and thermopower calculations for Mg_2Si , Mg_2Ge and Mg_2Sn. *Physical Review B* **89,** 115205 (2014).
32. Al Rahal Al Orabi, R., Mecholsky, N. A., Hwang, J., Kim, W., Rhyee, J.-S., Wee, D. & Fornari, M. Band Degeneracy, Low Thermal Conductivity, and High Thermoelectric Figure of Merit in SnTe–CaTe Alloys. *Chemistry of Materials* **28,** 376 (2016).
33. Ma, Z., Wang, C., Lei, J., Zhang, D., Chen, Y., Wang, Y., Wang, J. & Cheng, Z. Core–shell nanostructures introduce multiple potential barriers to enhance energy filtering for the improvement of the thermoelectric properties of SnTe. *Nanoscale* **12,** 1904 (2020).
34. Haldolaarachchige, N., Gibson, Q., Xie, W., Nielsen, M. B., Kushwaha, S. & Cava, R. J. Anomalous composition dependence of the superconductivity in In-doped SnTe. *Physical Review B* **93,** 024520 (2016).
35. Zhong, R. D., Schneeloch, J. A., Shi, X. Y., Xu, Z. J., Zhang, C., Tranquada, J. M., Li, Q. & Gu, G. D. Optimizing the superconducting transition temperature and upper critical field of $Sn_{1-x}In_xTe$. *Physical Review B* **88,** 020505 (2013).
36. Zhang, C., He, X.-G., Chi, H., Zhong, R., Ku, W., Gu, G., Tranquada, J. M. & Li, Q. Electron and hole contributions to normal-state transport in the superconducting system $Sn_{1-x}In_xTe$. *Physical Review B* **98,** 054503 (2018).
37. Ohorodniichuk, V. Influence of nanostructuring on thermoelectric properties of p-type bulk materials based on (Bi, Sb, Te). (2014).
38. Ibrahim, D. Synthèse et caractérisation de matériaux à base de SnTe pour la conversion d'énergie par effets thermoélectriques. (2018).

39. Erickson, A. S., Chu, J.-H., Toney, M. F., Geballe, T. H. & Fisher, I. R. Enhanced superconducting pairing interaction in indium-doped tin telluride. *Physical Review B* **79,** 024520 (2009).
40. Brebrick, R. F. Deviations from stoichiometry and electrical properties in SnTe. *Journal of Physics and Chemistry of Solids* **24,** 27 (1963).
41. Brebrick, R. F. & Strauss, A. J. Anomalous Thermoelectric Power as Evidence for Two-Valence Bands in SnTe. *Physical Review* **131,** 104 (1963).
42. Kafalas, J. A., Brebrick, R. F. & Strauss, A. J. Evidence that SnTe is a semiconfuctor. *Applied Physics Letters* **4,** 93 (1964).
43. O'Neill, C. D., Sokolov, D. A., Hermann, A., Bossak, A., Stock, C. & Huxley, A. D. Inelastic x-ray investigation of the ferroelectric transition in SnTe. *Physical Review B* **95,** 144101 (2017).
44. Kobayashi, K. L. I., Kato, Y., Katayama, Y. & Komatsubara, K. F. Carrier-Concentration-Dependent Phase Transition in SnTe. *Physical Review Letters* **37,** 772 (1976).
45. Littlewood, P. B. The crystal structure of IV-VI compounds. I. Classification and description. *Journal of Physics C: Solid State Physics* **13,** 4855 (1980).
46. Littlewood, P. B. The crystal structure of IV-VI compounds. II. A microscopic model for cubic/rhombohedral materials. *Journal of Physics C: Solid State Physics* **13,** 4875 (1980).
47. Iizumi, M., Hamaguchi, Y., F. Komatsubara, K. & Kato, Y. Phase Transition in SnTe with Low Carrier Concentration. *Journal of the Physical Society of Japan* **38,** 443 (1975).
48. Brillson, L. J., Burstein, E. & Muldawer, L. Raman observation of the ferroelectric phase transition in SnTe. *Physical Review B* **9,** 1547 (1974).
49. Pawley, G. S., Cochran, W., Cowley, R. A. & Dolling, G. Diatomic Ferroelectrics. *Physical Review Letters* **17,** 753 (1966).
50. Muldawer, L. Low temperature transformation in SnTe. *Bull. Am. Phys, Soc.* **16,** 84 (1971).
51. Muldawer, L. New studies of the low temperature transformation in SnTe. *J. Nonmetals* **1,** 177 (1973).
52. Tan, G., Zhao, L.-D., Shi, F., Doak, J. W., Lo, S.-H., Sun, H., Wolverton, C., Dravid, V. P., Uher, C. & Kanatzidis, M. G. High Thermoelectric Performance of p-Type SnTe via a Synergistic Band Engineering and Nanostructuring Approach. *Journal of the American Chemical Society* **136,** 7006 (2014).
53. Tan, G., Shi, F., Hao, S., Chi, H., Zhao, L.-D., Uher, C., Wolverton, C., Dravid, V. P. & Kanatzidis, M. G. Codoping in SnTe: Enhancement of Thermoelectric Performance

through Synergy of Resonance Levels and Band Convergence. *Journal of the American Chemical Society* **137,** 5100 (2015).

54. Tan, G., Shi, F., Hao, S., Chi, H., Bailey, T. P., Zhao, L.-D., Uher, C., Wolverton, C., Dravid, V. P. & Kanatzidis, M. G. Valence Band Modification and High Thermoelectric Performance in SnTe Heavily Alloyed with MnTe. *Journal of the American Chemical Society* **137,** 11507 (2015).
55. Tan, G., Shi, F., Doak, J. W., Sun, H., Zhao, L.-D., Wang, P., Uher, C., Wolverton, C., Dravid, V. P. & Kanatzidis, M. G. Extraordinary role of Hg in enhancing the thermoelectric performance of p-type SnTe. *Energy & Environmental Science* **8,** 267 (2015).
56. Tan, G., Zeier, W. G., Shi, F., Wang, P., Snyder, G. J., Dravid, V. P. & Kanatzidis, M. G. High Thermoelectric Performance SnTe–In_2Te_3 Solid Solutions Enabled by Resonant Levels and Strong Vacancy Phonon Scattering. *Chemistry of Materials* **27,** 7801 (2015).
57. Zhou, M., Gibbs, Z. M., Wang, H., Han, Y., Xin, C., Li, L. & Snyder, G. J. Optimization of thermoelectric efficiency in SnTe: the case for the light band. *Phys. Chem. Chem. Phys.* **16,** 20741 (2014).
58. He, J., Tan, X., Xu, J., Liu, G.-Q., Shao, H., Fu, Y., Wang, X., Liu, Z., Xu, J., Jiang, H. & Jiang, J. Valence band engineering and thermoelectric performance optimization in SnTe by Mn-alloying via a zone-melting method. *J. Mater. Chem. A* **3,** 19974 (2015).
59. Banik, A., Shenoy, U. S., Anand, S., Waghmare, U. V. & Biswas, K. Mg Alloying in SnTe Facilitates Valence Band Convergence and Optimizes Thermoelectric Properties. *Chemistry of Materials* **27,** 581 (2015).
60. Zhao, L.-D., Zhang, X., Wu, H., Tan, G., Pei, Y., Xiao, Y., Chang, C., Wu, D., Chi, H., Zheng, L., Gong, S., Uher, C., He, J. & Kanatzidis, M. G. Enhanced Thermoelectric Properties in the Counter-Doped SnTe System with Strained Endotaxial SrTe. *Journal of the American Chemical Society* **138,** 2366 (2016).
61. Zhang, L., Wang, J., Cheng, Z., Sun, Q., Li, Z. & Dou, S. Lead-free SnTe-based thermoelectrics: enhancement of thermoelectric performance by doping with Gd/Ag. *Journal of Materials Chemistry A* **4,** 7936 (2016).
62. Banik, A., Vishal, B., Perumal, S., Datta, R. & Biswas, K. The origin of low thermal conductivity in $Sn_{1-x}Sb_xTe$: phonon scattering via layered intergrowth nanostructures. *Energy & Environmental Science* **9,** 2011 (2016).
63. Al Rahal Al Orabi, R., Hwang, J., Lin, C.-C., Gautier, R., Fontaine, B., Kim, W., Rhyee, J.-S., Wee, D. & Fornari, M. Ultralow Lattice Thermal Conductivity and Enhanced

Thermoelectric Performance in SnTe:Ga Materials. *Chemistry of Materials* **29,** 612 (2017).

64. Wang, L., Tan, X., Liu, G., Xu, J., Shao, H., Yu, B., Jiang, H., Yue, S. & Jiang, J. Manipulating Band Convergence and Resonant State in Thermoelectric Material SnTe by Mn–In Codoping. *ACS Energy Letters* **2,** 1203 (2017).
65. Li, W., Zheng, L., Ge, B., Lin, S., Zhang, X., Chen, Z., Chang, Y. & Pei, Y. Promoting SnTe as an Eco-Friendly Solution for p-PbTe Thermoelectric via Band Convergence and Interstitial Defects. *Advanced Materials* **29,** 1605887 (2017).
66. Wang, N., West, D., Liu, J., Li, J., Yan, Q., Gu, B.-L., Zhang, S. B. & Duan, W. Microscopic origin of the p -type conductivity of the topological crystalline insulator SnTe and the effect of Pb alloying. *Physical Review B* **89,** 045142 (2014).
67. Zheng, L., Li, W., Lin, S., Li, J., Chen, Z. & Pei, Y. Interstitial Defects Improving Thermoelectric SnTe in Addition to Band Convergence. *ACS Energy Letters* **2,** 563 (2017).
68. Hu, L., Zhang, Y., Wu, H., Li, J., Li, Y., Mckenna, M., He, J., Liu, F., Pennycook, S. J. & Zeng, X. Entropy Engineering of SnTe: Multi-Principal-Element Alloying Leading to Ultralow Lattice Thermal Conductivity and State-of-the-Art Thermoelectric Performance. *Advanced Energy Materials* **8,** 1802116 (2018).
69. Roychowdhury, S., Shenoy, U. S., Waghmare, U. V. & Biswas, K. An enhanced Seebeck coefficient and high thermoelectric performance in p-type In and Mg co-doped $Sn_{1-x}Pb_xTe$ via the co-adjuvant effect of the resonance level and heavy hole valence band. *Journal of Materials Chemistry C* **5,** 5737 (2017).
70. Ibrahim, D., Ohorodniichuk, V., Candolfi, C., Semprimoschnig, C., Dauscher, A. & Lenoir, B. Improved Thermoelectric Properties in Melt-Spun SnTe. *ACS Omega* **2,** 7106 (2017).
71. Zhou, Z., Yang, J., Jiang, Q., Luo, Y., Zhang, D., Ren, Y., He, X. & Xin, J. Multiple effects of Bi doping in enhancing the thermoelectric properties of SnTe. *J. Mater. Chem. A* **4,** 13171 (2016).
72. Li, J. Q., Huang, S., Chen, Z. P., Li, Y., Song, S. H., Liu, F. S. & Ao, W. Q. Phases and thermoelectric properties of SnTe with (Ge, Mn) co-doping. *Phys. Chem. Chem. Phys.* **19,** 28749 (2017).
73. Balakrishnan, G., Bawden, L., Cavendish, S. & Lees, M. R. Superconducting properties of the In-substituted topological crystalline insulator SnTe. *Physical Review B* **87,** 140507 (2013).

74. Allen, P. B. & Cohen, M. L. Carrier-Concentration-Dependent Superconductivity in SnTe and GeTe. *Phys. Rev.* **177,** 704 (1969).
75. Bushmarina, G. S., Drabkin, I. A., Kompaniets, V. V., Parfen'ev, R. V., Shamshur, D. V. & Shakhov, M. A. Superconducting transition in SnTe doped with In. *Fizika Tverdogo Tela* **28,** 1094 (1986).
76. Prokof'eva, L. V., Shabaldin, A. A., Korchagin, V. A., Nemov, S. A. & Ravich, Y. I. Lorentz number and Hall factor in degenerate semiconductors during resonance scattering of charge carriers. *Semiconductors* **42,** 1161 (2008).
77. Matusiak, M., Tunnicliffe, E. M., Cooper, J. R., Matsushita, Y. & Fisher, I. R. Evidence for a charge Kondo effect in $Pb_{1-x}Tl_xTe$ from measurements of thermoelectric power. *Physical Review B* **80,** 220403 (2009).
78. Jaworski, C. M., Nielsen, M. D., Wang, H., Girard, S. N., Cai, W., Porter, W. D., Kanatzidis, M. G. & Heremans, J. P. Valence-band structure of highly efficient p-type thermoelectric PbTe-PbS alloys. *Physical Review B* **87,** 045203 (2013).
79. Taylor, P. L., Taylor, P. L. & Heinonen, O. *A quantum approach to condensed matter physics*. (Cambridge University Press, 2002).
80. Heikes, R. R. & Ure, R. W. *Thermoelectricity: science and engineering*. (Interscience Publishers, 1961).
81. Kobayashi, K., Ai, Y., Jeschke, H. O. & Akimitsu, J. Enhanced superconducting transition temperatures in the rocksalt-type superconductors $In_{1-x}Sn_xTe$ ($x \leq 0.5$). *Physical Review B* **97,** 104511 (2018).
82. Hsieh, T. H., Lin, H., Liu, J., Duan, W., Bansil, A. & Fu, L. Topological crystalline insulators in the SnTe material class. *Nature Communications* **3,** 982 (2012).
83. Novak, M., Sasaki, S., Kriener, M., Segawa, K. & Ando, Y. Unusual nature of fully gapped superconductivity in In-doped SnTe. *Physical Review B* **88,** 140502(R) (2013).
84. Smylie, M. P., Claus, H., Kwok, W.-K., Louden, E. R., Eskildsen, M. R., Sefat, A. S., Zhong, R. D., Schneeloch, J., Gu, G. D., Bokari, E., Niraula, P. M., Kayani, A., Dewhurst, C. D., Snezhko, A. & Welp, U. Superconductivity, pairing symmetry, and disorder in the doped topological insulator $Sn_{1-x}In_xTe$ for $x \geq 0.10$. *Physical Review B* **97,** 024511 (2018).
85. Maeda, S., Hirose, R., Matano, K., Novak, M., Ando, Y. & Zheng, G. Spin-singlet superconductivity in the doped topological crystalline insulator $Sn_{0.96}In_{0.04}Te$. *Physical Review B* **96,** 104502 (2017).

86. Xu, Z., Schneeloch, J. A., Zhong, R. D., Rodriguez-Rivera, J. A., Harriger, L. W., Birgeneau, R. J., Gu, G. D., Tranquada, J. M. & Xu, G. Low-energy phonons and superconductivity in $Sn_{0.8}In_{0.2}Te$. *Physical Review B* **91,** 054522 (2015).
87. Bevolo, A. J., Shanks, H. R. & Eckels, D. E. Molar heat capacity of GeTe, SnTe, and PbTe from 0.9 to 60 K. *Physical Review B* **13,** 3523 (1976).
88. Smith, T. F., Birch, J. A. & Collins, J. G. Low-temperature heat capacity, thermal expansion and Gruneisen parameters for SnTe. *Journal of Physics C: Solid State Physics* **9,** 4375 (1976).
89. Brebrick, R. F. & Gubner, E. Composition Stability Limits of PbTe. II. *The Journal of Chemical Physics* **36,** 1283 (1962).
90. Callaway, J. Model for Lattice Thermal Conductivity at Low Temperatures. *Physical Review* **113,** 1046 (1959).
91. Klemens, P. G. Thermal Resistance due to Point Defects at High Temperatures. *Physical Review* **119,** 507 (1960).
92. Li, W., Chen, Z., Lin, S., Chang, Y., Ge, B., Chen, Y. & Pei, Y. Band and scattering tuning for high performance thermoelectric $Sn_{1-x}Mn_xTe$ alloys. *Journal of Materiomics* **1,** 307 (2015).
93. Yao, Z., Li, W., Tang, J., Chen, Z., Lin, S., Biswas, K., Burkov, A. & Pei, Y. Solute manipulation enabled band and defect engineering for thermoelectric enhancements of SnTe. *InfoMat* **1,** 571 (2019).
94. Tan, G., Shi, F., Sun, H., Zhao, L.-D., Uher, C., Dravid, V. P. & Kanatzidis, M. G. SnTe–$AgBiTe_2$ as an efficient thermoelectric material with low thermal conductivity. *J. Mater. Chem. A* **2,** 20849 (2014).
95. McKinney, R. W., Gorai, P., Stevanović, V. & Toberer, E. S. Search for new thermoelectric materials with low Lorenz number. *Journal of Materials Chemistry A* **5,** 17302 (2017).
96. Thesberg, M., Kosina, H. & Neophytou, N. On the Lorenz number of multiband materials. *Physical Review B* **95,** 125206 (2017).
97. Kim, H. S., Liu, W., Chen, G., Chu, C.-W. & Ren, Z. Relationship between thermoelectric figure of merit and energy conversion efficiency. *Proceedings of the National Academy of Sciences* **112,** 8205 (2015).
98. Allgaier, R. S. & Houston, B. Weak-Field Magnetoresistance and the Valence-Band Structure of SnTe. *Physical Review B* **5,** 2186 (1972).

Chapter 4

InTe: An emerging thermoelectric material

4.1 Introduction

The binary compound InTe has recently emerged as an interesting thermoelectric material with a high thermoelectric figure of merit of 0.9 at 600 K.[1] One of its remarkable key properties is the extremely low lattice thermal conductivity reaching ~ 0.3 – 0.4 W m^{-1} K^{-1} at 600 K.[1–3] As already mentioned in Chapter 1, only a handful of studies is available for this material.[1–7] This chapter is dedicated to our in-depth experimental study of InTe with the aim to explore its basic physical properties at low and high temperatures on both single-crystalline and polycrystalline samples. Studying single-crystalline specimen is of particular relevance to study its lattice dynamics in detail and determine the physical mechanism underlying the poor ability of this compound to transport heat. Moreover, the low number of investigations dedicated to this compound leaves lot of room for further enhancing its thermoelectric properties.

In a first part, we will describe the In-Te phase diagram and the main crystallographic properties, highlighting the possible presence of defects in this compound. We will then discuss the electronic band structure of this compound based on a short literature survey. The second part of the chapter will be dedicated to the growth and structural characterization of single-crystalline InTe. The growth of single crystal by the conventional vertical Bridgman-Stockbarger method will be presented. To confirm the single-crystalline nature of the grown crystal, analyses based on single crystal X-ray diffraction, Laue diffraction and scanning electron microscopy (SEM) with energy dispersive X-ray spectroscopy (EDXS) were performed. Electronic band structure calculations were performed in collaboration with Dr. Céline Barreteau and Dr. Jean-Claude Crivello from the Institut de Chimie et des Matériaux Paris-Est in Thiais (France). The specific heat measurements were performed down to 0.35 K using the ^{3}He option of the PPMS in collaboration with Dr. Jiri Hejtmanek and Dr. Petr Levinsky from the Academy of Science of the Czech Republic in Prague. Finally, the physical properties (electrical resistivity, thermopower, thermal conductivity and Hall effect) of the single crystal was studied systematically over a wide range of temperatures (5 – 800 K).

The last part of the chapter will focus on the detailed study of polycrystalline InTe. To carefully control its inherent defect concentration, the saturation-annealing technique was implemented to probe the maximum deviations from the ideal stoichiometry on both the In- and Te-rich sides of the solidus. This technique was utilized on polycrystalline compounds synthesized using a conventional solid-state process. All the synthesized materials were

structurally (XRD) and chemically (SEM-EDS) characterized. The physical properties of the various samples were also measured over a wide range of temperatures (5 – 800 K).

4.2 General properties of InTe

4.2.1 Phase diagram

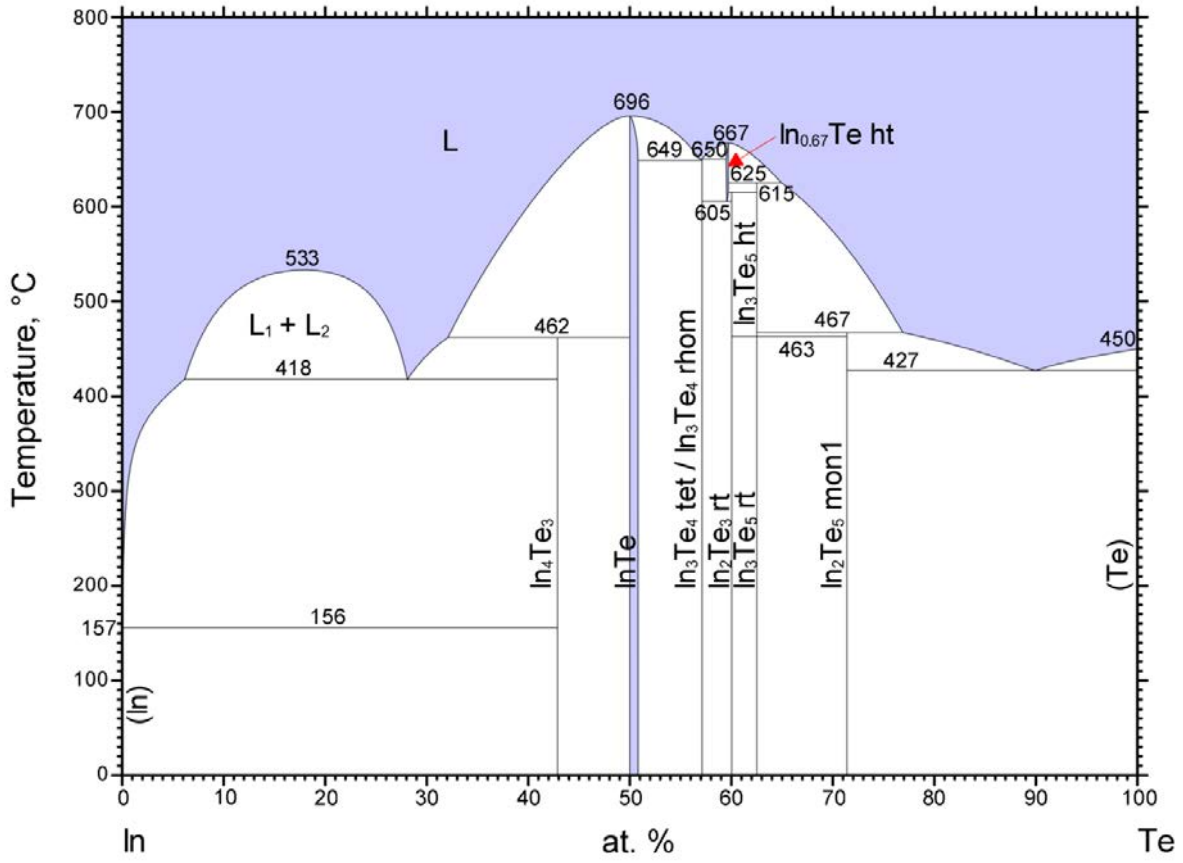

Figure 4.1: In-Te binary phase diagram as derived by Massalski *et al*.[8]

The first studies on the binary In-Te phase diagram were carried out by Klemm *et al*. and Grochowski *et al*. Later on, Massalski *et al*. further refined it and derived the complex binary phase diagram shown in Figure 4.1.[8–10] As can be seen in the figure, several binary compounds are present. Similar to SnTe, the binary InTe shows deviations from the ideal stoichiometry. These deviations range from ~ 50.0 to ~ 50.9 at % below 649°C and seem to be temperature dependent above this temperature.[10] InTe melts congruently at 696°C (see Figure 4.1).[8,10] The inherent off-stoichiometry is linked to the presence of defects in the crystal structure, supposed to be In vacancies.[2] However, no detailed studies on the nature of these defects were performed

leaving open the possibility that other types of defects, such as antisite defects or Te vacancies, might also coexist with In vacancies. As already demonstrated by the results obtained on SnTe, such off-stoichiometry is an important property that will inevitably lead to variations in the transport properties depending on the synthesis process used.

4.2.2 Crystal structure

InTe crystallizes in a TlSe structure type described in the tetragonal space group *I*4/*mcm* under ambient conditions (Figure 4.2).[1,7,11,12] The elementary cell contains 8 In atoms and 8 Te atoms ($Z = 8$). In atoms occupy two independent crystallographic sites, named hereafter In1 (0, 0, ¼) and In2 (0, ½, ¼), while the Te atoms solely occupy a (x, y, 0) site. The reduced atomic positions $x = 0.1821(3)$ and $y = 0.6821(3)$ were inferred at 295 K from refinements of single-crystal X-ray diffraction data by Chattopadhyay *et al.*[11] Due to distinct bonding environment between the two In atoms, both In^{+} (In1) and In^{3+} (In2) have been proposed to be present in equal proportion in InTe. Hence, the chemical formula of this compound may be written as $In^{+}In^{3+}Te_2$.[13]

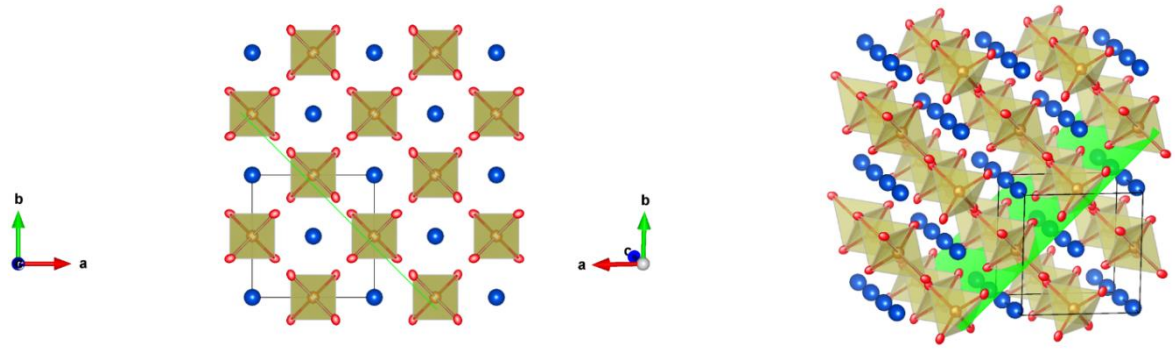

Figure 4.2: (Left) Crystal structure of InTe projected along the c direction. Blue spheres, golden spheres and red spheres represent In^{+}, In^{3+} and Te^{2-}, respectively. (Right) Perspective view with the green plane depicting the cleavage plane (110).

The In^{3+} ions are tetrahedrally coordinated with Te^{2-} ions forming edge-sharing $(In^{3+}Te_4^{2})^{-}$ chains of tetrahedra similar to those found in SiS_2 (with sp^3 hybridization). These long, negatively-charged atomic chains are elongated along the tetragonal *c* direction (Figure 4.2 (a)). On the other hand, the In^{+} ions are surrounded by 8 Te atoms (Figure 4.2 (a)), forming an eight-fold tetragonal anti-prismatic coordination.[1] The $(In^{3+}Te_4^{2})^{-}$ chains are weakly-bonded

to each other while the iono-covalent bonds between the atoms within the chains are strong. Due to the presence of weak interchain bonds, InTe crystals may be easily cleaved along the (110) planes of the crystal structure (Figure 4.2 (b)).[5,14] Parlak *et al.* reported that it is practically impossible to cleave the crystal perpendicularly to the *c* axis.[5] At 300 K, the lattice parameters of InTe are $a = b = 8.454$ Å and $c = 7.152$ Å.[15] Other studies reported close lattice parameters ($a = b = 8.441$ Å and $c = 7.141$ Å and $a = b = 8.444$ Å and $c = 7.136$ Å at ~ 300 K).[11] The small differences observed by these authors could be attributed to different concentration of defects in their respective crystals.

InTe transforms into a rocksalt structure when a hydrostatic pressure of 30 kbar is applied between 670 and 770 K. This high-temperature, high-pressure allotrope is superconducting with a critical temperature as high as 3.5 K.[11,13,16–18]

4.2.3 Electronic band structure

Electronic band structure calculations reported in the literature evidenced that the valence band structure of InTe is characterized by multiple bands.[1,2] At the M and Z points of the Brillouin zone, the conduction and valence bands tend to touch each other, giving rise to a narrow, direct band gap at the M point of ~ 0.15 eV.[2] A considerable disagreement exists on the existence and width of this electronic band gap in the literature. While Hussein reported a band gap of 0.34 eV via Hall coefficient studies,[7] Pal *et al.* reported a much higher value of ~ 1.16 eV.[6] More recent investigations carried out by Jana *et al.* reported an experimental small band gap of 0.06 eV measured by diffuse reflectance spectroscopy. However, their band structure calculations did not evidence a band gap, but rather a small overlap of the conduction and valence bands at the M and Z points of the Brillouin zone.[1] Similarly, Zhu *et al.* reported an experimental value of ~ 0.8 eV, despite a semi-metallic state predicted by their calculations. Finally, Back *et al.* also predicted a semi-metallic state via calculations performed at 0 K. However, upon including thermal effects at 300 K, they predicted the opening of a band gap. These dispersed, and sometimes contradicting data suggest that the electronic band structure of InTe is strongly sensitive to the details of the calculation technique used and, possibly, to slight changes in the crystal structure induced by thermal effects. The absence of consensus of the presence of a band gap and, if any, of its width, reinforces the interest of further studying both experimentally and theoretically this particular point.

4.3 InTe as a thermoelectric material

Surprisingly, limited efforts were devoted over the last decades to study the transport properties of InTe and its ternary derivatives. To the best of our knowledge, the first study of the electrical and optical properties of InTe was performed in the late 1970s in Russia.[19,20] These studies were mainly reported on polycrystalline samples until 1981 when Riede *et al.* studied the infrared optical properties on a single-crystalline specimen.[14] They reported a *p*-type electrical conduction with an isotropic carrier concentration on the order of 10^{18} – 10^{19} cm^{-3} at 300 K. They further reported for the first time that the Hall mobilities along and perpendicular to the cleavage plane strongly differ with a difference being as high as five times.[14]

In 1989, Hussein studied the electrical conductivity and Hall coefficient of single-crystalline InTe.[7] He notably suggested that the growth rate of the crystal could have a drastic impact on the transport properties as well as on the energy band gap of this compound, if any. The crystals synthesized exhibited an estimated electrical resistivity of ~ 50 μΩm (the direction along which these measurements were performed were not indicated in the paper), despite a very low carrier density of ~ 10^{15} – 10^{16} cm^{-3}, which was highly dependent on the growth rate. Unlike Riedel *et al.*, however, he also claimed that the Hall coefficient is isotropic irrespective of the carrier density of the crystal.[7,14] The main drawback in this study was related to the transport properties measurements, which were not carried out along the two independent directions of the crystal structure, leaving many questions open.

The first thermopower measurement on single-crystalline InTe was performed by Pal *et al.* in 1995.[6] They observed anisotropic thermopower values, with a maximum value of 630 $\mu V\ K^{-1}$ in samples measured along the direction perpendicular to the cleavage plane. However, the cleavage plane reported by these authors was the [001] plane at odds with prior reports.[14] Moreover, they confirmed the anisotropy in the carrier mobility along the *a* and *c* axes of the crystal structure. The carrier concentration of their single crystal was as high as ~ 1.5×10^{18} cm^{-3} at 300 K.[6]

In another study, Parlak *et al.* experimentally demonstrated the presence of anisotropy in the electrical properties in *p*-type single crystalline InTe samples along directions parallel and perpendicular to the cleavage plane (that is, parallel or perpendicular to the *c* axis).[5] A nearly temperature-independent carrier concentration of 7.5×10^{18} cm^{-3} was inferred. In agreement with Riede *et al.*, the Hall mobility was also found to be anisotropic.[14]

It was not until recently, however, that the thermoelectric properties of polycrystalline InTe were reported.[1] Intentionally starting from In-deficient chemical compositions, Jana *et al.* showed that the hole concentration varies depending on the nominal In concentration, suggesting the presence of inherent In vacancies, in agreement with the In-Te phase diagram.[1] However, these authors did not measure the transport properties parallel and perpendicular to the pressing direction. The Hall mobility values were similar to those reported by Pal *et al.* and Parlak *et al.*[5,6] Moreover, the thermopower values were lower than those measured by Pal *et al.* due to a stronger metallic character of transport. Intriguingly, Jana *et al.* evidenced that InTe features intrinsically very low lattice thermal conductivity values as low as 0.30 W m^{-1} K^{-1} at 625 K. Based on lattice dynamics calculations, they ascribed this remarkable property to bonding asymmetry and lattice anharmonicity. Of note, these calculations could not converge based on the crystal structure of InTe determined at 300 K, showing negative phonon frequencies. Calculations could only converge upon compressing the unit cell theoretically, mimicking the application of an external pressure of 3 GPa. Owing to the very thermal conductivity values of InTe and the possibility to tune the electronic properties via In deficiency, a maximum *ZT* of ~ 0.85 was obtained at 600 K (Figure 4.3).[6]

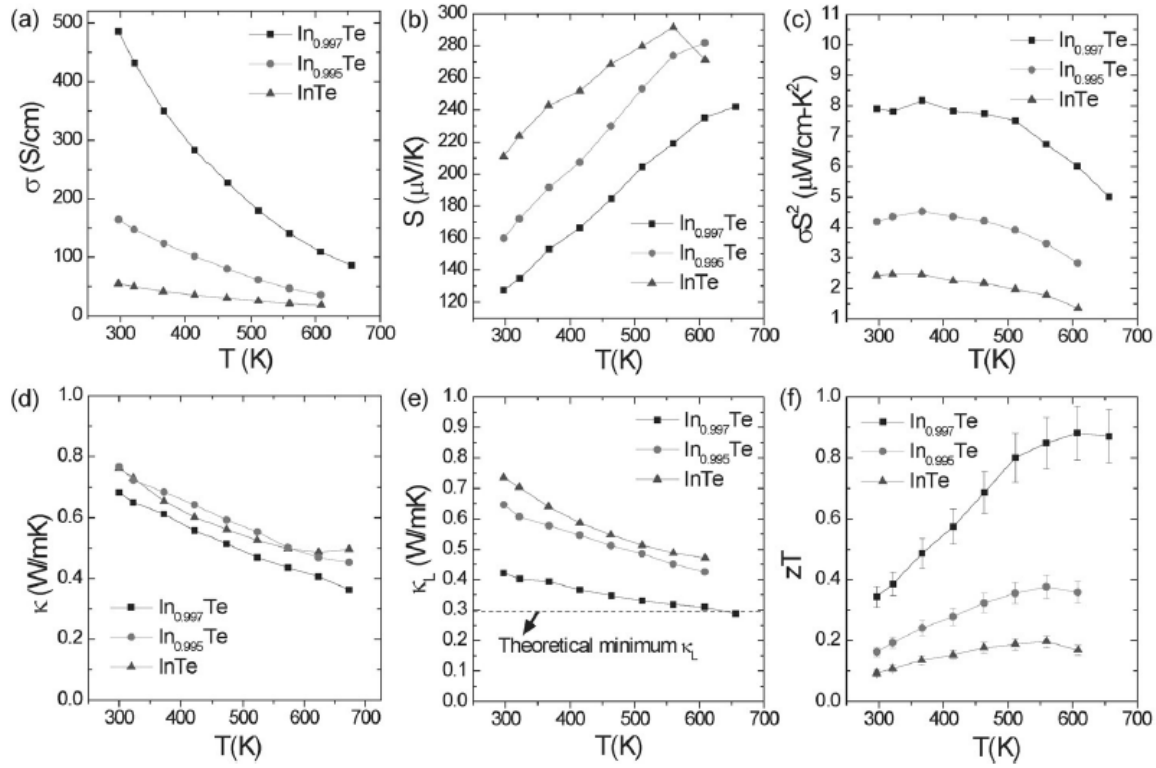

Figure 4.3: Temperature dependence of a) the electrical conductivity, b) the thermopower, c) the power factor, d) the total thermal conductivity, e) the lattice thermal conductivity and f) the dimensionless thermoelectric figure of merit.[1]

Very recently, Back *et al.* also studied the thermoelectric properties of polycrystalline InTe, confirming an ultralow thermal conductivity of 0.47 W m^{-1} K^{-1} at 625 K (Figure 4.4).[2] A maximum *ZT* of ~ 0.65 was obtained at 625 K. This lower value, with respect to that achieved by Jana *et al.*, is due to the difference in the hole concentration between the two samples. The samples prepared by Back *et al.* had a comparatively higher hole concentration of ~ 6.8×10^{19} cm^{-3} at 300 K.[2] Unlike prior works, Back *et al.* further tried to prepare In-rich samples with the aim to study the other side of the solidus line.[1,2] To this end, they prepared samples with Te deficiency of up to 20%. Although they were able to reduce the thermal conductivity of the samples even further, the overall *ZT* of the samples followed the same trend (Figure 4.4).

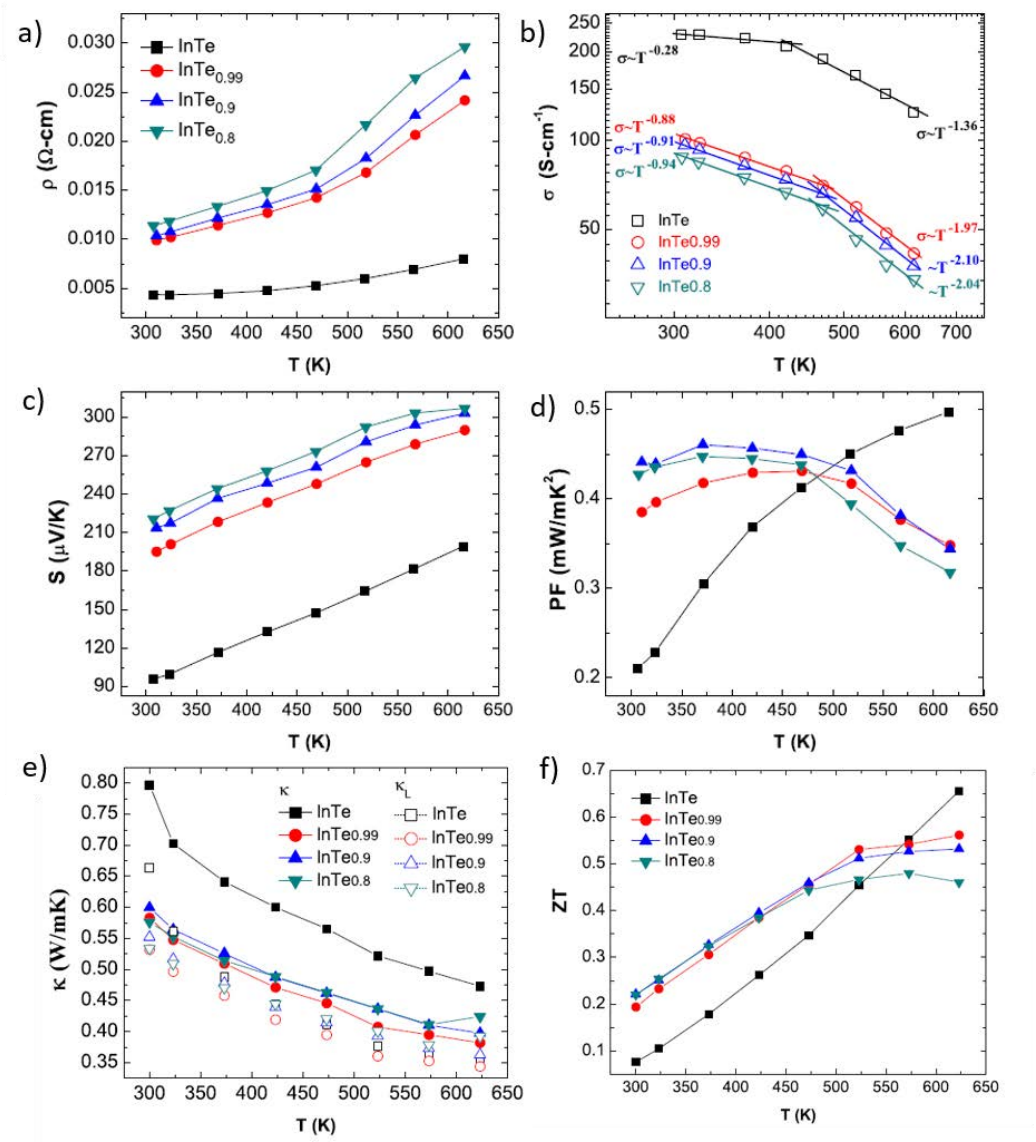

Figure 4.4: Temperature dependence of the a) electrical resistivity, b) the electrical conductivity, c) the thermopower, d) the power factor, e) the total thermal conductivity and, f) the *ZT* values.[2]

These authors also studied the thermoelectric properties of these compounds at helium temperatures down to 2 K (Figure 4.5 (a)).[4] Compared to the binary InTe, the transport properties of Te-deficient samples showed different behaviors at low temperatures. Unlike rocksalt-high-pressure InTe, InTe shows no superconducting transition down to 2 K. Unusual transitions in the electronic transport properties were observed in the Te-deficient samples, which were ascribed to a tetragonal-to-orthorhombic transition occurring at 185 K followed by a Fermi surface reconstruction arising from the development of a charge-density-wave (CDW) setting in at 87 K (Figure 4.5) leaving the orthorhombic symmetry unchanged. Based on temperature-dependent powder X-ray diffraction, the low-temperature crystal structure was described in the orthorhombic space group *Ibam* with lattice parameters a = 8.456(0) Å, b = 8.405(9) Å and c = 7.122(4) Å.

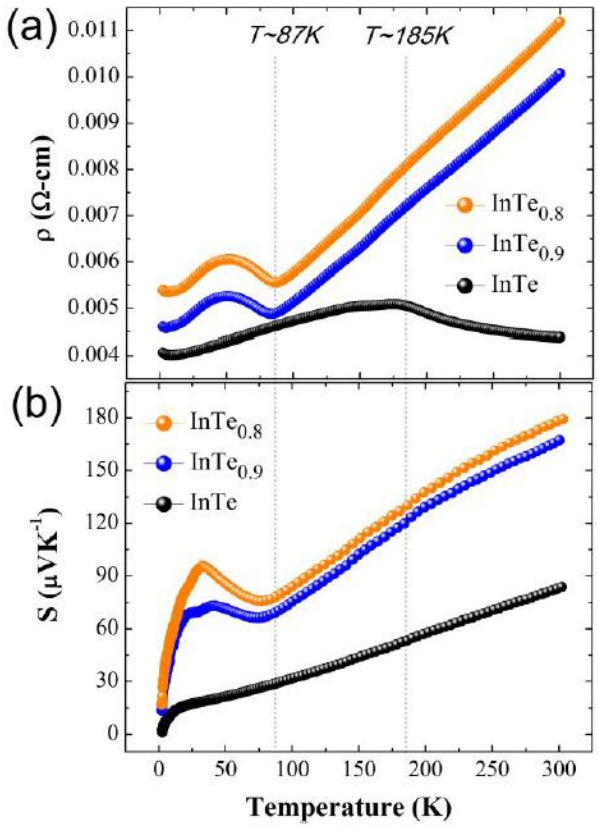

Figure 4.5: Low-temperature dependence of the electrical resistivity and thermopower showing the different behaviors of the binary InTe and the Te-deficient InTe samples studied by Back *et al.*[4]

These authors further suggested that the appearance of additional reflections below 125 K results from the development of a commensurate modulation running along the *a* axis that

doubles this axis. The resulting crystal structure is then described in the *Pbca* space group with lattice parameters a = 17.127(1) Å, b = 8.396(1) Å and c = 7.115(1) Å. However, because no detailed analysis of the chemical composition of these samples was performed, it is difficult to conclude whether Te deficiency of up to 20 %, at odds with the binary phase diagram, can indeed be achieved. In addition, no direct evidence for the above-mentioned commensurate modulation was obtained via, for instance, electron diffraction. Interestingly, the transport properties of these Te-deficient samples are similar to those measured in stoichiometric InTe samples despite the significant modifications in the electronic band structure such high off-stoichiometry should imply.[4]

Zhu *et al.* studied the influence of Sb addition on the physical properties of polycrystalline InTe.[3] These authors obtained a maximum *ZT* of 0.6 for their binary sample, which was improved to 0.8 at 623 K for InTe–$Sb_{0.01}$. The addition of Sb was shown to form nano-precipitates that were proposed to alter the scattering mechanism of holes advantageously by suppressing inter-valley scattering. Similar to previous reports on InTe, a very low lattice thermal conductivity of ~ 0.35 W m^{-1} K^{-1} was obtained at high temperatures for the InTe–$Sb_{0.01}$ sample (Figure 4.6).

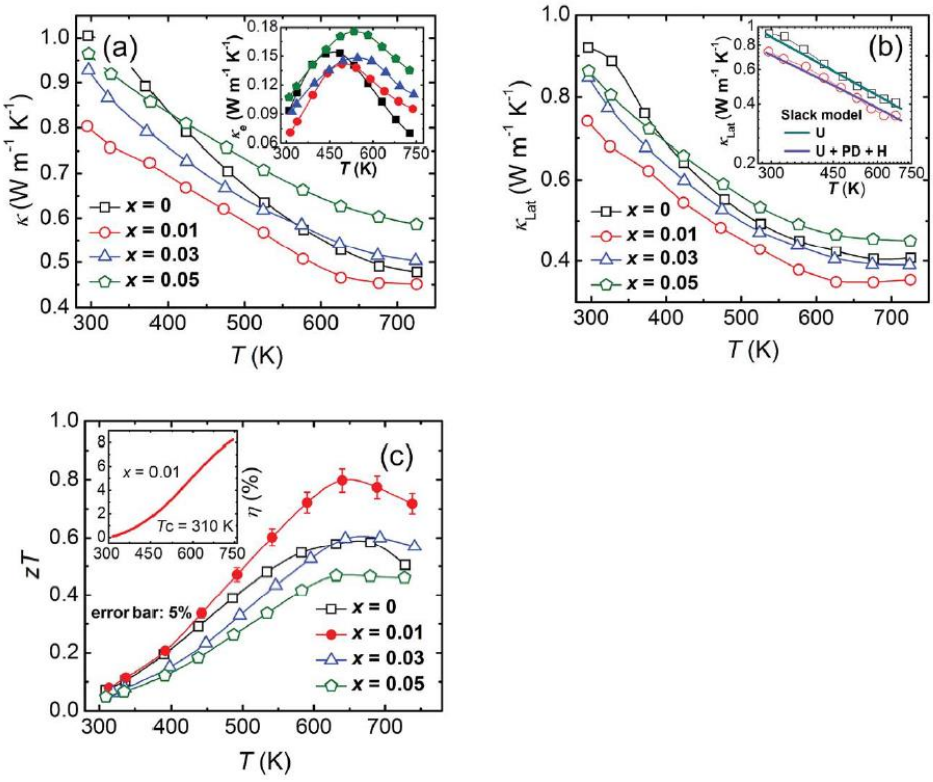

Figure 4.6: Temperature dependence of a) the total thermal conductivity, b) the lattice thermal conductivity and c) the *ZT* values for InTe–Sb_x polycrystalline samples reported by Zhu *et al.*[3]

4.4 Motivations

As mentioned above, InTe is a very interesting candidate for thermoelectric applications at high temperatures due to its ultralow lattice thermal conductivity resulting in high thermoelectric *ZT* values. Because there has been a very limited number of studies on this compound, the basic properties and physical mechanisms governing them are yet to be pinpointed in both single-crystalline and polycrystalline samples. The main motivations for the study presented in this chapter are:

- *Electronic band structure calculations*
  Only a handful of previous studies have reported electronic band structure calculations for InTe.[1,2] Due to the different results obtained, further calculations need to be performed to verify the electronic band structure of InTe and get information on the energy band gap and the multivalley valence band structure.

- *Introductory investigation of transport properties in single crystalline InTe*
  As already underlined in the previous paragraphs, the first studies on the transport properties of single-crystalline InTe show some discrepancy amongst each other. Despite several reports on the electronic properties measured on single-crystalline InTe, no detailed investigation of its thermal properties have been undertaken so far.[5–7,14] The possibility to measure the transport properties at low temperatures may help elucidate the basic mechanisms governing the transport properties of this compound. Moreover, growing large single crystals of InTe would open up interesting possibilities to study in detail its lattice dynamics by spectroscopic techniques in order to better understand the microscopic origin of its very low lattice thermal conductivity.

- *Transport properties in polycrystalline InTe prepared by saturation annealing*
  The literature data have shown that a careful control of the defect chemistry of InTe is paramount to optimizing its thermoelectric properties at high temperatures. As a powerful tool to determine the maximum deviations from the ideal stoichiometry on both the In and Te-rich sides of the solidus, saturation annealing, performed under strict thermodynamic equilibrium conditions, will provide interesting information and allow for tuning the

transport properties. This technique has the notable advantage to yield reproducible results from sample to sample.

4.5 Electronic band structure and lattice dynamics calculations

Electronic band structure and phonon calculations were performed in collaboration with Dr. Céline Barreteau and Dr. Jean-Claude Crivello from the Institut de Chimie des Matériaux Paris-Est in Thiais (France). These calculations were realized with various techniques to determine the influence of the calculation details on the electronic band structure computed. Similarly, various attempts at calculating the phonon dispersion curves were carried out to determine whether convergence can be achieved without decreasing artificially the lattice parameters to mimic a high external pressure. DFT calculations were conducted using the projector augmented wave (PAW) method, implemented in the Vienna *ab-initio* Simulation Package (VASP).[21–24] The exchange correlation was described by the generalized gradient approximation modified by Perdew, Burke, and Ernzerhof (GGA-PBE).[25] Energy bands up to a cut off energy E = 600 eV were used in all calculations. A high-density k-points meshing was employed for Brillouin zone integrations (15×15×17). These parameters ensured good convergence for the total energy. The convergence tolerance for the calculations was selected as a difference of the total energy within 10^{-6} eV. Upon performing volume and ionic relaxation steps, Blöchl correction was applied in a final step calculation.[26] Phonon dispersion bands, phonon density of states (PDOS) and vibrational free energy at $T > 0$K were obtained by computing the atomic forces for different, finite atomic displacements,[27] and a subsequent calculation and integration over the corresponding phonon frequencies, within the harmonic approximation, that is, without any volume dependence, using the Phonopy code.[28,29] The phonon calculations were carried out within a 2×2×2 of the conventional cell, that is, using a supercell of 128 atoms with 4 atomic displacements.

4.5.1 Electronic band structure

The results of the calculations, performed considering the experimental unit cell parameters determined at 300 K and a pressurized unit cell ($0.88V_0$, where V_0 is the volume of the unit cell, corresponding to a pressure of 3 GPa) are shown in Figure 4.7 (a) and (b) , respectively.

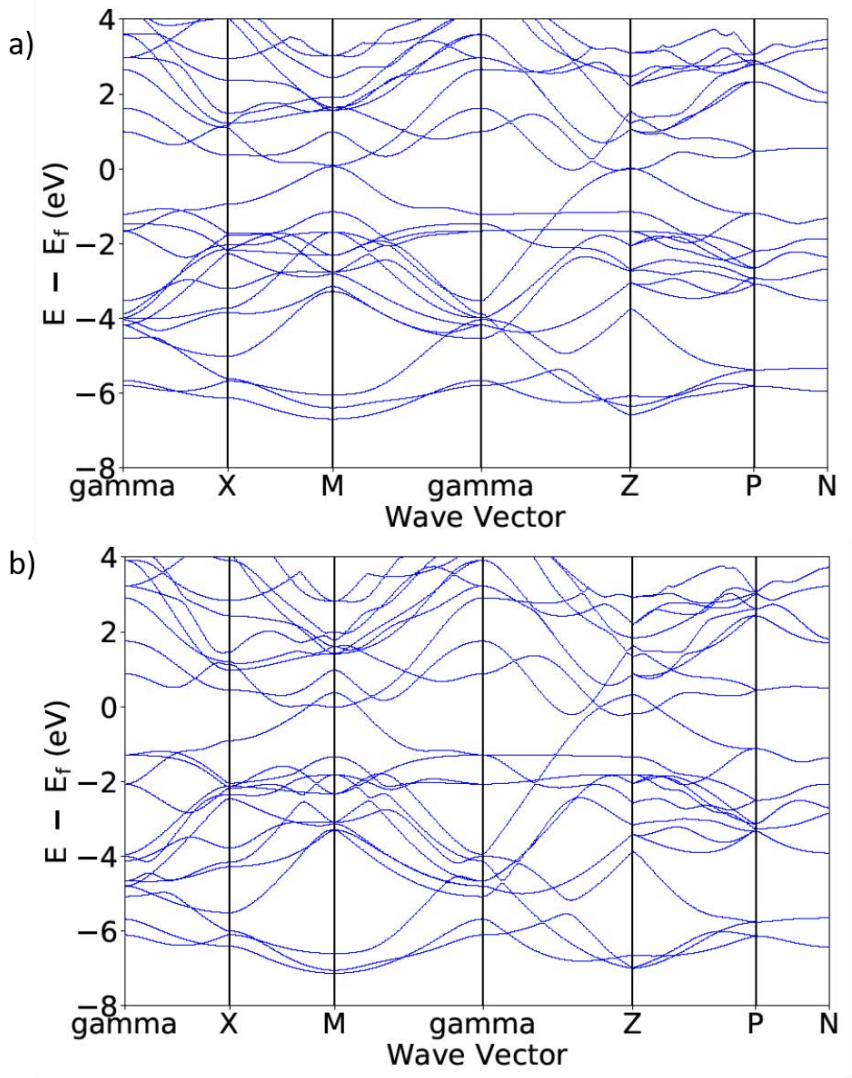

Figure 4.7: Electronic band structures of InTe calculated by considering a) a unit cell with experimental room temperature lattice parameters and b) a unit cell volume of $0.88V_0$.

The results obtained on the unit cell using the experimental lattice parameters determined at 300 K by single crystal XRD data (see below) evidence several important features (Figure 4.7 (a)). First, the valence band structure is characterized by two main bands located at the M and Z points of the Brillouin zone, in agreement with prior studies. Second, these calculations did not evidence the presence of a band gap due to the overlapping of the conduction and valence bands observed. Thus, these first calculations predict a semi-metallic behavior with a small overlap of the valence and conduction bands. These calculations globally agree with those carried out by Jana *et al.* who reported a slight band overlap at the M point, a band inversion at the Z point. These results tend to show that the positions of the conduction and valence bands near the Fermi level are very sensitive to the details of the calculations and to the exchange-correlation functional used.

Compressing the unit cell does not drastically modify the overlap of the electronic bands at these two points (Figure 4.7 (b)). The main differences observed are a shift towards higher (lower) energies of the valence (conduction) bands.

4.5.2 Lattice dynamics

Phonon dispersion curves were calculated by adopting two strategies: **i)** by using the experimental lattice parameters determined at 300 K and **ii)** by compressing the unit cell volume up to 88 % of its room-temperature value, equivalent to an external pressure of 3 GPa. The simulated phonon spectra related to the two approaches, (Figure 4.8) present some similarities with those reported by Jana *et al.*,[1] with, most notably, the presence of negative phonon energies that appear at the N and Γ points as shown in Figure 4.8 (a).

However, our calculations do not reproduce the unstable branches observed along the Γ – X direction in their study. Despite these differences, our results confirm that the negative energies can be mostly ascribed to the dynamics of the In1 atoms located in the large voids between the octahedra chains. Based on electron localizability indicators, these instabilities have been suggested to arise from the partially-hybridized $5s^2$ lone pairs of the In1 and Te atoms.[1]

Ab-initio calculations of the free energy under pressure (not shown) show that the structure is stabilized upon compressing the unit cell volume. The phonon spectrum obtained (Figure 4.8 (b)) only exhibit positive phonon energies, confirming prior results.[1] A notable difference between our results and those reported in Ref. 1 is related to the low-energy, nearly-flat optical branches along the path Γ – X – M – Γ, which shift towards higher energies in our case. Of note, considering other possible subgroups (such as $P4_2/mcm$ and $P4_2/mmc$), related to the $I4/mcm$ space group reported for InTe but corresponding to a lower symmetry, did not result in the disappearance of the negative phonon energies.

In agreement with prior results,[1] the average sound velocities of the acoustic branches, extracted from the zone center dispersions, are 2916 m s^{-1} and 1670 m s^{-1} for the longitudinal and transverse polarizations, respectively. The transverse acoustic branches merge with low-energy, flat optical branches with energies of around ~ 2.0 and ~ 4.0 meV, at the Γ, M and X points. The longitudinal acoustic branches hybridize with optical branches with energies of around 5 meV.

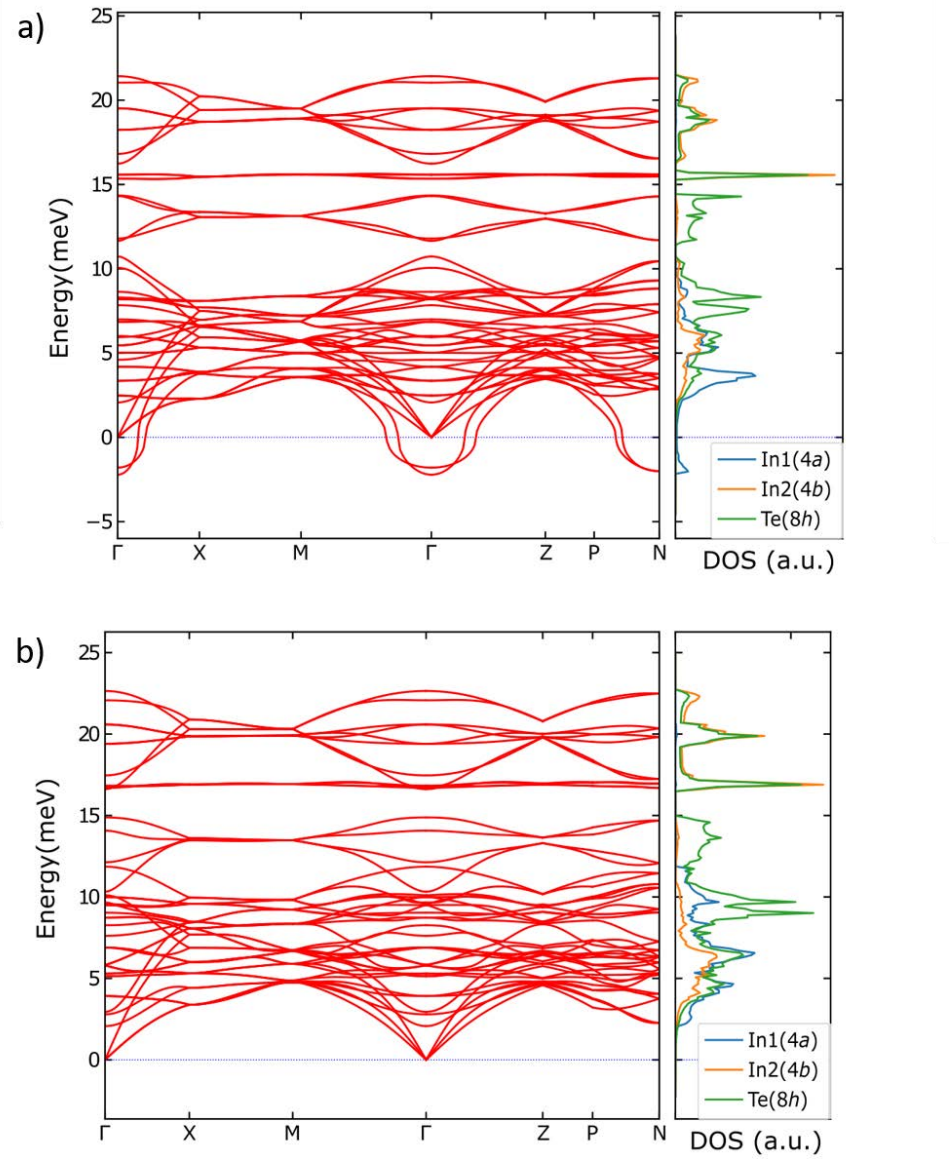

Figure 4.8: Phonon dispersion curves and projected partial phonon density of states of InTe as a function of energy calculated by considering a) a unit cell with experimental room-temperature lattice parameters and b) a pressurized unit cell volume up to 88% of its room-temperature value, equivalent to an external pressure of 3 GPa.

The projection of these dispersion curves on the energy axis yields the phonon density of states (PDOS), shown in Figure 4.8. The results show that the low-energy modes are mainly associated with the atomic motion of In1 atoms, the contribution of which mainly dominates at the lowest energies. This point is in agreement with our single-crystal X-ray diffraction data (see below), evidencing that the In1 atoms exhibit the highest atomic thermal displacement parameters (ADP).[1–4,11] Usually, high ADP reflect the dynamics of loosely-bound atoms and

are associated with low-energy, optical modes in the phonon spectrum, as observed in several cage-like materials or minerals such as tetrahedrites.[30–44]

4.6 Single crystalline InTe

In order to study the structural, chemical and physical properties of single-crystalline InTe, we used the vertical Bridgman-Stockbarger technique to grow a large, centimeter-sized single crystal of InTe. Before describing the synthesis process in detail, we first mention the basic principle and advantages of this technique.

4.6.1 Bridgman-Stockbarger method

This crystal growth technique was first suggested by P. W. Bridgman who used this technique to grow single crystals of metallic elements.[45] The basic principle of this technique remains quite straightforward: it involves lowering an ingot placed inside a crucible through a high-temperature stationary-heater furnace. The temperature of the heater is generally kept a little above the melting point of the material to make sure that a proper liquid-to-solid transition occurs when the crucible passes through the heater. As the crucible is vertically pulled or pushed, the temperature profile of the furnace induces a progressive freezing of the melt in the crucible. The overall process is sketched in Figure 4.9, which shows a possible version of the Bridgman-Stockbarger method. The temperature and speed of the crucible depends on the materials to be grown. However, a slow process and a high temperature gradient at the solidification interface are usually recommended to avoid inhomogeneities at the solid-liquid interface that would yield strongly inhomogeneous crystals for compounds composed of two or more elements. Hence, the speed ideally falls between 0.1 and 200 mm h^{-1} and the temperature gradient higher than 20 K cm^{-1}.[46]

The process of crystal growth based on this technique can be made with or without the use of a seed. A crystal seed is defined as a small piece of single crystal used in addition to the same material inside the crucible to promote and enhance the growth. The crystal seed can be excluded by substituting it with a narrow, V-shaped end of the crucible is placed (see Figure 4.9). This narrow portion of the crucible is required to promote the nucleation process. Once formed, the crystallization process begins and propagates itself until the other part of the ingot. The main point to be considered when using the Bridgman-Stockbarger technique is that the

material should not react with the crucible. Hence, the crucible has to be carefully selected and should show a small thermal expansion coefficient to avoid inducing strain and stress in the crystal upon cooling.

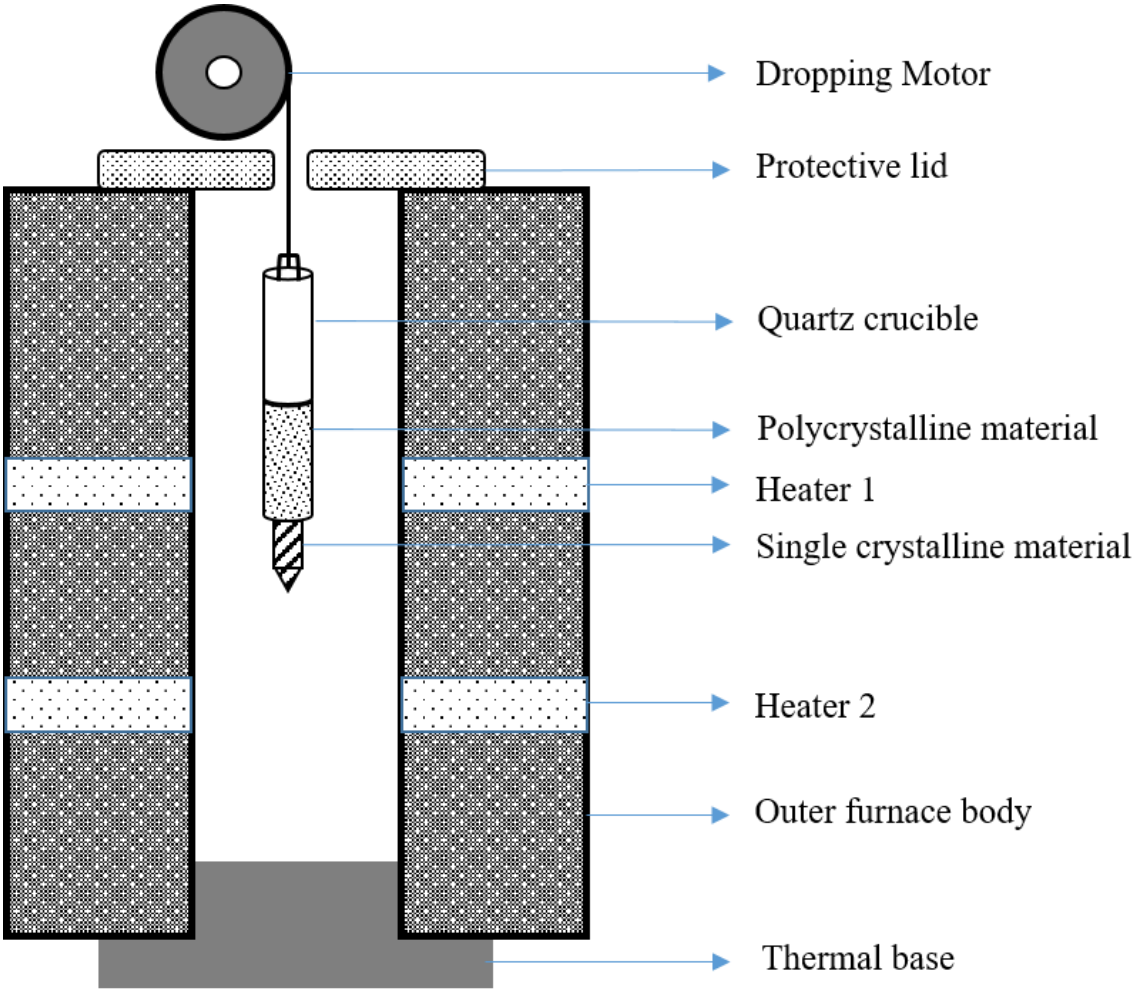

Figure 4.9: Sketch of the vertical Bridgman-Stockbarger growth system. The designed end of the silica ampoule to favor seed growth is schematically represented by a V-shaped end.

4.6.2 Crystal growth of InTe

In this work, we have adopted an unseeded Bridgman-Stockbarger method. The crystal growth of InTe was realized via a two-step process. As a first step, a polycrystalline ingot of InTe with a nominal stoichiometry of 50-50 was prepared by direct reaction of elemental In and Te (Table 4.1) at 750°C in pre-evacuated, sealed silica tubes with outer diameter 18 mm

and thickness of 1.5 mm. Once sealed, the silica tube was placed in a rocking furnace with a heating program as shown in Figure 4.10.

Table 4.1: Summary of the elements used.

Element	Purity (%)	Form	Re-purification
Te	99.999	Granules/ powder	Yes
In	99.999	Shots	Used as received

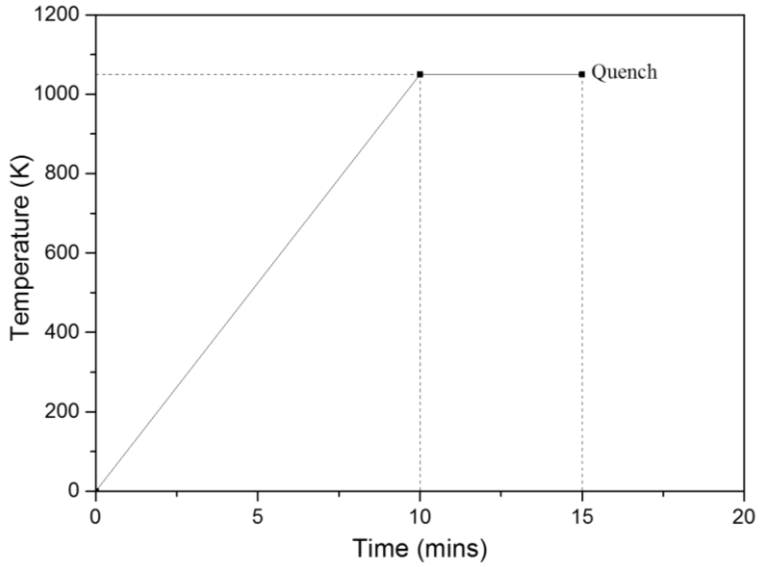

Figure 4.10: Synthesis profile used for polycrystalline InTe.

The silica tube was quenched in room-temperature water and subsequently broken inside a glove box. The surface of the obtained ingot of ~ 13 cm in length and ~ 15 mm in diameter (Figure 4.11) was polished gently using a SiC paper to remove any potential oxides.

Figure 4.11: Prepared polycrystalline InTe ingot before introduction in the carefully-designed V-shaped-end silica tube for Bridgman-Stockbarger process.

After polishing, the ingot was introduced into a special silica tube with outer diameter 18 mm and thickness 1.5 mm, and with a carefully-designed V-shaped end to reduce the number of seeded crystals at the beginning of the solidification. The tube was degassed overnight before sealing it under secondary vacuum. A quartz hook was manually sealed at the top of the silica tube to be hanged on by the hook from the dropping motor. The sealed tube was then placed in a special two-zone furnace used for the crystal growth (Figure 4.12).

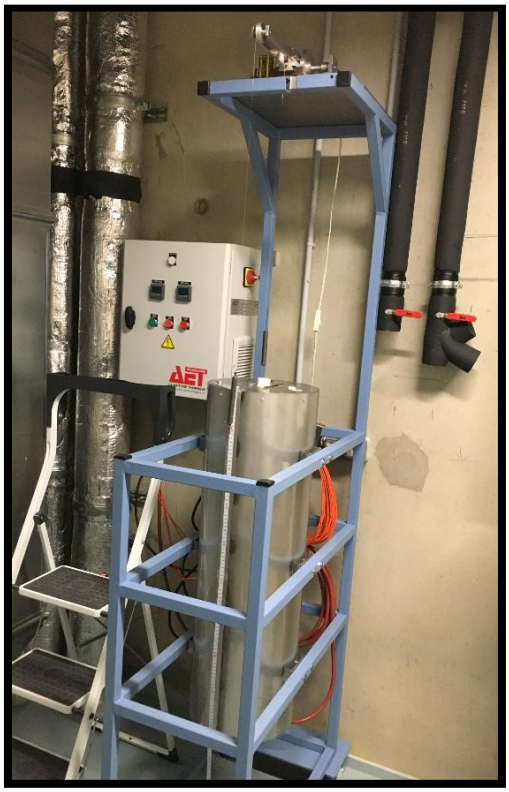

Figure 4.12: Two-zone vertical Bridgman furnace.

The first zone (top of the furnace) was kept at 1000 K while the electrical power of the second zone was kept off to let the crystallization process occurs at a natural cooling rate. It is important to mention that the furnace was calibrated prior to use and the reference temperature of the silica tube was carefully adjusted. The pulling rate (that is, the speed at which the silica tube was lowered) was maintained at a low value of 0.352 mm h^{-1} and the gradient was around 15 K cm^{-1}. The temperature profile of the furnace is shown in Figure 4.13. The longitudinal distance x was considered to be the tip of the tube/sample.

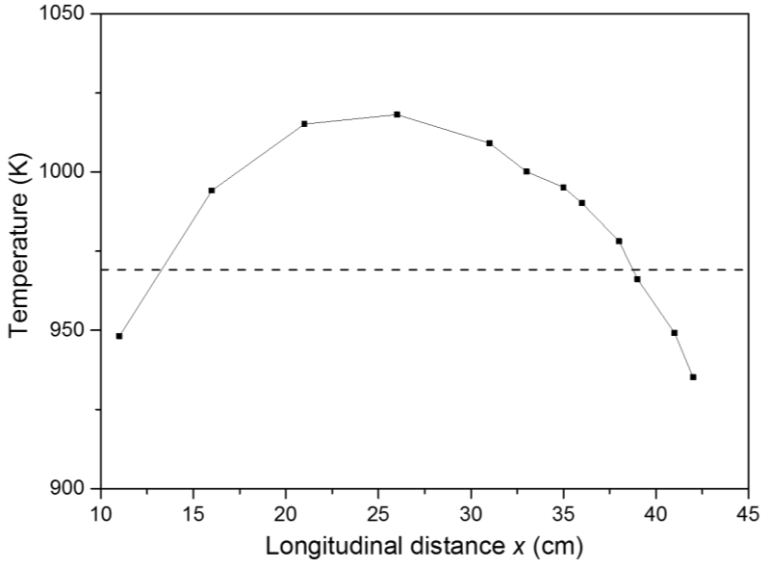

Figure 4.13: Temperature profile of the Bridgman furnace with respect to the longitudinal distance. The dotted line represents the melting point of InTe (~ 970 K). The heater of the furnace was kept at 1000 K.

The furnace was switched off after 30 days while the lowering of the tube was allowed for two additional days. The resulting ingot was ~ 11 cm in length, a part of which is shown in Figure 4.14. As mentioned in prior studies, this ingot tends to easily cleave in a particular direction yielding a mirror-like surface suggesting a single crystalline nature. This breaking/cleavage plane was found to be systematically the same and will be further discussed in the next paragraph.

Figure 4.14: Grown InTe single crystal using the vertical Bridgman technique. The mirror-like cleavage plane is indicated. Note that the other side of the crystal was broken and does not correspond to a natural cleavage plane.

The experimental density of this ingot, determined from its weight and geometrical dimensions, was 6.23 g cm^{-3}, which is in excellent agreement with the values obtained in the

literature for InTe. This value indicates that the ingot was fully dense with a relative density of over ~ 99 %.[15] Noteworthy, even though the ingot was fully dense, it appeared to be very brittle and fragile along the cleavage plane. Thus, cutting samples for transport properties measurements along the direction perpendicular to the cleavage plane was a very challenging task due to its tendency to systematically cleaves during the cutting process. For this reason, cutting samples suitable for all transport properties measurements was not always possible.

4.6.3 Structural and chemical characterizations

The crystal structure, single-crystalline nature and phase purity of the obtained ingot was first analyzed by powder X-ray diffraction using Bruker D8 advance diffractometer at 300 K. Further analysis of structural properties was performed by single crystal X-ray diffraction using a Bruker Kappa APEX II diffractometer at 300 and 80 K. The refinements were carried out using the SHELX software. To confirm the orientation of the cleavage plane, Laue diffraction was performed. The chemical homogeneity and distribution of the ingot was assessed by Scanning Electron Microscope (SEM) with electron dispersive X-Ray spectroscopy (EDXS) using a Quanta FEG microscope. The details and working principle of each technique/instrument in well described in Appendix B.

The PXRD pattern, shown in Figure 4.15, collected on crushed pieces randomly taken from the ingot shows its single-phased nature, with all the peaks being indexed by the tetragonal crystal structure of InTe, described in the *I*4/*mcm* space group. Single-crystal XRD clearly demonstrated the single-crystalline nature of the grown ingot. Refinements against the single-crystal XRD data yielded lattice parameters $a = b = 8.438$ Å and $c = 7.141$ Å at 300 K consistent with those obtained in prior studies.[11,15] These refinements further confirm that the structure is best described in the *I*4/*mcm* space group (Tables 4.2 to 4.6). Refinements of data collected at 80 K are consistent with a lattice contraction expected upon cooling. Interestingly, these results did not provide any signs of structural transition or lattice distortion. Attempts at refining the data measured at 80 K by considering other possible tetragonal space groups resulted in higher reliability factors compared to those achieved when considering the *I*4/*mcm* space group. However, such distortion accompanying charge density waves are often too weak to be observed by this technique that measures an average structure. The development of commensurate or incommensurate lattice distortion can be evidenced by electron diffraction.

Thus, the present data does not necessarily rule out the presence of a lattice distortion near 185 K suggested by Back *et al.*[4]

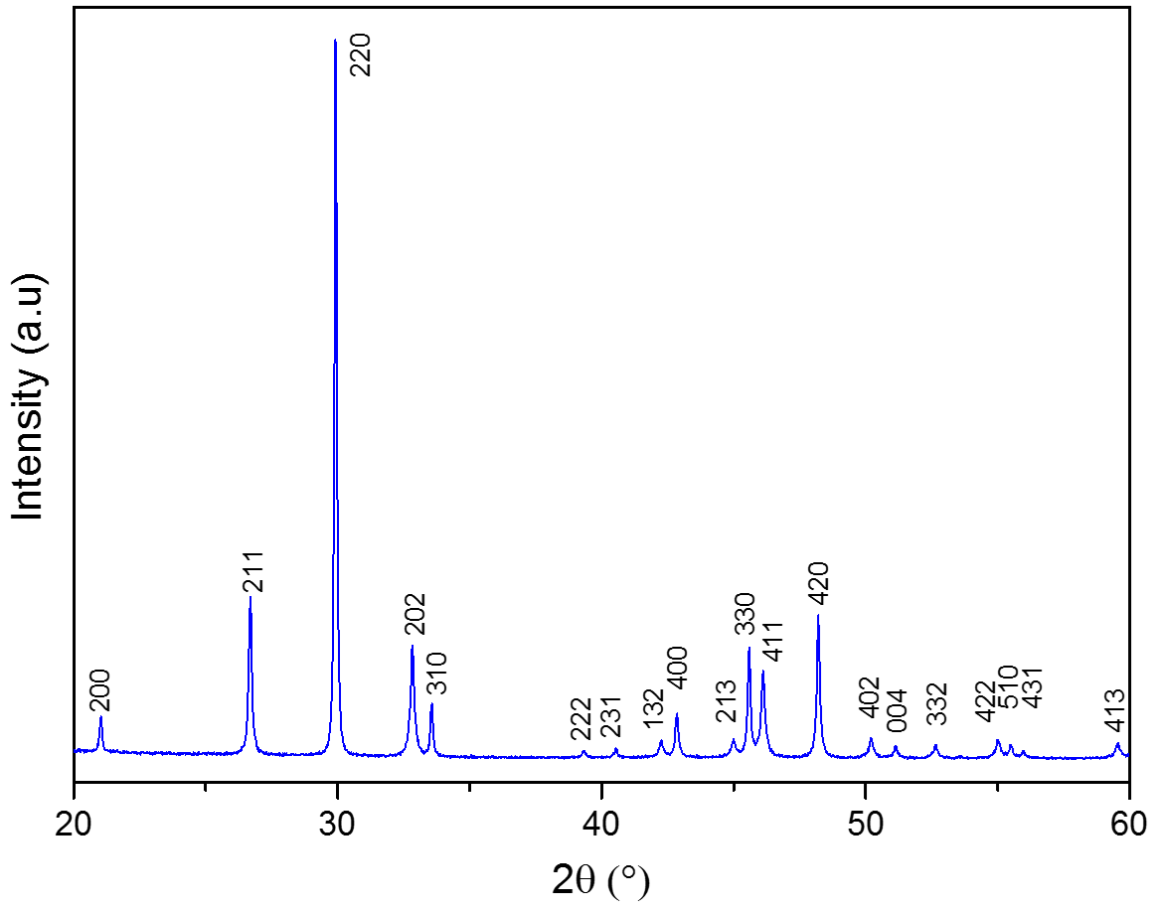

Figure 4.15: PXRD pattern collected on ground single-crystalline pieces of InTe.

The refinements confirm the high anisotropic thermal displacement parameters (ADP) of the In1 atoms located in the tunnels of the crystal structure. The high values of these parameters are consistent with the low-energy features observed in the calculated phonon spectrum associated with the In1 atoms. Within a quantum harmonic oscillator model, if we assume linear temperature dependences of the ADP values between 300 and 80 K, the slope of the $U_{ij}(T)$ curves can be used to infer Einstein temperatures θ_E describing the thermal motions of the In1 atoms following the formula:

Equation 4.1:

$$U_{ij}(T) = \frac{h^2 T}{4\pi^2 m k_B \theta_E^2}$$

where h is the Planck constant, k_B is the Boltzmann constant and m is the mass of the atoms expressed in a.m.u. This relation yields θ_E values of 34.3 and 29.2 K for $U_{11} = U_{22}$ and U_{33}, respectively. These values correspond to 2.96 and 2.52 meV, respectively. These values are in reasonable agreement with the lowest energy peak seen in the phonon spectrum near 2.5 meV.

Table 4.2**:** Crystal data and structure refinements of single-crystalline InTe at 300 K and 80 K.

Temperature (K)	**300 K**	**80 K**
Molar mass (g mol^{-1})	242.42	242.42
Symmetry	Tetragonal	Tetragonal
Space group	I4/mcm	I4/mcm
***a* (Å)**	8.438 (1)	8.345 (3)
***c* (Å)**	7.141 (1)	7.107 (3)
***V* (Å^3)**	508.46 (2)	498.50 (2)
Z	8	8
ρ_{calc} (g cm^{-3})	6.33	6.46
***2θ* range (°)**	1.60 – 98.23	1.64 – 72.89
Radiation (Å)	Mo Kα; λ = 0.71073	Mo Kα; λ = 0.71073
Absorption coefficient (mm^{-1})	20.12	20.53
Index range	- 15 ≤ h ≤ 17 - 17 ≤ k ≤ 17 - 15 ≤ l ≤ 15	- 11 ≤ h ≤ 14 - 12 ≤ k ≤ 12 - 11 ≤ l ≤ 11
Data/restraints/parameters	9274 / 0 / 717	4486 / 0 / 349
R indices [F_o>4σ(F_o)]	R1 = 0.0255 wR2 = 0.0431	R1 = 0.0542 wR2 = 0.1082
Goodness-of-fit on F^2	2.041	2.436

Table 4.3. Atomic coordinates and equivalent isotropic displacement parameters (Å^2) for single-crystalline InTe at 300 K. U_{eq} is defined as one-third of the trace of the orthogonalized U_{ij} tensor.

Atom	*x*	*y*	*z*	U_{eq}
In1	0	0	0.25	0.0539(2)
In2	0	0.5	0.25	0.0177(1)
Te	0.18223(2)	-0.31777(2)	0	0.0167(1)

Table 4.4. Anisotropic thermal displacement parameters (Å^2) for single-crystalline InTe at 300 K. By symmetry, U_{23}, U_{12} and U_{13} are equal to zero for In1 and In2 atoms.

Atom	U_{11}	U_{22}	U_{33}	U_{12}
In1	0.0424(3)	0.0424(5)	0.0770(6)	0
In2	0.0214(1)	0.0214(1)	0.0103(1)	0
Te	0.0172(1)	0.0172(1)	0.0156(1)	-0.0025(1)

Table 4.5. Atomic coordinates and equivalent isotropic displacement parameters (Å^2) for single-crystalline InTe at 80 K. U_{eq} is defined as one-third of the trace of the orthogonalized U_{ij} tensor.

Atom	*x*	*y*	*z*	U_{eq}
In1	0	0	0.25	0.0245(5)
In2	0	0.5	0.25	0.0071(4)
Te	0.18351(9)	-0.31649(9)	0	0.0070(3)

Table 4.6. Anisotropic thermal displacement parameters (Å^2) for single-crystalline InTe at 80 K. By symmetry, U_{23}, U_{12} and U_{13} are equal to zero for In1 and In2 atoms.

Atom	U_{11}	U_{22}	U_{33}	U_{12}
In1	0.0194(8)	0.0194(8)	0.035(1)	0
In2	0.0097(6)	0.0097(6)	0.020(5)	0
Te	0.0089(4)	0.0089(4)	0.003(3)	-0.0010(4)

In order to determine the orientation along which the InTe singe crystal grew, a large piece of the crystal was placed on a three-axis goniometer head with the natural cleavage surface facing the detector of the Laue diffractometer. The diffraction patterns obtained were analyzed using the Orientex software, which enables superimposing the experimental and the calculated patterns (red dots in Figure 4.16). These analyses demonstrated that the cleaved surface corresponds to the (110) plane, that is, parallel to the *c*-axis of the crystal structure. The growth direction was confirmed to be along the [111] direction.

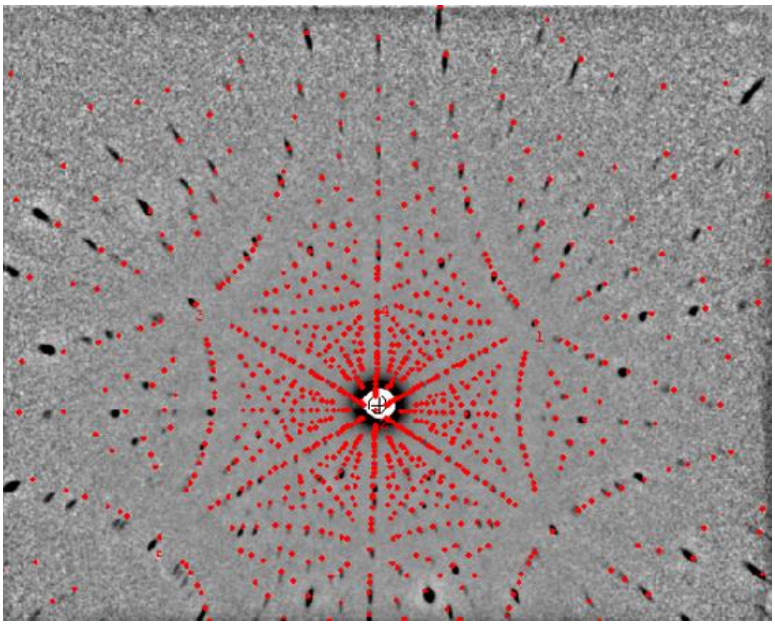

Figure 4.16: Laue diffraction pattern of the cleavage plane confirming (110) plane orientation.

The crystal was subsequently orientated and different samples were cut for physical property measurements (explained in detail in Appendix A). It is important to mention that all the patterns were clear and uniform indicating high crystallinity of the grown crystal. Elemental X-ray mapping showed a homogenous distribution of In and Te (Figure 4.17), revealing the good chemical homogeneity of our grown crystal.

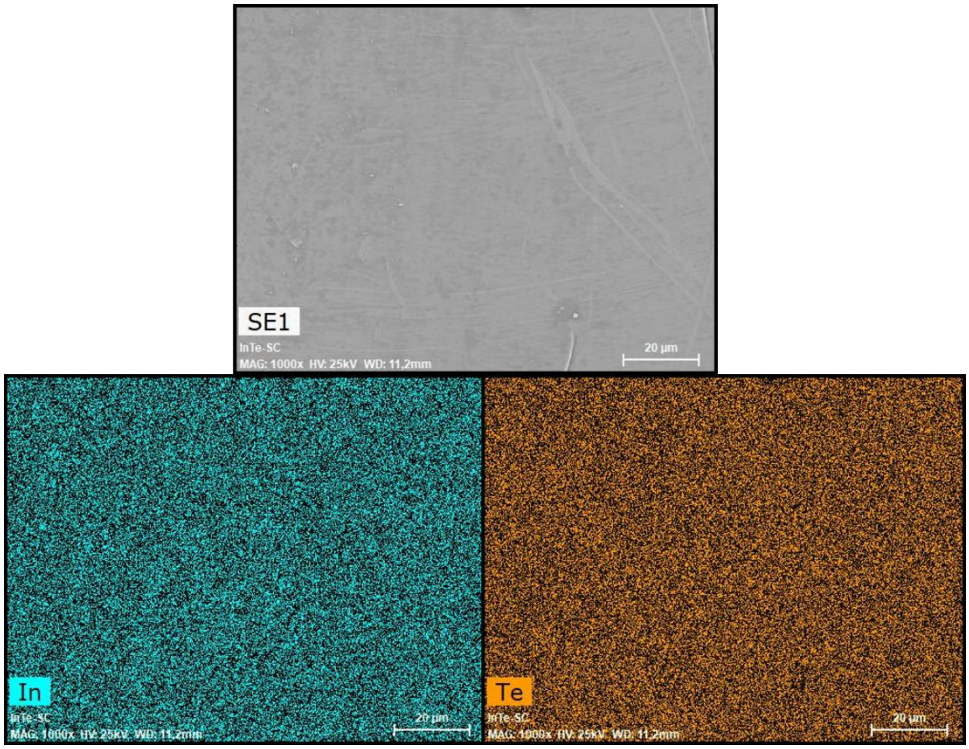

Figure 4.17: Elemental mapping for single crystalline InTe performed by SEM-EDXS analysis.

4.6.4 Specific heat capacity of single crystalline InTe

In agreement with recent specific heat measurements performed on polycrystalline InTe,[3] the temperature dependence of the specific heat C_p for single crystalline InTe, shown in Figure 4.18, does not evidence any obvious signatures of a lattice distortion that would accompany a CDW transition developing at 185 K. Moreover, no specific peak at 185 K is observed, that might correspond to a first-order, second-order (lambda-type anomaly), or a second-and-a-half-order (Lifshitz transition) phase transition. The measured values at room temperature were in excellent agreement with the Dulong-Petit values as could be seen in Figure 4.18. Hence, at higher temperatures (> 300 K) the values estimated by the Dulong-Petit law were used. Of note, additional measurements performed on a polycrystalline dense piece of InTe (see below) led to similar results. Thus, the origin of the recently-observed, possible transition at 185 K remains to be elucidated.

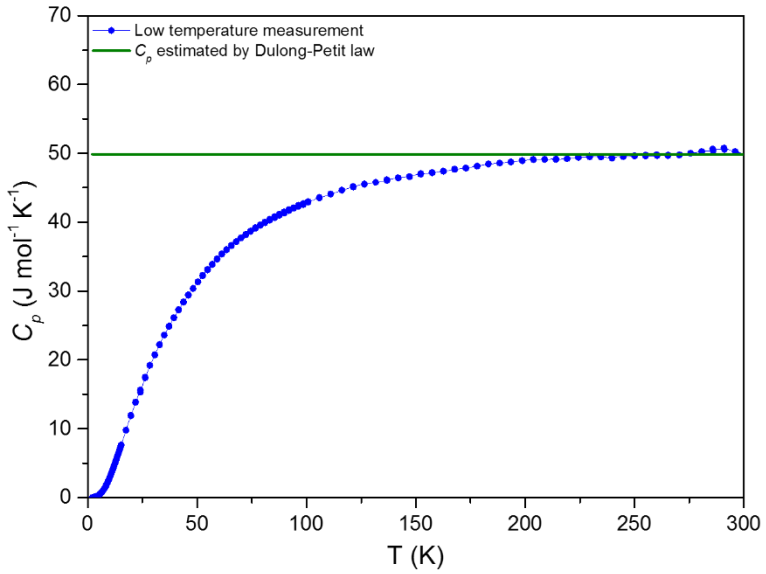

Figure 4.18: Temperature dependence of the specific heat C_p of single-crystalline InTe. The Dulong-Petit value is represented by the horizontal solid line.

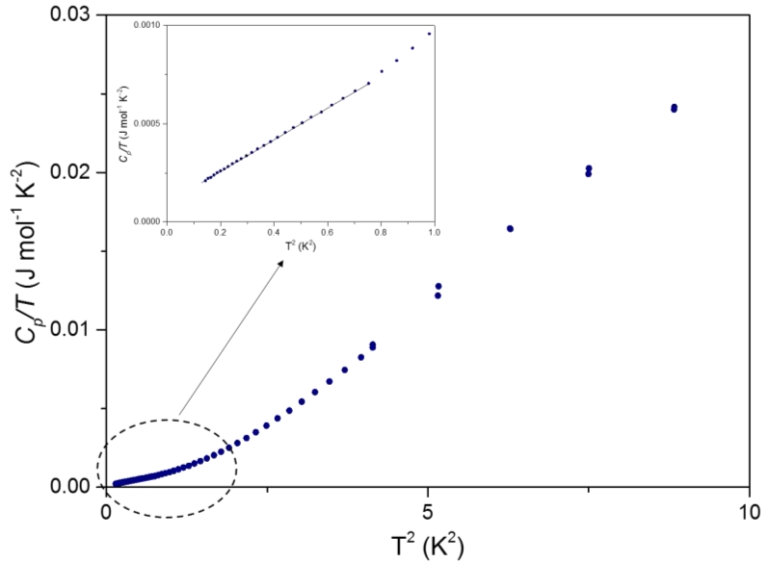

Figure 4.19: C_p/T as a function of T^2 for single-crystalline InTe measured using the ^{3}He option of the PPMS. Inset shows the magnification of the low-temperature data for T^2 values lower than 1 K^2. The black solid line represents the best linear fit to the data.

The low-temperature $C_p(T)$ data was further analyzed using the relation $C_p/T = \gamma + \beta T^2$ where γ is the Sommerfeld coefficient corresponding to the electronic contribution and βT^2 is the phononic contribution with the β parameter being related to the Debye temperature θ_D by the relation $\theta_D = (12\pi^4 NR/5\beta)^{1/3}$ where N is the number of atoms per formula unit ($N = 2$ for InTe) and R is the gas constant (Figure 4.19). The best fit to the data between 0.02

and 0.8 K^2 yields a γ value of 9.74×10^{-5} J mol^{-1} K^{-2} (see inset in Figure 4.19), which is of the same order of magnitude as that of elemental bismuth, indicating the presence of a finite density of states at the Fermi level, in agreement with the semi-metallic nature of InTe suggested by our electronic band structure calculations and the metallic-like temperature dependence of the electrical resistivity (see below). The θ_D value of 169 K inferred is similar to those of other chalcogenide semiconductors such as SnTe (~ 140 K) or PbTe (~ 175 K) and with the value of 200 K estimated from $C_p(T)$ measurements by Zhu *et al.*[3]

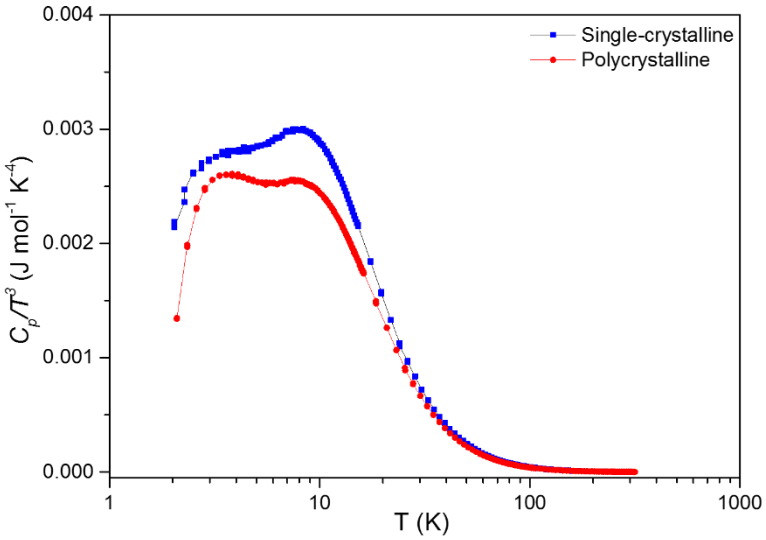

Figure 4.20: C_p/T^3 as a function of T for single-crystalline and polycrystalline InTe measured using the ^{4}He option of the PPMS system. No subtraction of the electronic contribution γT has been performed.

One intriguing aspect that marks InTe as distinct among chalcogenide semiconductors is revealed by the $C_p(T)$ data plotted as C_p/T^3 versus T to highlight low-temperature deviations from the Debye model typified by an excess specific heat usually peaking around 10 K (Figure 4.20). This excess is related to low-energy optical phonon modes that play an important role in determining the thermal transport. In the present case, the data evidence the presence of two, well-defined low-temperature peaks at 3.5 and 8 K, which contrast with a single peak usually observed. Of relevance is the fact that a similar behavior is observed on the data collected on a polycrystalline sample (see Figure 4.20), making this double-peak structure a robust property of InTe.

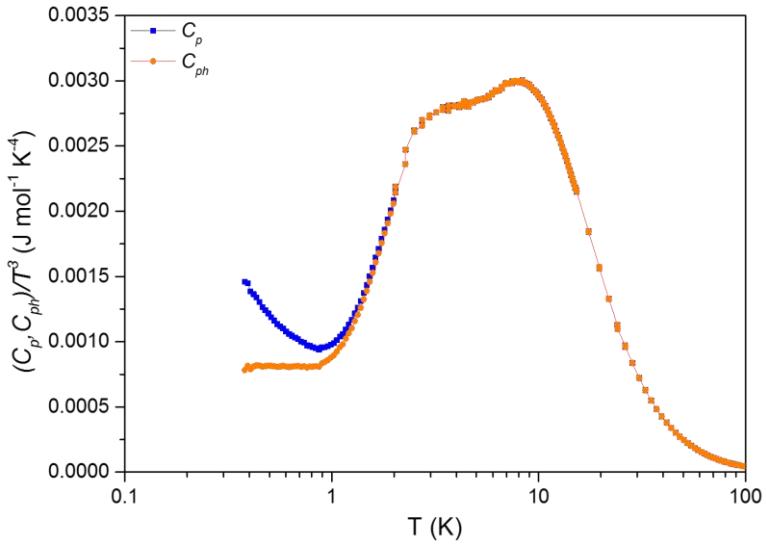

Figure 4.21: C_p/T^3 as a function of T for single-crystalline InTe measured down to 0.35 K. Subtraction of the electronic contribution γT has been performed, yielding the lattice contribution C_{ph}.

We further tried to describe the $C_p(T)$ data within the Debye theory assuming that the vibrations responsible for this double-peak structure can be modelled by Einstein-like contributions in addition to the framework vibrations modelled as Debye oscillators. This model is similar to that used by Zhu *et al.* in their study.[3] This model was implemented on the C_p/T^3 vs T plot after subtracting the electronic contribution from the total specific heat capacity, shown in Figure 4.21. This analysis, notably used in cage-like materials, allows for distinguishing between atoms considered as rattlers and the other atoms forming the rigid framework. Because the rattling ions are those exhibiting the highest thermal displacement parameters inferred from single-crystal X-ray diffraction, only the In1 atoms were considered as rattlers while the In2 and Te atoms were treated as Debye oscillators. Within these assumptions, the $C_p(T)$ data were modelled by the relation:

Equation 4.2:

$$C_p = C_D + C_{Ei} = 9N_D R\left(\frac{T}{\theta_D}\right)^3 \int_0^{\theta_D/T} \frac{x^4 e^x}{(e^x-1)^2} dx + \sum_i p_i N_{Ei} R \left(\frac{\theta_{Ei}}{T}\right)^2 \frac{e^{\theta_{Ei}/T}}{(e^{\theta_{Ei}/T}-1)^2}$$

where C_D is the lattice contribution within the Debye model, C_{Ei} is the Einstein contribution of the i^{th} vibrational mode of the rattling atoms, $x = \hbar\omega/k_B T$ with $\hbar$ the reduced Planck constant

and k_B the Boltzmann constant, N_D is the number of Debye oscillators per formula unit and $p_i N_{Ei}$ and θ_{Ei} are the spectral weight and Einstein temperature related to the i^{th} vibrational mode, respectively.

We used two Einstein terms to model the two distinct peaks in $C_p(T)$ (see Figure 4.21). Considering θ_D, N_D, $p_1 N_{E1}$, θ_{E1}, $p_2 N_{E2}$ and θ_{E2} as free parameters, the best fit to the data yielded $\theta_D = 148$ K, $N_D = 1.464$, $p_1 N_{E1} = 0.039$, $\theta_{E1} = 15.1$ K, $p_2 N_{E2} = 0.992$ and $\theta_{E2} = 46$ K for the single-crystalline specimen. For the polycrystalline samples, a similar analysis gives $\theta_D = 111$ K, $N_D = 0.81$, $p_1 N_{E1} = 0.047$, $\theta_{E1} = 18$ K, $p_2 N_{E2} = 0.716$ and $\theta_{E2} = 49.8$ K. These two sets of values, consistent with each other, suggests that low-energy features characterize the phonon density of states with characteristic energies of around 1.5 meV and 4.3 meV corresponding to the Einstein temperatures θ_{E1} and θ_{E2}, respectively. These values are lower than those obtained by Zhu *et al.*[3] who found the lowest Einstein temperatures to be around 30 K.

The low-energy modes inferred from the $C_p(T)$ data are in fair agreement with our phonon calculations predicting the presence of low-energy optical modes in the phonon density of states at 2 meV and 4 meV. The presence of these modes, consistent with the large thermal motion of the In1 cations evidenced by refinements of the single-crystal X-ray diffraction data, likely plays an important role in shaping the main traits of the thermal transport in InTe. In particular, the low lattice thermal conductivity can be explained by the strongly-limited phase space available for the acoustic branches, contributing to decrease the acoustic sound velocities. Furthermore, low-energy optical modes open novel channels of Umklapp processes, which also contribute to limiting the heat transport above the Debye temperature.

4.6.5 Transport properties

Because InTe crystallizes in a quadratic system, that is, in an uniaxial system, the number of independent coefficients of tensors describing either the electrical or the thermal properties is limited to two: one along the *c*-axis and one perpendicular to it (within *ab* plane). As mentioned above, the high fragility of the singe crystal in the direction perpendicular to the (110) cleavage plane prevented its transport properties from being measured along the two interesting directions of the crystal structure. Nevertheless, we managed to cut two samples: one along the *c*-axis for low and high-temperature measurements, and one bar-shaped sample perpendicular to the *c*-axis for high-temperature measurements.

We will focus in this part on the transport properties measured in a wide range of temperatures (5 – 800 K). Hereafter, the sample cut along the *c* axis parallel to the (110) plane will be referred to as "parallel" and the sample cut perpendicular to the *c* axis, that is, along the [110] direction, will be referred to as "perpendicular".

4.6.5.1 Low-temperature transport properties

We first consider the transport properties measured parallel to the *c* axis. The temperature dependence of the electrical resistivity ρ and thermopower α are shown in Figures 4.22 (a) and 4.23 (b), respectively. $\rho(T)$ increases quasi-linearly with increasing T indicative of a metallic character. Despite the single-crystalline nature of the sample, the residual ρ value of ~ 40.5 μΩm is high and in agreement with the values measured on polycrystalline InTe.[4] This first results seems to be in agreement with a semi-metallic ground state predicted by our electronic band structure calculations but at odds with the specific heat measurements suggesting a γ value of zero. This seeming contradiction may be due to a very low density of states at the Fermi level giving rise to a very small γ value, as observed for instance in elemental Bi. In such a case, additional specific heat measurements down to 0.35 K may be necessary to better resolve a possible residual γ value.

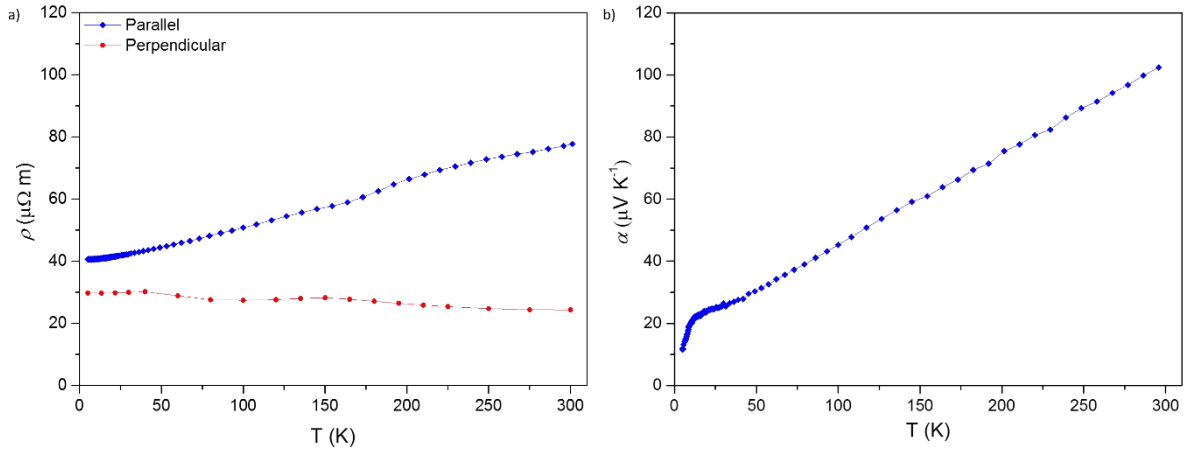

Figure 4.22: Temperature dependence of a) the electrical resistivity measured along the *c* axis and along the [110] direction and b) the thermopower measured along the *c* axis for single-crystalline InTe. The solid curves are guides to the eye.

Upon warming, the values further increase to reach 77.8 μΩm at 300 K. These high ρ values may be due to very low mobility of the charge carriers combined with a relatively low carrier concentration, consistent with a semi-metallic state suggested by our electronic band structure calculations. The behavior observed near room temperature strongly differs from that observed by Back *et al.*[4], which evidences a metal-semiconductor transition around 185 K. Electrical resistivity measured along the [110] axes showed a similar behaviour with a change of slope observed around 175 K. Although the values remained nearly temperature independent, the value of ~ 24 μΩm measured at 300 K slightly increases to 29.7 μΩm upon cooling to 5 K.

In our case, we nevertheless observe a change of slope near this temperature, possibly indicating the presence of a structural distortion accompanying a CDW transition. Such a transition implies a restructuration of the Fermi surface due to the partial removal of the density of states at the Fermi level on crossing the transition temperature. This drastic change in the Fermi surface should impact the temperature dependence of the thermopower, which is a sensitive probe of the Fermi surface and of any change in its topology upon cooling, under applied magnetic fields or external pressure. However, as seen in Figure 4.22 (b), $\alpha(T)$ does not show any evident sign of this type of transition near 185 K. If a CDW transition indeed sets in near 185 K, its impact on the Fermi surface should be thus weak enough to be practically undetectable in $\alpha(T)$.

The positive sign of the α values is consistent with the *p*-type electrical conduction observed in polycrystalline samples in prior studies and with our electronic band structure calculations. α decreases linearly upon cooling from 103 μV K^{-1} at 300 K down to 30 μV K^{-1} at 50 K. This behavior is in agreement with the degenerate nature of transport of InTe indicated by the $\rho(T)$ data. Both the *p*-type nature of the electronic properties and the relatively high α values measured suggest the presence of a small concentration of defects in InTe. This is in contrast to SnTe for which the more metallic character of the transport is due to a large concentration of Sn vacancies, as discussed in Chapter 3. The *p*-type conduction in InTe might be related to a small concentration of In vacancies, although the presence of antisite defects cannot be ruled out. Further energy defect calculations will be important to determine the dominant type of defects in InTe. Below 50 K, $\alpha(T)$ presents a maximum around 20 K before strongly decreasing upon further cooling. This low-temperature behavior is reminiscent to what was observed in the SnTe samples at similar temperatures. By analogy, this behavior thus

suggests the presence of a phonon-drag contribution superimposed to the diffusive term that evolves linearly with temperature.

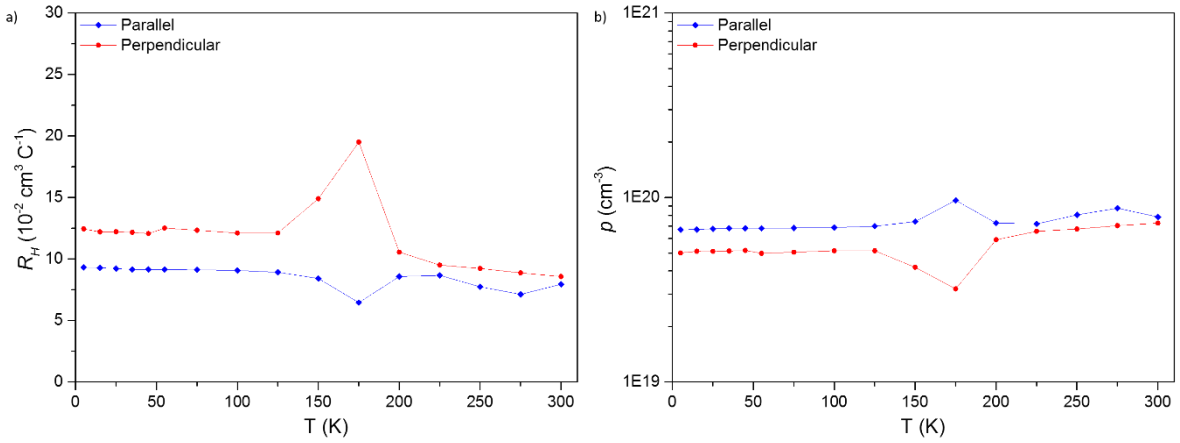

Figure 4.23: Temperature dependence of a) Hall coefficient and b) carrier concentration for single-crystalline InTe. The solid lines are guide to the eye.

Figure 4.23 shows the temperature dependence of the Hall coefficient R_H and of the hole concentration measured along the two directions. The positive sign of R_H indicates the dominant role of hole-like contribution, which is in good agreement with the positive sign of the thermopower (Figure 22 (b)). An observable but weak anisotropy was observed between both directions (Figure 4.23 (a)). Hence, the use of the single-carrier formula $p = 1/R_H e$ is reasonable in the present case. At 300 K, the hole concentration was measured to be ~ 7.5×10^{19} cm^{-3} along both directions, remaining almost independent of temperature across the entire temperature range (Figure 4.23 (b)). However, a clear hump can be observed along both directions around 175 K, which also observed in the electrical resistivity (Figure 4.22 (a)). This hump was attributed by Back *et al.* to be the tetragonal-to-orthorhombic structural transition. Further studies would be required to fully understand the nature of this anomaly.

Due to significant anisotropy observed in the electrical resistivity data, the Hall mobility showed an anisotropy ratio close to 3.5 at 300 K (Figure 4.24). At 300 K, μ_H is equal to 10.2 cm^2 V^{-1} s^{-1} and 35.2 cm^2 V^{-1} s^{-1} along the *c* and [110] directions, respectively. This anisotropy in μ_H is in good agreement with previous reports on single-crystalline InTe. Due to the shoulder present in the electrical resistivity and Hall coefficient, a similar sharp hump was observed in the μ_H data near ~ 175 K, as shown in Figure 4.24. While μ_H tends to remain temperature independent up to about 100 K, the values start to decrease upon heating above this

temperature. Furthermore, a similar scattering mechanism was observed along both directions, with $\mu_H(T)$ following a $T^{-0.5}$ law characteristic of alloy scattering.

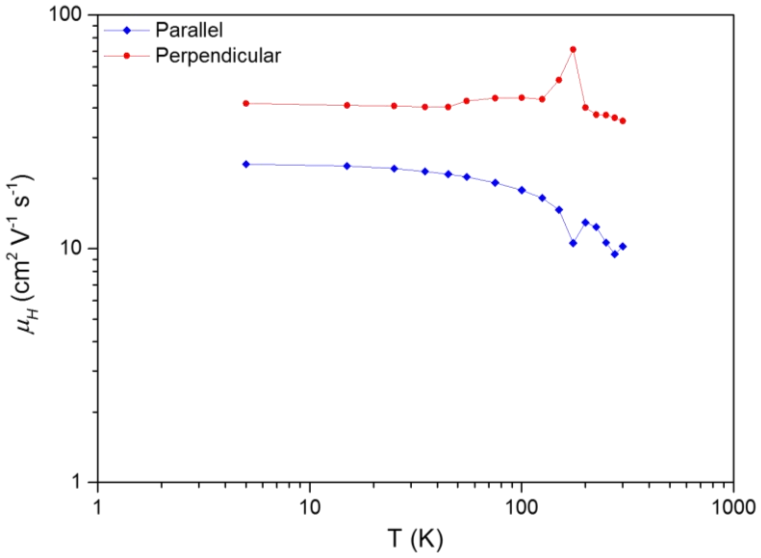

Figure 4.24: Temperature dependence of the Hall mobility μ_H for single-crystalline InTe. The solid lines are guide to the eye.

The temperature dependence of the total (κ) and lattice thermal conductivity (κ_{ph}) is shown in Figure 4.25. Because of the rather high ρ values, the electronic contribution is small across the entire temperature range and hence, as a first approximation, κ can be considered as being nearly equivalent to the lattice contribution κ_{ph}. The room-temperature value of 1.2 W m^{-1} K^{-1} is higher than that measured in polycrystalline samples due to the absence of grain boundary scattering in single crystals.[1–4] Upon cooling, $\kappa_{ph}(T)$ smoothly increases up to about 2 W m^{-1} K^{-1} around 50 K. At this temperature, a strong upturn in the temperature dependence in observed, with the κ_{ph} values rising rapidly down to the lowest temperature measured where $\kappa_{ph} \approx 6.5$ W m^{-1} K^{-1}. The maximum, that would correspond to the Umklapp peak, is not yet reached at 5 K, although the slight change in the slope observed near 5 K suggests that a maximum would be probably attained slightly below this temperature. The presence of an Umklapp peak contrasts with the glass-like temperature dependence observed in some single-crystalline thermoelectric materials such as tetrahedrites or clathrates in which no Umklapp peak is observed at low temperatures. In InTe, the fact that the Umklapp peak is shifted towards very low temperatures is consistent with the very low Debye temperature of 109 K inferred from the $C_p(T)$ data as mentioned in the previous section. The value of the Debye temperature

is lower than that used by Zhu *et al.* for their polycrystalline InTe sample.[3] Their observation of an Umklapp peak at ~ 19 K, that is, at a significantly higher temperature than in our samples,[3] is related to the presence of grain boundary scattering in their sample, which limits the heat transport at low temperatures.

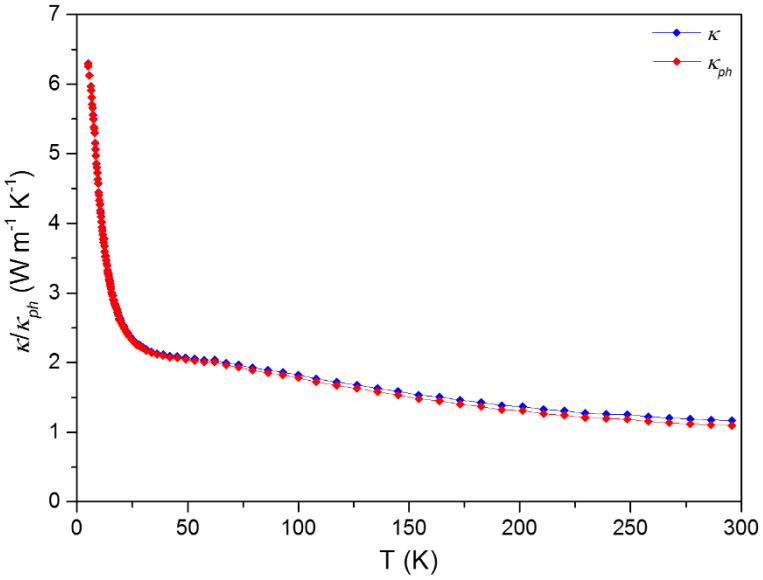

Figure 4.25: Temperature dependence of the total and lattice thermal conductivity of single-crystalline InTe measured along the c axis.

4.6.5.2 High-temperature transport properties

The temperature dependence of the electrical resistivity of single-crystalline InTe measured between 300 and 800 K along the *c* direction and along the [110] direction is shown in Figure 4.26 (a). In agreement with the low-temperature data, both samples show metallic behavior with values increasing as the temperature increases from 24.4 μΩm and 77.8 μΩm at 300 K to 67.8 μΩm and 182.2 μΩm at ~ 790 K along the [110] and *c* directions, respectively. These measurements further evidence a clear anisotropy in the $\rho(T)$ data. The anisotropy ratio, defined as the ratio between the ρ values measured in each direction, is equal to around 3.2 at 300 K and decreases to 2.8 at 800 K.

Figure 4.26 (b) shows the temperature dependence of the thermopower measured in both directions. $\alpha(T)$ increases with increasing temperature in both directions up to about 600 K. α reaches 179 and 170 μV K^{-1} at 765 and 780 K, respectively, along the *c* and [110] direction, respectively. Above this temperature, the α values tend to level off along the *c* direction,

eventually peaking near 700 K before slightly decreasing upon further warming. In contrast, the α values measured in the other direction increase monotonically up to 780 K. A tendency towards leveling off is nevertheless discernable at the highest temperature, suggesting that a maximum would be reached at slightly higher temperatures. Interestingly, while the thermopower is often isotropic in materials crystallizing in an anisotropic structure, α shows some anisotropy in InTe over the entire temperature range. The anisotropy is similar to that observed in the $\rho(T)$ data, that is, the highest ρ values correspond to the highest α values.

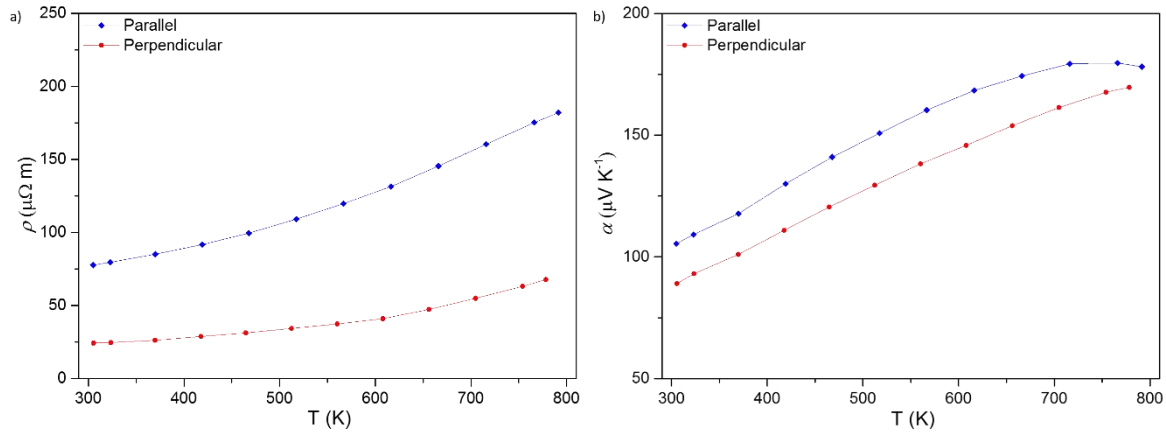

Figure 4.26: Temperature dependence of the a) electrical resistivity ρ and b) thermopower $\alpha(T)$ for single-crystalline InTe measured along the c axis (parallel) and along the [110] direction (perpendicular). The solid lines are guides to the eye.

The fact that α is not strictly equivalent in these two directions indicates an asymmetry in the electron-hole density-of-states effective masses due to asymmetric dispersions of the valence and conduction bands, in agreement with our electronic band structure calculations. The presence of a maximum in $\alpha(T)$ suggests that minority carriers start playing a prominent role above 700 K. Using the Goldsmid-Sharp relation $E_g = 2e\alpha_{max}T_{max}$, which relates the thermal band gap E_g to the maximum thermopower value α_{max} reached at the peak temperature T_{max}, yields $E_g = 0.25$ eV. This value contrasts with the absence of a band gap in our band structure calculations or the calculations performed in prior studies. This value is, however, in good agreement with the calculations performed by Back *et al.* at 300 K, indicating an indirect band gap of 0.3 eV. However, these calculations were performed for a strongly Te-deficient sample ($InTe_{0.75}$) and whether this result can be extended to our present sample is nevertheless questionable.

Due to the high ρ values, a moderate value of the power factor α^2/ρ is achieved (Figure 4.27). The anisotropy observed in both ρ and α results in anisotropic power factors with an average anisotropy ratio of 2.4. A maximum value of 0.52 mW m^{-1} K^{-2} is achieved at ~ 600 K along the [110] direction. Above this temperature, the values tend to decrease with increasing temperature due to the high ρ values and the downturn in α.

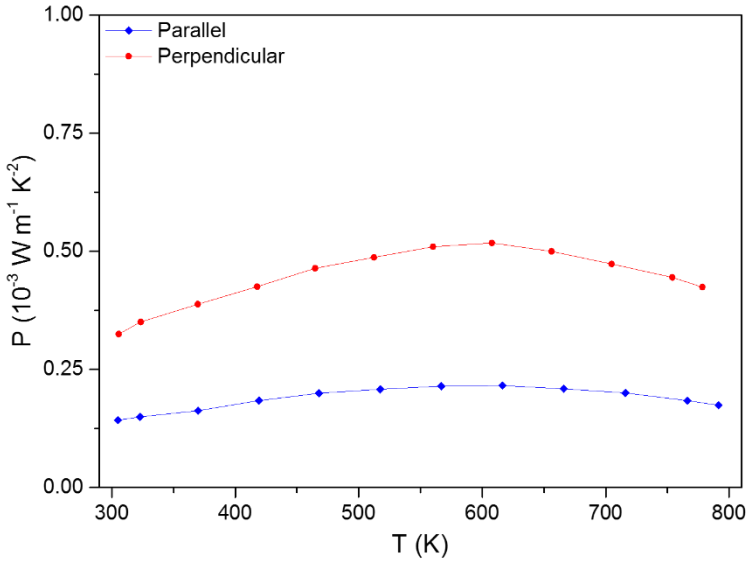

Figure 4.27: Power factor as a function of temperature for single-crystalline InTe. The solid lines are guide to the eye.

Figure 4.28 shows the temperature dependence of the total thermal conductivity κ. The room-temperature κ value of 0.71 W m^{-1} K^{-1} further decreases to 0.46 W m^{-1} K^{-1} at 800 K. This value is in good agreement with that obtained by Jana *et al.* for polycrystalline InTe.[1] The lattice thermal conductivity κ_{ph}, calculated by the Wiedemann-Franz law using a single-parabolic-band model with acoustic phonon scattering to calculate the Lorenz number, reaches an extremely low value of 0.26 W m^{-1} K^{-1} at 800 K, in agreement with prior studies on polycrystalline samples.

The temperature dependence of the *ZT* values for the sample cut perpendicularly to the *c* axis is shown in Figure 4.29. Due to the relatively high power factor and, most notably, the very low thermal conductivity, a peak *ZT* value of 0.71 has been achieved at ~ 780 K, a promising value that may be further optimized in polycrystalline samples, discussed in the next paragraph.

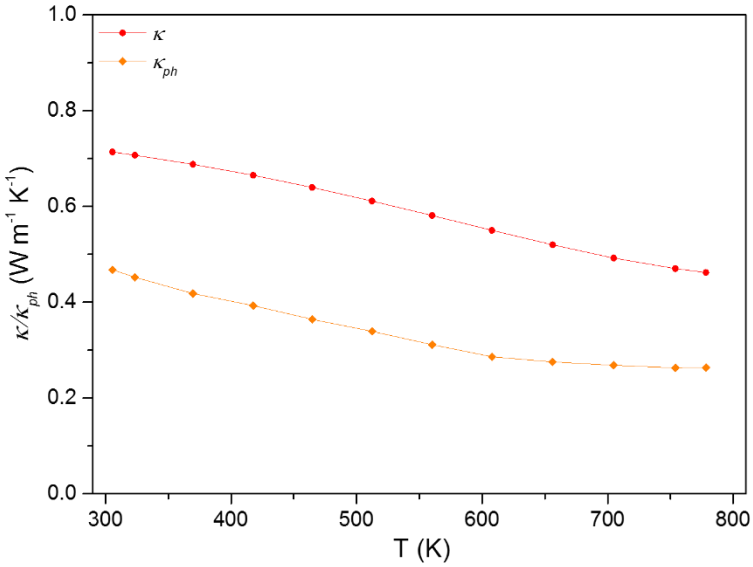

Figure 4.28: Temperature dependence of the total thermal conductivity κ and lattice thermal conductivity κ_{ph} measured in the perpendicular direction (along ab axes). The solid lines are guide to the eye.

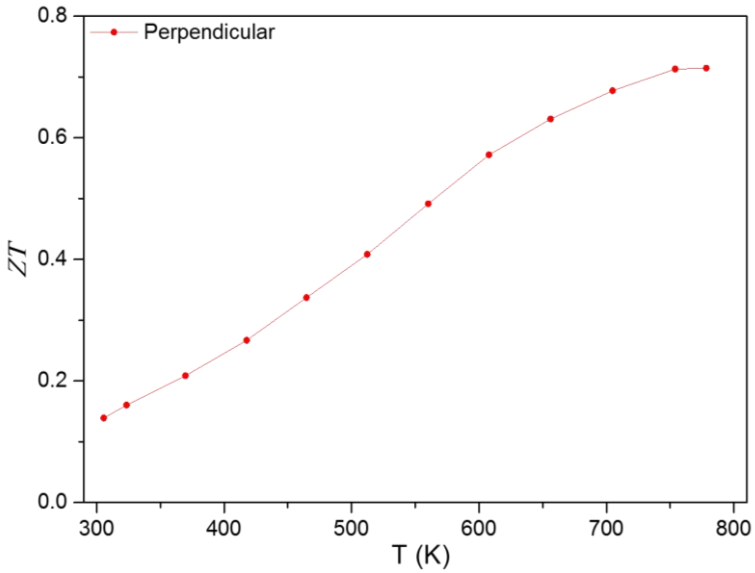

Figure 4.29: Temperature dependence of the dimensionless thermoelectric figure of merit ZT for single-crystalline InTe measured along the ab axes (perpendicular sample). The solid lines are guide to the eye.

4.7 Polycrystalline InTe

4.7.1 Saturation Annealing

According to the phase rule, the thermodynamic state of a binary compound in equilibrium with its vapor is not solely defined by the temperature. An additional parameter is required to determine the state of the system. This could be either the partial pressure of one of the components or the deviation of the composition from the ideal stoichiometry. The Gibb's phase rule provides a direct relationship between these different parameters:

Equation 4.3:

$$F = C - P + 2$$

where F is the number of degrees of freedom or variance of the system, C is the number of components and P is the number of phases present in the system. Applying this rule to InTe, which inherently shows deviations from the ideal stoichiometry, yields $F = 1$ as the number of components is 2 (In and Te) and P is equal to 3 at high temperatures (solid, liquid and gas). Hence, it is clear that either the pressure or the temperature fixes the equilibrium state of the system.

Saturation annealing is the technique of choice to precisely control the deviations from the ideal stoichiometry in materials, should they be in single or polycrystalline form, and to investigate the maximum deviations at a given temperature on either side of the solidus line. This technique can also allow to avoid the detrimental influence of secondary phases on the transport properties that might form during the synthesis process.[47] This technique has already been successfully applied for several thermoelectric materials such as PbTe, Bi_2Te_3, SnTe, etc.[47–53] In the present case, we tried to determine and control the maximum deviations from stoichiometry in InTe, that is, to bring the material composition towards the equilibrium composition on either side of the solidus line of the phase diagram at a given temperature. An isothermal saturation annealing treatment, in which the sample is in equilibrium with its vapor phase, makes it possible to fix its composition throughout the sample and hence, its carrier concentration, and to probe the full range of carrier concentrations accessible experimentally. Following our previous study performed on polycrystalline SnTe,[22] we tried to apply a similar experimental procedure to polycrystalline InTe. In practice, the saturation annealing technique will require to put in a sealed silica tube small samples of InTe the final composition of which

at the annealing temperature T will be determined by the presence of $In_{1-x}Te_x$ initially in the form of a homogeneous powder, partially liquid and solid at T. This second material is called the source and its initial composition should be carefully chosen. The preparation of the different materials and the experimental protocol are described in more detail in the following.

4.7.2 Preparation and experimental protocol

4.7.2.1 Preparation of InTe polycrystalline sample

The preparation of the polycrystalline InTe ingot follows the same steps as described in Section 4.6.2. Using an agate mortar, the prepared ingot was hand-crushed into fine powders inside the glove box. The powders were then densified by SPS as described in the previous Chapter, Section 3.4.1. The temperature and pressure profiles are shown in Figure 4.30. The resulting InTe sample was polished carefully using SiC papers to remove any traces of graphite. The samples were cleaned with ethanol and acetone in an ultrasonic bath between each polishing step. Finally, small samples in the form of bars, discs or squares were cut from the SPS sample using a diamond-wire saw.

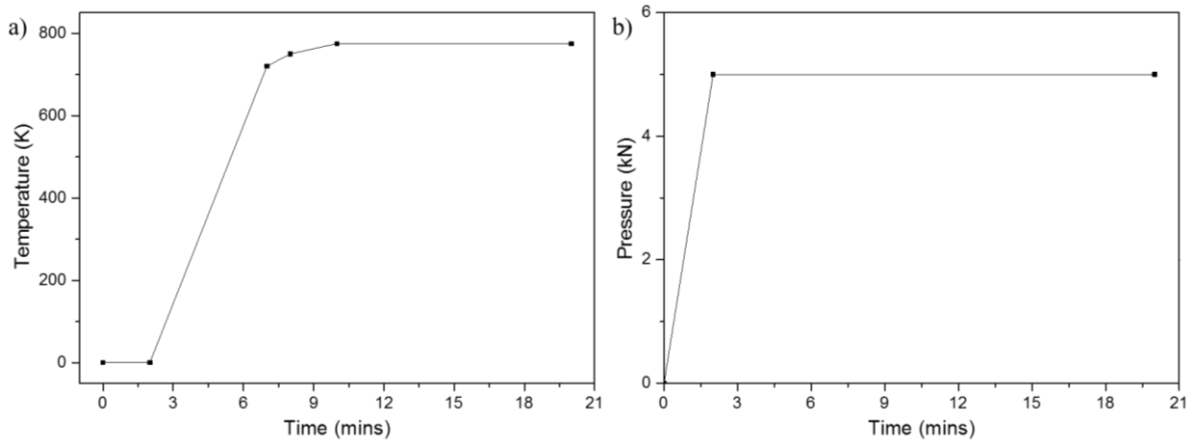

Figure 4.30: Temperature and pressure profiles used during SPS for polycrystalline InTe samples.

4.7.2.2 Preparation of the source

The $In_{1-x}Te_x$ ingots (used as the sources) were prepared using the same technique as described before for the polycrystalline InTe ingot. The resulting ingots were then crushed into fine powders inside the glove box. Two different sources were prepared for the saturation annealing process: one corresponding to the In-rich side of the solidus and the other one to the Te-rich side. The compositions were selected based on the solidus line of the In-Te phase diagram, as shown in Figure 4.31.

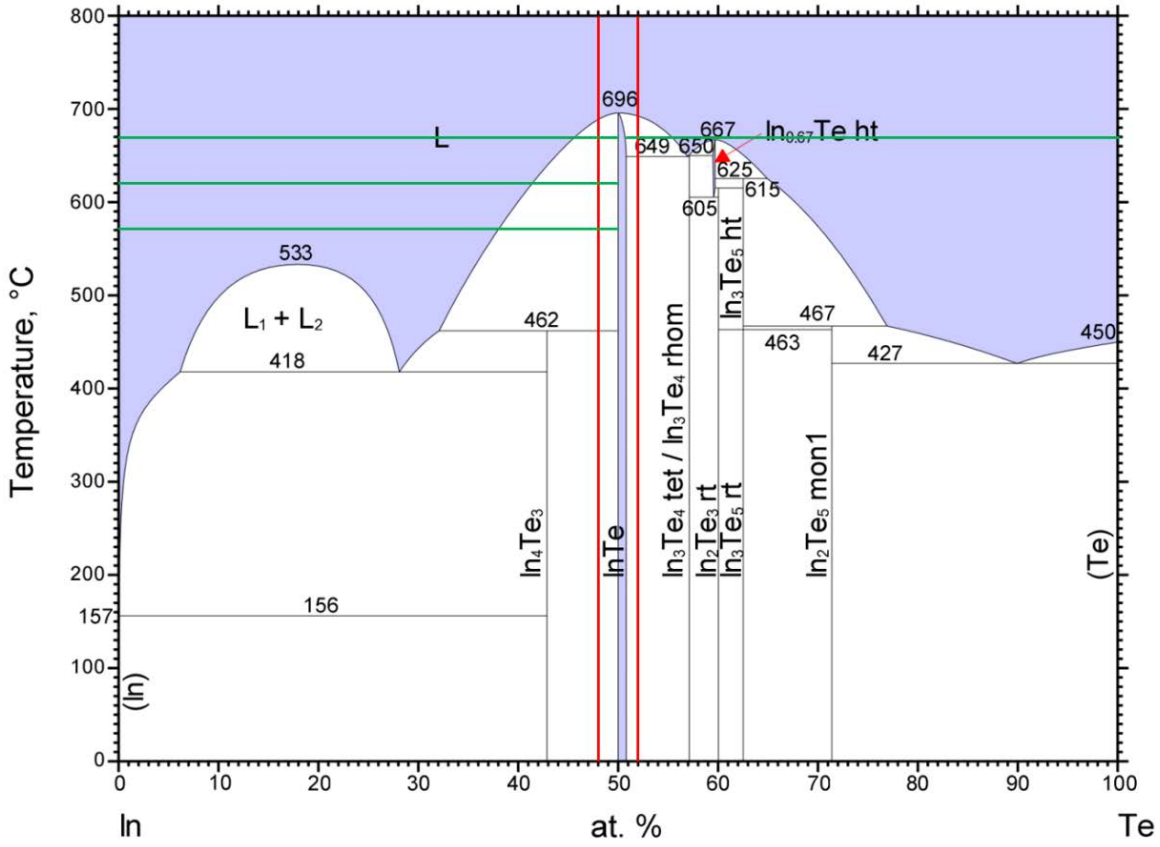

Figure 4.31: Phase diagram of InTe as derived by Massalski *et al.*[8] The red vertical lines represent the composition of the source used for saturation annealing and the green horizontal lines represent the selected saturation temperatures.

For the In-rich source, we have chosen the composition $In_{52}Te_{48}$ while for the Te-rich side we selected a composition of $In_{48}Te_{52}$ (Table 4.7). The composition of the source depends on whether In-rich or Te-rich samples are targeted and the temperature at which the annealing is performed. For example, as seen from the phase diagram of In-Te, it is clear that the annealing cannot be performed below 649°C on the Te-rich side of the homogeneity region.

The same holds true for temperatures below 462°C on the In-rich side. Hence, the annealing temperature and chemical composition of the sources were carefully selected to ultimately result in homogenous binary InTe compounds. During the annealing, all the three phases, solid, liquid and gas, are in equilibrium. Thus, the InTe samples acquires the solidus composition by atomic exchange with the gaseous phases at the annealing temperature.

Table 4.7: Summary of the source composition and the annealing temperature.

Target side	Annealing temperature (°C)	Source	Nomenclature
In rich	670	$In_{52}Te_{48}$	In670
In rich	620	$In_{52}Te_{48}$	In620
In rich	570	$In_{52}Te_{48}$	In570
Te rich	670	$In_{48}Te_{52}$	Te670

4.7.2.3 Experimental protocol

Saturation annealing is a protracted annealing of samples in a controlled atmosphere in the presence of a source of saturation. At a given temperature *T*, the source consists of a liquid and solid phase with the partial pressure of gases (in this case InTe and Te_2). These gases are essential because they allow the sample to progressively adopt the composition of the solidus at *T*, which occurs by the relocation of point defects within the solid or at the surface. The silica tube and the sample "boat" (Figure 4.32) were cleaned and degassed using the same experimental protocol as mentioned before. The samples and the source (typical mass ~ 5 g) were placed on the silica boat which were sealed inside a silica tube under secondary vacuum (around 10^{-6} Torr). The sealed silica tube was then kept inside a horizontal heating furnace (Figure 4.33), already at the required temperature and in which the temperature was constant over ~ 5 cm length. A type K thermocouple was fixed inside the furnace to control the temperature. The main purpose of using the horizontal furnace was to avoid any disturbances/mixing of samples and source.

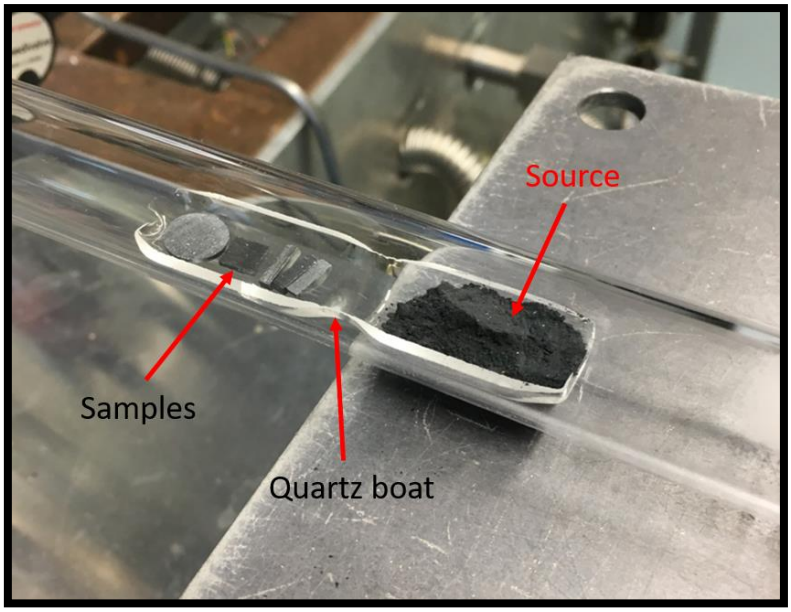

Figure 4.32: Photograph of the silica “boat” in which the cut InTe samples and the source are placed inside. This boat is loaded into a silica tube, degassed prior to the process of saturation annealing.

Figure 4.33: Horizontal heating furnace used for the process of saturation annealing.

At the end of the saturation annealing process, the silica tubes were very carefully yet quickly quenched in room-temperature water. Due to the high vapor pressure of Te, it is important to avoid deposition of Te gas onto the samples while cooling. Hence, the source end was first quenched to condense Te and then the rest of the ampoule (Figure 4.34).

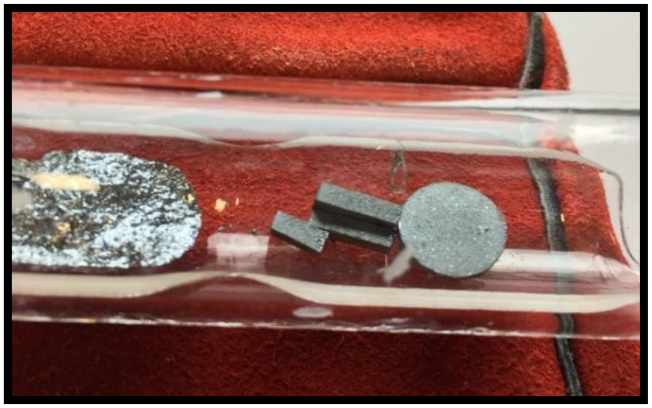

Figure 4.34: Photograph of InTe samples and source after the process of saturation annealing at T = 620°C on the In rich-side.

The time required for annealing at a given temperature was estimated according to our experience on SnTe.[54] The summary of the annealing time and the relative densities of the samples after completion of the process are gathered in Table 4.8. On the In-rich side, we can say that the density of all the saturated samples remained similar. However, the sample saturated on the Te-rich side showed a decrease of 9% in its density, suggesting a loss of elements or a change in the crystal structure.

After quenching in room-temperature water, we observed growth of very small, shiny crystals on the surface of nearly all the samples (Figure 4.35). These crystals, that likely corresponds to the InTe phases, show that mass exchange between the source and the samples was realized. The higher the annealing temperature, the more the crystallization was observed. All the samples were well polished to remove these crystals before measuring any chemical, structural or physical property.

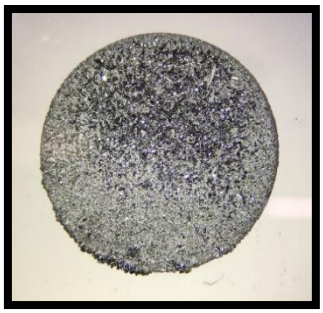

Figure 4.35: Photograph of a sample post saturation annealing on the Te rich side at T = 670°C.

Table 4.8: Summary of annealing time and relative densities for each synthesized sample in the series.

Sample	Annealing time (days)	Relative density (%)
InTe before Annealing	-	99
In670	7	97
In620	15	98
In570	30	99
Te670	7	91

4.7.3 Structural and chemical properties

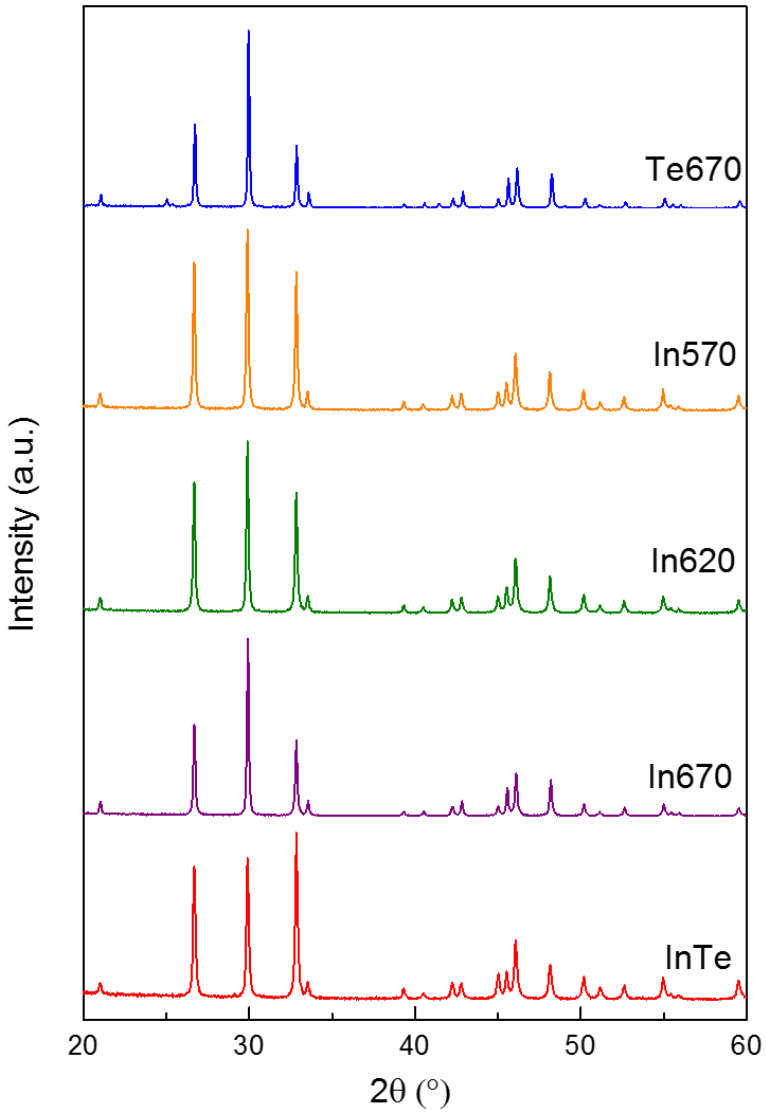

Figure 4.36: PXRD patterns for InTe SA samples.

The crystal structure and phase purity of polycrystalline non-annealed and annealed InTe samples were carried out by powder X-Ray diffraction at 300 K (Figure 4.36). Similar to the PXRD pattern of single crystalline InTe (shown in Figure 4.15), all the In-rich samples are single phased, with all the reflections indexed to the tetragonal crystal structure of InTe. In contrast, the Te670 sample shows some additional reflections (at 2θ value ~ 25°), which imply the presence of a secondary phase, possibly In_2Te_3.

Figures 4.37 to 4.40 depict the elemental X-ray maps of the binary InTe and of the different In-rich polycrystalline samples performed by SEM-EDXS. All the samples showed a homogeneous distribution of In and Te throughout the surface. These results are in excellent agreement with the PXRD patterns for all samples.

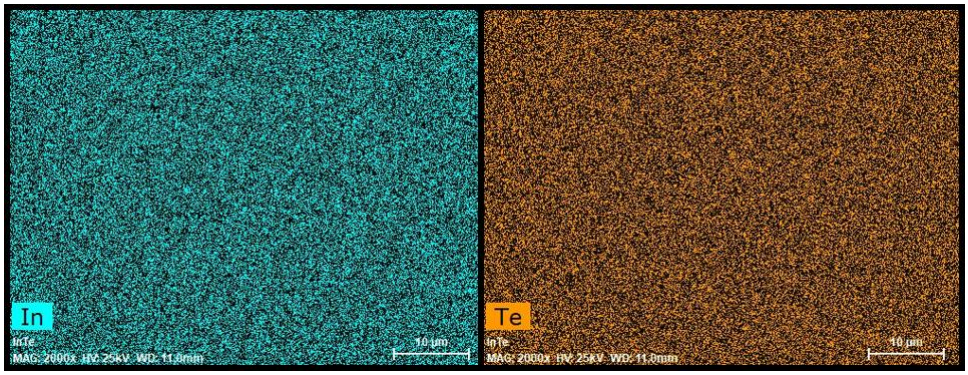

Figure 4.37: Elemental mapping for polycrystalline, non-annealed InTe sample performed by SEM-EDXS analysis.

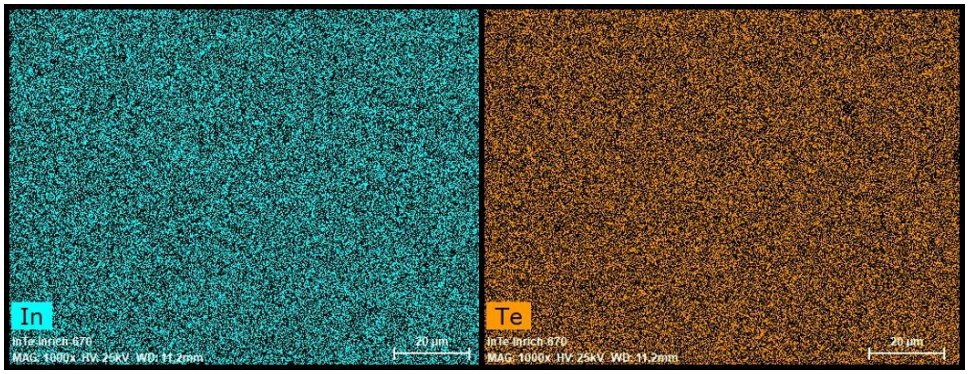

Figure 4.38: Elemental mapping for the saturation-annealed In670 sample performed by SEM-EDXS analysis.

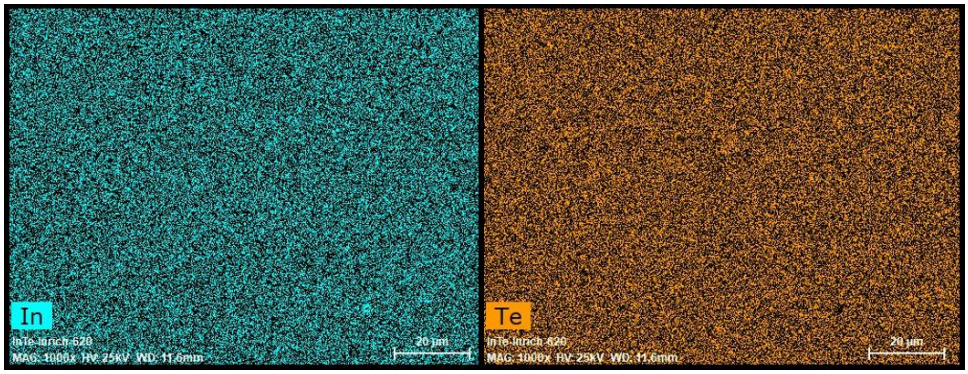

Figure 4.39: Elemental mapping for the saturation-annealed In620 sample performed by SEM-EDXS analysis.

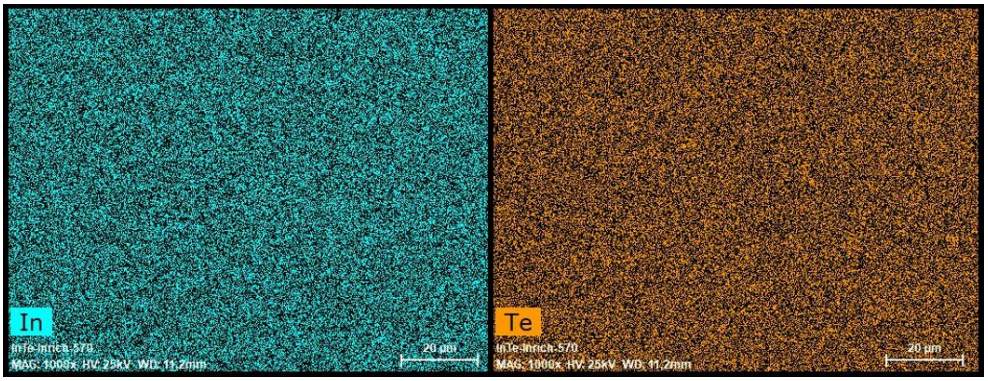

Figure 4.40: Elemental mapping for the saturation-annealed In570 sample performed by SEM-EDXS analysis.

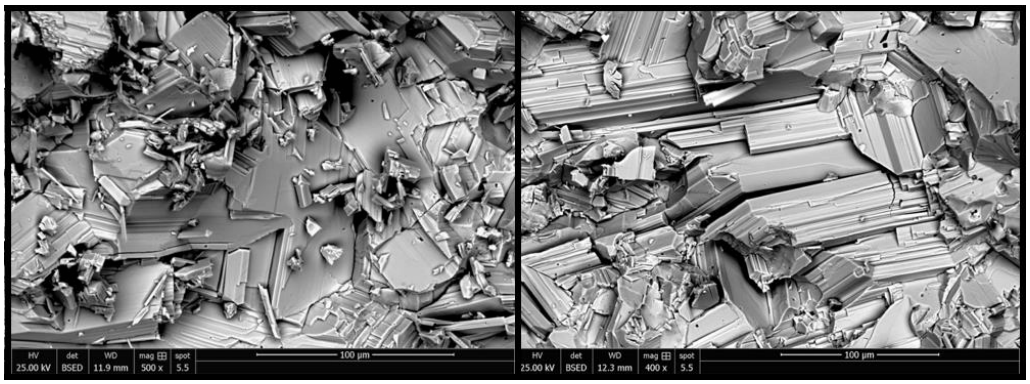

Figure 4.41: SEM images for saturated In620 sample.

Figure 4.41 shows the SEM analysis performed on a fractured surface of the illustrative In620 sample. Similar microstructural properties were observed in other saturation-annealed samples. Several grains are formed by plate-like InTe layers stacked along the same direction due to the anisotropic crystal structure of InTe, indicating that some anisotropy in the transport properties should be observed in polycrystalline samples.

The only difference observed in SEM-EDXS analysis was observed in the Te670 sample where regions/lines of slightly Te-rich phase was observed (Figure 4.42). This is in agreement with the presence of secondary phases evidenced by PXRD, although the small concentration of Te is likely below the detection limit of PXRD.

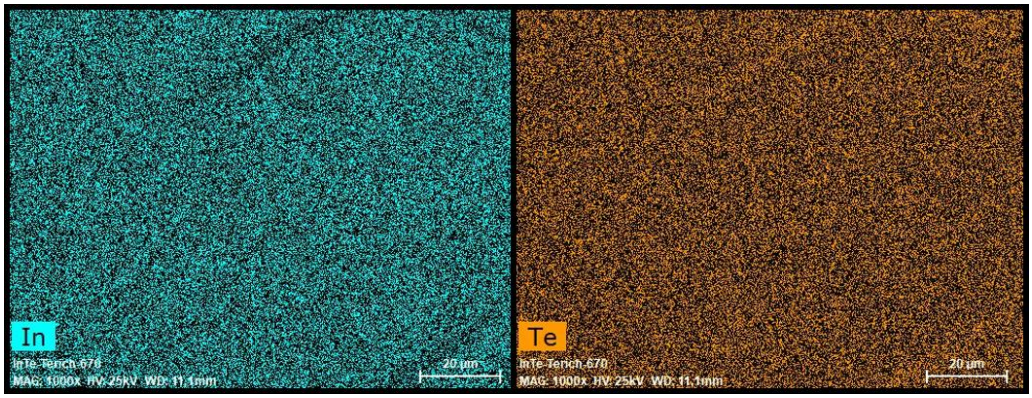

Figure 4.42: Elemental mapping for the saturation-annealed Te670 sample performed by SEM-EDXS analysis.

4.7.4 Transport properties

The first sub-section is dedicated to the study and comparison of the transport properties (5 – 800 K) of polycrystalline InTe samples cut parallel and perpendicular to the pressing direction. The second part of the section focuses on the transport properties in a wide range of temperatures (5 – 800 K) of the saturation-annealed samples, the direction of which is perpendicular to the pressing direction.

4.7.4.1 Anisotropy in as-synthesized polycrystalline InTe

Figure 4.43 presents the temperature dependence of the electrical resistivity for polycrystalline InTe measured both parallel and perpendicular to the pressing direction. The $\rho(T)$ data evidence a complex temperature dependence. Below 300 K, $\rho(T)$ shows a different behavior when compared to our single-crystal data and contrasts with its metallic character observed. The data measured in the parallel direction are rather characteristic of semiconducting-like behavior, that is, the ρ values tend to decrease with increasing temperature. Such a temperature dependence, however, is not necessarily linked to a true semiconducting behavior and can be observed in semi-metals such as for instance in the Bi_{1-}

$_x$Sb$_x$ alloys for $x \leq 7\%$. The increase in ρ may thus be induced by variations in the electron and hole concentrations and mobilities upon cooling.

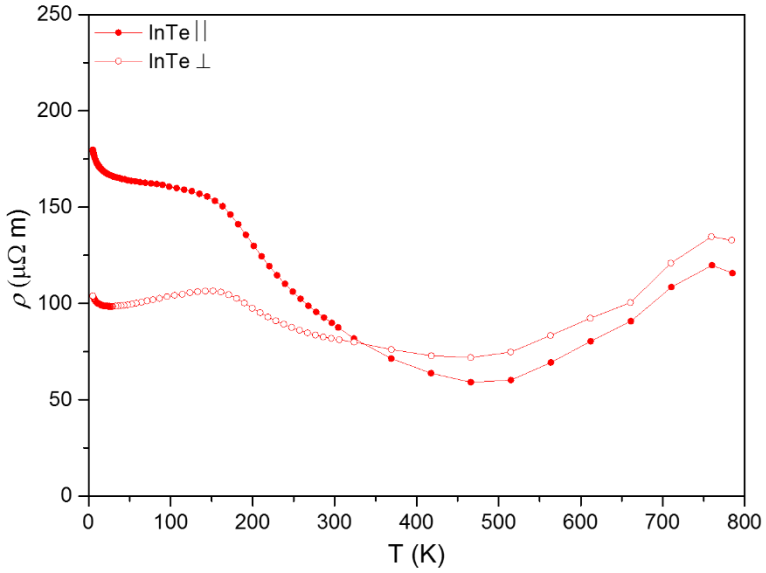

Figure 4.43: Temperature dependence of the electrical resistivity for polycrystalline InTe measured along and perpendicular to the SPS pressing direction.

Surprisingly, the data measured in the perpendicular direction show a different behavior with a slight but noticeable increase in the ρ values between 15 and 150 K. The fact that clear shoulders occurs between 150 and 200 K might correspond to an electronic transition, as suggested by Back *et al.* Above 150 K, ρ starts decreasing upon further warming. The room-temperature ρ values show only a small degree of anisotropy, with values of 80 μΩm and 87 μΩm for the perpendicular and parallel direction, respectively. The anisotropy ratio is around ~ 1.1 and remains practically temperature-independent above 300 K. However, interestingly, a crossover is observed at ~ 340 K where the anisotropy reverses above this temperature. Above 300 K, $\rho(T)$ is similar in both directions, with a first decrease in the ρ values up to about 500 K followed by an increase upon further warming to the highest temperature of 760 K. At 760 K, the ρ values are 120 μΩm and 135 μΩm in the parallel and perpendicular direction, respectively. The absence of an electronic band gap that would be associated with the semiconducting-like dependence of $\rho(T)$ below about 500 K is demonstrated by specific heat measurements performed at low temperatures (Figure 4.44). A fit of the low-temperature data to the conventional relation $C_p/T = \gamma + \beta T^2$ yielded a γ value of around 10 mJ mol^{-1} K^{-2} and a Debye temperature, inferred from the β parameter, of 115 K. While the Debye temperature is consistent with that determined on the single crystal (109 K), the clearly finite γ value points

to the presence of a sizeable density of states at the Fermi level. This difference between single-crystalline and polycrystalline samples is likely due to different defect concentrations. These results further imply a lower defect concentration in the single crystal compared to the present polycrystalline sample due to the nearly zero γ value derived in the former. As observed in the single crystal, the room-temperature value is very close to the Dulong-Petit value (See figure 4.44).

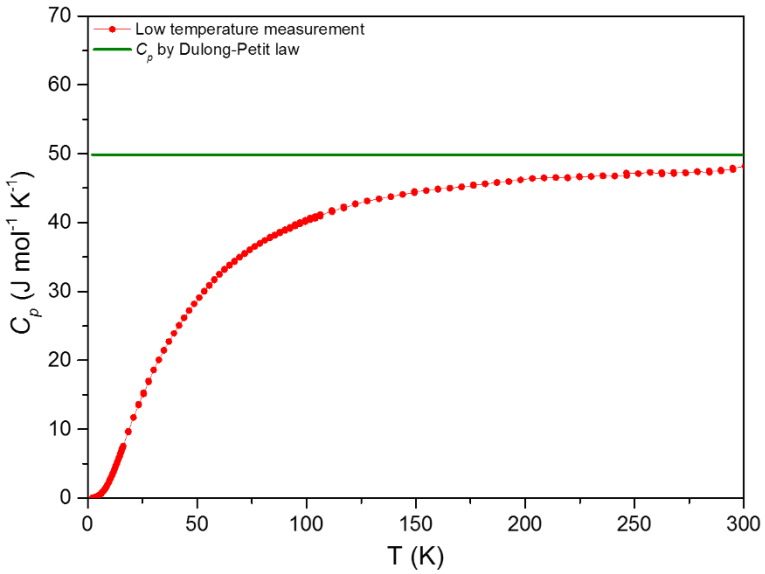

Figure 4.44: Temperature dependence of the specific heat C_p of polycrystalline InTe.

Figure 4.45 shows the temperature dependence of the thermopower α of samples cut in both directions. The α values remain positive across the entire temperature range indicating a p-type electrical, in agreement with our single-crystal data. Below 50 K, $\alpha(T)$ shows a small but clear maximum near 20 K, suggesting a phonon-drag contribution, as shown in PbTe and SnTe. Unlike $\rho(T)$, $\alpha(T)$ is similar to that observed in single-crystalline InTe, with values monotonically increasing from 27 μV K^{-1} at 50 K up to about 225 μV K^{-1} at 700 K. Above 700 K, $\alpha(T)$ peaks and then starts decreasing with further increasing temperature, possibly due to the activation of minority carriers across the band gap. The band gap width E_g can be estimated using the Goldsmid-Sharp relation $E_g = 2e\alpha_{max}T_{max}$ where e is the elemental charge. Using $\alpha_{max} \approx 225$ μV K^{-1} reached at $T_{max} \approx 725$ K yields $E_g \approx 0.33$ eV. This value is similar to that induced for our single crystal and once more, is at odds with the predictions of our band structure calculations and those reported in prior studies. In contrast to single crystalline InTe, no anisotropy is observed over the entire temperature range. Interestingly, no clear hump is

observed near 180 K where the shoulder in $\rho(T)$ is observed. Because the thermopower is a sensitive probe of modifications of the Fermi surface, the absence of clear anomaly due to the complete or partial opening of a gap in the density of states at the Fermi level that would accompany a CDW transition suggests that the observed shoulder may have another physical origin.

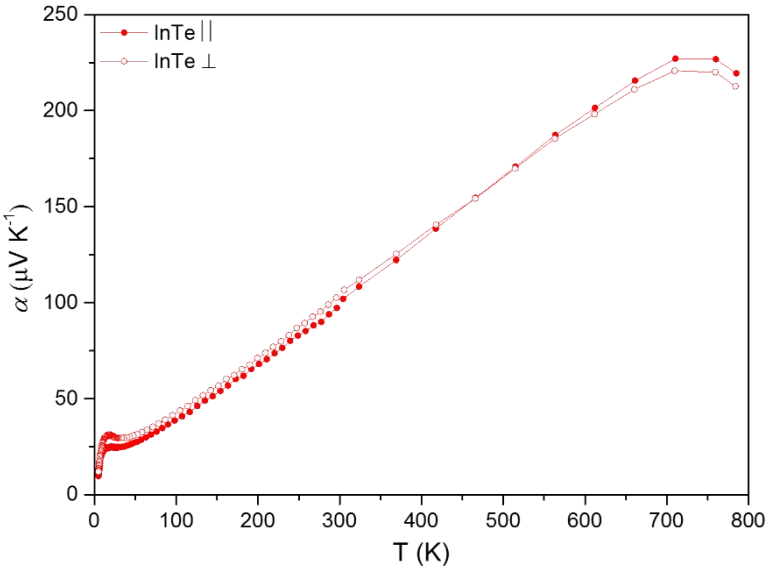

Figure 4.45: Temperature dependence of the thermopower for binary InTe sample measured parallel and perpendicular to the pressing direction.

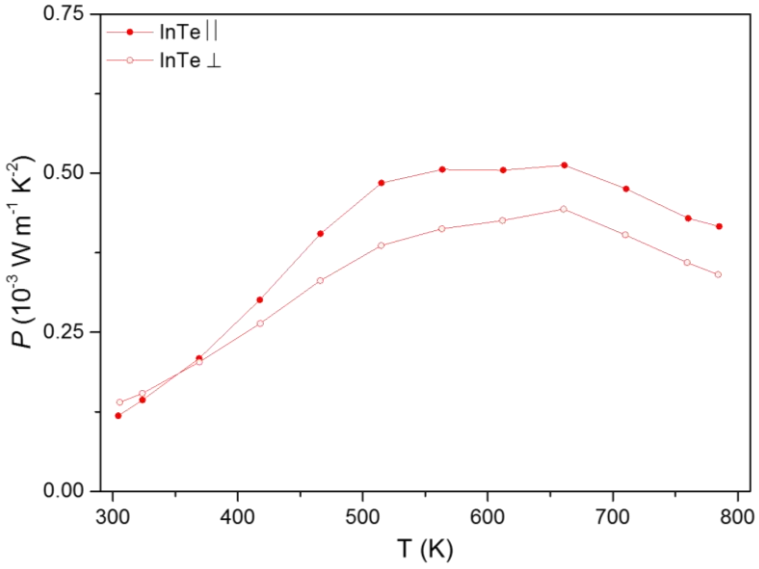

Figure 4.46: High-temperature dependence of the power factor for polycrystalline InTe sample.

Due to the high ρ values, a moderate value of the power factor is obtained along the two directions (Figure 4.46). The anisotropy in the power factor entirely reflects the anisotropy in ρ, giving rise to a moderate anisotropy ratio of ~ 1.2 at 600 K. The values of the power factor are in good agreement with those obtained in single-crystalline InTe, with a maximum value of 0.51 mW m^{-1} K^{-2} achieved near 660 K in the parallel sample.

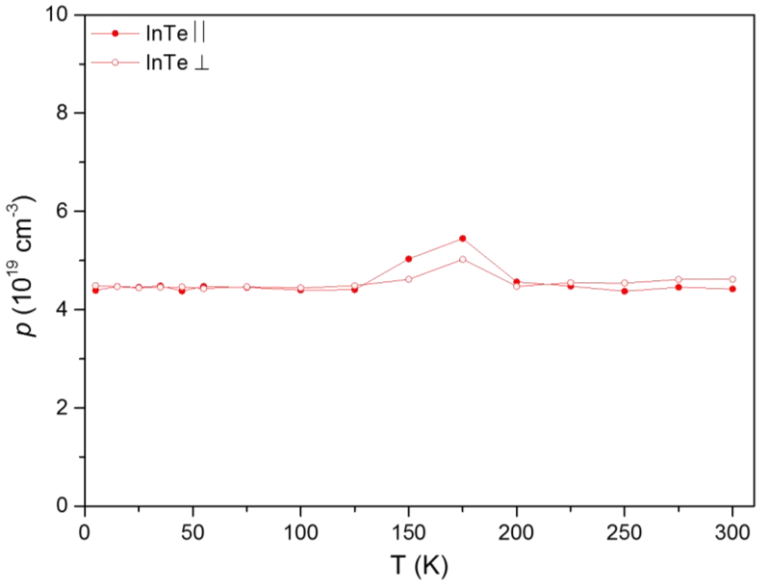

Figure 4.47: Low temperature dependence of carrier concentration for binary InTe sample.

The temperature dependence of the carrier concentration is shown in Figure 4.47. Across the entire temperature range, the Hall coefficient R_H is positive indicative of a dominant hole-like contribution, in agreement with the positive sign of the thermopower. Of note, the Hall resistivity ρ_H data were found to vary linearly with the applied magnetic field over the range covered (between – 1 and +1 T). This linear variation shows that the hole-like contribution dominates a possible electron-like contribution that would be expected in a semi-metallic compound. As shown by the specific heat data, the large, finite value of the density of states at the Fermi level may imply that the chemical potential is sufficiently deep inside the valence bands to make an electron-like contribution absent. The very weak anisotropy observed between the parallel and perpendicular directions makes the use of the single-band formula, $p = 1/R_H e$, a very good approximation in the present case. At 300 K, the hole concentration p is 4.5 $\times 10^{19}$ cm^{-3}. This value is comparatively higher than that reported in previous reports,[1,5–7] but in good agreement with the polycrystalline sample prepared by Back *et al.*[4] p hardly evolves in temperature, a behavior consistent with a degenerate character of transport and

hence with a semi-metallic state of the present sample. Surprisingly, a clear hump is observed around 175 K, which corresponds to the temperature where the shoulder is observed in $\rho(T)$ and close to the possible structural transition suggested by Back *et al.* Variations in the carrier concentration are expected upon crossing a CDW transition due to a complete or partial removal of the density of states at the Fermi level. However, what makes this observation puzzling is the fact that the hole concentration measured below 125 K is similar to that measured above 200 K. If a structural transition is at the origin of this hump, the distortion of the crystal structure should be then weak enough to induce only small perturbations of the electronic band structure. Moreover, in such a case, the data measured in both directions should show a similar anomaly, which is not what is observed in the present data. Indeed, the measurements performed in the perpendicular direction shows a smaller hump with respect to that in the parallel direction. Thus, whether the observed hump is an artifact or signals a true structural or electronic transition remains so far an open question.

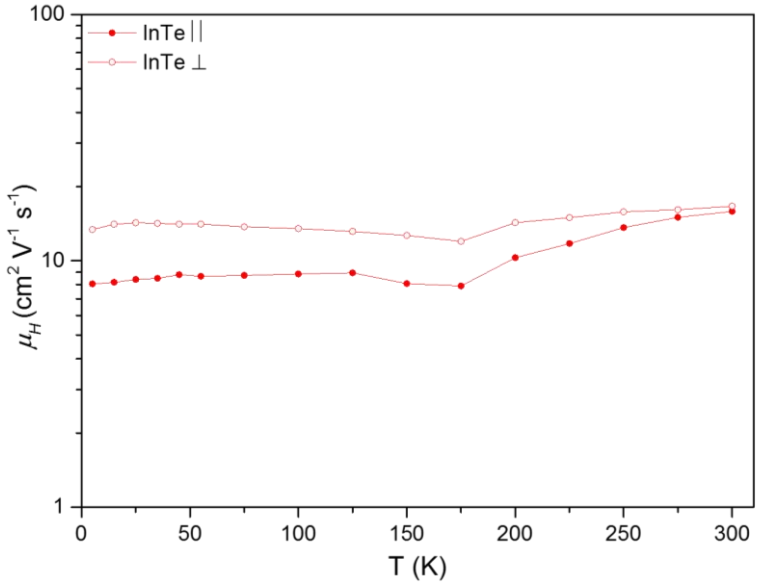

Figure 4.48: Low-temperature dependence of the Hall hole mobility μ_H for polycrystalline InTe measured along and perpendicular to the pressing direction.

Due to the shoulder in $\rho(T)$ and the hump in the Hall data, reflected in $p(T)$, the Hall mobility μ_H, shown in Figure 4.48, exhibits a corresponding anomaly near 175 K. While μ_H remains relatively constant up to 175 K, above this temperature it tends to increase with increasing temperature. This holds true in both the directions. At 300 K, μ_H is equal to 15.8 cm^2 V^{-1} s^{-1} and 16.6 cm^2 V^{-1} s^{-1} in the parallel and perpendicular directions, respectively, stating

almost no anisotropy with a ratio almost equal to 1. A clear anisotropy is seen at lower temperatures due to difference in electrical resistivity at this temperature range. The anisotropy measured at low temperatures between both directions is in agreement with early reports on single crystals.[5,6] An anisotropic ratio of ~ 1.5, which remains practically constant down to 5 K, is obtained at 175 K.

Figure 4.49 (a) shows the temperature dependence of total thermal conductivity κ. Below 300 K, InTe behaves as a typical crystalline compound with $\kappa(T)$ featuring an Umklapp peak reached near 18 K, in agreement with our single-crystalline data and with the study of Back *et al.* However, this peak is reached at a higher temperature with respect to our single-crystalline sample. This difference in the low-temperature behavior is likely due to grain boundary scattering (size effect) that acts as an additional source of phonon diffusion and affects the amplitude and the temperature of the dielectric maximum. At 300 K, κ amounts to ~ 0.8 W m^{-1} K^{-1} and 0.87 W m^{-1} K^{-1} in the parallel and perpendicular direction, respectively. Upon warming, the values gradually decrease to very low values of ~ 0.40 W m^{-1} K^{-1} and ~ 0.45 W m^{-1} K^{-1} reached at 800 K for the perpendicular and parallel sample, respectively. These values are slightly lower than those previously reported.[1,2] While at low temperatures, κ shows some degree of anisotropy, the high-temperature dependences indicates that the anisotropy is small above 300 K.

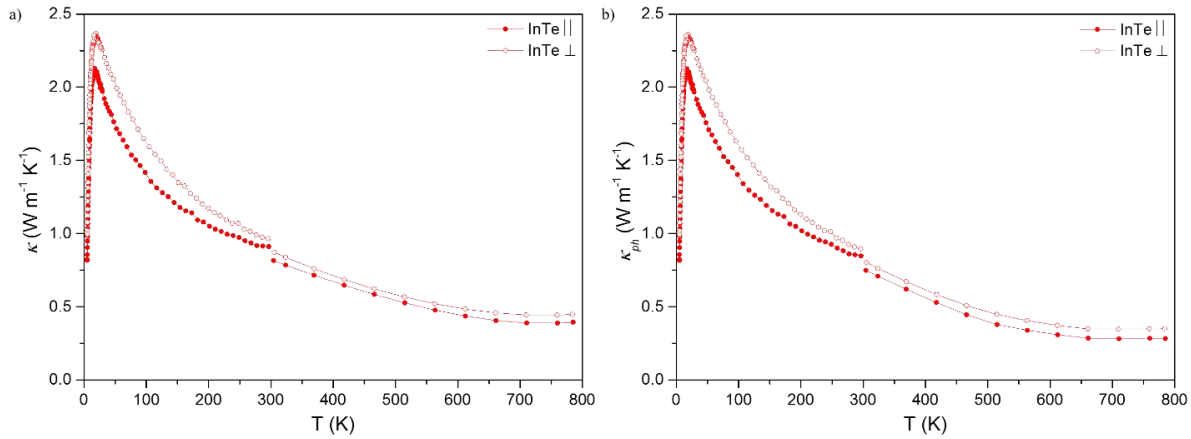

Figure 4.49: Temperature dependence of the a) total thermal conductivity κ and b) lattice thermal conductivity κ_{ph} for our non-annealed polycrystalline InTe sample.

In order to study the contribution of phonons on thermal conductivity its temperature dependence is shown in Figure 4.49 (b). The lattice thermal conductivity was estimated by calculating the Lorenz number using the Wiedemann-Franz law. The Lorenz number was

estimated using a single parabolic band model with acoustic phonon scattering. This justification of this model will be made in the next section. Due to extremely low electronic contribution the lattice thermal conductivity was the main contributor and had values closer to the total thermal conductivity.

The temperature dependence of the dimensionless thermoelectric figure-of-merit is shown in Figure 4.50. Due to the relatively high power factors achieved in the 500 – 700 K temperature range and to the remarkably very low thermal conductivity values, a high *ZT* value close to 0.9 was achieved at 710 K for the parallel sample. The anisotropy observed in the $\rho(T)$ data, which is not entirely compensated by the small anisotropy in $\kappa(T)$, gives rise to anisotropic *ZT* values with a maximum *ZT* of 0.65 at 710 K obtained in the perpendicular sample.

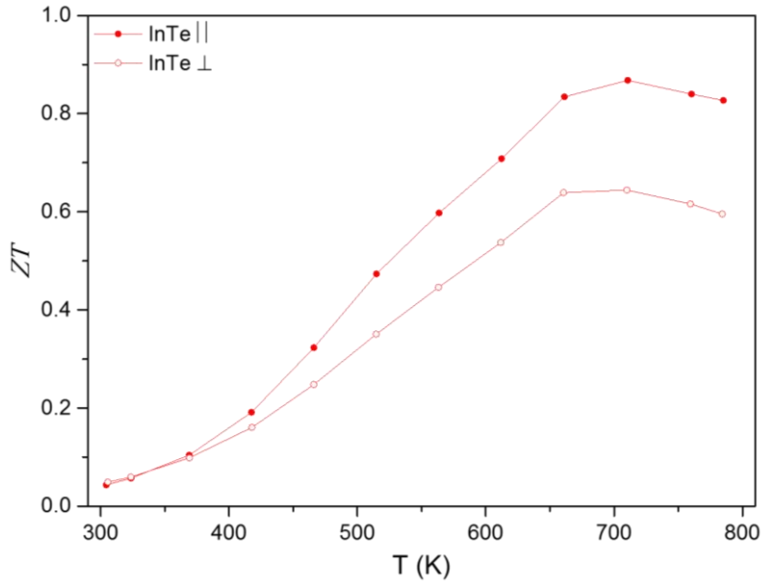

Figure 4.50: High temperature dependence of the *ZT* values for polycrystalline InTe sample.

4.7.4.2 Effect of saturation annealing on InTe

In this section, we turn to the presentation of the physical properties of polycrystalline InTe samples prepared by the saturation annealing technique. For comparison purposes, we have systematically added the data measured on the as-prepared InTe sample discussed in the previous section. For sake of clarity and because the samples show only a small degree of anisotropy, we will focus on measurements performed in the parallel direction (that is, measured along the SPS pressing direction; for detailed sample orientations, see Appendix A),

the direction along which the thermoelectric performances are the highest. For a general overview of the measurements performed along the perpendicular direction, the reader can refer to the Appendix E.

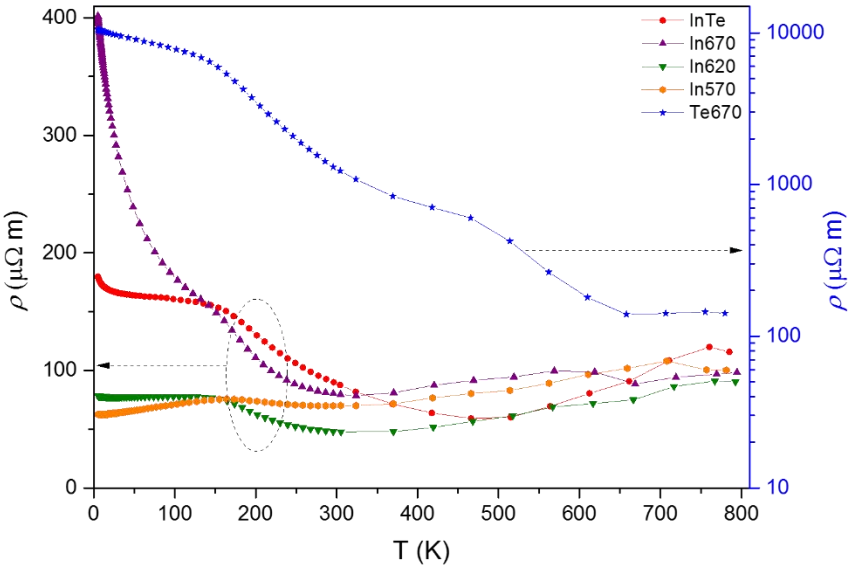

Figure 4.51: Temperature dependence of the electrical resistivity for In-rich and Te-rich polycrystalline samples. Due to the higher ρ values measured in the Te-rich annealed sample, the values are plotted on a logarithmic scale (right y axis).

Figure 4.51 shows the temperature dependence of ρ for samples prepared by saturation annealing on the In-rich side and Te-rich side of the solidus. With no exception, all the samples show distinct behaviors of $\rho(T)$ indicating the effectiveness of the saturation annealing process. For samples corresponding to the In-rich side, no clear trend in ρ with the annealing temperature emerges above 300 K. The three annealed samples show a behavior similar to that of the non-annealed InTe sample. Clear differences are however observed below room temperature. While there is also no clear trend between ρ and the annealing temperature, the samples annealed at 620 and 570°C show lower ρ values compared to the non-annealed sample. Distinct from this trend is the $\rho(T)$ curve of the sample annealed at 670°C which shows a monotonic, steep rise in the ρ values below 300 K without any sign of saturation down to 5 K. Of note, a common feature of these four samples is the presence of the shoulder, which is still visible in the samples annealed at 670 and 620°C and discernible, although strongly lessened, in the sample annealed at 570°C. Regardless of the exact origin of this shoulder, these data show that it is not entirely removed by the saturation annealing process. The sample annealed

at 670°C on the Te-rich side exhibit a $\rho(T)$ dependence, which strongly resembles that observed for the non-annealed sample, with, notably, the shoulder observed near 185 K. Above 300 K, the only difference is related to the presence of a hump near 500 K, which is absent in the other samples. The main obvious difference in this sample with respect to the four others is tied to the significantly higher ρ values which increase upon cooling to reach values two orders of magnitude higher than in the other samples. This strong difference is partly explained by the lower relative density of this sample during the annealing process. Moreover, the different microstructure of this sample, with the presence of Te-rich phases, probably also contributes to increase the measured ρ values.

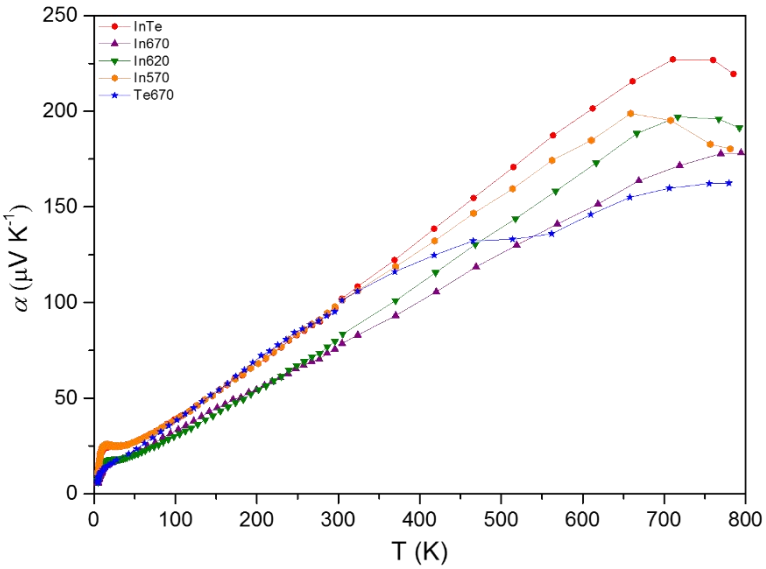

Figure 4.52: Temperature dependence of the thermopower for the saturation-annealed polycrystalline samples on the In-rich and Te-rich side of the solidus.

Similar to data acquired on the single crystal and on the non-saturated sample, all the saturated samples are *p*-type, as demonstrated by the positive thermopower values (Figure 4.52). Below 300 K, all the samples exhibit a temperature dependence similar to that of the non-annealed sample. The α values measured in the samples annealed on the In-rich side at 620 and 670°C are lower than those of the non-saturated sample, in agreement with the lower ρ values of these two samples. Above 300 K, more significant differences in the α values can be observed between the different samples. While the temperature dependences of the non-saturated sample and the samples annealed at 670 and 620°C are similar, the behavior of the two other samples markedly differ. First, the sample annealed at 570°C reaches a peak α value at 650 K, that is, at a lower temperature than in the other samples. Second, the sample annealed

at 670°C on the Te-rich side exhibits a temperature dependence with a lower slope compared to other samples, eventually reaching the lowest α value at 780 K. The fact that the maximum in α slightly varies with the annealing temperature suggests that both the hole concentration and the thermal band gap are not equivalent in these different samples and would thus be very sensitive to the concentration of defects in InTe.

The best compromise between low values and high values is achieved in the sample annealed on the In-rich side at 620°C with a maximum power factor of 0.47 mW m^{-1} K^{-2} at ~ 665 K (Figure 4.53). However, regardless of the annealing temperature, all the samples exhibit lower power factors compared to that achieved in the non-annealed InTe sample.

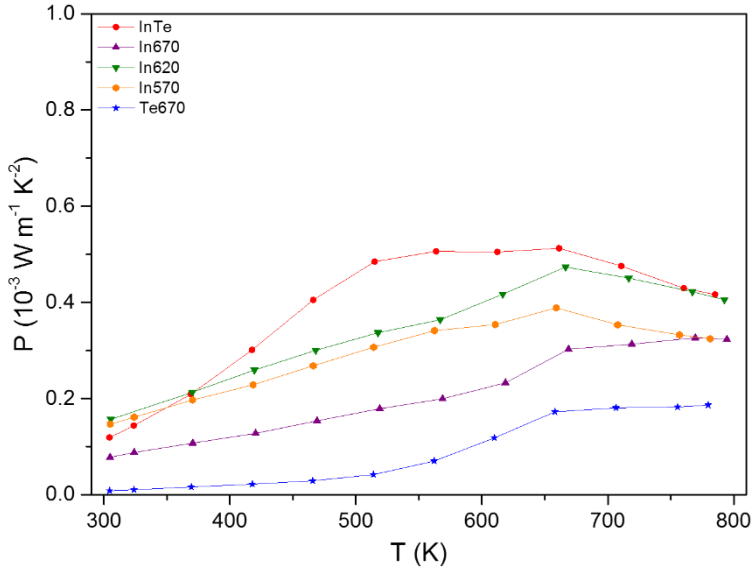

Figure 4.53: Temperature dependence of the power factor for the saturation-annealed polycrystalline samples on the In-rich and Te-rich side of the solidus.

Figure 4.54 shows the temperature dependence of the carrier concentration for the different annealed samples. Due to the high ρ values of the sample annealed at 670°C on the Te-rich side upon cooling, no reliable data could be collected for this sample below 300 K. At 300 K, the hole concentration p for this sample is 5.2×10^{19} cm^{-3}. We will therefore only consider in the following the samples annealed on the In-rich side. In agreement with the sign of the thermopower, holes are the dominant carrier type in all samples. Common to all samples is the temperature-independent hole concentration down to 5 K, which is consistent with their degenerate nature. While the sample annealed at 620°C shows the same anomaly near 175 K, no clear anomaly could be observed near this temperature in the samples annealed at 570 and 670°C, that is, in the two samples where the shoulder observed in $\rho(T)$ is strongly lessened.

Moreover, data collected in the perpendicular direction did not evidence a similar hump, suggesting that the sudden increase in p may rather be an artifact. If this hump is not an artifact, the fact that the samples annealed at 570 and 670°C do not show an obvious anomaly may allow for a systematic comparison of structural data below 200 K that might help to pinpoint the origin of this anomaly.

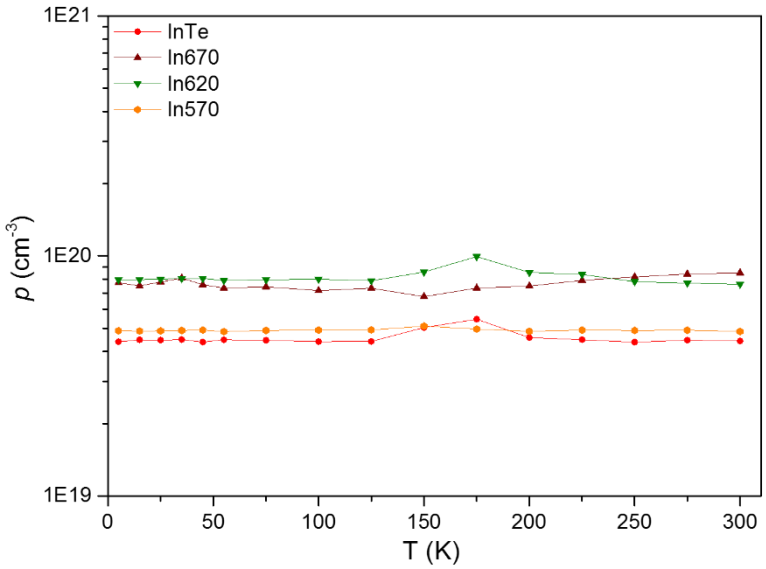

Figure 4.54: Temperature dependence of the hole concentration for the saturation-annealed polycrystalline samples on the In-rich side of the solidus.

These data demonstrate that the saturation annealing had a clear impact on the hole concentration, further demonstrating the effectiveness of this technique in the present case. The highest hole concentration of 5.2×10^{19} cm^{-3} at 300 K was achieved for the sample annealed at 670°C. These data seem to further indicate that at 300 K, the hole concentration tends to decrease with decreasing the annealing temperature (see Figure 4.55). However, this trend is no longer valid below 250 K due to the crossover between the samples annealed at 620 and 670°C.

Figure 4.56 shows the temperature dependence of the Hall mobility μ_H for the different samples annealed on the In-rich side. The room-temperature hole concentrations and Hall mobilities are gathered in Table 4.9. For the In570 and In620 samples, $\mu_H(T)$ follows a similar behavior to that observed for the non-annealed sample. Below 100 K, $\mu_H(T)$ remains constant down to the lowest temperature measured suggestive of scattering by neutral impurities. Above 100 K, an upturn can be observed in all three samples due to the hump seen in the Hall data near 175 K and the shoulder in the $\rho(T)$ data. Up to 300 K, $\mu_H(T)$ monotonically increases

with increasing temperature. The steep rise in μ_H might correspond to grain boundary scattering that has been shown to dominate the transport in several thermoelectric materials, such as in the Zintl phase Mg_3Sb_2 for instance.[55] The In670 sample shows a very different behavior with a monotonic increase in μ_H with increasing temperature from 5 to 300 K. This temperature dependence may also indicate that grain boundary scattering prevails in this sample, possibly due to a different microstructure compared to the other samples.

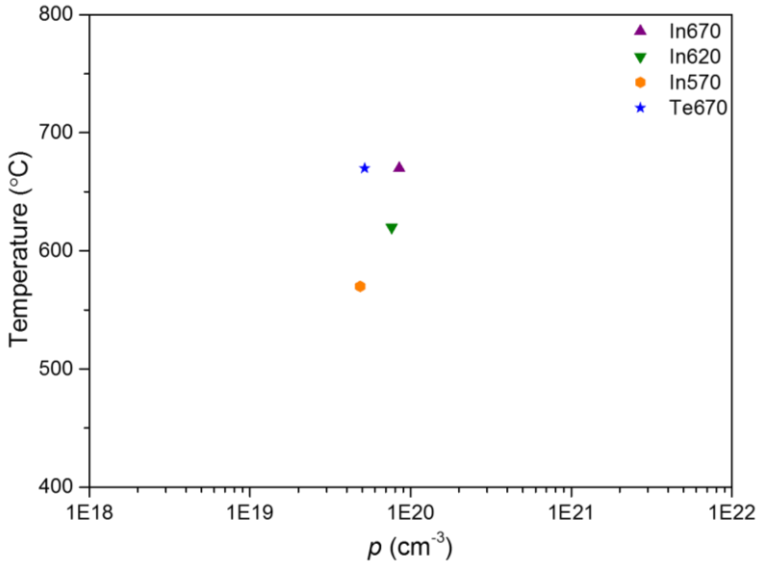

Figure 4.55: Carrier density values obtained at 300 K as a function of the saturation-annealing temperature.

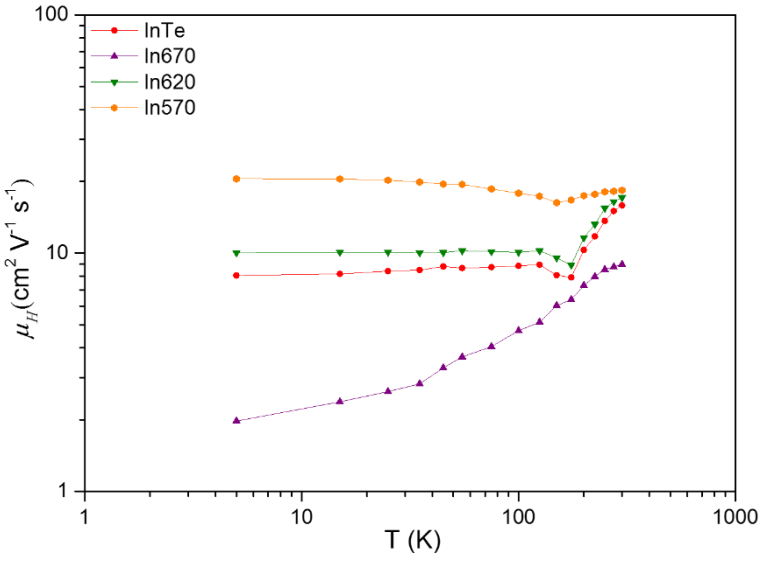

Figure 4.56: Temperature dependence of the Hall mobility for the polycrystalline samples saturation-annealed on the In-rich side of the solidus.

Table 4.9: Summary of carrier densities and hall motilities for different samples at 300 K.

Sample	p (10^{19} cm^{-3})	μ_H (cm^2 V^{-1} s^{-1})
InTe	4.4	15.9
In670	8.5	9.0
In620	7.6	17.1
In570	4.9	18.4
Te670	5.2	1.0

Combining the Hall data and the thermopower measurements, we further tried to model the transport in InTe. Figure 4.57 shows the Ioffe-Pisarenko plot at 300 K with the data measured on the five polycrystalline samples we have prepared. For comparison purposes, the data reported in the literature have also been added. Electronic band structure calculations have shown that the Fermi level crosses two valence bands near the M and Z points. While the shape of the valence band near the M point is close to be parabolic, the less-dispersive band located at the Z point exhibits a more complicated shape. Nevertheless, as a first approximation, the theoretical relation $\alpha(p)$ was calculated by considering a single-parabolic band model. Moreover, we further assume that acoustic phonon scattering prevails near room temperature as observed in many thermoelectric chalcogenide compounds. In this model, the thermopower and hole concentration are given by the following expressions:

Equation 4.4:

$$\alpha = \frac{k_B}{e}\left(\frac{(2+\lambda)F_{1+\lambda}(\eta)}{(1+\lambda)F_{\lambda}(\eta)} - \eta\right)$$

Equation 4.5:

$$p = 4\pi\left(\frac{2m^* k_B T}{h^2}\right)^{\frac{3}{2}} F_{\frac{1}{2}}(\eta)$$

In these relations, k_B is the Boltzmann constant, h is the Planck constant, η is the reduced Fermi energy, m^* is the density-of-states effective mass, λ is the scattering parameter that

depends on the dominant scattering mechanism ($\lambda = 0$ for acoustic phonon scattering) and $F_i(\eta)$ is the Fermi integral defined as:

Equation 4.6:

$$F_i(\eta) = \int_0^\infty \frac{\xi^i d\xi}{1 + e^{\xi - \eta}}$$

where ξ is the reduced energy of the charge carriers. This model yields a density-of-states effective mass of $0.74m_e$ (m_e is the bare electron mass) using the experimental α and n values measured in our samples.

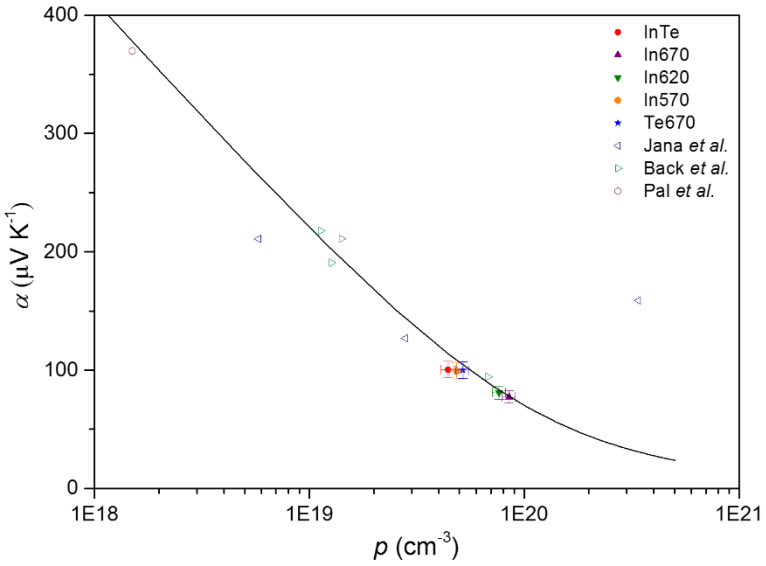

Figure 4.57: Ioffe-Pisarenko plot at 300 K for pristine and saturated annealed InTe samples compared with previous reports.[1,2,6] (Error bars corresponding to 7% have been included for both axes). The solid black curve was calculated by the SPB model.

As shown in Figure 4.57, a single value of m^* is sufficient to describe our data in the narrow hole concentration range covered. The theoretical curve also agrees with most of the data points reported in prior studies. Notable exceptions are two of the three points measured by Jana *et al.* While the point near 6×10^{18} cm^{-3} is reasonably close to the theoretical curve, the point measured at 3.5×10^{20} cm^{-3} cannot be captured by this model. This specisfic point signals either the breakdown of the present model due to the contribution of other bands, as the Ioffe-Pisarenko curve of SnTe for instance, or a problem in the reported measurements. We note that

our data, up to about 1.0×10^{20} cm^{-3} do not seem to show an increase as would be expected in the case of the contribution of a second band. Additional InTe samples with higher hole concentrations should be studied in order to clarify this point. The good agreement between the SPB model and the experimental points over nearly two orders of magnitude further show that non-parabolic effects associated with the possible narrow band gap of InTe or with the shape of the valence band around the Z point can be neglected up to hole concentrations of at least 1.0×10^{20} cm^{-3}.

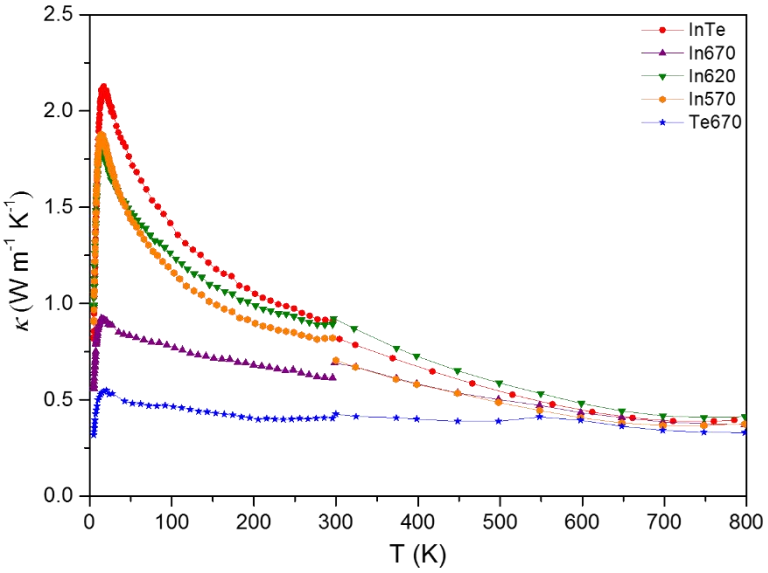

Figure 4.58: Temperature dependence of the total thermal conductivity for the polycrystalline samples saturation-annealed on the In-rich and Te-rich sides of the solidus.

The total thermal conductivity κ as a function of temperature is shown in Figure 4.58. Below 300 K, all samples exhibit a crystalline-like behavior with a well-defined Umklapp peak near 20 K. While the samples saturated at 570 or 620°C has little influence on $\kappa(T)$, the samples annealed at 670°C on both the In and Te-rich sides lead to significantly lower κ values with a strongly reduced magnitude of the Umklapp peak, which is nevertheless still discernible. The strong observed between these different samples corroborates what was observed on the electronic properties, that is, annealing at 670°C results in stronger variations with respect to the non-annealed samples. The origin of this behavior may be related to microstructural effects as well as the lower relative density measured for the Te670 sample. At high temperatures, all the curves tend to converge to similar values ranging between 0.3 and 0.50 W m^{-1} K^{-1} at 800 K. These low values are a robust, intrinsic property of InTe, independent of the annealing temperature. To further shed light on the phonon contribution, the lattice thermal conductivity

was estimated by subtracting the electronic contribution determined by the Wiedemann-Franz law. The temperature dependence of the Lorenz number was taken into account via a single-parabolic band model. Due to the rather high ρ values measured at low temperatures for all samples, the electronic contribution is very small. Thus, the temperature dependence of κ_{ph} (Figure 4.59) is equivalent to that of κ, regardless of the annealing temperature. At high temperatures, κ_{ph} further decreases with increasing temperature to reach a very low values of ~ 0.25 W m^{-1} K^{-1} at 800 K, a value shared by all samples.

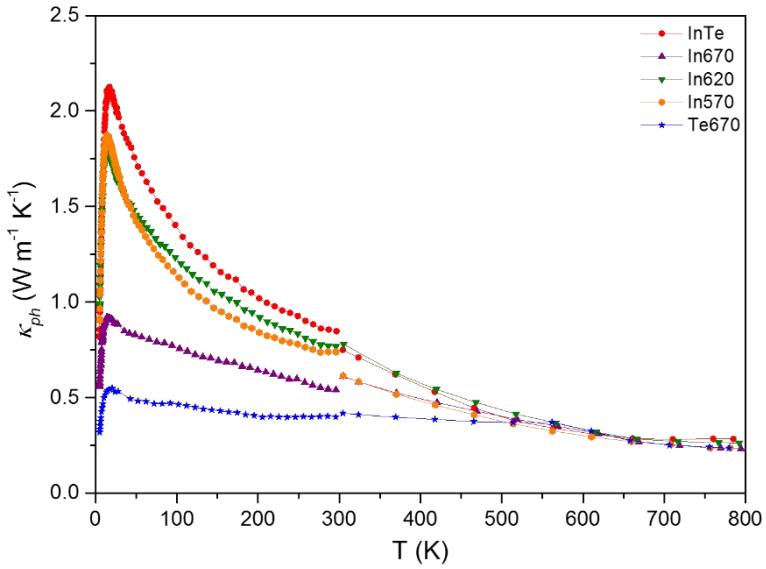

Figure 4.59: Temperature dependence of the lattice thermal conductivity for the polycrystalline samples saturation-annealed on the In-rich and Te-rich sides of the solidus.

Figure 4.60 shows the temperature dependence of the dimensionless thermoelectric figure of merit *ZT*. Due to the high electrical resistivity values measured below 300 K, we only show the *ZT* values calculated at high temperatures. The favorable combination of moderately high power factors and very low thermal conductivity leads to *ZT* values ranging between 0.7 and 0.8 at 770 K for the three samples annealed at the In-rich side. These values are consistent with that obtained for single-crystalline InTe. Moreover, all the annealed samples show slightly lower values compared to the non-annealed sample. In contrast, the Te670 sample exhibits significantly lower *ZT* values due to the very high ρ values resulting in a reduced power factor.

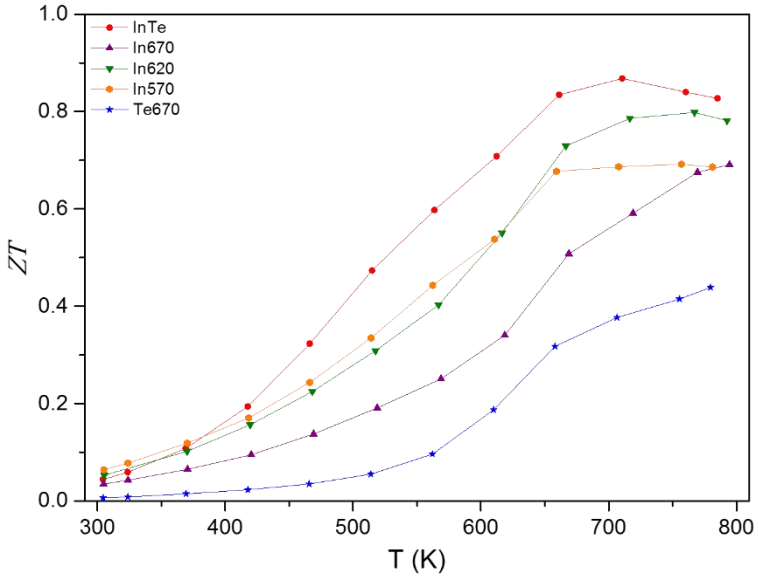

Figure 4.60: Temperature dependence of the *ZT* values for the polycrystalline samples saturation-annealed on the In-rich and Te-rich sides of the solidus.

4.8 Conclusion

In this chapter, we reported on a detailed investigation of the thermoelectric properties of single-crystalline and polycrystalline InTe. The various theoretical and experimental techniques used to characterize this binary compound have all highlighted that InTe stands out among chalcogenide semiconductors. While a rapid consensus has been reached regarding the electronic and phonon band structure of SnTe or SnSe for instance, this is not yet the case for InTe. Our calculations were globally in line with prior studies, although the details of the electronic band structure and the semi-metallic or semiconducting nature of the ground state remains an open question. The lattice dynamics calculations are also challenging due to the systematic appearance of negative frequencies in the phonon spectrum. These can be nevertheless removed by theoretically compressing the unit cell volume. These difficulties originate from the In1 atoms which feature large anisotropic displacement parameters, as demonstrated by single-crystal X-ray diffraction data.

The study of single-crystalline InTe was allowed by the successful growth of a large single crystal of InTe using the Bridgman technique, the study of which helped to provide a first overview of the transport properties of this compound over a broad range of temperatures (5 – 800 K). In particular, as observed in prior studies, InTe exhibit very low lattice thermal

conductivity. Our results also confirmed the cleavage plane of single-crystalline InTe to correspond to the (110) plane.

Compared to single-crystalline InTe, a very high ZT of ~ 0.9 was obtained at 710 K in a non-annealed, as-prepared polycrystalline sample thanks to even lower thermal conductivity due to the presence of grain boundary scattering. The intrinsic *p*-type nature of the electrical conduction observed in both single crystalline and polycrystalline samples further suggests that InTe exhibits defects, possibly In vacancies, but in a concentration significantly lower than that observed in SnTe. The possible off-stoichiometry of InTe might explain differences in the transport properties reported in the literature.

To control the defect chemistry in InTe, polycrystalline samples were subjected to the saturation annealing technique. InTe samples were treated on both sides of the solidus, that is, on both the In-rich and Te-rich sides, at different annealing temperatures. The results revealed that the hole concentration only weakly depends on the annealing temperature and varies over a narrow concentration window. This last property is consistent with the presence of a low defect concentration. Although these experiments did not yield enhanced thermoelectric performances, they consistently confirmed that InTe is an emerging thermoelectric materials that warrants further studies. In particular, how far its transport properties can be manipulated through substitutions on either the In or Te sites remains to be thoroughly explored. The peculiar behavior of low temperature specific heat data, which feature two low-temperature peaks, need to be further confirmed by studying the lattice dynamics by inelastic neutron scattering.

References

1. Jana, M. K., Pal, K., Waghmare, U. V. & Biswas, K. The Origin of Ultralow Thermal Conductivity in InTe: Lone-Pair-Induced Anharmonic Rattling. *Angewandte Chemie* **128,** 7923 (2016).
2. Back, S. Y., Cho, H., Kim, Y.-K., Byeon, S., Jin, H., Koumoto, K. & Rhyee, J.-S. Enhancement of thermoelectric properties by lattice softening and energy band gap control in Te-deficient $InTe_{1-\delta}$. *AIP Advances* **8,** 115227 (2018).
3. Zhu, H., Zhang, B., Wang, G., Peng, K., Yan, Y., Zhang, Q., Han, X., Wang, G., Lu, X. & Zhou, X. Promoted high temperature carrier mobility and thermoelectric performance of InTe enabled by altering scattering mechanism. *Journal of Materials Chemistry A* **7,** 11690 (2019).
4. Back, S. Y., Kim, Y.-K., Cho, H., Han, M.-K., Kim, S.-J. & Rhyee, J. S. Temperature-Induced Lifshitz Transition and Charge Density Wave in $InTe_{1-\delta}$ Thermoelectric Materials. *ACS Applied Energy Materials* (2020).
5. Parlak, M., Erçelebi, ç., Günal, I., Özkan, H. & Gasanly, N. M. Anisotropy of Electrical Resistivity and Hole Mobility in InTe Single Crystals. *Crystal Research and Technology* **31,** 673 (1996).
6. Pal, S. & Bose, D. N. Growth, characterisation and electrical anisotropy in layered chalcogenides GaTe and InTe. *Solid State Communications* **97,** 725 (1996).
7. Hussein, S. A. Temperature dependences of the electrical conductivity and hall coefficient of indium telluride single crystals. *Crystal Research and Technology* **24,** 635 (1989).
8. Massalski, T., Okamoto, H., Subramanian, P. & Kacprzak, L. *Binary alloy phase diagrams*. **2,** (ASM International, 1990).
9. Klemm, W. & v. Vogel, H. U. Messungen an Gallium- und Indium-Verbindungen. X. Über die Chalkogenide von Gallium und Indium. *Zeitschrift für anorganische und allgemeine Chemie* **219,** 45 (1934).
10. Grochowski, E. G., Mason, D. R., Schmitt, G. A. & Smith, P. H. The phase diagram for the binary system indium-tellurium and electrical properties of In_3Te_5. *Journal of Physics and Chemistry of Solids* **25,** 551 (1964).
11. Chattopadhyay, T., Santandrea, R. P. & Von Schnering, H. G. Temperature and pressure dependence of the crystal structure of InTe: A new high pressure phase of InTe. *Journal of Physics and Chemistry of Solids* **46,** 351 (1985).

12. Schubert, K. V., Dorre, E. & Kluge, M. Zur kristallchemie der B-metalle. 3. kristallstruktur von GaSe und InTe. *Zeitschrift fur Metallkunde* **46,** 216 (1955).
13. Geller, S., Jayaraman, A. & Hull, G. W. Crystal chemistry and superconductivity of pressure-induced phases in the In-Te system. *Journal of Physics and Chemistry of Solids* **26,** 353 (1965).
14. Riede, V., Neumann, H., Sobotta, H. & Lévy, F. Infrared optical properties of InTe. *Solid State Communications* **38,** 71 (1981).
15. Hogg, J. H. C. & Sutherland, H. H. Indium telluride. *Acta Crystallographica Section B* **32,** 2689 (1976).
16. Geller, S. & Hull, G. W. Superconductivity of Intermetallic Compounds with NaCl-Type and Related Structures. *Physical Review Letters* **13,** 127 (1964).
17. Banus, M. D., Hanneman, R. E., Stroncin, M. & Gooen, K. High-Pressure Transitions in $A^{(III)}B^{(VI)}$ Compounds: Indium Telluride. *Science* **142,** 662 (1963).
18. Bömmel, H. E., Darnell, A. J., Libby, W. F., Tittmann, B. R. & Yencha, A. J. Superconductivity of Metallic Indium Telluride. *Science* **141,** 714 (1963).
19. Abrikosov, N. K., Bankina, V. F., Poretskaya, L. V., Skudnova, E. V. & Chizhevskaya, S. N. *Semiconducting chalcogenides and alloys and their basic*. (1975).
20. Sheremet, G. P., Gerasimenko, V. S. & Zakharov, V. P. Vibration spectra of alloys of the In-Te system and its phase state diagram. *Ukrainskij Fizicheskij Zhurnal* **23,** 1326 (1978).
21. Kresse, G. & Furthmüller, J. Efficient iterative schemes for ab initio total-energy calculations using a plane-wave basis set. *Phys. Rev. B* **54,** 11169 (1996).
22. Kresse, G. & Hafner, J. Ab initio molecular dynamics for liquid metals. *Phys. Rev. B* **47,** 558 (1993).
23. Kresse, G. & Joubert, D. From ultrasoft pseudopotentials to the projector augmented-wave method. *Phys. Rev. B* **59,** 1758 (1999).
24. Hafner, J., Kresse, G., Vogtenhuber, D. & Marsman, M. The Vienne Ab-Initio Simulation Package (VASP) https://www.vasp.at/.
25. Perdew, J. P., Burke, K. & Ernzerhof, M. Generalized Gradient Approximation Made Simple. *Phys. Rev. Lett.* **77,** 3865 (1996).
26. Blöchl, P. E., Jepsen, O. & Andersen, O. K. Improved tetrahedron method for Brillouin-zone integrations. *Phys. Rev. B* **49,** 16223 (1994).
27. Parlinski, K., Li, Z. Q. & Kawazoe, Y. First-Principles Determination of the Soft Mode in Cubic ZnO_2. *Phys. Rev. Lett.* **78,** 4063 (1997).

28. Togo, A. & Tanaka, I. First principles phonon calculations in materials science. *Scripta Materialia* **108,** 1 (2015).
29. Togo, A., Oba, F. & Tanaka, I. First-principles calculations of the ferroelastic transition between rutile-type and $CaCl_2$-type SiO_2 at high pressures. *Phys. Rev. B* **78,** 134106 (2008).
30. Suekuni, K., Avila, M. A., Umeo, K. & Takabatake, T. Cage-size control of guest vibration and thermal conductivity in $Sr_8Ga_{16}Si_{30-x}Ge_x$. *Phys. Rev. B* **75,** 195210 (2007).
31. Nolas, G. S., Cohn, J. L., Dyck, J. S., Uher, C. & Yang, J. Transport properties of polycrystalline type-I Sn clathrates. *Phys. Rev. B* **65,** 165201 (2002).
32. Aydemir, U., Candolfi, C., Borrmann, H., Baitinger, M., Ormeci, A., Carrillo-Cabrera, W., Chubilleau, C., Lenoir, B., Dauscher, A., Oeschler, N., Steglich, F. & Grin, Y. Crystal structure and transport properties of $Ba_8Ge_{43}\square_3$. *Dalton Trans.* **39,** 1078 (2010).
33. Aydemir, U., Candolfi, C., Ormeci, A., O*ZT*an, Y., Baitinger, M., Oeschler, N., Steglich, F. & Grin, Y. Low-temperature thermoelectric, galvanomagnetic, and thermodynamic properties of the type-I clathrate $Ba_8Au_xSi_{46-x}$. *Phys. Rev. B* **84,** 195137 (2011).
34. Bentien, A., Nishibori, E., Paschen, S. & Iversen, B. B. Crystal structures, atomic vibration, and disorder of the type-I thermoelectric clathrates $Ba_8Ga_{16}Si_{30}$,$Ba_8Ga_{16}Ge_{30}$,$Ba_8In_{16}Ge_{30}$ and $Sr_8Ga_{16}Ge_{30}$. *Phys. Rev. B* **71,** 144107 (2005).
35. Aydemir, U., Candolfi, C., Ormeci, A., Baitinger, M., Burkhardt, U., Oeschler, N., Steglich, F. & Grin, Y. Electronic band structure and low-temperature transport properties of the type-I clathrate $Ba_8Ni_xGe_{46-x-y}\square_y$. *Dalton Trans.* **44,** 7524 (2015).
36. Aydemir, U., Candolfi, C., Ormeci, A., Baitinger, M., Oeschler, N., Steglich, F. & Grin, and Y. High temperature thermoelectric properties of the type-I clathrate $Ba_8Ni_xGe_{46-x-y}\square_y$. *Journal of Physics: Condensed Matter* **26,** 485801 (2014).
37. Candolfi, C., Aydemir, U., Koza, M. M., Baitinger, M., Grin, Y. & Steglich, F. Inelastic neutron scattering study of the lattice dynamics in the clathrate compound $BaGe_5$. *Journal of Physics: Condensed Matter* **27,** 485401 (2015).
38. Candolfi, C., Koza, M. M., Aydemir, U., Carrillo-Cabrera, W., Grin, Y., Steglich, F. & Baitinger, M. Vibrational dynamics of the type-I clathrates $A_8Sn_{44}\square_2$ (A = Cs, Rb, K) from lattice-dynamics calculations, inelastic neutron scattering, and specific heat measurements. *Journal of Applied Physics* **127,** 145104 (2020).
39. Safarik, D. J., Klimczuk, T., Llobet, A., Byler, D. D., Lashley, J. C., O'Brien, J. R. & Dilley, N. R. Localized anharmonic rattling of Al atoms in VAl_{10}. *Phys. Rev. B* **85,** 014103 (2012).

40. Koza, M. M., Leithe-Jasper, A., Sischka, E., Schnelle, W., Borrmann, H., Mutka, H. & Grin, Y. Effect of the electropositive elements A = Sc, La, and Ce on the microscopic dynamics of AV_2Al_{20}. *Phys. Chem. Chem. Phys.* **16,** 27119 (2014).
41. Suekuni, K., Tsuruta, K., Kunii, M., Nishiate, H., Nishibori, E., Maki, S., Ohta, M., Yamamoto, A. & Koyano, M. High-performance thermoelectric mineral $Cu_{12-x}Ni_xSb_4S_{13}$ tetrahedrite. *Journal of Applied Physics* **113,** 043712 (2013).
42. Lara-Curzio, E., May, A. F., Delaire, O., McGuire, M. A., Lu, X., Liu, C.-Y., Case, E. D. & Morelli, D. T. Low-temperature heat capacity and localized vibrational modes in natural and synthetic tetrahedrites. *Journal of Applied Physics* **115,** 193515 (2014).
43. Bouyrie, Y., Candolfi, C., Pailhès, S., Koza, M. M., Malaman, B., Dauscher, A., Tobola, J., Boisron, O., Saviot, L. & Lenoir, B. From crystal to glass-like thermal conductivity in crystalline minerals. *Phys. Chem. Chem. Phys.* **17,** 19751 (2015).
44. Candolfi, C., Guélou, G., Bourgès, C., Supka, A. R., Al Rahal Al Orabi, R., Fornari, M., Malaman, B., Le Caër, G., Lemoine, P., Hardy, V., Zanotti, J.-M., Chetty, R., Ohta, M., Suekuni, K. & Guilmeau, E. Disorder-driven glasslike thermal conductivity in colusite $Cu_{26}V_2Sn_6S_{32}$ investigated by Mossbauer spectroscopy and inelastic neutron scattering. *Phys. Rev. Materials* **4,** 025404 (2020).
45. Bridgman, P. W. Certain Physical Properties of Single Crystals of Tungsten, Antimony, Bismuth, Tellurium, Cadmium, Zinc, and Tin. *Proceedings of the American Academy of Arts and Sciences* **60,** 305 (1925).
46. Brice, J. C. *Crystal Growth Processes*. (Blackie & Sons Ltd., 1986).
47. Ibrahim, D., Misra, S., Migot, S., Ghanbaja, J., Dauscher, A., Malaman, B., Semprimoschnig, C., Candolfi, C. & Lenoir, B. Transport properties of polycrystalline SnTe prepared by saturation annealing. *RSC Advances* **10,** 5996 (2020).
48. Hewes, C. R., Adler, M. S. & Senturia, S. D. Annealing studies of PbTe and $Pb_{1-x}Sn_xTe$. *Journal of Applied Physics* **44,** 1327 (1973).
49. Fleurial, J. P., Gailliard, L., Triboulet, R., Scherrer, H. & Scherrer, S. Thermal properties of high quality single crystals of bismuth telluride-Part I: Experimental characterization. *Journal of Physics and Chemistry of Solids* **49,** 1237 (1988).
50. Brebrick, R. F. & Gubner, E. Composition Stability Limits of PbTe. II. *The Journal of Chemical Physics* **36,** 1283 (1962).
51. Brebrick, R. F. Composition stability limits of binary semiconductor compounds. *Journal of Physics and Chemistry of Solids* **18,** 116 (1961).

52. Brebrick, R. F. Analysis of the solidus lines for PbTe and SnTe. *Journal of Electronic Materials* **6,** 659 (1977).
53. Brebrick, R. F. Deviations from stoichiometry and electrical properties in SnTe. *Journal of Physics and Chemistry of Solids* **24,** 27 (1963).
54. Ibrahim, D. Synthèse et caractérisation de matériaux à base de SnTe pour la conversion d'énergie par effets thermoélectriques. (2018).
55. Chen, X., Wu, H., Cui, J., Xiao, Y., Zhang, Y., He, J., Chen, Y., Cao, J., Cai, W., Pennycook, S. J., Liu, Z., Zhao, L.-D. & Sui, J. Extraordinary thermoelectric performance in n-type manganese doped Mg_3Sb_2 Zintl: High band degeneracy, tuned carrier scattering mechanism and hierarchical microstructure. *Nano Energy* **52,** 246 (2018).

General conclusion

The search for finding alternative Pb-free materials for mid-temperature range thermoelectric applications was addressed in this thesis by studying two highly-efficient and promising tellurium-based materials (XTe; X = Sn, In). The aim of this thesis work was to synthesize, characterize and optimize the thermoelectric properties of these two chalcogenide compounds.

In a first part, a detailed theoretical and experimental investigation of the influence of the In-induced resonant level (RL) on the low- and high-temperature thermoelectric properties was reported. The theoretical calculations have been carried out using the Korringa-Kohn-Rostoker method with the coherent potential approximation (KKR-CPA). These calculations have confirmed the formation of an In-induced RL in the valence bands of SnTe, revealing a narrow and sharp peak in the density of states (DOS) induced by the hybridization of the indium *s*-states with the electronic states of the host framework. The calculations of Bloch spectral functions further evidence that indium does not form any separate impurity band but rather leads to a strong smearing of the valence bands. As a result, the RL induces an increase in the DOS effective mass. An optimum In concentration of 2 % was predicted to give the optimum thermopower value.

These predictions were experimentally confirmed on a series of polycrystalline $Sn_{1.03-x}In_xTe$ samples across the entire compositional range accessible at ambient pressure (that is, for $0.0 \leq x \leq 0.40$). The structural and chemical characterizations of the samples by powder X-Ray diffraction (PXRD) and scanning electronic microscopy with energy dispersive X-Ray spectroscopy (SEM-EDXS) confirmed the successful insertion of In and the good chemical homogeneity of the samples. A maximum thermopower of 52 $\mu V\ K^{-1}$ was measured for $Sn_{1.01}In_{0.02}Te$ at 300 K, which was almost three times higher than the binary $Sn_{1.03}Te$ compound. A rather surprising crossover from positive to negative values of thermopower was observed for samples with In content $0.0015 \leq x \leq 0.0045$ at around 100 K. This phenomenon was attributed to phonon-drag effect and/or interband scattering. Hall data evidenced an In^+ valence state that does not support the possibility of charge-Kondo effect. The role of the RL was shown to prevail up to $x = 0.05$, after which this phenomenon tends to disappear. Increasing the In content above $x > 20$ % leads to strong modifications in the electronic band structure of SnTe. In particular, *n*-type behavior was observed at low temperatures in agreement with literature data. No superconducting transition was observed for sample with In content x =

0.0035 down to 0.40 K, confirming earlier reports on these compounds. In contrast, a superconducting transition temperature as high as 4.4 K was observed for $x = 0.4$. At high temperatures, lessened but significant impact of RL was evidenced leading to a maximum *ZT* value of 0.75 at 800 K for $x = 0.0035$. The beneficial role of the RL on the practical applications was underlined as it yields high average *ZT* values over an extended temperature range. Our results also provided strong evidence that existing valence band models for estimating the lattice contribution of the thermal conductivity in SnTe:In are insufficiently adequate, as they give rise to too low Lorenz numbers. Finally, these results and understanding of the behavior of resonant dopant in SnTe sets out a clear indication that the selection of co-dopant remains an important task to avoid the movement of the chemical potential away from the resonant state.

The second part of this thesis confirmed InTe as a promising thermoelectric material for applications in power generation. Both the electronic and phonon band structure were calculated, and were found in good agreement with literature data. A large, centimeter-sized single-crystal of InTe was grown using the Bridgman-Stockbarger technique. This successful synthesis enabled a detailed study of the crystallographic properties using several diffraction techniques such as PXRD, Laue XRD and single-crystal XRD. The transport properties were studied over a broad temperature range (5 – 800 K) in order to unravel its basic physical properties. A clear anisotropy was observed in single crystalline InTe along the two measured directions. An extremely low lattice thermal conductivity of 0.25 W m^{-1} K^{-1} was obtained for sample along the [110] direction, a remarkable value for a perfectly-ordered crystalline lattice. A high *ZT* value of 0.7 was obtained for a sample measured along the [110] direction.

Along with single-crystalline InTe, polycrystalline samples were prepared yielding a high *ZT* value of 0.9 at 710 K. To confirm the possible off-stoichiometry of InTe, likely arising from In vacancies, polycrystalline samples were subjected to the technique of saturation annealing. This study further show that different hole concentration can be achieved by varying the annealing temperature. From our results, it remains however unclear whether a structural transition below 185 K suggested in the literature really sets in InTe. The remarkable and intriguing transport properties of InTe clearly call for further theoretical and experimental studies. In particular, various doping strategies may be use to further enhance the thermoelectric performances of InTe. In addition, determining the dominant type of defects as a function of the hole concentration warrants further energy defect calculations. The very low lattice thermal conductivity in InTe makes the study of its lattice dynamics by inelastic neutron

scattering a worthwhile undertaking in the future. Finally, whether *n*-type InTe can be synthesized remains an open, yet interesting, question.

Appendix A

Material densification and orientation

After synthesis, the ingots needed to be crushed and densified into a bulk, dense pellet to perform various physical property measurements. The densification was made using the spark plasma sintering (SPS). The first part of this appendix is dedicated to the principle of the SPS technique and description of the instrument used. The second part describes briefly the different orientations of the samples that were used during this thesis for physical property measurements. It is important to note that the assessment of the dimensionless thermoelectric figure of merit *ZT* value of a material requires careful measurements of the electrical resistivity, the thermopower and the thermal conductivity along the same direction. The case of single-crystalline InTe will be first presented before turning to the case of polycrystalline SnTe and InTe.

A.1 Spark Plasma Sintering

SPS is a technique to consolidate nano- or microcrystalline conducting or insulating powders into a dense pellet at lower sintering temperatures and in shorter time than conventional methods (hot press, etc.). It is a uniaxial pressure technique accompanied with a pulsed current. It is considered that, for conducting powders, the arc or/and the plasma generated during the electrical discharge cleans the grain surface of the material leading to the formation of improved bridges between the grains that increase the diffusion phenomenon. The strong rise in the plasma temperature promotes a quick phase change locally from solid to liquid to gas that increases the mass transfer kinetics and leads to densification and grain coarsening.[1] However, many questions remain open as for the exact physical mechanism and the existence of the plasma. For a better and deep understanding about this technique the reader can refer to the monograph of Cavaliere.[2] The advantage of this technique of densification is the speed of sintering with low thermal inertia of the system that reaches high temperatures in few minutes.

In this thesis work, we used a Dr Sinter 5145S model manufactured by the SPS syntex Inc., Japan (Figure A.1). This particular model is capable of delivering a current pulse of

maximum intensity of 1500 A and a maximum applied force of 5 kN. The experiments can be performed under primary or secondary vacuum or even in the presence of argon.

Figure A.1: Dr Sinter 515S SPS Syntex Inc. at IJL, Nancy.[3]

As already mentioned in the main text, graphite dies were used for the SPS process. They can sustain a temperature of up to 2000°C and a uniaxial pressure of 200 MPa. A schematic view is shown in Figure A.2 for a simplified understanding of the graphite matrix.

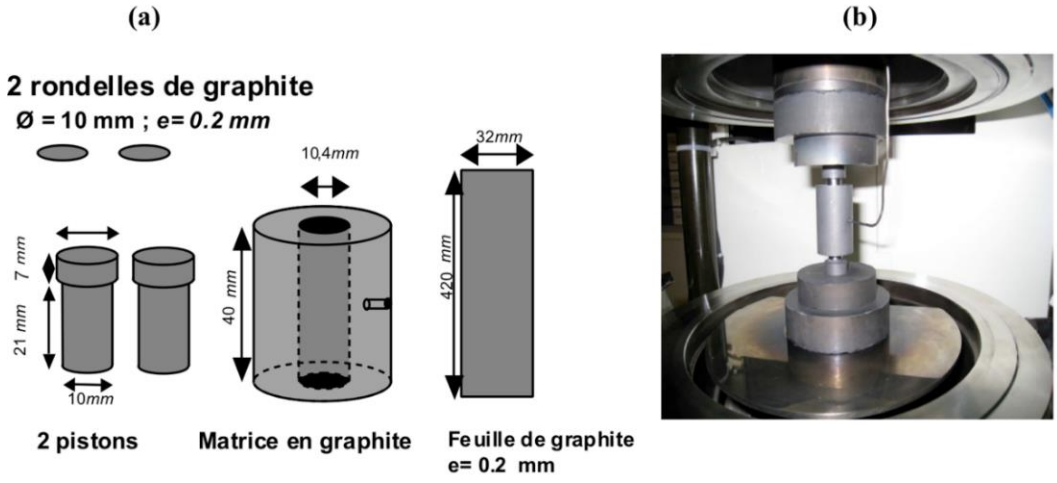

Figure A.2. a) Schematic details of graphite matrix and punches used in this thesis work b) Photograph of the die inside the SPS chamber.[3]

A.2 Orientation

A.2.1 Single crystalline InTe

After determining the orientation of the single crystal of InTe synthesized in Chapter 4 by Laue XRD, samples were cut parallel and perpendicular to the *c*-axis to obtain samples in the two different main directions: one along the *c*-axis (parallel) and another one along the [110] direction (perpendicular to the *c*-axis). As we used two distinct instruments for measuring the physical properties at low and high temperatures (see Appendix X), it was necessary to cut several different samples with distinct, yet appropriate, shape and size. Figure A.3 shows the protocol followed to obtain the desired samples. A reference crystal image was presented in Chapter 4, Figure 4.16.

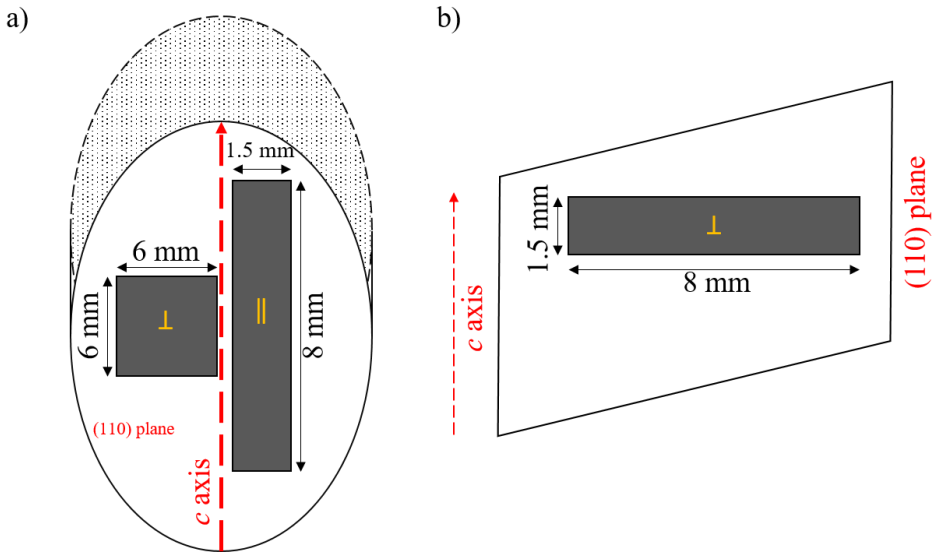

Figure A.3: a) Schematic top view of the InTe single crystal as seen from the cleavage plane b) side view of the single crystal.

Two bar-shaped samples of approximate geometrical dimensions 8×1.5×1.5 mm^3 were cut along the *c*-axis (see Figure A.3 (a)). The first bar-shaped sample was used to measure the thermoelectric properties at low temperatures (5 – 300 K) using a PPMS and the second bar-shaped sample was used to measure the electrical resistivity and thermopower at high temperatures (300 – 800 K) using a ZEM-3 system. A square-shaped sample of dimensions 6×6×1.5 mm^3 (see Figure A.3 (a)) was cut in the same plane to measure the high-temperature

thermal diffusivity along the [110] direction using a LFA system. Another bar-shaped sample was cut perpendicularly to the (110) plane (see Figure A.3 (b)), that is, along the [110] direction, which was used for high temperature electrical property measurements (ZEM-3). Unfortunately, due to the easy cleavage of the crystal along the (110) plane, cutting a square-shaped sample along the *c*-axis and a bar-shaped sample along the [110] direction was not possible despite several attempts.

A.2.2 Polycrystalline *X*Te (*X* = Sn, In)

For cubic crystal, the transport properties measured parallel and perpendicular to the pressing direction are identical to within experimental uncertainty if the SPS process does not induce any texture (this is usually the case for thermoelectric cubic materials). However, for anisotropic crystal structures, it is essential to measure these properties in along and perpendicular to the pressing direction and to combine them correctly to obtain a correct estimation of the *ZT* values.

Because SnTe crystallizes in a cubic crystal structure ($a = b = c$), the transport properties are not direction dependent. Hence, we prepared a bulk of total height ~ 4 – 5 mm and diameter 10 mm (see Figure A.4). A disc of thickness ~ 2 mm was cut, from which two bar-shaped samples ($8\times1.5\times1.5$ mm^3) were cut. One bar was used for measurements at low temperatures (PPMS) and the other one was utilized for measurements at high temperatures (ZEM-3). Another disc of thickness ~ 1 mm was cut as shown in Figure A.4, and used for high-temperature thermal diffusivity measurements (LFA). The remaining sample was utilized for additional experiments whenever necessary such as XRD, SEM-EDXS, etc. Note that all the samples were carefully polished after cutting to obtain a constant section over the length of the bars and a constant thickness for the discs.

For InTe, which crystallizes in an anisotropic crystal structure ($a = b \neq c$), the transport properties are direction dependent. Thus, a larger quantity of powders was densified to obtain a dense cylindrical pellet of a total height of ~ 9 mm. Four bar-shaped ($8\times1.5\times1.5$ mm^3), one disc-shaped (10 mm in diameter and 1.5 mm in thickness) and one square-shaped ($6\times6\times1.5$ mm^3) samples were cut parallel and perpendicular to the pressing direction, as shown in Figure A.4.

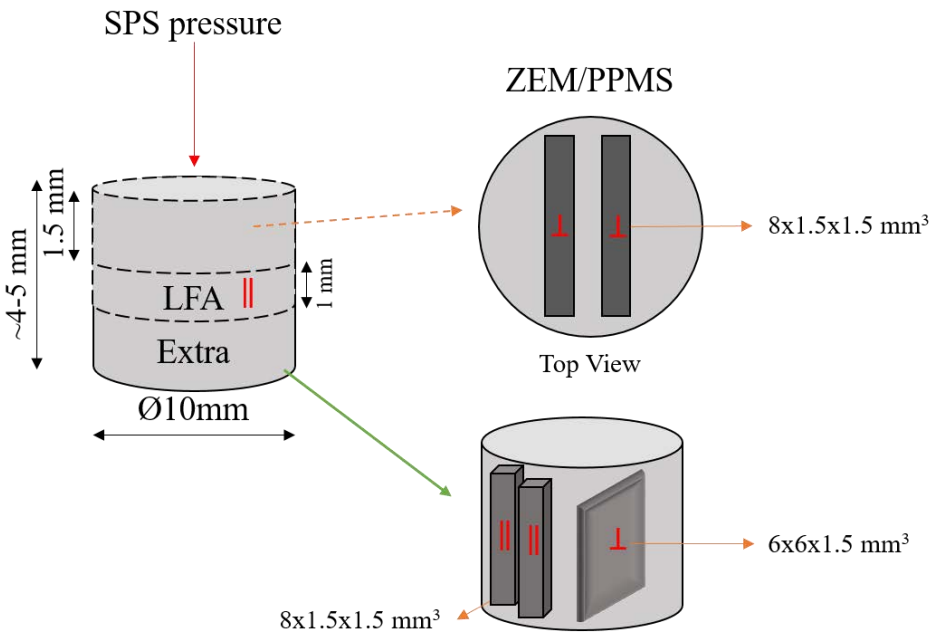

Figure A.4: Simple schematic of polycrystalline samples cut parallel and perpendicular to the SPS uniaxial pressure direction.

References

1. Tokita, M. Development of Large-Size Ceramic/Metal Bulk FGM Fabricated by Spark Plasma Sintering. *Materials Science Forum* **308–311,** 83 (1999).
2. Cavaliere, P. *Spark Plasma Sintering of Materials: Advances in Processing and Applications*. (Springer International Publishing, 2019).
3. Ibrahim, D. Synthèse et caractérisation de matériaux à base de SnTe pour la conversion d'énergie par effets thermoélectriques. (2018).

Appendix B

Structural and chemical spectroscopies

In this thesis, several different X-ray diffraction techniques (powder, single crystal and Laue) were used on both single and polycrystalline samples. In addition to the structural analysis, chemical properties were analyzed using the scanning electron microscope with energy dispersive X-ray spectroscopy (SEM-EDXS). This appendix briefly describes these techniques and the instruments used.

B.1 Powder X-Ray Diffraction (PXRD)

PXRD was used to determine the sample purity and crystal structure. It is a technique that uses Bragg's law to determine the diffracted X-rays caused by the interaction of X-rays with the electron cloud in a material. A Bruker D8 Advance diffractometer was used with the Cu $K\alpha_1$ radiation (λ = 1.54056 Å). A single crystal of Ge with orientation (111) acts as the primary monochromator that discriminates between the $K\alpha_1$ and $K\alpha_2$ lines. This model contains two super-fast detectors, namely LynEye and SolX, that can be used in Bragg-Brentano or Debye-Scherrer geometry. The materials were hand-crushed in a mortar inside a glove box into fine powders prior to measurements and were placed on a silicon-glass sample holder using cyclohexane. For all samples, the data was collected at 300 K over the angular range (2θ) of 20 – 80°. The counting time was set between one and several hours depending on the desired statistics. All the data obtained were indexed using EVA software while Rietveld refinements were performed using the FullProf software to determine the lattice parameters.

B.2 Laue X-Ray Diffraction

To confirm the single crystalline nature and determine the orientation of the InTe single crystal synthesized, Laue XRD technique was implemented with the help of a homemade diffractometer available at the institute. The single crystal was placed on a 3-axis goniometer with the cleavage plane facing (see Figure B.1) and being exactly perpendicular to the incident source of "white" radiation. Radiation from the target metal having high atomic number is

bombarded at the crystal sample and back-reflection photograph is taken on an X-ray sheet. This diffraction was taken at several spots to confirm the single crystallinity of InTe.

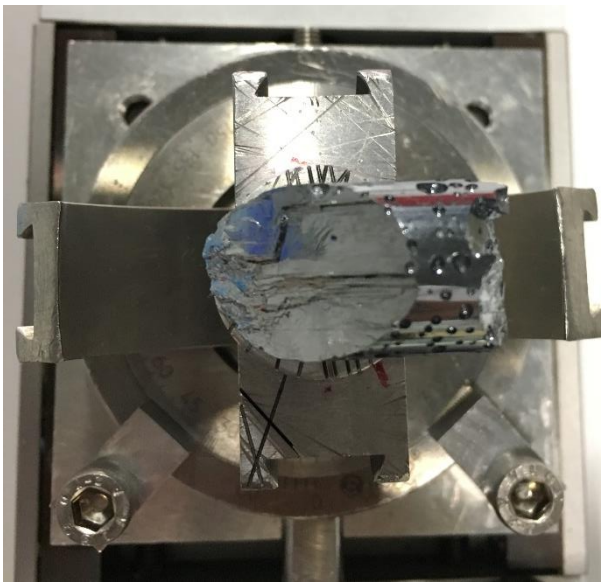

Figure B.1: InTe single crystal placed on a 3-axis goniometer.

B.3 Single crystal X-Ray Diffraction

To further verify the crystal structure of InTe and follow its response upon cooling, single crystal XRD was performed in collaboration with Pr. Bernard Malaman of our institute. A Bruker APEX-II diffractometer equipped with a CCD detector was used to perform the experiment at 300 and 80 K using the Mo Kα radiation (λ = 0.71073 Å). A very small piece of the single crystal was taken from the large single crystal and mounted on a tip using a tiny amount of grease. The crystal structure was determined by direct methods and full-matrix least-square refinements were carried out using Sir97 and SHELX-2013, respectively, implemented in the WinGX program package.

B.4 Scanning electron microscopy

A scanning electron microscope equipped with energy dispersive X-ray spectroscopy was used to determine the surface morphology and composition of the sample. The sample surface was polished using SiC paper to achieve a mirror-like surface. The surface was scanned using a focused beam of electrons. A FEI quanta 600 Field Emission Gun SEM was used,

equipped with a Quanta SDD detector EDS (Bruker AXS, Esprit software, optimal conditions: 10000 counts, working distance ~ 11 mm).

Appendix C

Measurement techniques of physical properties

Experimental techniques used in this thesis work to measure the different physical properties are described in this Appendix. To calculate the dimensionless thermoelectric figure of merit *ZT* requires measuring the thermopower, the electrical resistivity and the thermal conductivity of the samples synthesized in a wide range of temperatures (2 – 800 K). Different instruments and techniques were used for each kind of measurement at either low (2 – 300 K) or high temperatures (300 – 800 K). In addition to the three parameters mentioned above, galvanomagnetic measurements (Hall Effect) at low temperatures were also performed to determine the Hall coefficient and infer the carrier concentration and mobility. Specific heat measurements were additionally performed at low temperatures to obtain information about the density of states at the Fermi level and the low-energy features that govern the low-temperature data. For a descriptive and detailed explanation of these techniques, the reader can refer to the following thesis.[1]

C.1 Low-temperature measurements

At low temperatures (2 – 300 K), all measurements were performed using a physical property measurement system (PPMS), shown in Figure C.1.

C.1.1 Thermal Transport Option

The thermopower, the thermal conductivity and the electrical resistivity were simultaneously measured between 2 – 300 K using the continuous mode in the Thermal Transport Option (TTO) of the PPMS. Bar-shaped sample of typical dimensions 8×2×2 mm^3 were used. To avoid any important uncertainty in the length and cross sections of the samples, they were well polished using a SiC paper to ensure that all the sides were perfectly parallel. All the measurements were done under secondary vacuum. A standard four-probe resistivity

measurement method was used at low temperatures. A current was applied on the end contacts of the sample and difference in voltage was measured by two contacts positioned onto the long face of the samples. The electrical resistivity was finally calculated using the Ohm's law. To measure the thermopower and thermal conductivity of the samples, the standard stationary method required to heat one side of the sample while the other one was connected to a heat sink. The thermal conductivity was calculated using the input power and the resulting temperature difference. For the thermopower, the temperature difference and the voltage difference were directly measured on the two sides of the sample.

Figure C.1: Experimental setup of Quantum Design PPMS installed at IJL, Nancy.

C.1.2 Alternating Current Transport Option

Hall effect measurements were performed between 5 and 300 K with a five-probe configuration using the AC transport option of the PPMS. Good electrical contacts were realized on the bar-shaped samples by brazing copper wires onto the samples with a low-melting point braze. The Hall resistivity ρ_H was determined by measuring the antisymmetric component of the transverse ρ_{xy} voltage under magnetic field reversal following the formula $\rho_H = \left[\rho_{xy}(+\mu_0 H) - \rho_{xy}(-\mu_0 H)\right]/2$. The Hall coefficient R_H was derived from the slope of the $\rho_H(\mu_0 H)$ data for fields $-1 \leq \mu_0 H \leq 1$T. The Hall hole concentration p and the Hall mobility μ_H were determined from the single-carrier relations $p = 1/R_H e$ and $\mu_H = R_H/\rho$

where e is the elemental charge. Additional measurements under magnetic field were done in the range of -7 to 7 T using the superconducting coil equipping the PPMS system.

C.1.3 Specific heat option

A small piece of sample (typical mass of 20 mg) was glued on a heat capacity puck using a minute amount of Apiezon N grease to ensure a good thermal contact between the sample and the platform of the puck. The specific heat of the grease was first measured without the sample. A second measurement of the sample + grease was subsequently performed and the contribution of the grease was subtracted to the total signal to calculate the specific heat of the sample. These measurements were performed under secondary vacuum (< 1 mTorr) to avoid any convective losses in the chamber. A heater on the platform of the puck produces a constant heat pulse. The system fits the measurement of the relaxation of the heat pulse sent to the sample and calculate the specific heat capacity.

C.2 High-temperature measurements

C.2.1 Thermal conductivity

The thermal diffusivity a was measured on the disc/square-shaped samples between 300 and 800 K with a Netzsch laser flash instrument (LFA 427). A heat pulse is provided by the Nd:GdGG (Neodymium: Gallium-Gadolinium-Garnet) laser operating at a wavelength of 1064 nm, delivering a maximum power of 20 J/pulse. All the measurements were performed under protective and constant flow of argon (75 ml/min).

The sample preparation was carefully done to minimize geometrical uncertainties. Slices with thicknesses ranging between 0.7 and 1 mm were cut with the help of a diamond-wire saw from the sintered cylindrical ingot with diameter ~ 10 mm (err ± 0.05 mm). For anisotropic materials, the sample dimension changes to a square ($6\times6\times1$ mm^3) with thickness being the same. All samples for LFA measurements were polished with high accuracy using a dry-sand polishing paper ($\Delta e \leq 0.02$ mm). Prior to measurements, the samples were spray-coated with a thin layer of graphite to ensure a homogeneous signal absorption and emission on the respective surfaces.

It is a well-known fact that above the ambient temperature the heat losses by radiation (varying like T^3) are important. This limits the use of stationary methods for determining the thermal conductivity of a material. Amongst the most used alternative method is the indirect measurement technique known as the Flash method. This dynamic method, first developed by Parker[2], could be used to measure the thermal diffusivity of solid, powders and liquid samples. The thermal diffusivity was used to calculate the total thermal conductivity κ via the formula $\kappa = aC_p d$ where C_p is the specific heat and d is the experimental density determined from the weight and geometric dimensions of the consolidated pellets. C_p was approximated by the Dulong-Petit law $C_p = 3NR$ where N is the number of atoms per formula unit and R is the perfect gas constant. The temperature dependence of the density was not taken into account in the present case.

In this technique, a cylindrically-shaped solid material (ideal case) is thermally excited by a laser on the front surface. The resulting time dependent temperature difference is detected on the other surface of the sample. The time in which the energy reaches the other side of the sample is directly proportional to the thermal conductivity of the sample. It can be explained by the following equation:

Equation C.1:

$$d = 0.1388 \frac{e^2}{t_{1/2}}$$

where e is the thickness of the material and $t_{1/2}$ is the time to reach the half of the maximum temperature. The sample must be opaque at a given laser wavelength, homogenous, isotropic with constant thermophysical properties. The sample is subjected to heat losses occurring on the three faces (front, back and lateral) which are uniform on the surface and constant with time. A thermogram, which is the temperature evolution with time at the detector, determines the thermal diffusivity of a sample.

Figure C.2: Netzsch LFA 427 installed at IJL, Nancy.

Several models to examine these thermograms and infer the thermal diffusivity of the sample exist. Among them, the Cape-Lehman model was considered. This model considers a 2D transfer and take into account heat losses on the surfaces. This model incorporates corrections for a finite width of the laser pulse.

C.2.2 Thermopower and electrical resistivity

The thermopower and electric resistivity measurements were performed simultaneously using a ZEM-3 apparatus (Ulvac-Riko; see Figure C.3). The sample is placed in between two alumina blocks using a clamp system. The measurement principle remains similar to that used at low temperatures. Two contacts on the ends (alumina blocks) of the bar-shaped sample and other two thermocouples on the long face. This equipment is capable of measuring α and ρ under controlled atmosphere from 300 to 1373 K. One block acts as a heat sink while the another one as a heater. The ends of the samples must be strictly parallel to each other and well-polished for good electrical and thermal contacts. The ZEM-3 systems contain a lamp-oven, which regulates the heating rate (50 K min^{-1}) and measure ΔT. For each measurement, four temperature differences (10, 20, 25, 30) were imposed between the platinum electrodes, controlled using a computer software.

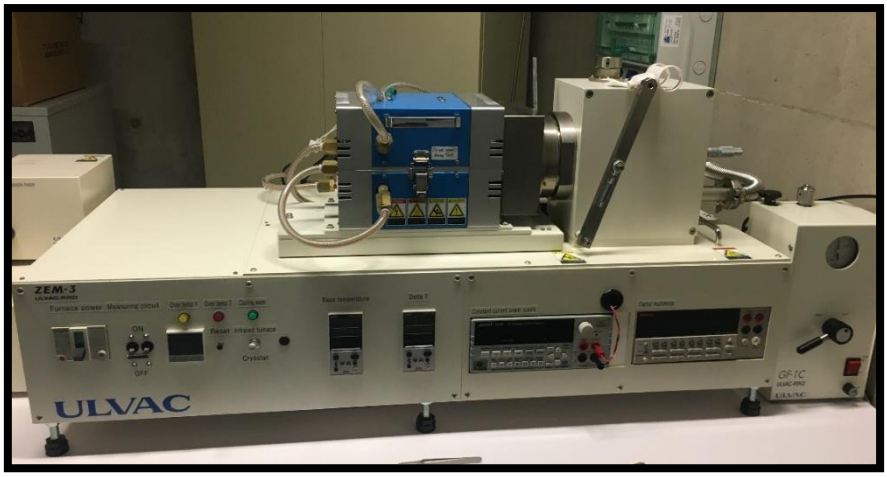

Figure C.3: ZEM-3 installed at IJL, Nancy.

References

1. Ohorodniichuk, V. Influence of nanostructuring on thermoelectric properties of p-type bulk materials based on (Bi, Sb, Te). (2014).
2. Parker, W. J., Jenkins, R. J., Butler, C. P. & Abbott, G. L. Flash Method of Determining Thermal Diffusivity, Heat Capacity, and Thermal Conductivity. *Journal of Applied Physics* **32,** 1679–1684 (1961).

Appendix D

Transport models

Over the course of this thesis work, we have used several models to calculate the Ioffe-Pisarenko curves and the Lorenz number in order to estimate the lattice thermal conductivity via the Wiedemann-Franz law. The relations giving the thermopower and the Lorenz number for the models considered are given in this appendix. All the following models are obtained from solutions to the Boltzmann transport equation.

- Single Parabolic Band (SPB) model with acoustic phonon scattering

In the SPB model,[1,2] the thermopower is calculated by the relation:

Equation D.1:

$$\alpha = \pm\frac{k_B}{e}\left(\frac{2F_1(\eta)}{F_0(\eta)} - \eta\right)$$

where k_B is the Boltzmann constant, e is the elementary charge, $F_n(\eta)$ is the Fermi integral and η is the reduced chemical potential. Using the value of η obtained from the experimental α value, the Lorenz number L can be then estimated by the relation:

Equation D.2:

$$L = \left(\frac{k_B}{e}\right)^2\left[\frac{3F_2(\eta)}{F_0(\eta)} - \left(\frac{2F_1(\eta)}{F_0(\eta)}\right)^2\right]$$

In both relations, the Fermi integral $F_n(\eta)$ is given by:

Equation D.3:

$$F_n(\eta) = \int_0^\infty \frac{x^n}{1 + e^{x-\eta}}\,dx$$

where x is the reduced carrier energy. The hole concentration p is then given by:

Equation D.4:

$$p = 4\pi \left(\frac{2m^* k_B T}{h^2}\right)^{3/2} F_{1/2}(\eta)$$

where m^* is the density-of-states effective mass and h is the Planck constant.

- Two Valence Band (TVB) model with acoustic phonon scattering

This model was considered for the SnTe samples. The valence band structure is approximated by a light non-parabolic valence band and a second heavy parabolic valence band. The Lorenz number L for Temperature Dependent Two Valence Band (TD-TVB) model was calculated using the following formula:[2–4]

Equation D.5:

$$L = (\sigma_{lh} L_{lh} + \sigma_{hh} L_{hh})/(\sigma_{lh} + \sigma_{hh})$$

where σ is the electrical conductivity and the subscripts lh and hh refer to the light valence band and heavy valence band, respectively. The different contributions to the Lorenz number, that is, from the light and heavy valence bands where calculated using the following equations:

Equation D.6:

$$L_{lh} = \left(\frac{k_B}{e}\right)^2 \left[\frac{{}^{2}_{.}F^{1}_{-2}(\eta, \alpha)}{{}^{0}_{.}F^{1}_{-2}(\eta, \alpha)} - \left(\frac{{}^{1}_{.}F^{1}_{-2}(\eta, \alpha)}{{}^{0}_{.}F^{1}_{-2}(\eta, \alpha)}\right)^2\right]$$

where $\alpha = k_B T/E_g$ is the non-parabolicity parameter with E_g is the energy gap and T is the temperature. In this relation, the functions the ${}^{2}_{.}F^{1}_{-2}$ are the generalized Fermi integral given by:

Equation D.7:

$${}^{n}_{.}F^{m}_{l} = \int_0^\infty \left(-\frac{\partial f}{\partial \varepsilon}\right) \varepsilon^n (\varepsilon + \alpha\varepsilon^2)^m [(1 + 2\alpha\varepsilon)^2 + 2]^{l/2} d\varepsilon$$

where f is the Fermi-Dirac distribution and ε is the reduced energy of the carriers.

Equation D.8:

$$L_{hh} = \left(\frac{k_B}{e}\right)^2 \left[\frac{{}^2F_{-2}^1(\eta - \Delta_V, 0)}{{}^0F_{-2}^1(\eta - \Delta_V, 0)} - \left(\frac{{}^1F_{-2}^1(\eta - \Delta_V, 0)}{{}^0F_{-2}^1(\eta - \Delta_V, 0)}\right)^2\right]$$

where $\Delta_V = \Delta E / k_B T$ is the energy offset between the two valence band maxima. In this relation, the choice $\alpha = 0$ makes the heavy-hole band parabolic. η was calculated using the following relation for the total thermopower:

Equation D.9:

$$S_{lh+hh} = \frac{k_B}{e} \frac{\xi\left({}^1F_{-2}^1(\eta, \alpha) - \eta\, {}^0F_{-2}^1(\eta, \alpha)\right) + \left({}^1F_{-2}^1(\eta - \Delta_V, 0) - (\eta - \Delta_V)\, {}^0F_{-2}^1(\eta - \Delta_V, 0)\right)}{\xi\, {}^0F_{-2}^1(\eta, \alpha) + {}^0F_{-2}^1(\eta - \Delta_V, 0)}$$

Equation D.10:

$$\xi = \frac{m_{hh}^* D_{hh}^2}{m_{lh}^* D_{lh}^2}$$

where m_{hh}^* is the density-of-states effective mass of the heavy valence band, m_{lh}^* is the density-of-states effective mass of the light valence band, D_{hh} is the heavy-valence-band acoustic deformation potential and D_{hh} is the light-valence-band acoustic deformation potential. The equations for hole concentrations are:

Equation D.11:

$$p_{hh} = \frac{1}{3\pi^2} \left(\frac{2{m_{hh}}^* k_B T}{\hbar^2}\right)^{3/2} {}^0F_0^{3/2}(\eta - \Delta_V, 0)$$

Equation D.12:

$$p_{lh} = \frac{1}{3\pi^2} \left(\frac{2{m_{lh}}^* k_B T}{\hbar^2}\right)^{3/2} {}^0F_0^{3/2}(\eta, \alpha)$$

The total Hall hole concentration p_H is then given by:

Equation D.13:

$$p_H = \frac{[bp_{lh} + p_{hh}]^2}{[A_{lh}b^2 p_{lh} + A_{hh}p_{hh}]}$$

where A_{lh} and A_{hh} are the Hall factors of the light and heavy-hole band, respectively, given by:

Equation D.14:

$$A_{hh} = \frac{3}{2}F_{1/2}\frac{F_{-1/2}}{2{F_0}^2}$$

Equation D.15:

$$A_{lh} = \frac{3K(K+2)}{(2K+1)^2}\frac{{}^0F_{-4}^{1/2}\,{}^0F_0^{3/2}}{({}^0F_{-2}^1)^2}$$

where $K = m_\parallel^*/m_\perp^*$ is the ratio between the effective mass due to the anisotropy of the valence band at the L point of the Brillouin zone. These two effective masses are related to the density-of-states effective mass via:

Equation D.16:

$$m^* = N_V^{2/3}\left({m_\perp^*}^2 m_\parallel^*\right)^{1/3}$$

where N_V is the band degeneracy.

In the calculations of the Ioffe-Pisarenko curve shown in Chapter 3, we used the following values for the various band parameters:

$E_g = 0.18$ eV, $m_{lh} = 0.168m_0$, $m_{hh} = 1.92m_0$, $\Delta_V = 0.35$ eV, $\frac{D_{hh}}{D_{lh}} = 0.5$, $K = 4$, $b = 4$, $N_{V,lh} = 4$, $N_{V,hh} = 12$

These parameters were used in prior studies on SnTe and corresponds to room-temperature values and were considered for the two-band model with temperature-independent parameters.[5] In the model where temperature-dependent parameters were used, the following temperature dependences were considered:

$\Delta_V = 0.49075 - 0.0003211T$, $m_{lh} = 0.11943 - 1.2537\times10^{-5}\,T + 1.9379\times10^{-7}\,T^2$, $m_{lh} = 1.182 - 0.0016126T + 5.7159\times10^{-7}\,T^2$

The other parameters were considered as temperature-independent.

References

1. May, A. F. & Snyder, G. J. in *Materials, Preparation, and Characterization in Thermoelectrics: Thermoelectrics and Its Energy Harvesting* (ed. Rowe, D. M.) (CRC Press, 2017).
2. Fistul', V. I. *Heavily Doped Semiconductors*. **1,** (Plenum Press, New York, 1969).
3. Zhang, Q., Liao, B., Lan, Y., Lukas, K., Liu, W., Esfarjani, K., Opeil, C., Broido, D., Chen, G. & Ren, Z. High thermoelectric performance by resonant dopant indium in nanostructured SnTe. *Proceedings of the National Academy of Sciences* **110,** 13261 (2013).
4. Thesberg, M., Kosina, H. & Neophytou, N. On the Lorenz number of multiband materials. *Physical Review B* **95,** 125206 (2017).
5. Zhou, M., Gibbs, Z. M., Wang, H., Han, Y., Xin, C., Li, L. & Snyder, G. J. Optimization of thermoelectric efficiency in SnTe: the case for the light band. *Phys. Chem. Chem. Phys.* **16,** 20741 (2014).

Appendix E

Comparison between the data measured parallel and perpendicular to the pressing direction for polycrystalline InTe samples prepared by saturation annealing

Hereafter, we present the transport data measured both parallel and perpendicular to the pressing direction on polycrystalline, saturation-annealed InTe samples. For comparison purposes, the data measured on non-annealed InTe have been added.

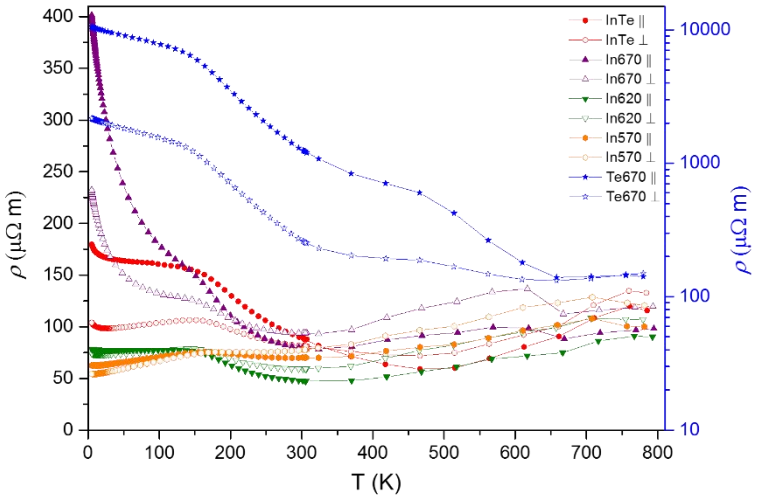

Figure E.1: Temperature dependence of the electrical resistivity ρ for InTe-based samples prepared by saturation annealing measured parallel and perpendicular to the pressing direction. Right (blue) scale is dedicated to the Te-rich sample (Te670) and the left scale is for all the other samples in the series.

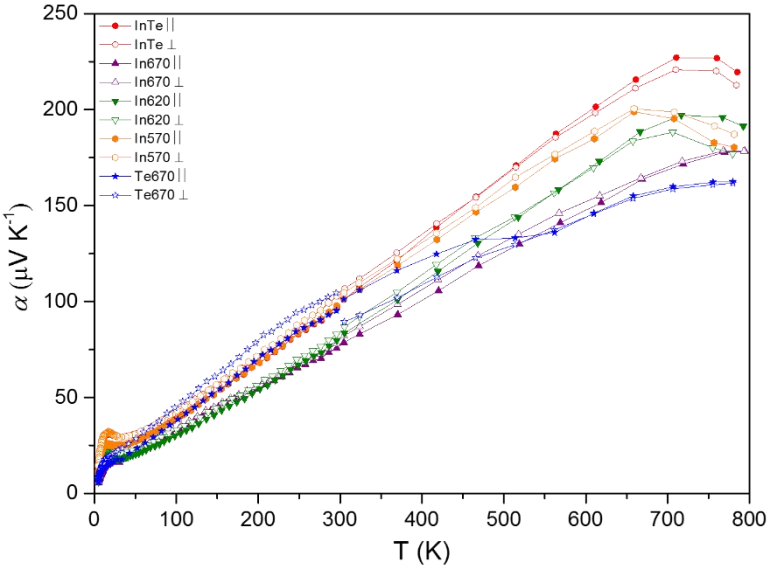

Figure E.2: Temperature dependence of the thermopower α for saturation-annealed InTe samples.

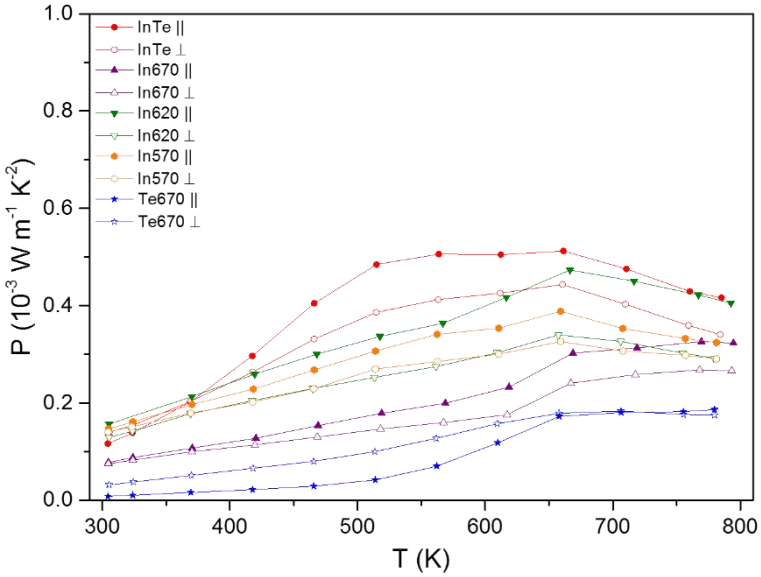

Figure E.3: High temperature dependence of power factor $P = \alpha^2/\rho$ for saturation-annealed InTe samples.

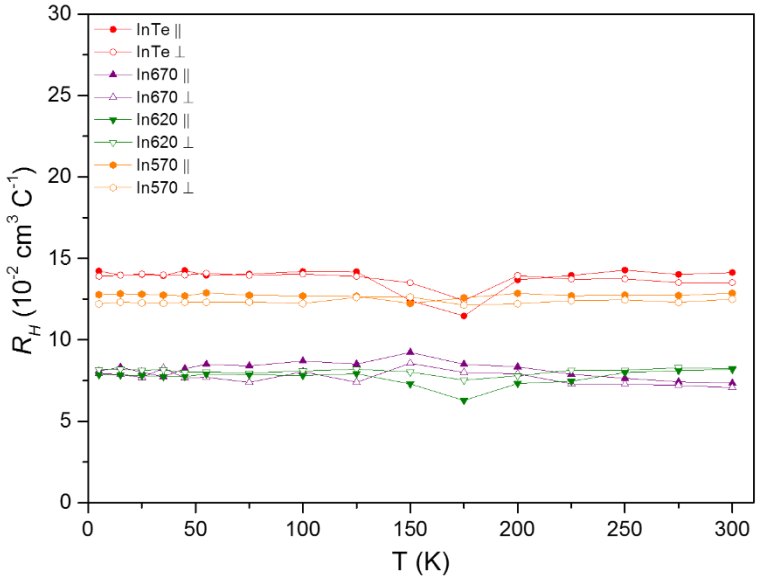

Figure E.4: Low-temperature dependence of the Hall coefficient R_H for saturation-annealed InTe samples.

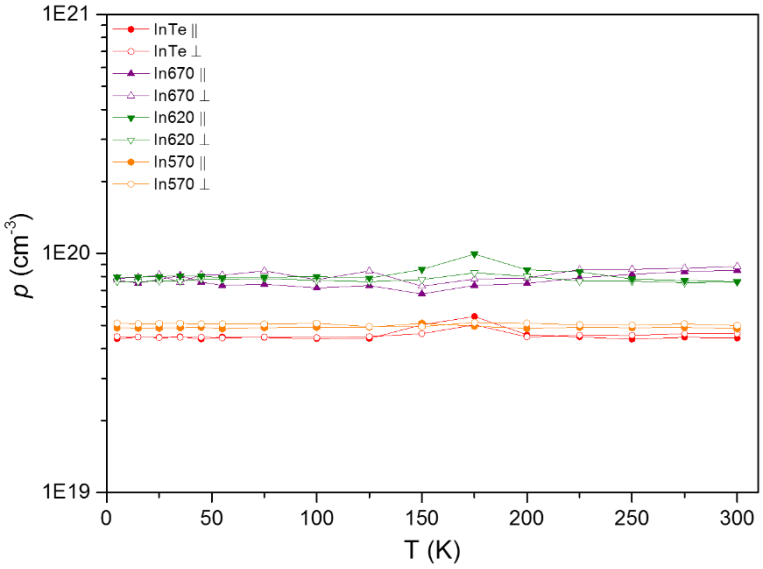

Figure E.5: Low-temperature dependence of the hole concentration p for saturation-annealed InTe samples.

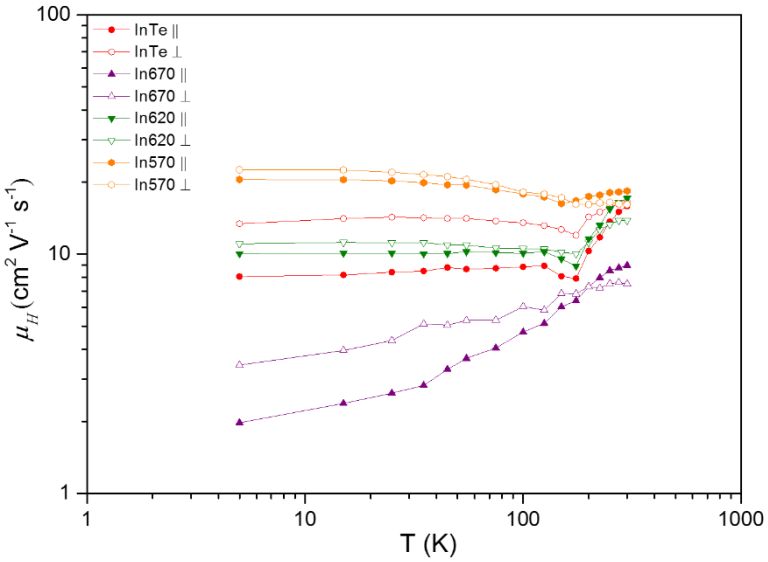

Figure E.6: Low-temperature dependence of the Hall mobility μ_H for saturation-annealed InTe samples.

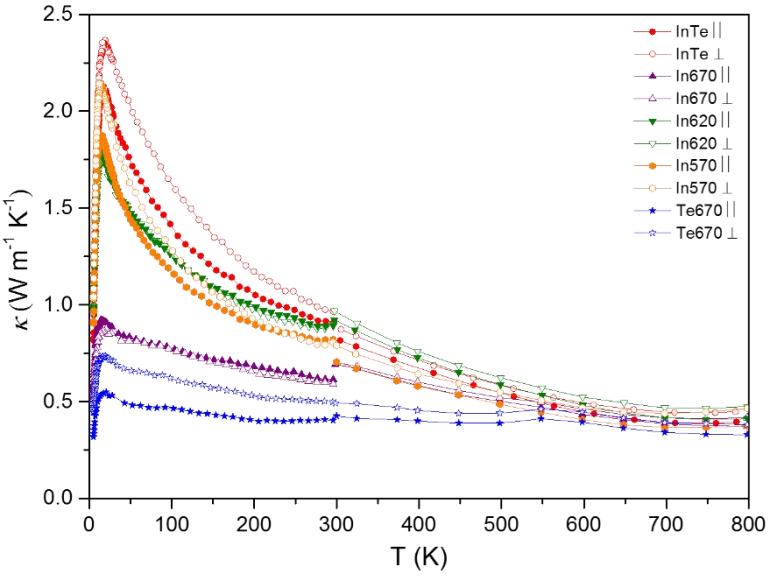

Figure E.7: Temperature dependence of the total thermal conductivity κ for saturation-annealed InTe samples.

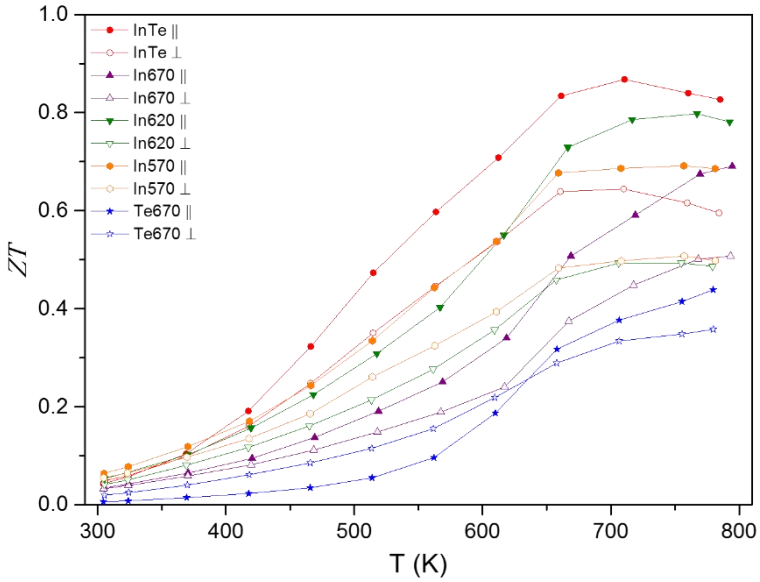

Figure E.8: High-temperature dependence of the dimensionless thermoelectric figure of merit *ZT* for saturation-annealed InTe samples.

Résumé

L'utilisation future de l'énergie impose de trouver des sources d'énergie alternatives qui ont moins d'impact sur l'environnement que les combustibles fossiles. Malgré les problèmes de limitation des ressources énergétiques, environ 70 % de l'énergie consommée dans les industries ou les ménages privés est perdue vers l'environnement. La conversion de cette chaleur perdue en énergie électrique utile contribuerait à réduire notre impact carbone. Une des technologies possibles pour aider à résoudre ce problème consiste à utiliser des dispositifs thermoélectriques. Au cours des dernières années, la thermoélectricité est devenue une technologie verte de premier plan pour la capture de la chaleur résiduelle dissipée afin de produire de l'énergie électrique. Les dispositifs thermoélectriques, qui peuvent convertir directement la chaleur résiduelle en énergie électrique ou vice versa, sont des dispositifs à base de semi-conducteurs qui peuvent être utilisés avec tout type de sources thermiques et présentent de nombreux avantages par rapport aux autres dispositifs de conversion d'énergie. Ces avantages comprennent leur compacité, l'absence de bruit et de vibrations due à l'absence de pièces mobiles, leur fiabilité pour des opérations de longue durée et l'absence d'émissions de gaz à effet de serre. Ces dispositifs peuvent donc être utilisés de manière autonome dans des environnements extrêmes et dans des industries à petite ou à grande échelle. Les dispositifs thermoélectriques, qu'il s'agisse de générateurs ou de réfrigérateurs, peuvent exceller dans les industries qui sont actuellement confrontées au problème du coût élevé et des faibles performances des autres technologies. Les générateurs thermoélectriques (TE) sont utilisés dans divers domaines pour lesquels la fiabilité des dispositifs l'emporte sur leur faible rendement de conversion. L'un des principaux domaines d'application est l'alimentation des sondes en espace profond et des rovers à l'aide de générateurs thermoélectriques à radio-isotopes (RTG) par la NASA depuis 1961. La durée de vie de ces générateurs est comparable à la durée de vie humaine, comme dans l'exemple des missions Voyager 1 et 2 qui ont récemment quitté le système solaire et pour lesquelles les dispositifs TE fonctionnent toujours après 42 ans. La mission la plus récente pour étudier la surface de Mars, Curiosity, est également alimentée par un RTG donnant une puissance électrique de sortie d'environ 110 Watts. Récemment, il a été démontré que l'utilisation de générateurs thermoélectriques dans les automobiles pourrait augmenter l'économie de carburant de 7 à 10 %. La thermoélectricité a également été introduite avec succès dans les générateurs solaires TE et les micro-générateurs où la puissance requise est faible. Les applications de refroidissement thermoélectrique (c'est-

à-dire la réfrigération) ont été utilisées avec succès dans la climatisation, les réfrigérateurs alimentaires et le refroidissement des détecteurs infrarouges de certains appareils électroniques.

Le semi-conducteur binaire PbTe, avec les alliages $Si_{1-x}Ge_x$, est l'un des matériaux les plus connus et les plus fiables pour les RTG en raison de ses hautes performances thermoélectriques et de ses propriétés de transport facilement ajustables. Au cours des dernières décennies, les chercheurs ont pu constamment améliorer le facteur de mérite thermoélectrique adimensionnel, $ZT = \alpha^2 T/\rho\kappa$, des matériaux à base de PbTe pour les applications à moyenne température. Dans cette formule, α est le pouvoir thermoélectrique (ou coefficient Seebeck), T est la température absolue, ρ est la résistivité électrique et κ est la conductivité thermique totale. Ce facteur régit directement l'efficacité des dispositifs thermoélectriques. PbTe est connu depuis longtemps comme un excellent matériau pour les applications thermoélectriques dans la production d'énergie. PbTe et ses dérivés ternaires et quaternaires sont utilisés pour des applications à moyenne température (500 - 800 K) où le matériau thermoélectrique de pointe Bi_2Te_3 ne peut plus être utilisé. Des études récentes ont affirmé que des valeurs de *ZT* très élevées (> 2) peuvent être obtenues dans les composés à base de PbTe. Bien que ce composé ait une structure cubique simple rendant ses propriétés de transport isotropes, la présence de Pb le rend également toxique et, par conséquent, difficile à utiliser à des fins industrielles à grande échelle. Ainsi, la recherche de matériaux de substitution sans Pb a fait l'objet d'intenses efforts expérimentaux. Dans ce contexte, de nombreuses études se sont orientées vers les semi-conducteurs de tellurure sans plomb tels que les composés GeTe ou SnTe. GeTe présente un comportement métallique de type *p* dû à une très forte concentration de trous, ce qui en fait un système très complexe pour modifier et contrôler ses propriétés de transport. De plus, le germanium présente un coût élevé, ce qui rend ce composé moins intéressant pour les applications commerciales. La recherche de matériaux alternatifs sans Pb pour les applications thermoélectriques à moyenne température a été au cœur de cette thèse. Nous avons étudié en particulier deux composés à base de tellure (*X*Te avec *X* = Sn, In) qui présentent des propriétés thermoélectriques très prometteuses.

Le composé SnTe est récemment réapparu comme un remplaçant de premier choix du PbTe en raison de sa structure cristalline cubique et de sa structure de bande de valence similaire. Le SnTe a fait l'objet de recherches intensives au milieu du XXe siècle avant d'être abandonné dans les années 1960 en raison de ses performances thermoélectriques intrinsèquement plus faibles que celles de PbTe. Au cours de la dernière décennie, SnTe est

revenu au premier plan de la recherche en chimie et en physique de la matière condensée en raison de plusieurs caractéristiques physiques intéressantes. Outre sa nature topologique non triviale et l'émergence de la supraconductivité dans des échantillons dopés avec des températures critiques atteignant 4,5 K, une amélioration notable du processus de synthèse et du contrôle de la concentration des trous a conduit à une augmentation spectaculaire de la valeur du *ZT* à haute température.

Au cours de nos travaux, ces prédictions ont été confirmées expérimentalement sur une série d'échantillons polycristallins de composition $Sn_{1.03-x}In_xTe$ dans toute la gamme de composition accessible à pression ambiante (c'est-à-dire pour $0.0 \leq x \leq 0.40$). De manière remarquable, la substitution de Sn par du In induit de profondes modifications de la structure de bandes de valence de SnTe dues à l'apparition d'un niveau résonant, c'est-à-dire d'une distorsion localisée des bandes de valence conduisant à une augmentation spectaculaire des propriétés électroniques (Figure 1). Les caractérisations structurales et chimiques des échantillons par diffraction des rayons X sur poudre (PXRD) et par microscopie électronique à balayage avec spectroscopie des rayons X à dispersion d'énergie (SEM-EDXS) ont confirmé l'insertion réussie des atomes de In dans la structure et la bonne homogénéité chimique des échantillons. Un pouvoir thermoélectrique maximum de 52 $\mu V\ K^{-1}$ a été mesuré pour le composé $Sn_{1.01}In_{0.02}Te$ à 300 K, ce qui représente une augmentation de presque 300 % par rapport au composé binaire $Sn_{1.03}Te$. De façon étonnante, le pouvoir thermoélectrique présente une transition de valeurs positives vers des valeurs négatives en dessous de 100 K dans les échantillons ayant une teneur en In de $0{,}0015 \leq x \leq 0{,}0045$. L'origine physique exacte de ce phénomène reste cependant encore à élucider. Les données de l'effet Hall ont mis en évidence un état de valence In^+ qui n'étaye pas la possibilité d'un effet Kondo de charge. Le rôle du niveau résonant a été démontré comme existant jusqu'à $x = 0{,}05$, concentration au-delà de laquelle ce phénomène tend à disparaître. L'augmentation de la teneur en In au-dessus de $x >$ 20 % entraîne de fortes modifications de la structure de la bande électronique du SnTe. En particulier, un comportement de type *n* a été observé à basse température en accord avec les données de la littérature. Aucune transition supraconductrice n'a été observée pour $x = 0{,}0035$ jusqu'à 0,40 K, ce qui confirme les études antérieures sur ces composés. En revanche, une température de transition supraconductrice atteignant 4,4 K a été observée pour $x = 0{,}4$. À hautes températures, l'impact réduit mais significatif du niveau résonant a été mis en évidence, conduisant à une valeur maximale de *ZT* de 0,75 à 800 K pour $x = 0{,}0035$ (Figure 2). Le rôle bénéfique du niveau résonant pour des applications pratiques a été souligné car il aboutit à des valeurs moyennes élevées de *ZT* sur une plage de température étendue. Nos résultats

fournissent également des preuves solides que les modèles de bande de valence existants pour estimer la contribution de réseau de la conductivité thermique dans ces composés sont inadéquats, car donnant lieu à des nombres de Lorenz trop faibles. Enfin, la compréhension fine de l'impact bénéfique du niveau résonant indique que la sélection d'un co-dopant reste une tâche importante pour éviter le déplacement du potentiel chimique hors de ce niveau.

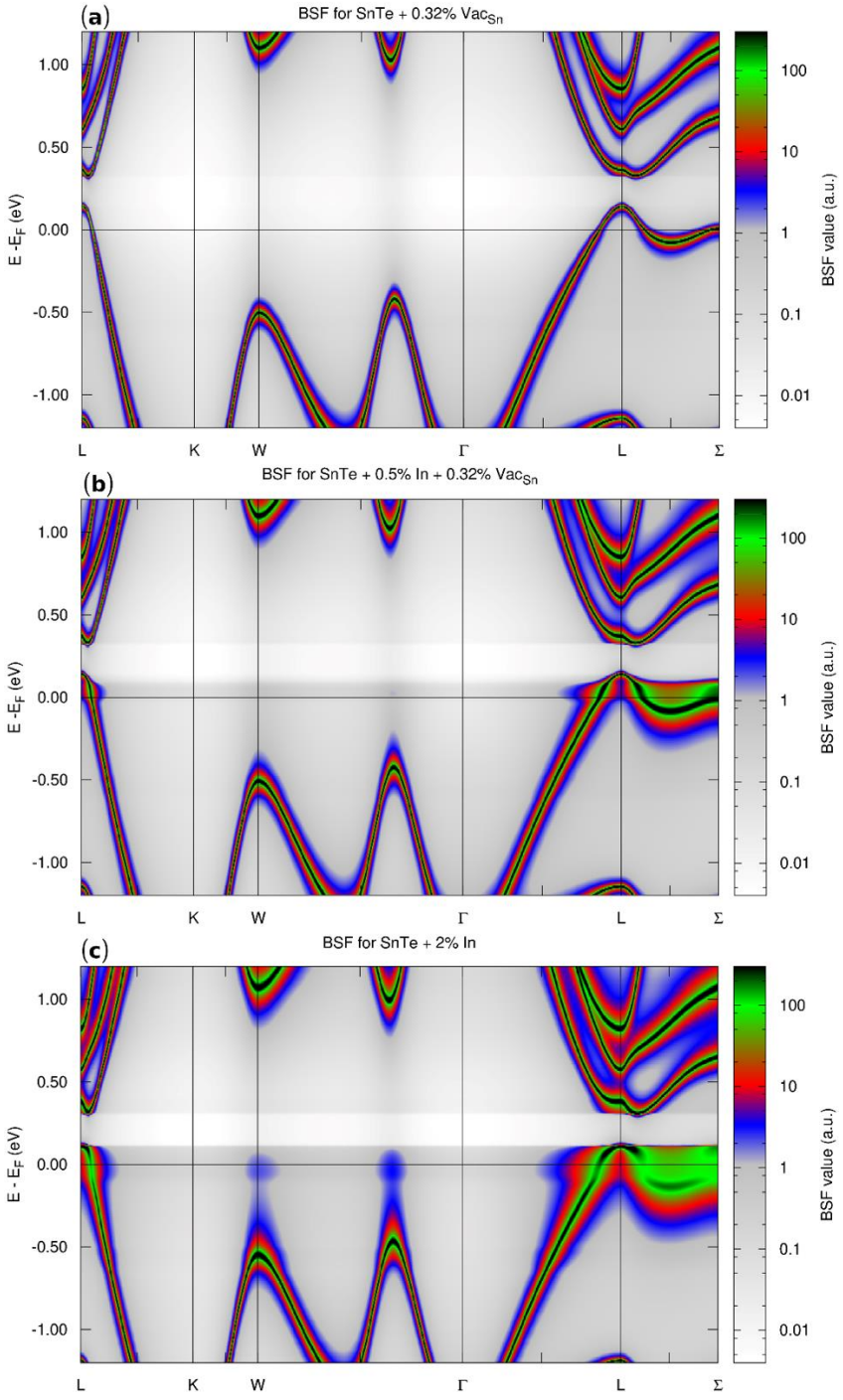

Figure 1 : Projection bidimensionnelle des fonctions spectrales de Bloch dans des directions de haute symétrie pour le SnTe : a) contenant 0,32% de lacunes de Sn ; b) dopé avec 0,5% In et avec 0,32% de lacunes de Sn ; c) dopé avec 2% In.

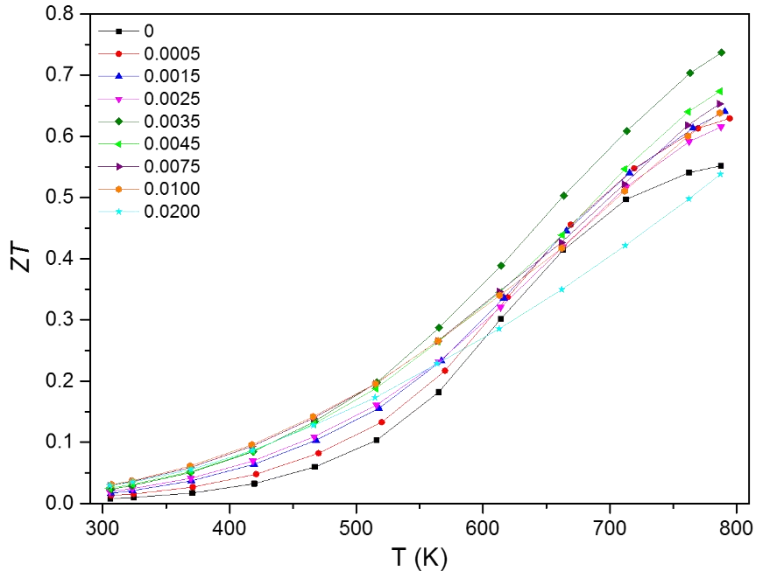

Figure 2 : Dépendance en température du facteur de mérite thermoélectrique adimensionnel *ZT* pour les échantillons $Sn_{1.03-x}In_xTe$ ($0.0 \leq x \leq 0.02$).

Le matériau binaire InTe a fait l'objet de la deuxième partie de cette thèse. Les propriétés physiques du composé InTe sous forme monocristalline et polycristalline a été réalisée sur une large gamme de températures (5 - 800 K). En raison des défauts chimiques (probablement lacunes de In) inhérents à ce composé, la technique de recuit à saturation est également utilisée. Cette technique permet de sonder les écarts maximums par rapport à la stœchiométrie idéale du côté riche en In et en Te du solidus. Les propriétés de transport mesurées ont été discutées sur la base de calculs de la structure de bande électronique et phononique. Les propriétés de transport des échantillons polycristallins tels que préparés et après des recuits de saturation ont été mesurées, soulignant en particulier la présence possible d'une transition structurelle à basse température. Ces travaux ont confirmé qu'InTe est un matériau thermoélectrique prometteur pour des applications dans la production d'énergie à haute température. La structure de la bande électronique et phononique sont en excellent accord avec les données de la littérature. Un large monocristal d'InTe, d'une longueur d'une dizaine de centimètre, a été synthétisé en utilisant la technique de Bridgman-Stockbarger. Cette synthèse a permis une étude détaillée des propriétés cristallographiques en utilisant plusieurs techniques de diffraction des rayons X. Les propriétés de transport ont été étudiées sur une large gamme de températures (2 - 800 K) afin de mettre en évidence ses propriétés physiques de base. Une anisotropie claire a été observée dans l'InTe monocristallin le long des deux directions mesurées. Une conductivité thermique de réseau extrêmement faible de 0,25 W m^{-1} K^{-1} a été obtenue pour l'échantillon le long de la direction cristalline [110], une valeur remarquable pour un réseau cristallin parfaitement ordonné. Une

valeur de *ZT* élevée de 0,7 à 780 K a été obtenue pour un échantillon mesuré le long de la cristalline [110] (Figure 3).

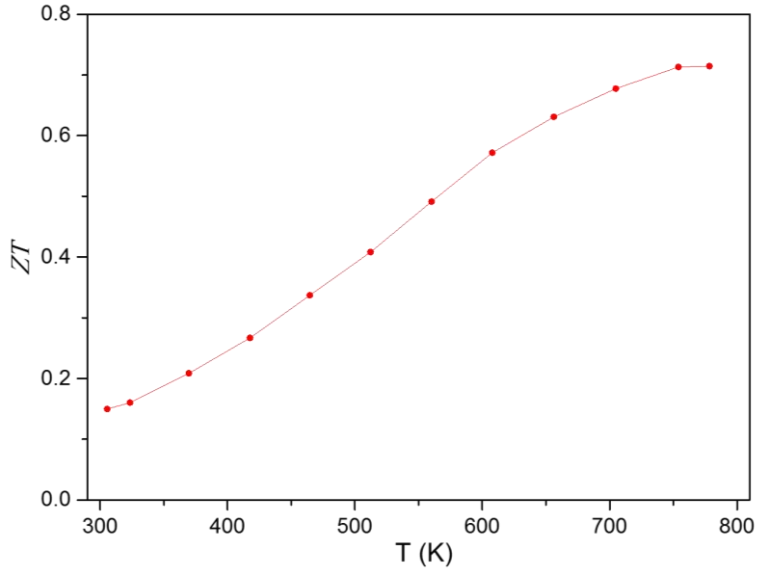

Figure 3 : Dépendance en température du facteur de mérite thermoélectrique adimensionnel *ZT* pour l'InTe monocristallin selon la direction cristalline [110].

En plus de cet échantillon monocristallin, des échantillons polycristallins ont été préparés aboutissant à une valeur de *ZT* très élevée de 0,9 à 710 K. Pour confirmer la possible hors-stœchiométrie de ce composé, des échantillons polycristallins ont été soumis à la technique du recuit de saturation. Cette étude a montré en outre qu'il est possible d'obtenir différentes concentrations de trous en faisant varier la température de recuit. D'après nos résultats, il n'est cependant pas clair si une transition structurelle en dessous de 185 K, suggérée dans la littérature, se produit réellement dans ce composé. Les propriétés de transport remarquables et intrigantes de ce composé appellent clairement à de plus amples études théoriques et expérimentales. En particulier, diverses stratégies de dopage pourraient être utilisées pour améliorer davantage ses performances thermoélectriques. De plus, la détermination du type de défaut dominant en fonction de la concentration de trous justifie des calculs d'énergie de formation des défauts. La très faible conductivité thermique de réseau de ce composé fait de l'étude de sa dynamique de réseau par diffusion inélastique des neutrons une étude très intéressante. Enfin, la question de savoir si des échantillons de type *n* peut être synthétisés reste ouverte.